



HAL
open science

Numerical modeling of the spark plasma sintering process

Pamela Mondalek

► **To cite this version:**

Pamela Mondalek. Numerical modeling of the spark plasma sintering process. Other. Ecole Nationale Supérieure des Mines de Paris, 2012. English. NNT : 2012ENMP0084 . pastel-00820191

HAL Id: pastel-00820191

<https://pastel.hal.science/pastel-00820191>

Submitted on 3 May 2013

HAL is a multi-disciplinary open access archive for the deposit and dissemination of scientific research documents, whether they are published or not. The documents may come from teaching and research institutions in France or abroad, or from public or private research centers.

L'archive ouverte pluridisciplinaire **HAL**, est destinée au dépôt et à la diffusion de documents scientifiques de niveau recherche, publiés ou non, émanant des établissements d'enseignement et de recherche français ou étrangers, des laboratoires publics ou privés.

Ecole doctorale n°364 : Sciences Fondamentales et Appliquées

Doctorat ParisTech

T H È S E

pour obtenir le grade de docteur délivré par

l'École nationale supérieure des mines de Paris

Spécialité “ Mécanique Numérique ”

présentée et soutenue publiquement par

Pamela MONDALEK

le 7 décembre 2012

Numerical modeling of the spark plasma sintering process

Modélisation numérique du procédé de frittage flash

Directeur de thèse : **Michel BELLET**

Encadrement de la thèse : **Luisa SILVA**

Jury

M. Umberto ANSELMI-TAMBURINI, Professeur, Département de Chimie, Université de Pavia

M. Jose CESAR DE SA, Professeur, IDMEC / FEUP, Université de Porto

M. Frédéric BERNARD, Professeur, LRRS, Institut Carnot de Bourgogne, Dijon

M. Alain COURET, Directeur de Recherche CNRS, CEMES Toulouse

M. Nikhil KARNATAK, Ingénieur de Recherche, Plateforme CEA MECACHROME, Vibraye

Rapporteur

Rapporteur

Examineur

Examineur

Examineur

T
H
È
S
E

Acknowledgments

Mes premiers remerciements iront tout naturellement à mon directeur de thèse Michel Bellet et ma co-directrice de thèse Luisa Silva. Je les remercie pour le soutien, les conseils et leur disponibilité. Merci de m'avoir guidé et conseillé. Michel, je rajouterai un grand merci pour les relectures minutieuses du manuscrit.

J'adresse mes sincères remerciements à Frédérique Bernard pour l'honneur qu'il m'a fait de présider mon jury. Je remercie également José Cesar De Sa et Umberto Anselmi Tamburini d'avoir accepté d'être les rapporteurs de cette thèse ainsi que Alain Couret et Nikhil Karnatak d'avoir accepté de juger cette thèse.

Je remercie également l'équipe du CEMES, Jean-Philippe Monchoux, Lise Durand et plus particulièrement Thomas Voisin pour tous nos échanges sur le SPS. Thomas merci pour tous les essais et pour ta réactivité.

Je remercie aussi Marie-Françoise, Françoise, Geneviève, Florence, Carole, Murielle, Brigitte et Sylvie.

Je voudrais remercier Emile, Larbi, Greg, Raph, Steph, Karim, Nadine, Ziad, avec vous j'ai partagé les hauts et les bas de la thèse, des soirées, des vacances... Vous savez à quel point votre amitié a compté.

Je remercie aussi ma famille pour leur soutien et leur aide et surtout leurs encouragements durant la période de rédaction. Enfin, je remercie la personne qui sans elle ce travail n'aurait pas pu être accompli, mon Touti, merci pour toutes les longues explications et discussions sur la mécanique et les matériaux et pour avoir été là, tout le temps. Inutile de te dire combien ta présence m'est indispensable.

Merci...

Table of contents

1	Introduction	1
	Bibliography	5
2	Bibliography review	7
2.1	Introduction	9
2.2	Process description	9
2.3	Resistance sintering history	11
2.4	Mechanisms during densification by Spark Plasma Sintering	14
2.5	State of the art of the process simulation	18
2.6	Conclusion	27
	Bibliography	31
3	Numerical modeling of the coupled thermal electrical problems	37
3.1	Introduction	40
3.2	Monolithic approach used in CimLib [®]	41
3.2.1	Level set method	41
3.2.2	Mixing laws	42
3.2.3	Anisotropic mesh adaptation	42
3.3	Modeling of the electrical problem	44
3.3.1	Governing equations	44
3.3.2	Weak form and discretization of the electrical problem	45
3.3.2.1	Discretization	45
3.4	Modeling of the thermal problem	46
3.4.1	Governing equations	46
3.4.1.1	Thermal boundary conditions	46
3.4.2	Weak form and discretization of the thermal problem	47

3.4.2.1	Discretization	47
3.5	Heating by Joule effect: Numerical tests	49
3.5.1	Numerical validation of Ohm's law	49
3.5.1.1	Modeling of Joule heating of a single material	49
3.5.1.2	Modeling of Joule heating of two materials in contact	51
3.6	Simulation of thermal electrical coupling for a simplified SPS geometry	53
3.6.1	Numerical results: <i>Electric problem</i>	55
3.6.2	Influence of the source term	59
3.6.3	Numerical results: <i>Temperature distribution</i>	60
3.6.4	Influence of thermal dependence of physical properties	62
3.7	Simulation of electrical thermal coupling: Comparison between two codes and experiments	64
3.7.1	Numerical results: <i>Electrical problem</i>	66
3.7.2	Numerical results: <i>Thermal problem</i>	67
3.8	Conclusion	73
Bibliography		75
4	Numerical modeling of powder compaction	77
4.1	Introduction	79
4.2	State of the art: Modeling of powder sintering	79
4.3	Modeling of the mechanical problem	82
4.3.1	Modeling of the compressible thermal viscoplastic behaviour based on Abouaf law	82
4.3.2	Momentum equation	85
4.3.2.1	Weak formulation and discretization	85
4.3.3	Mass conservation	89
4.3.3.1	Weak formulation and discretization	89
4.4	Numerical simulation of powder compaction	90
4.4.1	Simulation of a powder free uniaxial compression	91
4.4.1.1	c and f constant	91
4.4.1.2	c and f updated with the relative density	94
4.4.2	Simulation of a powder die compaction	95
4.4.2.1	c and f constant	95
4.4.2.2	c and f updated with the relative density	97

4.4.2.3	From Lagrangian to Eulerian approach	98
4.4.3	Conclusion	99
4.5	Numerical simulation of coupled electric thermal mechanical problems during SPS	100
4.5.1	Introduction	100
4.5.2	Equations and algorithm of the simulation	100
4.5.3	Mesh adaptation with tools motion	104
4.5.4	Symmetry due to geometry	105
4.5.5	Dependence of conductivities with powder relative density	107
4.6	Conclusion	113
Bibliography		115
5	Modeling of friction during SPS using the Eulerian approach	119
5.1	Introduction	121
5.2	Friction law	122
5.2.1	Powder/Wall friction models	124
5.2.2	Viscoplastic friction model for powder compaction	125
5.3	Modeling of friction in the Eulerian monolithic approach	126
5.3.1	Introduction	126
5.3.2	Description of the mechanical model	126
5.3.3	Description of the Eulerian model	127
5.3.4	Description of the Lagrangian model	129
5.3.5	Numerical study of the Eulerian approach	131
5.3.6	Possible developments in the Eulerian model	140
5.4	Conclusion	141
Bibliography		143
6	Inverse analysis and parameters identification	145
6.1	Introduction	147
6.2	Identification of the behavior law parameters: Required experiments	147
6.2.1	Identification of consistency and strain rate sensitivity on dense material	148
6.2.2	Identification of Abouaf functions	149
6.2.2.1	Hot isostatic pressing: identification of f	151

6.2.2.2	Uniaxial compression with constant lateral pressure	152
6.2.3	Limitation of the Paterson machine	156
6.2.3.1	Description of Paterson machine	156
6.2.3.2	Suggested experiments	158
6.2.3.3	Preliminary experiments	163
6.3	Identification of Abouaf functions using SPS	165
6.3.1	SPS experiments and measurements	166
6.3.2	Calibration of c and f using Matlab	175
6.3.2.1	Algorithm used in Matlab	177
6.3.3	Calibration of the friction coefficient	181
6.3.4	Conclusion	188
6.4	Numerical simulation of the spark plasma sintering test	192
6.4.1	Description of the models	192
6.4.2	Results	196
6.5	Conclusion	202
	Bibliography	205
7	Conclusion and perspectives	207
	Bibliography	213
	Appendix 1: Paterson preliminary tests	215

List of Figures

1.1	Air traffic growth from 1970 till 2008[1]	1
2.1	Typical electric current waveforms applied in SPS processes: (a) constant DC; (b) AC; (c) pulsed DC and (d) pulsed DC + DC [34]	10
2.2	Spark Plasma Sintering set up	11
2.3	Representative scheme of the set up invented by Weintraub and Rush [50] .	12
2.4	A fully automated tunnel-type sintering system developed by <i>Fuji Electronic Industrial Co., Ltd.</i> [1]	13
2.5	Number of publications related to sintering under electric current [33] . . .	13
2.6	Resistance sintering processes designation [33]	14
2.7	Mechanisms of sintering [20]	15
2.8	Effect of pulses on sintering mechanisms [43]	16
2.9	Neck formation between two particles as described by Tokita [43]	17
2.10	Set up designed by Yanagisawa <i>et al.</i> to study the effect of sparks on neck formation between powder particles [53]	18
2.11	Computational domain considered by Yoneya <i>et al.</i> [54] to model electrical and thermal problems summarized schematically by Orru <i>et al.</i> [33]. A 2D axial symmetry is considered	19
2.12	Computational domain considered by Wang <i>et al.</i> [48] to model electrical and thermal problems summarized schematically by Orru <i>et al.</i> [33]	20
2.13	Computational domain considered by Matsugi <i>et al.</i> [26] to model electrical and thermal problems	21
2.14	Current distribution in the SPS apparatus computed by Anselmi-Tamburini <i>et al.</i> [3] using the commercial software CFD-AFE+ : the 3D model has 35352 nodes with hexagonal and polygonal cells	22
2.15	Power dissipated by Joule effect computed by Anselmi-Tamburini <i>et al.</i> on the left for alumina, and on the right for copper [3]	23
2.16	Temperature gap between the center of the specimen and the die surface versus the temperature measured at the die surface: Comparison between experiments and simulation when neglecting or considering thermal contact resistance [55] using the commercial software Abaqus	24

2.17	Hydrostatic stress distribution inside alumina (a) and copper (b). Hydrostatic stress plotted over the lines AB and CD for alumina (c) and copper (d) [32]	25
2.18	Temperature plotted over the radial distance in the mid-thickness of the specimen for the different applied pressures computed by Song <i>et al.</i> [41] .	26
2.19	Temperature and relative density evolution when sintering a <i>TiAl</i> powder by SPS process	28
3.1	Thermal-electrical coupling scheme during spark plasma sintering process .	40
3.2	Comparison of the transition around the interface between two subdomains with and without anisotropic mesh adaptation	43
3.3	Representative scheme of the remeshed zone around the interface with the corresponding parameters	44
3.4	2D geometry with boundary conditions of the electrical problem	50
3.5	2D geometry with two materials and the boundary conditions of the thermal-electrical problem	51
3.6	Variation of electrical potential along the vertical direction	52
3.7	Distribution of the temperature ($^{\circ}C$) in the two domains	53
3.8	Comparison of the computational errors on the electrical potential using arithmetic mixing law and an harmonic mixing law for the electrical conductivity	53
3.9	Geometry of the apparatus considered in order to compare with literature [3] and the variation of the temperature imposed at the lower and upper surface of graphite spacers	55
3.10	Representation of the 3D geometry with an overview on the mesh with anisotropic remeshing around the powder/die interface	56
3.11	Influence of the electrical conductivities on the distribution of the norm of current density when thermal dependency is neglected	57
3.12	Radial variation of the density of the electrical current for the three samples: nickel, graphite and alumina from the centre of the sample towards the edge of the die, at mid-height of the sample	57
3.13	Radial variation of the electrical current density for nickel specimen from the center of the sample towards the edge of the die for different thickness considered in the mixing laws for the electric conductivity (Equation 3.7) .	58
3.14	Distribution of the source term of the heat equation inside the simplified SPS apparatus	59
3.15	Distribution of the source term of the heat equation along the vertical direction of the apparatus and a zoom inside the sample	60
3.16	Temperature evolution with time, at the center of the specimen ($r = 0$ mm, $H = 5$ mm) and at the center of the piston ($r = 0$ mm, $H = 10$ mm) .	61
3.17	Time evolution of temperature distribution ($^{\circ}C$) for nickel sample	61

3.18	Comparison of CimLib [®] thermal results and Abaqus results [3]: Temperature plotted along the vertical direction of the apparatus for Nickel specimen	62
3.19	Comparison of CimLib [®] thermal results and Abaqus results [3]: Temperature plotted along the vertical direction of the apparatus for Graphite specimen	62
3.20	Comparison of CimLib [®] thermal results and Abaqus results [3]: Temperature plotted along the vertical direction of the apparatus for alumina specimen	63
3.21	Variation of physical properties of nickel with temperature [12]	64
3.22	Temperature profile (in K) along the apparatus considering a nickel specimen with thermal dependent physical properties: a) $t = 1$ s, b) $t = 5$ s, c) $t = 300$ s,	65
3.23	Comparison of temperature evolution with time when considering constant physical properties or temperature dependent physical properties	66
3.24	3D Geometry used in the simulations with the mesh generated and a zoom in the region of the sample showing the refined elements around the sample/matrix interface)	67
3.25	Electrical conductivity of the global simulated assembly. The different components (including the TiAl disc sample at the center) can be distinguished through the display of the distribution of their electrical conductivity ($\Omega^{-1} \cdot \text{m}^{-1}$)	68
3.26	Distribution of the density of the electric current ($\text{A} \cdot \text{m}^{-2}$)	68
3.27	Evolution of the electrical conductivity ($\frac{1}{\Omega \cdot \text{m}}$) of graphite, <i>TiAl</i> and alumina with temperature	69
3.28	Variation of the current density along the radial direction from the center of specimen up to the edge of the die (A/mm^2)	70
3.29	Comparison of the variation of temperature along the vertical axis for the <i>TiAl</i> sample every 10 s	70
3.30	Comparison of the distribution of temperature along the vertical axis for the <i>TiAl</i> sample	71
3.31	Variation of temperature in the radial direction in <i>TiAl</i> specimen and graphite die after 10 s and 300 s	71
3.32	Variation of temperature in the radial direction of the alumina specimen after 10 s and 300 s	72
4.1	" <i>Densification map for aluminum powder</i> "[28]	81
4.2	Comparison of the experimental and finite element results by the models of Abouaf and McMeeking issued from the work of Kim and Jeon [20] . . .	82
4.3	Schematic representation of the variation of coefficients c and f versus the relative density	84
4.4	Tetrahedral $P1^+$, $P1$ mini-element	87
4.5	Powder uniaxial compaction	91

4.6	Isovalues of the vertical component of velocity and velocity vectors: a) at $t = 0 s$ and b) $t = 15 s$	93
4.7	Vertical stress (in Pa) plotted over time computed with CimLib [®] and analytically with c and f constant	93
4.8	Comparison of the radius evolution with time when computed with CimLib and analytically	94
4.9	Vertical stress (in Pa) plotted over time computed with CimLib [®] and R2Sol when c and f are updated according to density evolution	95
4.10	Powder die compaction	95
4.11	Vertical velocity field isovalues and velocity vectors for powder die compression when c and f are constant: a) at $t = 0 s$ and b) at $t = 20 s$	96
4.12	Vertical stress plotted over time: comparison between CimLib [®] results and analytic solution for powder die compression when c and f are constant	97
4.13	Vertical stress and relative density plotted over time: comparison between CimLib [®] results and analytic solution calculated with Matlab for powder die compression when c and f are updated with density	98
4.14	3D geometry considered in the eulerian approach for solving the powder die compaction test with the mesh an anisotropic elements in the neighborhood of the interface	99
4.15	Vertical stress plotted over time: comparison between CimLib [®] results using lagragian and eulerian approach and analytic solution for powder die compression when c and f are constant	100
4.16	Geometry of the SPS set-up with the generated mesh used in the simulation and a zoom in the region of the sample showing refined elements around the sample/matrix interface (radius of the sample $18mm$, of the matrix $35mm$)	101
4.17	Resolution algorithm	103
4.18	Example of a $2D$ geometry with and without the void around the mould showing the anisotropic elements added.	104
4.19	Regions of the geometry simulated where mesh velocity is controlled to update the coordinates	105
4.20	Regions of the geometry simulated where mesh velocity is controlled to update the coordinates: a zoom on the top corner where the piston penetrates in the mould	106
4.21	Temperature variation along the vertical axis for the TiAl sample for different time steps showing the effect of the symmetry	106
4.22	Temperature isovalues (in K) after $900 s$ when the symmetry is no longer respected	107
4.23	Temperature variation, consistency variation and relative density along the vertical axis inside the TiAl sample at $t = 900s$	108

4.24	Radial variation of current density when considering or neglecting the dependence on the porosity of thermal and electrical conductivities	109
4.25	Radial variation of the source term of heat equation at 100 s when considering or neglecting the dependence on the porosity	110
4.26	Variation of the thermal and electrical conductivities with relative density when temperature is fixed at $1000^{\circ}C$	111
4.27	Radial variation of temperature at different time steps when considering or neglecting the dependence on the porosity	112
5.1	Distribution of the porosity on a longitudinal section of the powder cylinder at $T = 1050^{\circ}C$ for an interrupted SPS cycle	121
5.2	Graphic representation of the different friction laws	123
5.3	Scheme of the geometry considered in the work of Cunningham <i>et al.</i> [5] to determine the friction coefficient	125
5.4	Geometry and dimensions of the set up and anisotropic meshing around the interface	127
5.5	Schematic representation of the boundary layer	128
5.6	Geometry of the set up with the intermediate layer incorporated between the mould and powder	129
5.7	Geometry of the Lagrangian model with the dimensions of the powder cylinder	130
5.8	Profile of the vertical velocity in the sample computed with the Lagrangian approach imposing a friction condition for three different coefficient $\alpha_{f1} = 0.7$, $\alpha_{f2} = 1.5$ and $\alpha_{f3} = 3.5$	131
5.9	Representation of the remeshing around the interface and the boundary layer. In the bottom resulting consistency from mixing law 6.51 ($\text{Pa}\cdot\text{s}^{-\text{m}}$). The coloured anisotropic elements are intercepted by the interface	132
5.10	Contour lines of the vertical velocity (m/s) for the Eulerian and Lagrangian model and lines representing the plot points	133
5.11	Vertical velocity plotted over the vertical distance (at $r = 17.5$ mm, green line): the results issued from two simulations using the Eulerian model for two consistencies and a fixed thickness $e = 1.07$ mm are compared with the results issued from the Lagrangian model for $\alpha_f = 1.5$	134
5.12	Comparison of the vertical velocity plotted over the radial distance (at $z = 10$ mm, red line) for $\alpha_f = 1.5$ in the Lagrangian model and $e = 1.07$ mm in the Eulerian model and for two consistencies	134
5.13	Zoom of the chart of Figure 5.12 at the region of the interface between the powder and boundary layer to the transition of the vertical velocity	135
5.14	Distribution of the vertical velocity computed using the Eulerian approach and a zoom on the transition inside the layer for $\alpha_f = 1.5$	135

5.15	Calculated error using expression 5.34 for $\alpha_f = 0.7$ and $e = 2.2$ mm testing different consistencies \tilde{K} in the boundary layer	136
5.16	Variation of the selected \tilde{K} versus the different friction coefficient for the three fixed thicknesses (here given in mm)	137
5.17	The inverse algorithm used for the identification of the parameters of the functions f_1 or f_2 or f_3 , once identified the function giving the lowest error is chosen later on for ulterior works	138
5.18	The interval of initial data of $x = (a, b, c)$ for minimizing the cost function of f_3	138
5.19	Different starting points, cost functions and identified parameters of the function f_3	139
5.20	Different starting points, cost functions and identified parameters of the function f_3	140
6.1	Required experiments in order to identify the four functions of the Abouaf model for compressible viscoplasticity	148
6.2	Example of the curve of stress plotted over the strain rate for a given temperature	149
6.3	Stress plotted over the strain rate for different temperatures. Results taken from literature	150
6.4	Pressure and temperature profiles applied in the identification experiments	150
6.5	Hot isostatic pressing	151
6.6	The relative density plotted over time for each couple (T, P) . Measurements issued from interrupted tests are interpolated, the functions allow computing the derivative $\dot{\rho}_r$ and the Abouaf function f [6]	153
6.7	Abouaf function plotted over the relative density [6]	153
6.8	Triaxial compression test with constant lateral pressure	153
6.9	The Paterson machine located at P' institute	156
6.10	Representative scheme of the Paterson machine	157
6.11	The set up inside of the machine	157
6.12	Temperature and pressure applied in the simulation of hot isostatic compression	158
6.13	Variation of temperature, pressure and porosity when the slope of pressure is 5 MPa/s and the slope of temperature 0.1°C/s	160
6.14	Variation of temperature, pressure and porosity when the slope of pressure is 5 MPa/s and the slope of temperature 20°C/s	161
6.15	Comparison of the evolution of the average porosity with time when applying different maximum pressure	161
6.16	Comparison of the evolution of the average porosity with time for different coefficients k_f and α	162

6.17	Experimental design proposed at CEMEF to identify About functions using the Paterson machine	163
6.18	Shape of the sample after applying the pressure (100 MPa, then 200 MPa, then 300 MPa during 30 min for each) at room temperature. Initial density 71.74%	164
6.19	The set up when the experiment is interrupted at 680°C, the circle shows the crack that occurs and causes the leak	165
6.20	The experiment set up when interrupted at 600°C because of the aluminium cover break, the leak mark is visible on the photo of the bottom	166
6.21	Photographs of the experimental set up: $\phi = 8\text{ mm}$, $\phi = 36\text{ mm}$ with the graphite felt before heating and $\phi = 36\text{ mm}$ with the graphite felt at $t = 15$ min	167
6.22	Dimensions of the samples and tooling. NB: the height of the sample is relative to its dense state at time=0	168
6.23	SPS cycles applied on Sample A: $h = 13.6\text{ mm}$, $\Phi = 8\text{ mm}$ and used in the identification experiments	168
6.24	SPS cycles applied on Sample B: $h = 8\text{ mm}$, $\Phi = 36\text{ mm}$ and used in the identification experiments	169
6.25	SPS cycles applied on Sample C: $h = 3\text{ mm}$, $\Phi = 36\text{ mm}$ and used in the identification experiments	169
6.26	Representative scheme of the height evolution during compaction	170
6.27	Evolution of the trial test displacement with time when the set up is composed of the tooling corresponding to the sample A $\phi = 8\text{ mm}$ and $h_f = 13.6\text{ mm}$	171
6.28	Evolution of the trial test displacement with time when the set up is composed of the tooling corresponding to the sample B $\phi = 36\text{ mm}$ and $h_f = 8\text{ mm}$	172
6.29	Evolution of the displacement during the trial test and during sintering the $\phi 8$ sample with and without correction	172
6.30	Experimental relative density plotted over time for the different interrupted cycles and the values measured at the end of the experiments represented with a margin of error	173
6.31	Cut in the transverse direction at the middle of the two samples in order to measure porosity distribution by the SEM	174
6.32	Porosity distribution when the cycles are interrupted at $T = 1050^\circ\text{C}$ and $T = 1110^\circ\text{C}$ for the $\Phi 36/h3$ sample	175
6.33	Transformation of the SEM image to black and white using the software Gimp	176
6.34	Grid covering the image used to compute the porosity rate represented by the percentage of black space in the squares of the grid	176

6.35	Grid covering the image used to compute the porosity and porosity distribution represented using Origin software before adjustment	177
6.36	Algorithm used in Matlab to identify Abouaf functions using the analytic solution	179
6.37	Variation of Abouaf functions with relative density for different set of parameters k_f α_c	179
6.38	Evolution of the relative density for different set of parameters k_f and α_c : On top for the sample $\phi 8/h13.6$ and bottom $\phi 36/h8$	180
6.39	Evolution of the imposed velocity for different set of parameters k_f and α_c : On top for the sample $\phi 8/h13.6$ and bottom $\phi 36/h8$	181
6.40	Comparison of the evolution of relative density measured during the different interrupted cycles and computed with Matlab when using the optimum Abouaf functions ($k_f = 1.3$, $\alpha_c = 10$): a) Sample A $\phi 8/h13.6$, b) sample B $\phi 36/h8$, c) sample C $\phi 36/h3$	182
6.41	Experimental velocity and its linearization when temperature reaches the 660°C in the mould equivalent to 700°C in the centre of the powder for the sample $\phi 8/h13.6$	183
6.42	Experimental velocity and its linearization when temperature reaches the 660°C in the mould equivalent to 700°C in the centre of the powder for the sample $\phi 36/h8$	183
6.43	Sample $\Phi 8/h13.6$: Distribution of relative density measured experimentally and computed with frictionless condition or with friction for $\alpha_f = 1.5$ and for $\alpha_f = 3.5$: on the left when the sample height is equal to 17.6 mm, in the center when the sample height is equal to 16 mm and on the right when the sample height is equal to 14.8 mm	186
6.44	Sample $\phi 8/h13.6$: Comparison of density gradient, maximum and minimum relative density in the sample for the experimental results and simulations when a frictionless condition is applied, a friction with $\alpha_f = 1.5$ and a friction with $\alpha_f = 3.5$	186
6.45	Sample $\Phi 36/h8$: Distribution of relative density measured experimentally and computed with frictionless condition or with friction for $\alpha_f = 6.6$: on top $h = 9.6$ mm, on the bottom $h = 8.4$ mm	189
6.46	Comparison of the distribution of relative density issued from the experiment when using two different grids in GIMP, the sample is $\Phi 8/h13.6$ for $h = 16$ mm: a) coarse grid, b) fine grid	190
6.47	generated mesh used in the simulation and a zoom in the region of the sample showing refined elements around the sample/matrix interface: a) sample $\Phi 8/h13.6$, b) sample $\Phi 36/h8$	193
6.48	SPS apparatus and a zoom on the heated apparatus with the graphite felt surrounding the mould [3]	194

6.49	Representative scheme of the mould/graphite felt interface	194
6.50	Regions of the geometry simulated where mesh velocity is controlled to update the coordinates	195
6.51	Comparison of the regulated temperature the experiment and the simulation	196
6.52	Comparison of the regulated vertical stress between the experiment and the simulation	197
6.53	Comparison of the evolution of the vertical velocity (a) and average relative density (b) between simulation and and experiments for sample $\Phi 8/h13.6$.	198
6.54	Comparison of the evolution of the vertical velocity (a) and average relative density (b) between simulation and and experiments for sample $\Phi 36/h8$. .	199
6.55	Distribution of vertical velocity for sample $\Phi 36/h8$ and a zoom on the transition in the boundary layer: a)vertical velocity and b) relative density	200
6.56	Distribution of relative density for sample $\Phi 8/h13.6$	201
6.57	Distribution of relative density for sample $\Phi 36/h8$	201

Chapter 1

Introduction

In the last decades, the increasing of air traffic together with the number of individual vehicles has stimulated the research in the energy, engines, and more generally transportations fields. The chart of Figure 1.1 shows the air traffic growth from 1970 till 2008. The number of annual departures is four times higher in 2008 than in 1970. Researchers are aware of the limited availability of low-cost fuels and the effects on the environment. They are interested in reducing the transportation costs as well as polluting emissions. Materials research is a major contributor to the improvement of performance, energy efficiency and mass reduction, both in internal combustion engines and turbo-engines. In particular, alloys like intermetallics may lead to significant benefits thanks to their physical properties like high mechanical and temperature resistance and low density. These materials should replace the currently used materials such as steels and superalloys which have much higher densities.

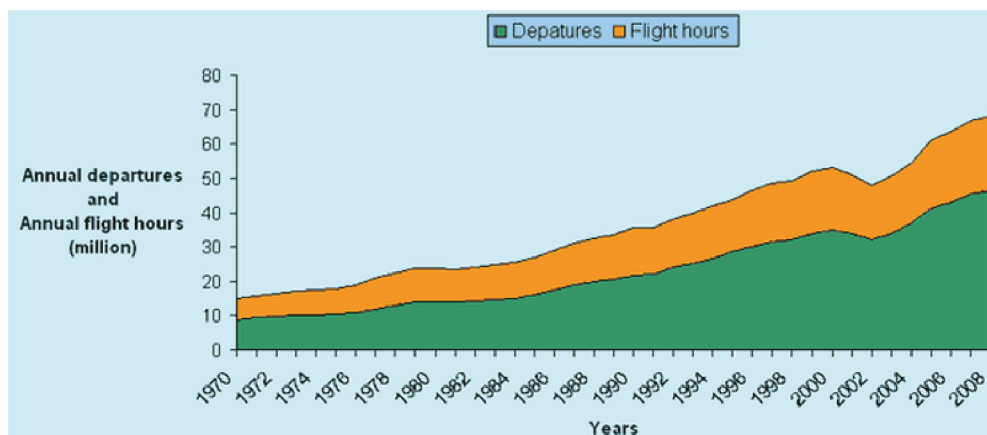


Figure 1.1: Air traffic growth from 1970 till 2008[1]

However, the use of intermetallics is limited by their low ductility that should be improved. Besides, their manufacturing is expensive because of their high melting point and

the necessity to control microstructure and homogeneity. For that reason, the development of a processing route for these intermetallic alloys is of prime importance for the development of their applications in engines. The developed process should enhance the physical properties of the materials comparing to the conventional processes and should be cost-effective.

Intermetallic alloys are difficult to form with conventional techniques such as casting process due to their different melting temperatures. During solidification, structural heterogeneities occur and these are detrimental for mechanical properties. In that respect, powder metallurgy (PM) is a very promising route for intermetallic materials to avoid the macro-segregation and reduce solidification texture. However, the conventional processes for powder compaction, such as hot isostatic pressing, are expensive since they require numerous time consuming steps from raw materials to final components.

Hot isostatic pressing (HIP) is one of the most commonly used processes in PM. HIP is a forming densification process, using gas or liquid under very high pressure. Isostatic pressure is applied uniformly on all sides of the object eliminating the porosity while approaching its net shape. This process presents many advantages. However, a cycle can last three hours, eight hours or even more because of the indirect heating technique. Spark plasma sintering (SPS) process is a revolutionary consolidation technique that appeared in the early nineties. This process consists in sintering a powder placed in a graphite die when heating it directly by Joule effect. This process attracts engineers because of its shorter time cycles. Powder is sintered in about 20 min. An electric current goes through the tools and the powder (if it is electrically conductive) which makes heating much more faster than in HIP. The short cycles are also advantageous concerning the microstructure. It allows the densified materials to conserve the fine initial microstructure of the powder.

The work of this thesis is a part of the IRIS project: Innovative manufacturing Route for Intermetallic alloys by spark plasma net Shaping. IRIS project is supported by the French agency of research (Agence nationale pour la recherche, ANR). The aim of this project is to establish the spark plasma technology in France for the manufacture of several aero engines components. The project gathers different academic and industrial partners. The industrial groups are Mecachrome, Snecma, the company of Safran group, Chastagner Delaize (a tool provider) and ONERA, the national office of aerospace studies and research. The academic partners are CEMEF, center for material forming, CEMES, "Centre d'élaboration de Matériaux et d'études Structurales", ICB, "Institute of Carnot de Bourgogne" and ENSMA, "Ecole Nationale Supérieure de Mécanique et d'aéronautique".

The task of the project, assigned to CEMEF, is to develop a numerical model of the entire process to provide a predictive tool. Predicting densification and microstructure of the

parts sintered by SPS process requires a good understanding of temperature distribution and stress in the apparatus. A 3D numerical model has been developed to simulate the coupled electrical thermal mechanical problems modeling the process. This model is then used to identify the behavior law of IRIS *TiAl* powder.

The numerical simulations are performed using CimLib[®] software developed at CEMEF. The software is based on an oriented object programming in C++. The library is implemented in a fully parallel environment. It can be used in different environment: Windows/Linux. One of the characteristics of the library is that the implementation of the models is achieved in a metalanguage and if not necessary the user doesn't interfere in the code source. It allows solving multi-phase, multi-scale and multiphysics problems like in the case of spark plasma sintering process.

The model that will be developed includes three coupled problems, an electrical problem, a thermal problem and a mechanical problem. A monolithic approach is chosen where a single mesh is used for the whole machine assembly and to model the displacement of tools. Level set functions and anisotropic mesh adaptation are the keys to use the monolithic approach to model this complex process.

The first chapter of the thesis is a bibliography review on the history of the spark plasma sintering process and the simulation of the process. The three chapters that follow present the numerical model implemented in CimLib[®] and its validation. We begin by presenting the electric thermal coupling, then we present the behavior law chosen for the mechanical problem and we introduce the coupling of the three physical problems. Afterwards the approach considered to model friction in the monolithic framework is presented. Finally, the last chapter deals with the identification of the behavior law of IRIS powder.

Bibliography

- [1] <http://www.1001crash.com/index-page-statistique1.html>.

Chapter 2

Bibliography review

Contents

2.1	Introduction	9
2.2	Process description	9
2.3	Resistance sintering history	11
2.4	Mechanisms during densification by Spark Plasma Sintering	14
2.5	State of the art of the process simulation	18
2.6	Conclusion	27

Résumé

Dans ce chapitre, une revue bibliographique de l'histoire du procédé et de sa simulation numérique est présentée. Le frittage sous courant électrique est une technique qui est apparue en 1906. Cette technique a évolué au cours du siècle dernier. Aujourd'hui, les chercheurs s'intéressent au procédé de frittage flash qui consiste à fritter des poudres en appliquant simultanément une pression et un courant électrique. Ce procédé est avantageux car la poudre est frittée dans un temps assez court, par conséquent, on réduit la croissance des grains et on conserve une microstructure fine. Dans ce chapitre, les mécanismes se produisant au cours d'un cycle de frittage flash sont discutés. Tout d'abord, on s'intéresse à la présence et à l'influence des décharges électriques au niveau des joints de grains, puis, aux vitesses de chauffage. Des températures élevées sont atteintes en un temps très court et la densification commence avant que la température ne devienne homogène dans la poudre. Afin de comprendre les hétérogénéités qui peuvent se produire au cours du procédé, la simulation numérique du procédé s'avère nécessaire. Dans ce chapitre, on présente un état de l'art de l'évolution de la modélisation numérique dans ce domaine. Cet état de l'art nous permet de mettre en évidence qu'excepté le travail de Mori [29], l'ensemble de la littérature ne portait que sur la simulation du couplage. Ces différentes publications montrent que le courant est concentré dans les pistons qui a une section réduite, par conséquent, la température y est toujours la plus élevée. Les simulations numériques ont aussi montré l'influence des propriétés électriques des poudres sur la distribution du courant et de la température. Par la suite, les modèles numériques ont évolué pour modéliser le problème mécanique. Un comportement élastique est considéré dans certaines publications [47] - [32] où la contrainte est calculée en considérant un échantillon dense. Des modèles plus représentatifs ont été pris en compte dans d'autres publications [41] - [27] pour calculer l'évolution et la répartition de la densité relative pendant le procédé. Ces modèles choisis ont été initialement développés pour la simulation de la compaction isostatique à chaud. Les modèles numériques, trouvés dans la littérature pour simuler le procédé SPS, sont réalisées en utilisant des logiciels commerciaux. Dans ce travail, l'objectif principal est de développer un modèle numérique multiphysique et multi-domaine du frittage flash en utilisant le code développé au CEMEF, CimLib. Dans un premier temps, les problèmes électriques thermiques sont modélisés. Les simulations sont réalisées pour différents matériaux afin de comprendre l'influence des propriétés physiques sur la température et la distribution de courant. Dans un second temps, on a modélisé le problème mécanique et le comportement de la poudre de TiAl au cours du procédé SPS. Enfin, le couplage entre les trois problèmes est réalisé en utilisant une approche eulérienne.

2.1 Introduction

The aim of the chapter is to present the Spark Plasma Sintering process. First, a general description of the sintering technique is given. Then, a quick review on sintering under electric current is presented with its history evolution. The last part of this chapter is the state of the art of the numerical simulation of the process, this topic being necessary to head for the coming chapters.

2.2 Process description

SPS is a breakthrough technology for producing high quality sintered objects from powder to nano materials. It features lower temperatures and drastically shorter sintering times than traditional processes such as thermal sintering or hot isostatic pressing. SPS allows sintering highly dense metals and ceramics at lower temperatures with shorter heating and cooling times. Sintering takes place in minutes in contrast to traditional methods requiring several hours or longer. SPS utilizes graphite dies and punches to encapsulate the powder compact in a highly electrically conductive arrangement. A combination of electrical current and pressure is applied to the powder simultaneously resulting in rapid volumetric heating. The current is applied through electrodes that are water cooled.

Different types of electric current might be used depending on the apparatus: direct current (DC), alternative current (AC), pulsed current [8] or pulsed DC-DC. The effects of pulses were discussed in the literature. Wang et al. [46] showed that, for low current ($< 700 A$), the maximum shrinkage displacement was reached faster (180 s) under pulsed current than without pulses (240 s). Whereas it was shown in other papers that pulses had no effect on sintering. Xie et al. [52] found no effect of pulsing on final density, electrical resistivity and mechanical properties of fully sintered aluminium. Besides, Chen et al. [8] studied the effect of pulses on the reactivity between layers of Si and Mo powder, the formation of the product layer between both was proved to be independent of the pulse pattern. Furthermore, Anselmi-Tamburini et al. [3] suggest that the electrical current can be modeled as a continuous function either AC or DC. Consequently, a DC current is always considered for all the simulations of this work.

The compacted powder is placed inside the graphite die between the two punches. Then, the set is precompacted (sometimes manually) at room temperature where the rearrangement of particles takes place. The set up is placed in a vacuum chamber in the SPS machine, the lower and upper punches maintain consistent pressure to the compact while an electric current is applied to the dies and the powder as presented in Figure 2.2. A proportional-integral-derivative system allows temperature and pressure control during the process. The walls of the chamber are water cooled. When dealing with electrically conductive materials, the high current generates Joule heating at the particle to particle contact providing true volumetric heating. This is in contrast to conventional sintering

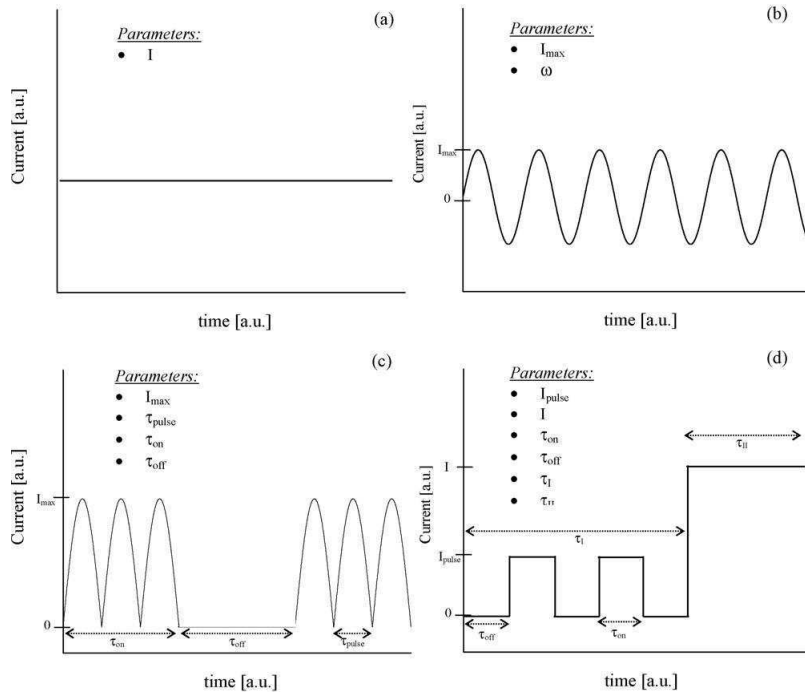


Figure 2.1: Typical electric current waveforms applied in SPS processes: (a) constant DC; (b) AC; (c) pulsed DC and (d) pulsed DC + DC [34]

Material	Initial Powder Size	Final Grain Size SPS (μm)	Final Grain Size Conventional(μm)
<i>Mg</i> [30]	180 μm	8-15	20-24
<i>TiO₂</i> [2]	40 <i>nm</i>	0.1	1
<i>BaTiO₃</i> [22]	13 <i>nm</i>	0.2-3	3

Table 2.1: Grain size comparison when using SPS or conventional processes

which heats the material from the outside to the inward by conduction. The combination of rapid heating (up to $400^{\circ}C/min$ and possibility $1000^{\circ}C/min$) and high pressure results in the densification of the powder and the reduction of the pore volume nearly to zero. The sintered sample is formed in about fifteen minutes. The short time required to heat up, sinter and cool down the powder produces a non porous, fully dense material with limited grain growth. The sintering temperatures are about $200^{\circ}C$ lower than in conventional processes. At the end of the process, the powder has a structure close to the original structure. Indeed, even if the initial structure change, the grain size evolves slightly. Consequently the powder maintains its physical properties. Many authors compared the grain size of sintered materials when using SPS and a conventional process [2]-[7]-[4] -[23]-[35], as repeated in table 2.1. As we can see, the grain size is lower for

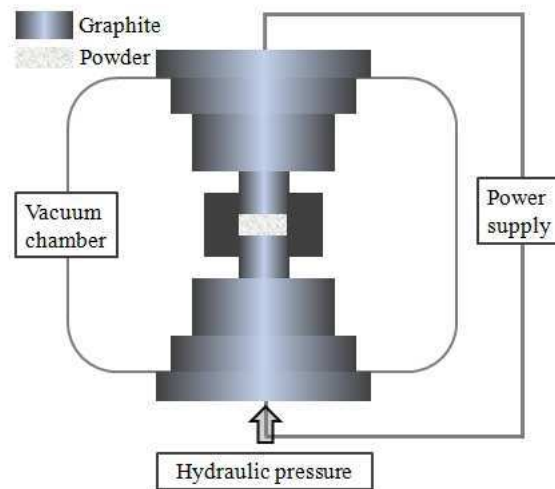


Figure 2.2: Spark Plasma Sintering set up

powder sintered by SPS.

2.3 Resistance sintering history

Powder sintering technique assisted by electrical current is a revolutionary high speed powder consolidation technology that arose in the early twentieth century.

Sintering under electrical current first appeared in 1906 when Bloxam compacted molybdenum and tungsten by applying the technique of sintering with direct electric current. This allowed the production of filaments for incandescent lamps with the advantage of reducing the rate of oxides on the surface [6]. Bloxam sintered this powder without the application of pressure.

Weintraub and Rush [50], in 1913, placed the powder in an electrically insulating tube and compressed it by two pistons serving also as electrodes for the electric current (parts 5 and 6 in Figure 2.3). They showed the benefits of surrounding the powder by a very high electrical insulating material for manufacturing rods of boron. They found that a homogeneous mass can be obtained which is not possible by melting and casting or by sintering by electric current when no insulating material surrounds it.

In 1922, Duval D'Adrian [11] used the technique invented by Weintraub earlier to produce zirconia, thoria and tantalia. The powder is placed between carbon electrodes and a high voltage is applied: a temperature of 2500°C is reached so that the particles of oxide become fused together.

In 1932, Taylor [42] brought out the very short sintering time when using a pulsed current. Taylor introduced the electric discharge sintering. A condenser is used in his apparatus connected to a source of direct current. The high electric current goes through the powder

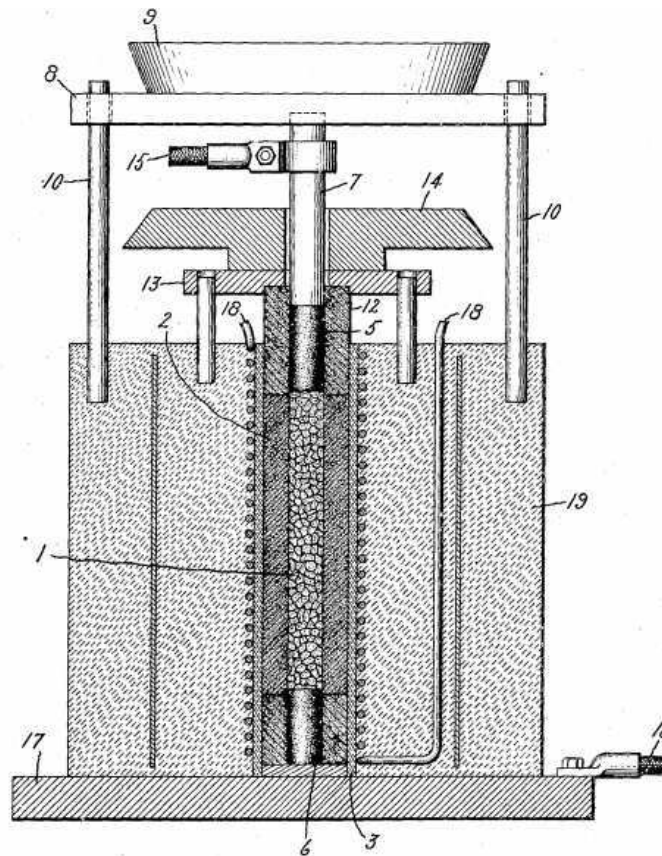


Figure 2.3: Representative scheme of the set up invented by Weintraub and Rush [50]

placed in a non conducting tube. Taylor claims that the pulse makes the powder less resistant to consolidation.

In 1944, Cremer [10] patented a resistance sintering method to consolidate metals such as copper, brass and bronze. He adapted a spot welding machine to sinter the metallic powders by applying simultaneously a pressure and an electric current. Lenel [21] also used a spot welding machine in 1955 to sinter metallic powders.

Spark sintering was introduced for the first time in 1966 by Inoue [18]. Inoue developed a spark sintering process where he studied the pulses of electric current that produce electric arcs favouring sintering.

Inoue design is used to develop the first SPS commercial machine produced by *Sumitomo Heavy Industries Ltd.* in Japan in 1990. This machine has graphite die and graphite punches that can handle a load going from 100 to 3000 *kN*. It utilizes an electric current between 2 and 20 *kA*. Today, several industries provide SPS machines like *FCT Systeme GmbH* in Germany since 2003, *Thermal Technology LLC* in the USA since 2008 and *Eltek Co.* in Korea. In Japan, SPS is now used for industrial applications. *Fuji Electronic Industrial Co., Ltd.* developed a fully automated tunnel type SPS manufacturing sys-

tem with materials handling robot. This system allows automatic powder stacking and automated powder die release (Figure 2.4). Elsewhere SPS is more used in research fields.



Figure 2.4: A fully automated tunnel-type sintering system developed by *Fuji Electronic Industrial Co., Ltd.* [1]

In the late twentieth century, researchers are more and more interested in sintering under electric current. In fact, a remarkable increase in the number of publications is observed around 1998 as we can see in the graphic of Figure 2.5.

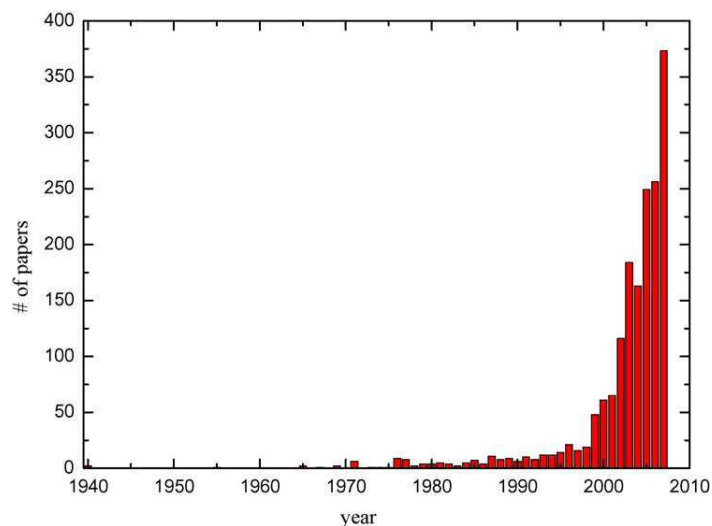


Figure 2.5: Number of publications related to sintering under electric current [33]

Different designations can be found in the literature regarding these processes but the most common is SPS for Spark Plasma Sintering (cf Figure 2.6). Some researchers do not agree with this name because of the open issue of the effective existence of electric discharges through plasma. This will be discussed in the following section.

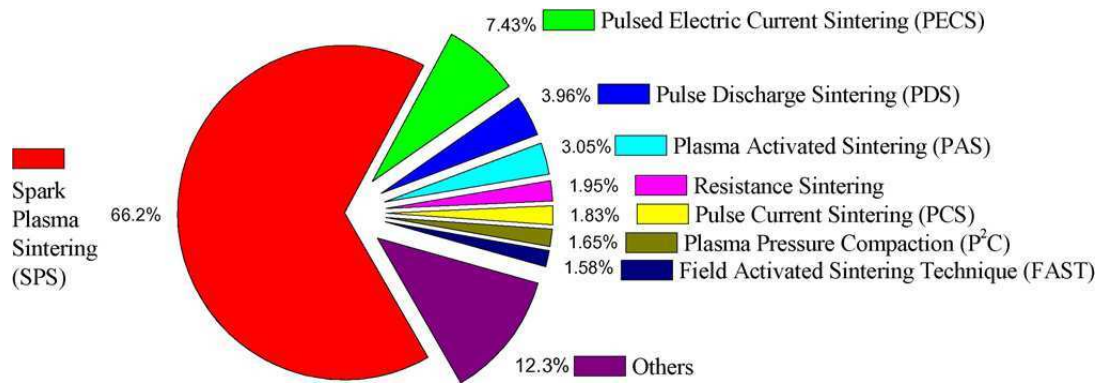


Figure 2.6: Resistance sintering processes designation [33]

In France, the activity in SPS began in 2000. The first machine was installed in the autumn of 2004 in Toulouse in the "Plateforme Nationale de Frittage Flash". It is a "Sumitomo Dr Sinter 2080" and it is the machine used in this thesis. Today, about ten machines are installed in France. There are both Sumitomo (at CMTR of ICMPE in Thiais, CTTC in Limoge, Mecachrome in Vibraye) and FCTmachines (MATEIS INSA Lyon, UCB in Bourgogne, University of Caen). The biggest machine is located at Vibraye in Mecachrome (coordinator of IRIS project). The maximum diameter of the powder can reach up to 350 *mm*.

2.4 Mechanisms during densification by Spark Plasma Sintering

Densification mechanisms during SPS are until today a major subject of discussion and disagreement between researchers. Sintering requires mass transfer through diffusion. Figure 2.7 summarizes the mechanisms of sintering. In the SPS process, the electric current applied simultaneously with the pressure causes very high heating rates that lead to an advantageous microstructure. However, these heating rates and the presence of electric current make the understanding of the diffusion mechanisms very complex. Additional mechanisms are involved due to the experimental conditions comparing to conventional sintering processes. Until now, the number of these mechanisms is unknown since they are very dependent on the material physical and chemical properties. The presence of sparks and electric arcs is one of the major subjects of discussions in this field. An electric spark is an electrostatic discharge that takes place in the presence of an electric field. It appears when an insulator such as air is ionized creating an electric conductive channel. An electric arc is when an insulator is ionized continuously for a long period of time.

In fact, an electric arc discharge results in high current ($> 10 A$) and low voltage ($< 20 V$).

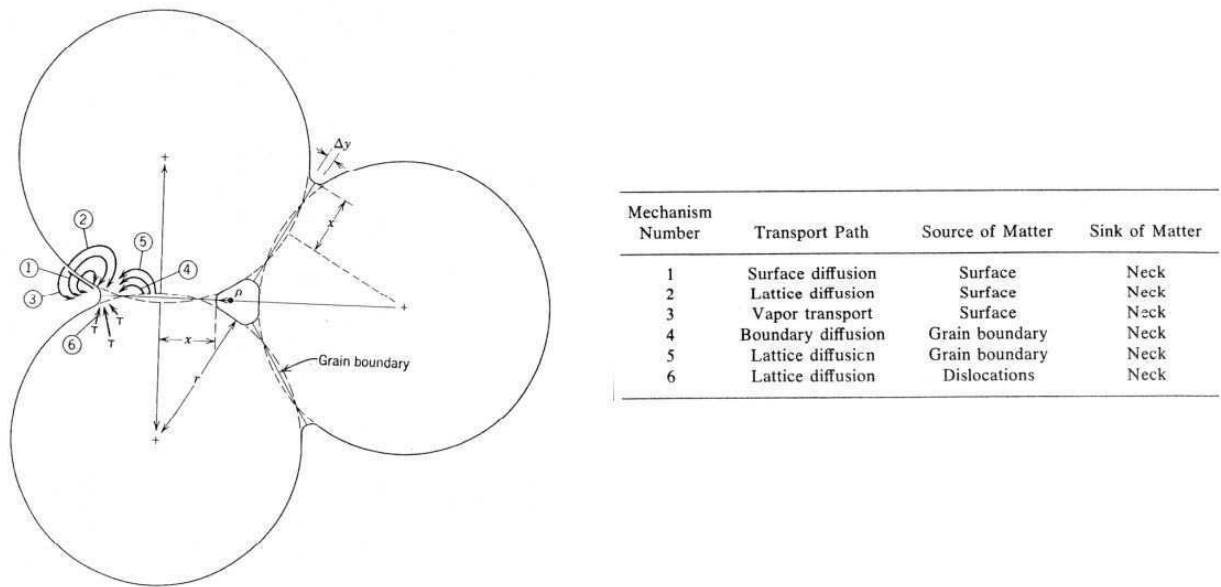


Figure 2.7: Mechanisms of sintering [20]

The spark discharge occurs when having very high current (kA) and voltage (kV). A low voltage is measured during SPS process (about 3 to 5 V). However, the voltage isn't measured at the material level. When dealing with electrically conductive powders, the two particles act like an electric dipole thus in the region of the particle/particle interface polarization effects might produce a local electric field with high voltage.

Tokita [43] discussed the ON/OFF effects that favour specific mechanisms. During the ON phase, sparks are generated and cause purification and melting around the joints and the OFF phase follows to facilitate thermal diffusion as seen in Figure 2.8.

Tokita claimed that the migration of ions between particles is faster which causes faster diffusion. He described neck formation as seen in Figure 2.9: during an electric discharge ions migrate from one particle to another producing plasma. Melting and vaporization take place at the surface of the particles, hence with the application of pressure it leads to neck formation. It should be noted however that not all researchers agree with the description of Tokita.

Yanagisawa *et al.* [53] developed the set up presented in Figure 2.10, where they replaced the graphite die by transparent thin quartz to place an optical microscope and follow the evolution of the process. They claimed that particles are bonded together when a spark occurs. But they also noticed: *"Regardless of whether or not a spark is observed, necks are formed at points of contact between particles and neck diameter increases with pulsed current density"* [53]. Hence, neck formation seems to be not dependent on the presence of sparks during sintering.

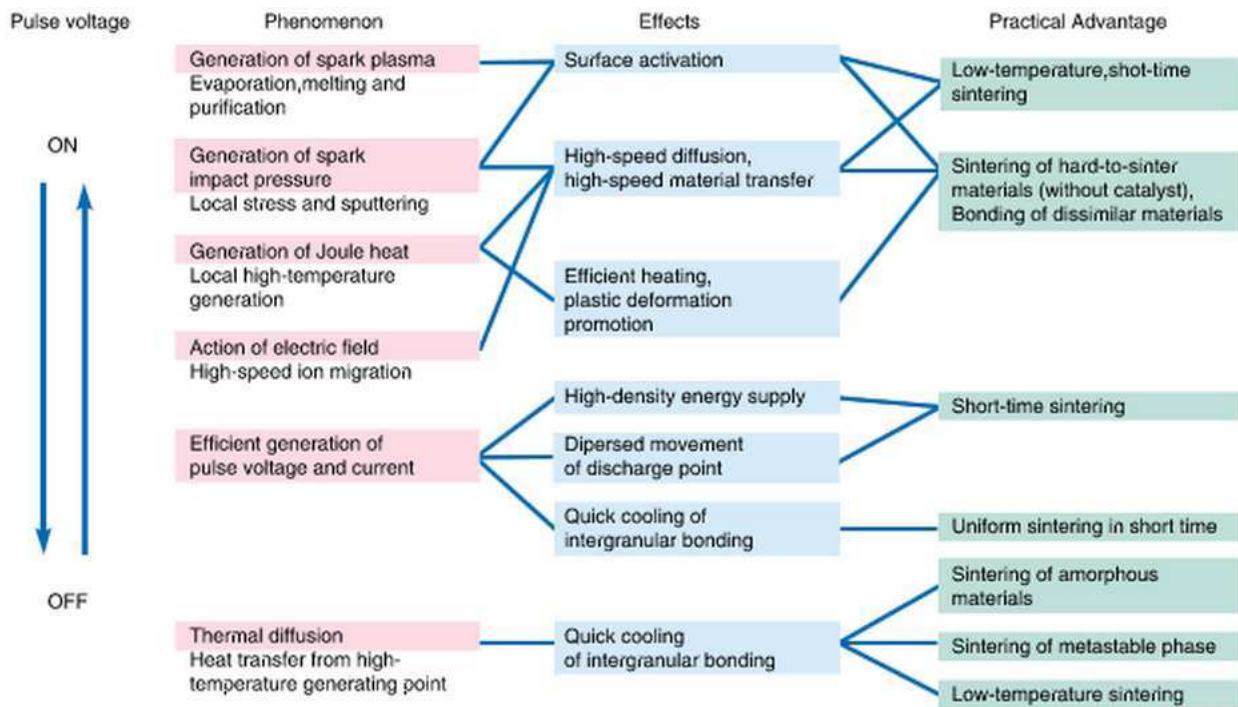


Figure 2.8: Effect of pulses on sintering mechanisms [43]

However, Hulbert *et al.* [17] declare that there is no plasma, no electric arc or discharge during SPS process. In fact, plasma is produced due to the excitation of electrons and when these electrons return to a stable state they emit photons that can be observed by spectroscopy. Spectroscopy showed that no particular features were observed referring to a spark or discharge even for copper. Besides, Hulbert *et al.* [17] showed that when measuring the voltage around the sample in the vertical and horizontal directions and when analysing the recordings with Fourier transformation the plots show that no high frequencies are detected hence no spark occurs.

Another mechanism that might occur during SPS is electromigration. Electromigration occurs in metals in the presence of high electric current. The electrons move creating voids and tension on one side and compression on the other side. Frei *et al.* [15] developed an experimental set up in SPS to evidence the effect of current intensity on neck formation. They showed that the size of the neck increases with current intensity which they justify by electromigration effects. Powder reactivity was used in other works to discuss the effect of electromigration [31]-[5].

The above described mechanisms are specially related to the application of current during the process. In addition, other mechanisms occur in SPS that can be found in usual hot pressing at high temperatures. High heating rates in SPS might influence the growth of the particles by the Soret effect[12].

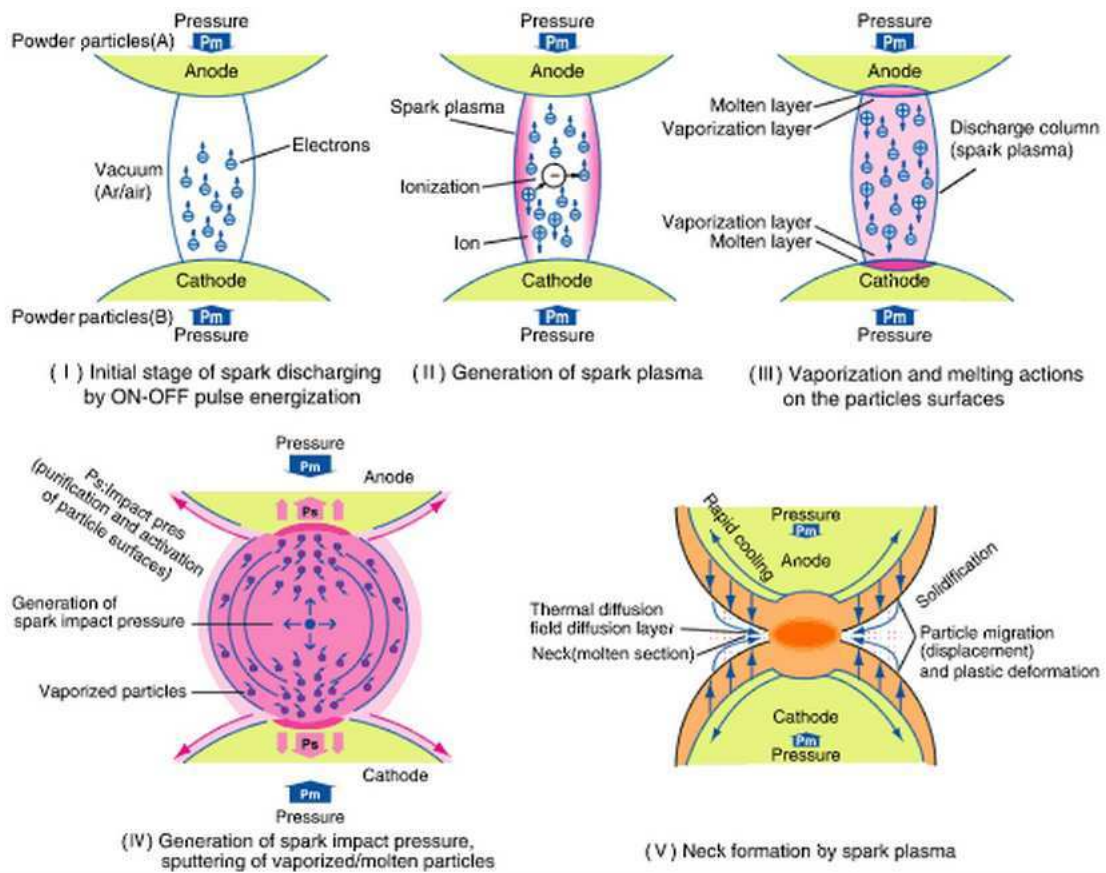


Figure 2.9: Neck formation between two particles as described by Tokita [43]

In the microscopic scale, gradients of temperature cause diffusion between particles and surface tension. The applied load also takes part in diffusion mechanisms. Olevsky [14] showed for an aluminium powder the influence of three mechanisms depending on the grain size and porosity. He considered three predominant mechanisms: surface tension, diffusion under applied load and electromigration. He showed that surface tension is dominant for small particles and small porosity, diffusion under applied load is dominant for small particles and high porosity or for large particles and high porosity, electromigration is dominant for large particles ($> 10^{-6} \mu\text{m}$) and low porosity. So in addition whether or not a mechanism takes place, for each powder it is necessary to identify the properties allowing it to occur.

Hence, mechanisms during SPS are difficult to evidence and authors opinions do not converge to the same conclusion. For this reason, in the framework of the present study, we choose a simplified model to describe densification where current effect is not explicitly considered. A detailed description of the model is presented in Chapter 4.

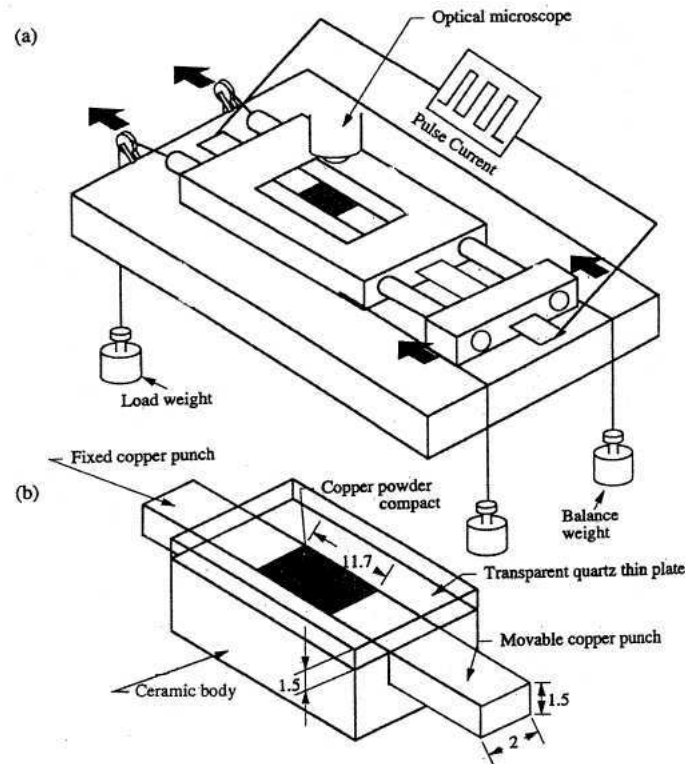


Figure 2.10: Set up designed by Yanagisawa *et al.* to study the effect of sparks on neck formation between powder particles [53]

2.5 State of the art of the process simulation

Sintering under electric current appeared in 1906. The first paper in numerical modeling of sintering assisted by electric current was published in 1989 by Raichenko and Chernikova [37]. They modeled the heating of a set up composed from two electrodes/punches and a powder with no die. Temperature evolution is described by a mathematical 1D model. In 1993, Raichenko *et al.* [38] studied electric heating of $WC - Co$. An analytic solution is used to compute temperature using a continuity condition between the powder and the electrodes. Physical properties are considered temperature dependent.

In 1998, Mori *et al.* [29] have developed a finite element model to compute electric current, temperature and density. Iron powder is compacted in a die by moving the upper punch downward. A global mesh is used to compute current and temperature whereas for density a mesh representing only the powder is considered. The mechanical behavior of the tool is not modeled. The model used for powder densification is based on the work of Shima (1976) [40]: it consists in a compressible viscoplastic model, close to the model of Abouaf that is used in the present work, and will be detailed in chapter 4. The model is developed in 2D considering the axial symmetry and the dependence of the parameters on temperature. Results show that the current density is higher in the punches. In the

mid height of the sample, the temperature is higher in the center and decreases when approaching the die. The distribution of relative density is not homogeneous due to friction and temperature. The model presented by Mori *et al.* [29] is the first to deal with the coupling between the 3 physical problems.

Afterwards, until 2007, authors studied only the electrical thermal coupling. Simplified geometries are considered to compute current and temperature distribution in 2D without considering the whole set up. Yoneya and Ikeshoji [54] considered the geometry presented in figure 2.11. The model is developed in 2D considering the axial symmetry. The equations are solved numerically using the *Method of Fundamental Solutions* coupled with Fourier transformation. Results are compared for two specimens: graphite and copper for a constant porosity value. As expected, for copper current density is the highest in the specimen, whereas for graphite it is higher in the die. As mentioned, the part of the pistons that is outside the die is not modeled. However, this part, because of its lowest section, presents normally the highest current density whatever the properties of the specimen. Yoneya *et al.* [54] showed that the pistons have the highest temperature which is a conclusion that many authors presented later on.

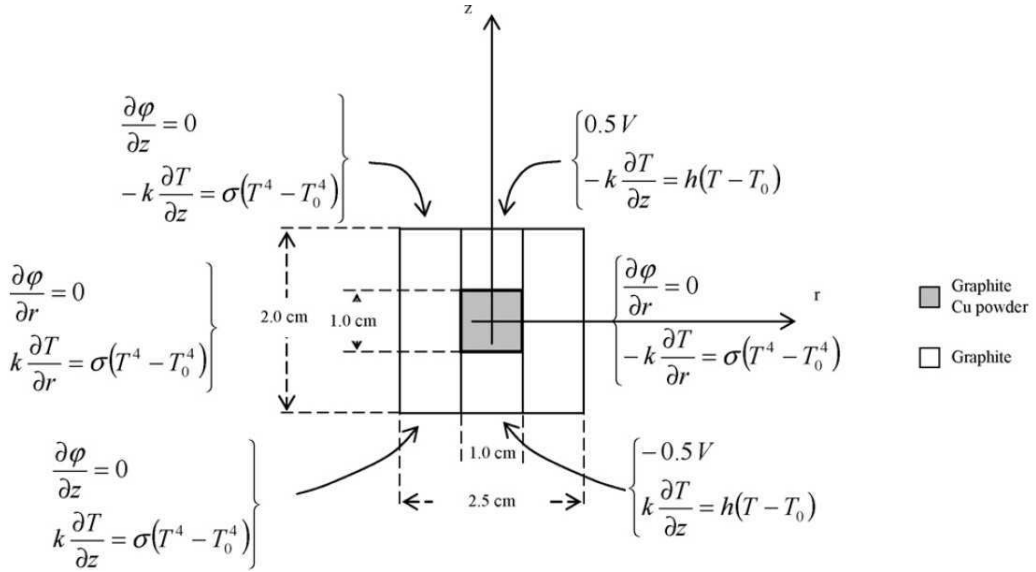


Figure 2.11: Computational domain considered by Yoneya *et al.* [54] to model electrical and thermal problems summarized schematically by Orru *et al.* [33]. A 2D axial symmetry is considered

Wang and Fu [48] considered a similar geometry as Yoneya [54] but with different dimensions to model the heating of TiB_2/BN , as in figure 2.12. They calculated steady state analytic solutions in two directions based on radial and axial symmetry. The two solutions are then merged together in order to deduce a 2D distribution of temperature

and current. The calculations showed a very important temperature difference inside the sample in the radial direction equal to 350°C , the highest temperature being in the center of the sample. They claimed that the gradient is even higher ($= 450^{\circ}\text{C}$) according to experimental measurements.

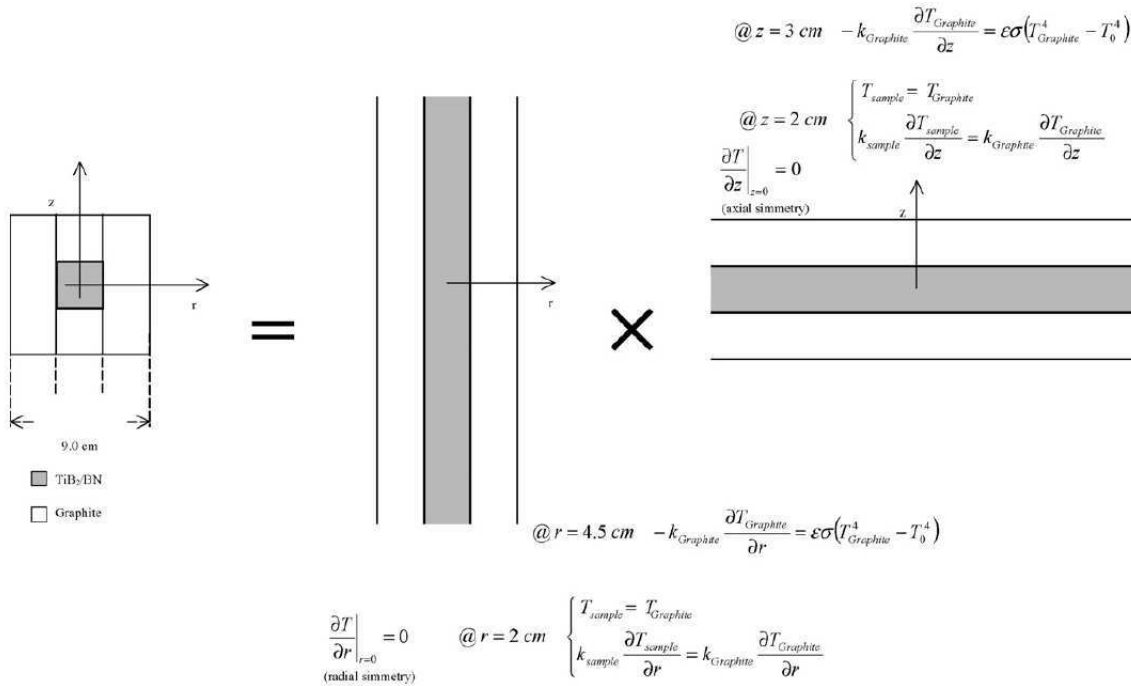


Figure 2.12: Computational domain considered by Wang et al. [48] to model electrical and thermal problems summarized schematically by Orru *et al.* [33]

In 2002, Keum *et al.* [19] used the finite element method in 1D to model the heating of an alumina specimen. The temperature is computed in the radial direction of the sample. They found that the temperature is lower in the center of alumina specimen. On the contrary, the previous papers (for ex. [48]) showed that for conductive materials, the center had the highest temperature and it decreases towards the die. This proved that electric resistance plays an important role in temperature distribution.

Three different methods were chosen in [54]-[48]-[19] to compute electric current and temperature in the die, the sample and in the part of the pistons located in the die. Results are comparable. For conductive materials, temperature is higher in the center of the sample contrary to the non conductive alumina. This conclusion is confirmed in succeeding papers.

Matsugi *et al.* [26] studied two materials, an insulator (alumina) and a conductor (ti-

tanium) to understand the influence of electric resistance on temperature. Punches, the die and the compact are modeled as seen in figure 2.13. Voltage and temperature are

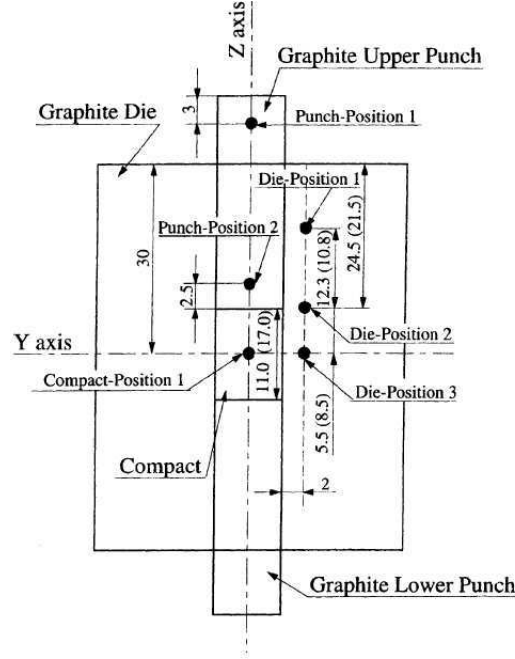


Figure 2.13: Computational domain considered by Matsugi *et al.* [26] to model electrical and thermal problems

computed by the finite difference method in steady state. No coupling with mechanical problem is considered. However, the physical properties are updated depending on relative density. This one is calculated using experimental measurements and using the following expression:

$$\rho_r(T, P) = \rho_{r0} + aP + b(T - T_0)^c \quad (2.1)$$

where ρ_r and ρ_{r0} are respectively current and the initial relative density, P the applied pressure, T_0 the initial temperature and a, b, c adjustable parameters. The numerical results are compared to experiments. Thermocouples are distributed in the die, punches and the center of the specimen. Comparisons show a very good agreement. Matsugi *et al.* [26] didn't notice significant differences in the global potential distribution for the two samples. Concerning thermal results, the maximum temperature observed is in the punches for both materials. They claimed that temperature distribution in the sample is different depending on the properties of the compact. Their results confirmed the conclusion that for insulators temperature is lower in the center of the sample in the radial direction contrary to the case of conductive materials. The numerical method used in [26] was also applied for a relatively complex shape in [25]. Matsugi *et al.* [25] modeled a geometry with a "T" shaped axisymmetric part. The computed temperature is higher in

the lower smaller section of the specimen, which results from the concentration of current in the sample that is more conductive than the graphite die.

Wang *et al.* [49] also brought out the heating of insulators by thermal conduction from the surrounding graphite. They modeled a geometry similar to [26] to study the heating of a *BN* powder. The calculations are carried out using a commercial finite element software, ANSYS. Results showed that temperature of the sample is lower than the one of the die in the early stage of sintering. Heat conduction from graphite induces an increasing of the sample temperature so it reaches approximately the die temperature.

Succeeding these first publications, achievements in numerical modeling of electric thermal problems during SPS deal commonly with the comparison between two materials and/or experiments [3]-[44]-[55] -[47]- [24]-[39]. However, authors can be differentiated by the geometries modeled, materials or the addition of certain boundary or contact conditions. The entire geometry of SPS apparatus is modeled in the papers cited below.

Anselmi-Tamburini *et al.* [3] considered the geometry of a Sumitomo apparatus. Simulations are carried out for alumina and copper. Electric results are presented in Figure 2.14, the current is concentrated in the pistons for both materials. In the die region, for alumina, because of its electric resistance, the current is absent in the sample contrary to copper that favours the crossing of the current. However, they showed that the power dissipated by Joule effect is negligible in both samples (cf. Figure 2.15), which means that the heating is of conductive type, from the die toward the compacted material. Hence, during the process, temperature profiles are similar and pistons present the highest temperature as it was shown previously by [54] and [26].

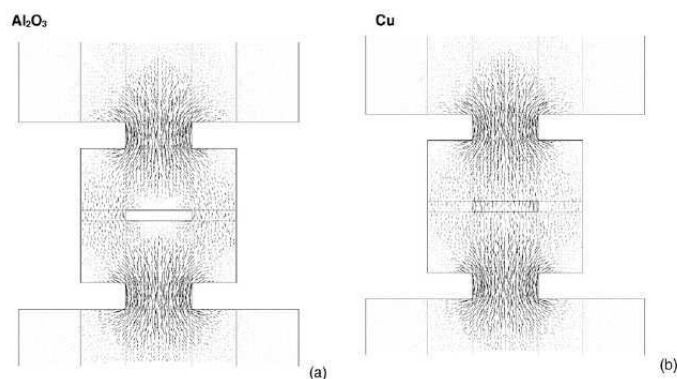


Figure 2.14: Current distribution in the SPS apparatus computed by Anselmi-Tamburini *et al.* [3] using the commercial software CFD-AFE+ : the 3D model has 35352 nodes with hexagonal and polygonal cells

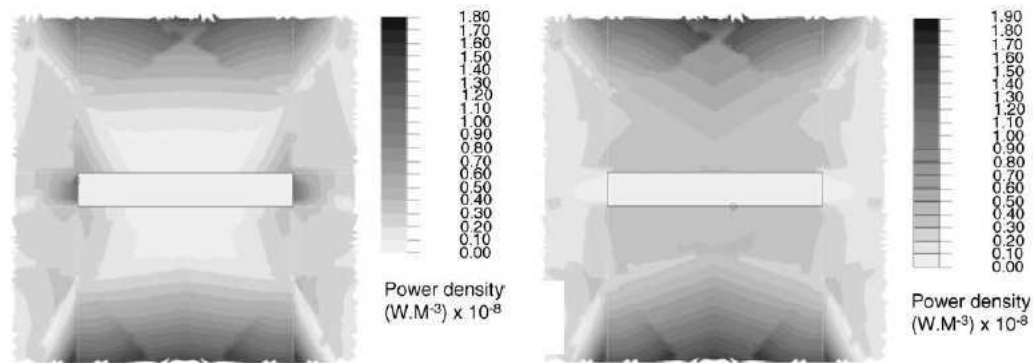


Figure 2.15: Power dissipated by Joule effect computed by Anselmi-Tamburini *et al.* on the left for alumina, and on the right for copper [3]

Zavaliangos *et al.* [55] also considered the geometry of a Sumitomo apparatus to model electrical thermal coupling during SPS and to compare the results with experiments. The numerical simulations are carried out with the commercial finite element software ABAQUS. In their model, they added interface heating effects. They have shown that thermal contact resistance improves temperature prediction as seen in figure 2.16. However, these results are achieved when using a dense graphite specimen. When neglecting thermal contact resistance, a continuity is observed in temperature distribution due to the homogeneities of physical properties (all the parts are made of graphite). It would be interesting to test this influence when considering a high electrical conductive powder, where a temperature field is already less continuous without taking into account the contact effect.

Rathel *et al.* [39] modeled the thermal electric coupling for a FCT apparatus using two samples: silicon nitride and tungsten carbide. The calculations show that electric current is concentrated in the piston similarly as in the case of a Sumitomo apparatus. Temperature distribution in the sample is compared for both samples when using either a thin or a thick die. When the die is thick, temperature is lower in the sample for both samples.

After Mori *et al.* [29], Wang *et al.* [47] addressed the mechanical problem in addition to the electrical thermal coupling. A dense sample is considered which means that the porosity is not computed. Displacements and stresses are calculated in the apparatus, the strain tensor is computed choosing a high compressible elastic behavior. Results are compared between alumina and copper. However, assuming a pure elastic behavior for powder compaction is critical.

McWilliams and Zavaliangos [27] developed a two part finite element approach to model a fully coupled electric thermal mechanical problem. Simulations are achieved in ABAQUS.

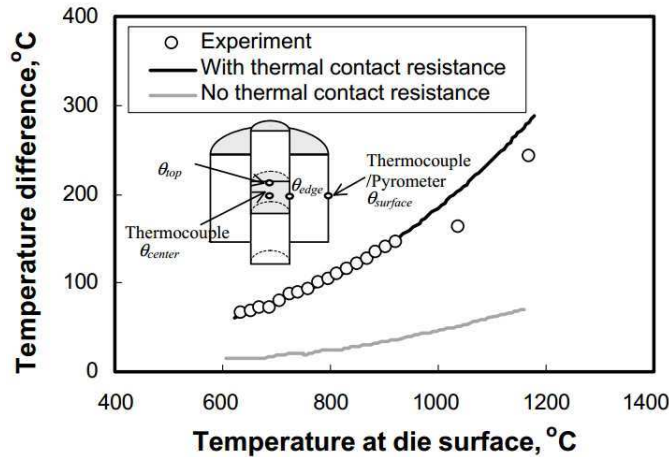


Figure 2.16: Temperature gap between the center of the specimen and the die surface versus the temperature measured at the die surface: Comparison between experiments and simulation when neglecting or considering thermal contact resistance [55] using the commercial software Abaqus

Like Mori, two meshes are used: the first one represents the whole apparatus and is used to solve electric thermal problems, the second one represents the powder and is used to solve sintering model. Sintering constitutive equation is based on the work of Gillia and Bouvard [16] where the strain rate follows a power law dependent on temperature, maximum relative density and current relative density. The total strain rate is the sum of the sintering strain rate, the viscoplastic strain rate and the thermoelastic strain rate. The sample to be sintered is composed of two layers with different initial densities once placed either in a series arrangement or in parallel. The evolution of the relative density differs depending on the positioning of the layers. Densification is faster for the series arrangement, the layer with higher density reaches the dense state a few seconds earlier than for the lower density layer. In the parallel case, densification is slower but identically the dense state is reached by the high density layer a few seconds before.

Wang *et al.* [45] simulated a coupled thermal-electrical-mechanical model using the commercial software Comsol. The mechanical problem is modeled identically as in [47] by choosing an elastic behavior. They showed that the sample temperature distribution varies when applying different heating rates and when changing the sample diameters (12, 20, 36, 50 mm). Munoz and Anselmi-Tamburini [32] used the finite element commercial code ANSYS to model the electrical thermal mechanical coupled problems. The temperature in the center of the powder is controlled using a PID loop. An elastic behavior is also considered in their work assuming that the yield stress is not reached for any material. The thermal results show that inside the copper sample temperature gradient is lower than inside the alumina sample ($5^{\circ}C$ for copper and $22^{\circ}C$ for alumina).

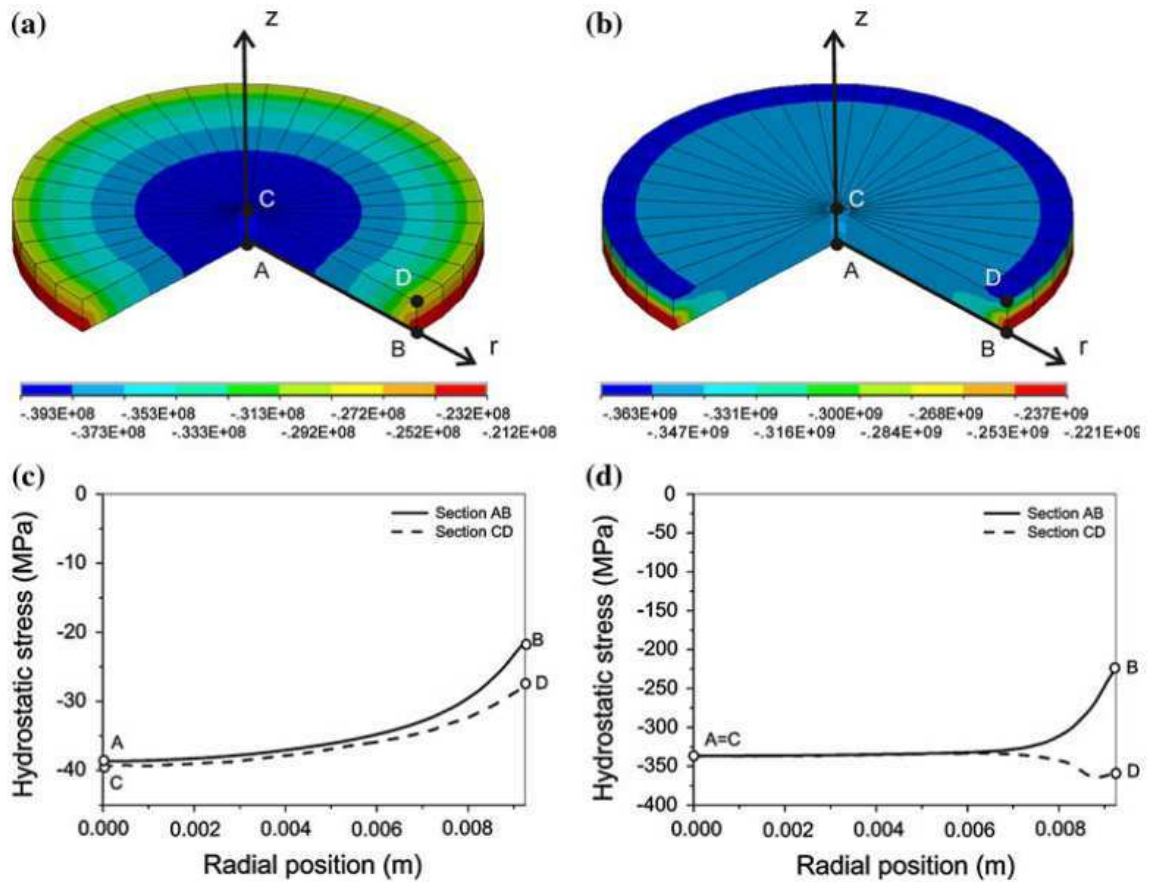


Figure 2.17: Hydrostatic stress distribution inside alumina (a) and copper (b). Hydrostatic stress plotted over the lines AB and CD for alumina (c) and copper (d) [32]

The sample highest temperature in the late stage of sintering ($t = 350$ s) is observed in its center for both materials. The hydrostatic stress distribution is computed by Munoz and Anselmi-Tamburini [32] inside both samples. A non homogeneous distribution is observed. At $t = 350$ s, for alumina a maximum value is observed at the center of the sample equal to 40 MPa and decreases towards the edge with the die. For copper, it is more homogeneous. However, close to the edge a gap of 100 MPa is observed in the vertical direction as seen in Figure 2.17.

A different model is developed by Song *et al.* [41] who simulated the mechanical thermal electric problems during SPS using the commercial software MARC. A Sumitomo apparatus is modeled. The material chosen for punches and spacers is graphite, for the die it is silicon nitride and for the powder it is iron. In their model, parameters are updated depending on temperature and relative density. An imperfect (electrical and thermal) contact condition is considered at the interfaces. The powder follows a thermal

viscoplastic behavior. At each time step, the stress increment is calculated as follows:

$$d\sigma = D^{el}(\varepsilon^{tot} - \varepsilon^{vp} - \varepsilon^{th}) \quad (2.2)$$

where D^{el} is the Hooke tensor, ε^{tot} , ε^{vp} , and ε^{th} are respectively the total, viscoplastic and thermal strain. Young modulus and Poisson ratio vary with relative density. The viscoplastic strain rate is computed using Abouaf law. In fact, Abouaf law is often chosen in modeling hot powder compaction as it will be presented in chapter 4. Once stress and strain computed, the relative density is calculated using the mass conservation equation. Simulations are carried out for three applied pressures. Results are compared with experiments. They found that the temperature gradients in the sample decrease when applying a greater pressure as seen in Figure 2.18.

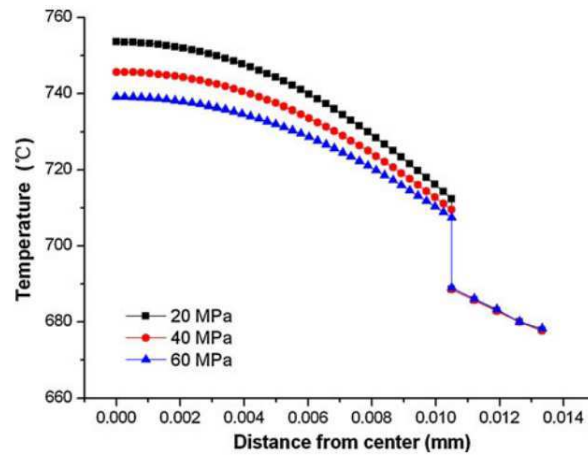


Figure 2.18: Temperature plotted over the radial distance in the mid-thickness of the specimen for the different applied pressures computed by Song *et al.*[41]

Song *et al.* [41] brought out an interesting point concerning the temperature axial symmetry, a subject that was discussed in our work Mondalek *et al.* [28]. In fact, the pressure during SPS is generally applied from the lower punch and spacers which means that only the lower parts of the apparatus are moving. This doesn't conserve the symmetry of the apparatus and hence of the temperature. This point will be discussed later in chapter 4. Song *et al.* [41] presented the displacement evolution with time for the 3 applied pressures. They found that in the early and late stage of the sintering, the displacement variation increases slowly whereas an explosive growth is observed in between. This is explained by the low temperature in the beginning and the high density when approaching the dense state that reduce displacement evolution.

Wolff *et al.* [51] developed a coupled electric thermal mechanical model using the software ABAQUS. An isotropic elastic-thermoviscoplastic behavior is considered in the mechanical problem. The thermal expansion coefficient, the bulk and shear modulus are expressed

functions of the relative density considering homogenisation of a two phases material (material and pores). A power law is chosen for the viscoplastic model adjusted according to the literature (Cocks [9], Duva *et al.* [13], Ponte-Castaneda [36]) to take into account the porous medium. Two terms f and c are added dependent on relative density. The author modified the expressions of these functions claiming the necessity to add the parameter ρ_c corresponding to the lowest relative density of the closed packed powder materials, which was already considered in Abouaf model. Results showed a gradient in the powder relative density equal to 5.7%. The sample is thin, its diameter is equal to 100 mm and its initial height is equal to 20 mm.

2.6 Conclusion

Sintering under electric current is a technique that arose in 1906. This technique evolved through the last century. Today, researchers are interested in Spark Plasma Sintering process which consists in sintering powders under electric current and applied pressure. This process is advantageous because powder is sintered in a rather short time, hence, reducing grain growth and conserving fine microstructure.

The simultaneous application of electric current and pressure yields to a misunderstanding in the mechanisms that interfere during the process. In this chapter, a bibliography review on the mechanisms during SPS has been presented.

The presence of electric spark discharge and its effect was studied by many authors. In [43], the author claims that sparks occur and causes melting and purification around the joints of particles. In [53], the authors claim that sparks occur but neck formation is not dependent on their presence. In [17], authors do not agree and assert that no spark discharge or plasma occur during the process. Electromigration takes also place during this process when dealing with conductive powders, however its influence depends on the grain size and porosity according to Olevsky [14]. In addition to mechanisms related to electric current, high heating rates improve the diffusion between particles.

Since, high temperatures are reached in a very short time during SPS, the densification begins before temperature becomes homogeneous in the powder. In order to understand the heterogeneities that occur during the process, numerical simulation of the process is necessary. In this chapter, a state of the art of the evolution of numerical modeling in this field is presented. The first publications dealt only with the thermal electric coupling apart of the work of Mori [29]. The distribution of electric current and temperature is studied. Numerical modeling of SPS process was limited in most publications to the electric thermal problems. When considering the mechanical problem, different models can be found. Elastic behavior is chosen in [32]-[45]-[47] assuming that yield stress is not reached. This choice could be critical since in SPS high temperatures are reached in a few minutes. Other models evolved to take into account the powder behavior at high temperature as in [27]-[41] where a thermal elasto-viscoplastic contribution is considered.

The results presented in the publications are sometimes compared with experiments. The current is concentrated in the pistons having a small section. Hence temperature is always the highest at this level. Numerical simulations showed the influence of electric properties of the powders on the distribution of current and temperature. For a conductive sample, temperature is higher in the center opposite to the non conductive material. Numerical models are developed to model the mechanical problem. An elastic behavior is considered in some publications [47]-[32] where stress is calculated considering a dense sample. More representative models were considered in other publications [41]-[27] to compute the evolution and distribution of relative density during the process. The models chosen were developed previously for conventional hot pressing.

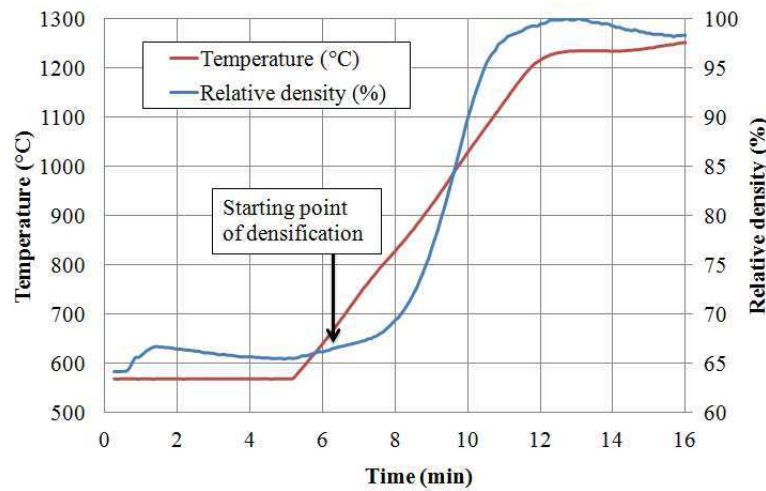


Figure 2.19: Temperature and relative density evolution when sintering a *TiAl* powder by SPS process

In IRIS project the aim is to model SPS process for a *TiAl* powder. The graphic of Figure 2.19 shows temperature and density evolution during an SPS cycle when sintering *TiAl* powder. These measurements were achieved by our colleagues at CEMES. As seen, the relative density starts to increase when temperature reaches 675°C (measured 3 mm away from the die edge). Hence, the deformation occurs at a temperature where it is more accurate to consider a viscoplastic model. In Chapter 4, modeling of the mechanical problem is presented. A viscoplastic behavior is considered, modified according to Abouaf law to take into account the densification. Densification mechanisms other than the plastic deformation of particles that might appear in SPS are not considered in our approach since until now their existence and influence is still uncertain. Besides, modeling microscopic mechanisms (such as mass transfer by diffusion or electromigration) would consist in adding many parameters that are difficult to identify.

The numerical models found in the literature to simulate SPS process are carried out

using commercial softwares. In this work, the main objective is to develop a multidomain and multiphysics numerical model of the Spark plasma Sintering Process using the code developed at CEMEF, CimLib.

First, the electric thermal problems are modeled. Simulations are carried out for different materials to understand the influence of physical properties on temperature and current distribution. The second part of the thesis consists in modeling the mechanical problem and powder behavior of *TiAl* during SPS. Then the coupling between the three problems is achieved using an Eulerian approach. The following chapter discuss modeling of friction in the monolithic framework in order to add it in the SPS model. Finally, an identification of the power law parameters related to the porous state is achieved for the *TiAl* powder followed by a complete SPS simulation compared to the experiments.

Bibliography

- [1] <http://sps.fdc.co.jp/products/products5.html>. 2011.
- [2] P. Angerer, L.G. Yu, K.A. Khor, and G. Krumpel. Spark-plasma-sintering (sps) of nanostructured and submicron titanium oxide powders. *Materials Science and Engineering: A*, 381:16 – 19, 2004.
- [3] U. Anselmi-Tamburini, S. Gennari, J.E. Garaya, and Z.A. Munir. Fundamental investigations on the spark plasma sintering/synthesis process ii. modeling of current and temperature distributions. *Materials Science and Engineering A*, 394:139–148, 2005.
- [4] G. Bernard-Granger, A. Addad, G. Fantozzi, G. Bonnefont, C. Guizard, and D. Vernat. Spark plasma sintering of a commercially available granulated zirconia powder: Comparison with hot-pressing. *Acta Materialia*, 58(9):3390–3399, 2010.
- [5] N. Bertolino, J. Garay, U. Anselmi-Tamburini, and Z. A. Munir. High-flux current effects in interfacial reactions in Au-Al multilayers. *Philosophical Magazine Part B*, 82(8):969–985, 2002.
- [6] A.G. Bloxam. Improved manufacture of electric incandescence lamp filaments from tungsten or molybdenum or an alloy thereof. *GB Patent*, 27,002, 1906.
- [7] M. Cabibbo, C. Paternoster, R. Cecchini, A. Fabrizi, A. Molinari, S. Libardi, and M. Zadra. A microstructure study of nanostructured Fe-Mo + 1.5 wt. % SiO₂ and +1.5 wt.% TiO₂ powders compacted by spark plasma sintering. *Materials Science and Engineering: A*, 496:121 – 132, 2008.
- [8] W. Chen, U. Anselmi-Tamburini, J.E. Garay, J.R. Groza, and Z.A. Munir. Fundamental investigations on the spark plasma sintering/synthesis process i. effect of dc pulsing on reactivity. *Materials Science and Engineering A*, 394:132–138, 2005.
- [9] A.C.F. Cocks. Inelastic deformation of porous materials. *Journal of the Mechanics and Physics of Solids*, 37:693–715, 1989.
- [10] G.D. Cremer. Sintering together powders metals such as bronze, brass or aluminum. *US Patent*, 2,355,954, 1944.

-
- [11] A. D'Adrian. Article of fused metallic oxide and process of producing the same. *US Patent*, 1,430,724, 1922.
- [12] S. Duhr and D. Braun. Why molecules move along a temperature gradient. *Proceedings of the National Academy of Sciences of the United States of America*, 103:19681, 2006.
- [13] J.M. Duva and J.W. Hutchinson. Constitutive potentials for dilutely voided nonlinear materials. *Mechanics of Materials*, 3:41–54, 1984.
- [14] Olevsky E. and Froyen L. Constitutive modeling of spark-plasma sintering of conductive materials. *Scripta Materialia*, 55:1175–1178, 2006.
- [15] J. M. Frei, U. Anselmi-Tamburini, and Z. Munir. Current effects on neck growth in the sintering of copper spheres to copper plates by the pulsed electric current method. *Journal of Applied Physics*, 101:114914, 2007.
- [16] O. Gillia and D. Bouvard. Phenomenological analysis of densification kinetics during sintering: application to WC-Co mixture. *Material Science Engineering A*, 279:185–191, 2000.
- [17] D.M. Hulbert, A. Anders, J. Andersson, E. Laverniaa, and A.K. Mukherjee. A discussion on the absence of plasma in spark plasma sintering. *Scripta Materialia*, 60:835–838, 2009.
- [18] K. Inoue. Electric discharge heat treatment of metals in electrolytes. *US Patent*, 3,188,245, 1965.
- [19] Y.T. Keum, J.H. Jeon, and K.H. Auh. Computer simulation of ceramic sintering processes. *Journal of Ceramic Processing Research*, 3:195–200, 2002.
- [20] W. D. Kingery, H. K. Bowen, and D. R. Uhlmann. *Introduction to Ceramics*. John Wiley and Sons, 2nd Edition, New York, 1975.
- [21] F.V. Lenel. Resistance sintering under pressure. *Transactions of the American Institute of Mining and Metallurgical Engineers*, 203:158–167, 1955.
- [22] W. Luan, L. Gao, H. Kawaoka, T. Sekino, and K. Niihara. Fabrication and characteristics of fine-grained BaTiO₃ ceramics by spark plasma sintering. *Ceramics International*, 30:405–410, 2004.
- [23] H. Maiwa. Preparation and properties of BaTiO₃ ceramics by spark plasma sintering. *Japanese Journal of Applied Physics*, 47(9):7646–7649, 2008.

-
- [24] G. Maizza, S. Grasso, Y. Sakka, T. Noda, and O. Ohashi. Relation between microstructure, properties and spark plasma sintering (sps) parameters of pure ultrafine wc powder. *Science and Technology of Advanced Materials*, 8:644–654, 2007.
- [25] K. Matsugi, H. Kuramoto, T. Hatayama, and O. Yanagisawa. A case study for production of perfectly sintered complex compacts in rapid consolidation by spark sintering. *Materials Science and Engineering A*, 354:234–242, 2003.
- [26] K. Matsugi, H. Kuramoto, T. Hatayama, and O. Yanagisawa. Temperature distribution at steady state under constant current discharge in spark sintering process of ti and al₂o₃ powders. *Journal of Materials Processing Technology*, 146:274–281, 2004.
- [27] B. McWilliams and A. Zavaliangos. Multi-phenomena simulation of electric field assisted sintering. *Journal of Materials Science*, 43:5031–5035, 2008.
- [28] P. Mondalek, L. Silva, and M. Bellet. A numerical model for powder densification by SPS technique. *Advanced Engineering Materials*, 13(7):587–593, 2011.
- [29] K. Mori, K. Maeda, K. Osakada, and S. Maki. Finite element simulation of electric current, temperature and densification behaviour in electrical heating powder compaction. *Simulation of Materials Processing: Theory, Methods and Applications*, Balkema:517–522, 1998.
- [30] W. Muhammad, Y. Mutoh, and Y. Miyashita. Microstructure and mechanical properties of magnesium prepared by spark plasma sintering. *Advanced Materials Research*, 129-131:764–768, 2010.
- [31] Z. Munir, U. Anselmi-Tamburini, and M. Ohyanaji. The effect of electric field and pressure on the synthesis and consolidation of materials : A review of the spark plasma sintering method. *Journal of Materials Science*, 41:763–777, 2006.
- [32] S. Munoz and U. Anselmi-Tamburini. Temperature and stress fields evolution during spark plasma sintering processes. *Journal of materials science*, 45:6528–6539, 2010.
- [33] R. Orru, R. Licheri, A.M. Locci, A. Cincotti, and G. Cao. Consolidation/synthesis of materials by electric current activated/assisted sintering. *Materials Science and Engineering: R*, 63:127–287, 2009.
- [34] R. Oru, Robera Licheri, A.M. Locci, A. Cincotti, and G. Cao. Consolidation/synthesis of materials by electric current activated/assisted sintering. *Materials Science and Engineering R*, 63:127–287, 2009.
- [35] D.S. Perera, M. Tokita, and S. Moricca. Comparative study of fabrication of Si₃N₄/SiC composites by spark plasma sintering and hot isostatic pressing. *Journal of The European Ceramic Society*, 18(4):401–404, 1998.

- [36] P. Ponte-Castaneda. The effective mechanical properties of nonlinear isotropic composites. *Journal of the Mechanics and Physics of Solids*, 39:45–71, 1991.
- [37] A. I. Raichenko and E. S. Chernikova. A mathematical model of electric heating of the porous medium using current-supplying electrode/punches. *Powder Metallurgy and Metal Ceramics*, 28:365–370, 1989.
- [38] A. I. Raichenko, E. S. Chernikova, and E.A. Olevsky. The analysis of the electric heating of the wc-co hard-alloy under consideration of the dependence of it's characteristics on the temperature. *Journal de physique IV, Colloque C7*, 3:1235–1239, 1993.
- [39] J. Rathel, M. Herrmann, and W. Beckert. Temperature distribution for electrically conductive and non-conductive materials during field assisted sintering (FAST). *Journal of the European Ceramic Society*, 29:1419–1425, 2009.
- [40] S. Shima and M. Oyane. Plasticity theory for porous metals. *Internatonal Journal of Mechanical Science*, 18:285–291, 1976.
- [41] J.Y. Song, Y. Li, Z. Zhou, Y. Lai, and Y. Ye. A multi-field coupled fem model for one-step-forming process of spark plasma sintering considering local densification of powder material. *Journal of Material Science*, 46:5645–5656, 2011.
- [42] G.F. Taylor. Apparatus for making hard metals compositions. *US Patent*, 1,896,854, 1933.
- [43] M. Tokita. Mechanism of Spark Plasma Sintering. page 23, 1999.
- [44] K. Vanmeensel, A. Laptev, J. Hennicke, J. Vleugels, and O. van der Biest. Modelling of the temperature distribution during field assisted sintering. *Acta Materialia*, 53:4379–4388, 2005.
- [45] C. Wang, L. Cheng, and Z. Zhao. FEM analysis of the temperature and stress distribution in spark plasma sintering: Modelling and experimental validation. *Computational Materials Science*, 49:351–362, 2010.
- [46] S.W Wang, L.D. Cheng, Y.S. Kangb, M. Niinob, and T. Hiraia. Effect of plasma activated sintering (PAS) parameters on densification of copper powder. *Materials Research Bulletin*, 35:619–628, 2000.
- [47] X. Wang, S.R. Casolco, G. Xu, and J.E. Garay. Finite element modeling of electric current-activated sintering: The effect of coupled electrical potential, temperature and stress. *Acta Materialia*, 55:3611–3622, 2007.
- [48] Y. Wang and Z. Fu. Study of temperature field in spark plasma sintering. *Materials Science and Engineering B*, 90:34–37, 2002.

-
- [49] Y.C. Wang, Z.Y. Fu, and W.M. Wang. Numerical simulation of the temperature field in sintering of bn by sps. *Key Engineering Materials*, 249:471–476, 2003.
- [50] G. Weintraub and H. Rush. Process and apparatus for sintering refractory materials. *US Patent*, 1,071,448, 1913.
- [51] C. Wolff. Modeling of conventional hot compaction and spark plasma sintering based on modified micromechanical models of porous materials. *Mechanics of Materials*, 49:72–91, 2012.
- [52] G. Xie, O. Ohashi, K. Chiba, N. Yamaguchi, M. Song, K. Furuya, and T. Noda. Frequency effect on pulse electric current sintering process of pure aluminum powder. *Materials Science and Engineering A*, 359:384–390, 2003.
- [53] O. Yanagisawa, H. Kuramoto, K. Matsugi, and M. Komatsu. Observation of particle behavior in copper powder compact during pulsed electric discharge. *Materials Science and Engineering: A*, 350:184 – 189, 2003.
- [54] M. Yoneya and T. Ikeshoji. A numerical calculation method advantageous for complex boundary problems -an application to the pulse discharge sintering process. *Materials Transactions*, 42:2165–2171, 2001.
- [55] A. Zavaliangos, J. Zhang, M. Krammer, and J.R. Groza. Temperature evolution during field activated sintering. *Materials Science and Engineering A*, 379:218–228, 2004.

Chapter 3

Numerical modeling of the coupled thermal electrical problems

Contents

3.1	Introduction	40
3.2	Monolithic approach used in CimLib[®]	41
3.2.1	Level set method	41
3.2.2	Mixing laws	42
3.2.3	Anisotropic mesh adaptation	42
3.3	Modeling of the electrical problem	44
3.3.1	Governing equations	44
3.3.2	Weak form and discretization of the electrical problem	45
3.4	Modeling of the thermal problem	46
3.4.1	Governing equations	46
3.4.2	Weak form and discretization of the thermal problem	47
3.5	Heating by Joule effect: Numerical tests	49
3.5.1	Numerical validation of Ohm's law	49
3.6	Simulation of thermal electrical coupling for a simplified SPS geometry	53
3.6.1	Numerical results: <i>Electric problem</i>	55
3.6.2	Influence of the source term	59
3.6.3	Numerical results: <i>Temperature distribution</i>	60
3.6.4	Influence of thermal dependence of physical properties	62
3.7	Simulation of electrical thermal coupling: Comparison between two codes and experiments	64

3.7.1	Numerical results: <i>Electrical problem</i>	66
3.7.2	Numerical results: <i>Thermal problem</i>	67
3.8	Conclusion	73

Résumé

La modélisation du couplage électrique thermique du procédé de frittage flash et sa résolution par la méthode d'éléments finis sont présentées dans ce chapitre. Dans le cadre de cette thèse, nous avons fait le choix de modéliser les problèmes électriques et thermiques via une approche monolithique. C'est à dire qu'un maillage unique représente le domaine de calcul et des fonctions level set sont utilisées pour représenter les interfaces entre les différents matériaux. Le couplage est d'abord validé par comparaison avec des calculs analytiques pour un test simple 2D. Puis, une géométrie 3D simplifiée est modélisée et les résultats obtenus sont comparés aux résultats de la littérature et effectués avec Abaqus [3] pour trois échantillons: l'alumine, le graphite et le nickel. Les comparaisons sont satisfaisantes pour le problème couplé électrique et thermique. Une autre géométrie est modélisée celle-ci correspond à une machine Sumitomo. Deux échantillons (TiAl et alumine) sont considérés pour cette géométrie. Les résultats obtenus avec CimLib, utilisant l'approche monolithique, sont comparés et validés grâce à des résultats numériques issus du logiciel Comsol. De plus, ces résultats ont été validés avec des résultats expérimentaux utilisant le changement de phase au niveau microstructurale afin d'en déduire la température. Dans cette étude, on a vu que la distribution de la température dans l'échantillon est principalement influencée par la conduction thermique du graphite qui entoure l'échantillon. De plus, la distribution de la température autour de l'échantillon est dépendante de ses propriétés électriques. Les résultats de ce chapitre montrent que la simulation par éléments finis du couplage électrique-thermique est nécessaire pour comprendre la distribution de la température pendant le procédé de frittage flash. Ces simulations devraient permettre aux ingénieurs de mieux choisir la nature des matériaux de l'outillage ainsi que leurs géométries, afin de réduire les hétérogénéités de température et, par conséquent, leur permettre un meilleur contrôle de microstructure.

3.1 Introduction

This chapter addresses the electric thermal coupling during spark plasma sintering process as presented in Figure 3.1. The evolution of powder densification is not treated. Models presented here do not include the powder porosity. Hence, physical properties are temperature dependent but independent of the powder density. The Coupling between the electric-thermal problem and the mechanical problem is treated later on in Chapter Three.

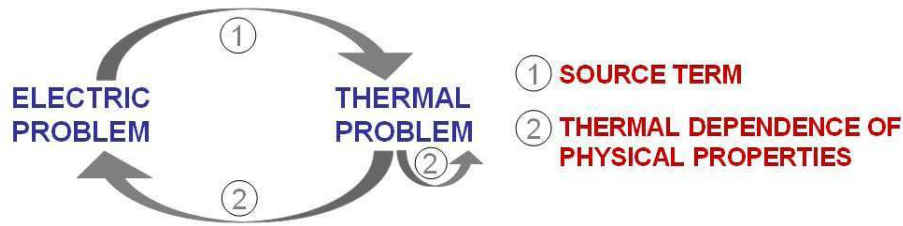


Figure 3.1: Thermal-electrical coupling scheme during spark plasma sintering process

The aim of this chapter is to show the effect of different phenomena on heating and temperature distribution. In fact, even if at this point the powder is considered as a dense medium and coupling with densification is not modeled, several mechanisms interfere and make coupling between the electrical and thermal problem complex. Physical properties of the sample are discussed first, in particular electric conductivity. Then we discuss the influence of thermal dependance, to finish with modeling heat losses that occur through water cooling and radiation to the chamber walls of the apparatus.

The monolithic approach is presented. It is used to simulate the electrical thermal coupling during the SPS process. First, the code as well as the numerical approach are introduced. The code used is CimLib developed at CEMEF. Secondly, two sections follow to describe, on the one hand, the model of the electric problem as well as the electric current waveforms applied in SPS and, on the other hand, the thermal model with the different heat transfer mechanisms. The finite element method is used to solve these problems and for each one the discretization of the equations is presented.

Afterwards, numerical tests will be used to validate the electrical effect on temperature, provided by Joule heating. Next, two SPS geometries are modeled, we begin by considering starting with a model where boundary conditions are simplified and for which we compare CimLib results with Abaqus results issued from the work of Couque *et al.* at ICB¹ (one of the partners of the IRIS project) but prior to IRIS [3]. This simplified model

¹ICB, Laboratoire Interdisciplinaire Carnot de Bourgogne, UMR 6303 CNRS - Université de Bourgogne, BP 47870, 21078 DIJON Cedex, France

is simulated with and without thermal dependence of the different material parameters to study its influence on heating. In a second step, a more complete geometry is considered where heat losses respect the experimental conditions. Here, CimLib results are compared with Comsol results which have been obtained by our colleagues in IRIS project at CEMES². A closer study is carried out for the temperature distribution for two different materials: *TiAl* and alumina.

3.2 Monolithic approach used in CimLib[®]

3.2.1 Level set method

The main idea of the monolithic approach developed in CimLib[®] is the use of one single mesh for the calculations. Either dealing with one or several materials, one mesh is defined composed by the computational domain Ω . More precisely, given an interface Γ_i bounding a region $\Omega_i \subset \Omega$, we define a continuous distance function $\alpha_i(\vec{x}, t)$ that represents the interface as the surface where $\alpha_i(\vec{x}, t) = 0$. The level set function α_i has the following properties: if $\vec{x} = (x_1, \dots, x_n) \in \mathbb{R}^n$

$$\begin{aligned} \alpha_i(\vec{x}, t) &> 0 && \text{for } \vec{x} \in \Omega_i \\ \alpha_i(\vec{x}, t) &< 0 && \text{for } \vec{x} \notin \Omega_i \\ \alpha_i(\vec{x}, t) &= 0 && \text{for } \vec{x} \in \partial\Omega_i = \Gamma_i(t) \end{aligned} \quad (3.1)$$

Once calculated, the level set function distribution allows us to define a presence function of the subset Ω_i . The presence function assigns to each node the value one or zero according to its location inside or outside the subset. A "smoothed" Heaviside function $H(\alpha_i)$ is used in this work, where a thickness ε_m is fixed in the surrounding of the interface in a way to avoid numerical problems coming from the discontinuous behavior in the transition region:

$$\begin{aligned} H(\alpha_i) &= 1 && \text{if } \alpha_i > \varepsilon_m \\ H(\alpha_i) &= \frac{1}{2} \left(1 + \frac{\alpha_i}{\varepsilon_m} + \frac{1}{\pi} \sin \left(\frac{\pi \alpha_i}{\varepsilon_m} \right) \right) && \text{if } |\alpha_i| \leq \varepsilon_m \\ H(\alpha_i) &= 0 && \text{if } \alpha_i < -\varepsilon_m \end{aligned} \quad (3.2)$$

In calculations, the value of ε_m is chosen accordingly to the mesh size in order to approach a sharp interface solution. Its minimum should not be lower than the double of the mesh size in the orthogonal direction to the interface. Furthermore, considering a number of subdomains Ω_i , each one representing a different phase or material, the objective is to

²CEMES, Center d'Elaboration de Matériaux et d'Etudes Structurales, 29 rue Jeanne Marvig, BP 94347, 31055 Toulouse Cedex 4, France

compute the physical properties on the entire domain Ω associating to each material its appropriate properties. For this reason, mixing laws are introduced.

3.2.2 Mixing laws

Mixing laws are defined as functions of the level set. Different expressions can be used to compute the values on the entire computational domain Ω . Either an arithmetic mean or an harmonic mean is chosen. In the electric and thermal equations different physical properties need to be mixed on the computational domain Ω such as the electric and thermal conductivities, the specific heat capacity and the density. In fact, it was shown [6] that for the density and specific heat capacity an arithmetic mean gives more accurate results. If the index i and j refer respectively to the subdomains Ω_i and Ω_j :

$$\rho = H(\alpha_i)\rho_i + (1 - H(\alpha_i))\rho_j \quad (3.3)$$

$$c_p = H(\alpha_i)c_{p_i} + (1 - H(\alpha_i))c_{p_j} \quad (3.4)$$

As ρ and c_p are considered via their time derivative term the heat transfer equation, and due to the fact that they vary inversely in each material (ρ is lower for the material having a higher c_p for *TiAl* and graphite), it is better to mix their product directly before introducing it in heat equation:

$$\rho c_p = H(\alpha_i)\rho_i c_{p_i} + (1 - H(\alpha_i))\rho_j c_{p_j} \quad (3.5)$$

On the other hand, for conductivities, an harmonic average is chosen, after [6] :

$$k = \left(\frac{H(\alpha_i)}{k_i} + \frac{1 - H(\alpha_i)}{k_j} \right)^{-1} \quad (3.6)$$

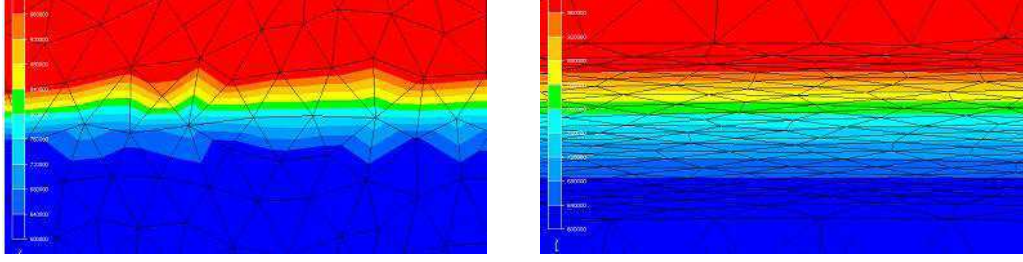
$$\sigma_e = \left(\frac{H(\alpha_i)}{\sigma_{ei}} + \frac{1 - H(\alpha_i)}{\sigma_{ej}} \right)^{-1} \quad (3.7)$$

Later on, in paragraph 3.5.1 a validation test is presented in order to justify the choice of the law for the conductivity.

3.2.3 Anisotropic mesh adaptation

An isotropic unstructured mesh can be generated directly in CimLib[®] through the "MTC" mesher developed by Coupez *et al.* [2][4]. Since the model involves different materials and so different properties, a refined mesh is needed at the interface in order to improve the accuracy of the discretization of the mixing law (H function). A coarse mesh near the interface would reduce dramatically the accuracy of the solution.

When dealing with complex shapes, if the mesh is not refined enough the geometry cannot be described properly with the level set function. However, if isotropic elements are used at this level, we face a large number of elements and the calculation time increases significantly. Consequently, in order to enhance the accuracy around the interface and optimize computational time, an anisotropic adaptive meshing is accomplished (Figure 3.2).



(a) Transition around the interface with a homogeneous mesh

(b) Smooth transition with an anisotropic mesh around the interface

Figure 3.2: Comparison of the transition around the interface between two subdomains with and without anisotropic mesh adaptation

More precisely, the approach consists in keeping an isotropic mesh far from interfaces with coarse mesh size and generating a refined mesh with anisotropic elements in their neighbourhood [5]. The metric used is dependent on the gradient of the level set function and is written as follows:

$$M = \begin{cases} \varepsilon_{rem}^2 \mathbb{I} & \text{if } |\alpha| > e \\ \left(\left(\frac{N}{2e} \right)^2 - \varepsilon_{rem}^2 \right) A + \varepsilon_{rem}^2 \mathbb{I} & \text{elsewhere} \end{cases} \quad \text{where } A = \frac{\nabla \alpha \otimes \nabla \alpha^T}{\|\nabla \alpha\|^2} \quad (3.8)$$

where N is the number of elements generated in the thickness $2e$ and in the direction of the gradient of the level set, and ε_{rem} is related to the background mesh size.

Figure 3.3 represents the scheme of the remeshing, indicating the different parameters. As the MTC remeshing procedure returns a unitary mesh in the sense of metric M , the isotropic background elements have a mesh size equal to $\frac{1}{\varepsilon_{rem}}$ and the anisotropic elements have the elongated edge size equal to $\frac{1}{\varepsilon_{rem}}$ and the one orthogonal to the interface equal to $\frac{2e}{N}$. ε_{rem} should be lower than ε_m used for the Heaviside function.

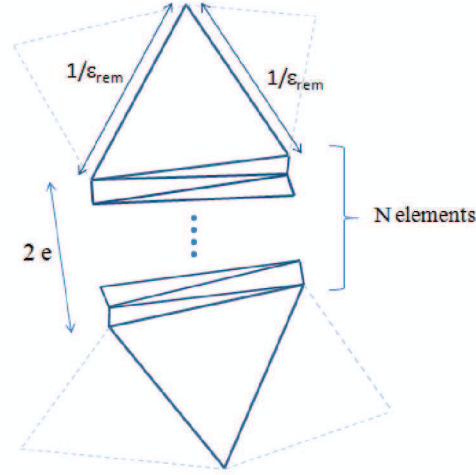


Figure 3.3: Representative scheme of the remeshed zone around the interface with the corresponding parameters

3.3 Modeling of the electrical problem

The powder is placed inside a graphite mould and is surrounded by two graphite pistons on the top and bottom. Heating of the apparatus during the spark plasma sintering process is generated directly from Joule effect. Since all the tools are conductive, the electric current goes through the whole assembly and generates heat. Besides, heating of the sample depends on its electrical properties, it could be provided either directly from the Joule effect or by conduction when it's a non conductor material.

Different types of electric current might be used depending on the apparatus. In this work, a DC current is always considered for all the simulations according to the bibliography presented in Chapter 2.

3.3.1 Governing equations

Once applied, the electrical current generates heat inside the conducting materials depending on their electrical conductivities. The modeling of the electrical problem during SPS process derives from the charge conservation law:

$$\nabla \cdot \vec{J} = 0 \quad (3.9)$$

where \vec{J} denotes the current density. Applying Ohm's law, \vec{J} can be written:

$$\vec{J} = \sigma_e \vec{E} = -\sigma_e \nabla U \quad (3.10)$$

where \vec{E} denotes the electric field, σ_e the electric conductivity and U the electric potential. Consequently, the electrical problem consists in solving the following Poisson type

equation to deduce the potential U :

$$\nabla \cdot (-\sigma_e \nabla U) = 0 \quad (3.11)$$

Considering $\Omega \subset \mathbb{R}^3$ the computational domain and $\Gamma = \partial\Omega$ its boundary, the electrical problem is summarized as follows:

Find U at each node of Ω such that at each instant t :

$$\begin{cases} \nabla \cdot (-\sigma_e \nabla U) & = 0 & \text{in } \Omega \\ \text{Boundary condition on } \Gamma & & \end{cases} \quad (3.12)$$

In fact, in the simulation either a voltage or an electrical flux is applied. When a voltage is applied, the boundary condition on Γ is written:

$$U = U_{imp} \quad (3.13)$$

Whereas, when an electrical flux is considered, the boundary condition on Γ is written:

$$-\sigma_e \nabla U \cdot \vec{n} = \Phi_{imp} \quad (3.14)$$

3.3.2 Weak form and discretization of the electrical problem

In order to solve the equations above by the finite element method, let us define the Sobolev space $H^1(\Omega)$ of functions with square integrable derivatives, the Lebesgue space $L^2(\Omega)$, and $H_0^1(\Omega)$ the space of functions in $H^1(\Omega)$ with vanishing values on the boundary Γ :

$$\begin{aligned} H^1(\Omega) &= \{\omega \in L^2(\Omega), \nabla \omega \in [L^2(\Omega)]^3\} \\ L^2(\Omega) &= \{\omega, \int_{\Omega} \omega^2 d\Omega < \infty\} \\ H_0^1(\Omega) &= \{\omega \in H^1(\Omega), \omega = 0 \text{ on } \Gamma\} \end{aligned}$$

The variational (or weak) form of the electrical equation is posed as follows:

$$\begin{cases} \text{Find } U \in H^1(\Omega) \text{ such that:} \\ \int_{\Omega} \sigma_e \nabla U \cdot \nabla \omega d\Omega - \int_{\Gamma_{flux}} \sigma_e \nabla U \cdot \vec{n} \omega d\Gamma_{flux} = 0 \quad \forall \omega \in H_0^1(\Omega) \end{cases} \quad (3.15)$$

3.3.2.1 Discretization

The standard Galerkin method consists in approximating the space Ω by the finite space Ω_h . Ω is substituted by a set of N elements, τ_h , built on the nodes of the domain Ω_h . H_h^1 is defined as the space of piecewise polynomial functions, the interpolation order is n per element. For the electrical problem we considered $n = 1$. Hence, $H_h^1 = \{\omega_h \in C^0(\Omega_h), \omega_h|_{\tau_h} \in P1\}$ and the discrete form is:

$$\left\{ \begin{array}{l} \text{Find } U_h \in H_h^1 \text{ such that:} \\ \int_{\Omega_h} \sigma_e \nabla U_h \cdot \nabla \omega_h d\Omega_h + \int_{\Gamma_{flux}} \Phi_{imp} \omega_h d\Gamma_{flux} = 0 \quad \forall \omega_h \in H_{0h}^1(\Omega) \end{array} \right. \quad (3.16)$$

n_s , the number of nodes in the mesh, is the dimension of the finite-dimensional space H_h^1 . The basis of this space is $\{N_i\}_{i=1}^{n_s}$ where N_i is continuous on Ω_h , linear on each element and $N_i(s_j) = \delta_{ij}$, s_j node of the mesh. Consequently:

$$\forall U_h \in H_h^1(\Omega) \quad U_h = \sum_{i=1}^{n_s} U_i N_i$$

and $\omega_h \equiv N_j$

3.4 Modeling of the thermal problem

3.4.1 Governing equations

The governing equation of the thermal problem is based on energy conservation in which the phase change term is neglected:

$$\nabla \cdot (-k \nabla T) + \rho c_p \frac{dT}{dt} = q_e \quad (3.17)$$

where k is the thermal conductivity, ρ the density, c_p the specific heat and q_e the heat source. The heat source and the coupling between the electrical and thermal problems in the SPS process will be discussed in section 3.6. Moreover, in the thermal problem, since the process is taking place in a vacuum chamber, heat losses by convection and conduction are neglected. All lateral surfaces have heat losses by radiation towards the chamber walls, which are supposed to be held at room temperature. Furthermore, to minimize heating rates in the SPS setup, two Inconel spacers are in contact with the graphite spacers and are water cooled. As a consequence, heat losses of the two extreme upper and lower Inconel surfaces can be modeled through a convective type heat flux.

3.4.1.1 Thermal boundary conditions

Conduction When two bodies are in contact, heat transfer appears from the region with the highest temperature towards the coolest region in order to attain heat equilibrium. Here, the hot Inconel spacer is in contact with water which is supposed to be kept at a constant temperature T_{water} . This phenomenon is described by the following equation concerning a convective flux:

$$\Phi_{conv} = -k \nabla T \cdot \vec{n} = h_{conv} (T - T_{water}) \quad \text{on } \Gamma_{top} \cup \Gamma_{bottom} \quad (3.18)$$

where \vec{n} is the outward unit normal water, h_{conv} is the heat transfer coefficient considered constant, T the local surface temperature of the Inconel spacers.

Radiation Radiation describes the phenomenon through which a hot body emits and propagates energy. In the SPS process it describes the energy losses from the heated tools. Radiation is modeled by the following equation on the lateral surface:

$$\Phi_{rad} = -k\nabla T \cdot \vec{n} = \sigma_B \varepsilon_r (T^4 - T_{wall}^4) \quad \text{on } \Gamma_{lateral} \quad (3.19)$$

σ_B is the Stefan-Boltzmann's constant, $\sigma_B = 5.6704 \times 10^{-8} \text{ W m}^{-2} \text{ K}^{-4}$, ε_r the emissivity of tools and T_{wall} the temperature of the chamber walls. Hence, the thermal problem is summarized by:

$$\nabla \cdot (-k\nabla T) + \rho c_p \frac{dT}{dt} = q_e \quad \text{on } \Omega \quad (3.20)$$

$$-k\nabla T \cdot \vec{n} = \Phi_{conv} \quad \text{on } \Gamma_{Top} \cup \Gamma_{Bottom} \quad (3.21)$$

$$-k\nabla T \cdot \vec{n} = \Phi_{rad} \quad \text{on } \Gamma_{Lateral}$$

Remark: If $-k\nabla T \cdot \vec{n} = \Phi = 0$ an adiabatic condition takes place and the corresponding surface Γ is insulated. If the flux is negative, the surface receives energy on the contrary a positive flux refers to an energy loss.

3.4.2 Weak form and discretization of the thermal problem

Similarly to the electrical problem, the space $H^1(\Omega)$ is considered to transform the partial differential equation of the thermal problem to a variational form. After multiplying by the test function $\omega \in H_0^1(\Omega)$, and integrating by parts, the weak form is expressed as follows:

$$\begin{cases} \text{Find } T \in H^1(\Omega) \text{ such that:} \\ \int_{\Omega} \rho c_p \frac{dT}{dt} \omega d\Omega + \int_{\Omega} k\nabla T \cdot \nabla \omega d\Omega - \int_{\Gamma} k\nabla T \cdot \vec{n} \omega d\Gamma = \int_{\Omega} q_e \omega d\Omega \\ \forall \omega \in H_0^1(\Omega) \end{cases} \quad (3.22)$$

After considering the conductive and radiative heat fluxes, the problem can be written:

$$\begin{cases} \text{Find } T \in H^1(\Omega) \text{ such that:} \\ \int_{\Omega} \rho c_p \frac{dT}{dt} \omega d\Omega + \int_{\Omega} k\nabla T \cdot \nabla \omega d\Omega \\ + \int_{\Gamma_{conv}} h_{conv} (T - T_{water}) \omega d\Gamma_{conv} + \int_{\Gamma_{rad}} \sigma_B \varepsilon_r (T^4 - T_{wall}^4) \omega d\Gamma_{rad} = \int_{\Omega} q_e \omega d\Omega \\ \forall \omega \in H_0^1(\Omega) \end{cases} \quad (3.23)$$

3.4.2.1 Discretization

Time integration: A time discretization scheme is associated to the space discretization. Many formulations can be found in the literature. Here, the two-time steps scheme

(θ -scheme) is used, for $\theta \in [0, 1]$:

$$\theta \frac{\partial T_{n+1}}{\partial t} + (1 - \theta) \frac{\partial T_n}{\partial t} = \frac{T_{n+1} - T_n}{\Delta t} \quad (3.24)$$

Depending on the value of θ , an implicit or explicit scheme can be considered. Schematically, with a function $F(T)$, the temperature T_{n+1} at a time t_{n+1} can be expressed using a function of T_n of the previous step t_n and the current temperature T_{n+1} :

$$T_{n+1} = T_n + \Delta t [(1 - \theta)F(T_n) + \theta F(T_{n+1})] \quad (3.25)$$

In the present work, an implicit scheme is considered to solve the thermal problem with $\theta = 1$.

Space integration: In the same framework of a standard Galerkin approximation, as for the electrical problem, the temperature is expressed in the finite space $H_h^1(\Omega)$, and the test function ω is expressed in its subspace $H_{0h}^1(\Omega)$:

$$\forall T_h \in H_h^1(\Omega) \quad T_h = \sum_{i=1}^{n_s} T_i N_i$$

and $\omega_h \equiv N_j$

In order to simplify the resolution of the weak form, an approximation is considered for the radiative heat flux of equation 3.19:

$$\begin{aligned} \Phi_{rad} &= \sigma_B \varepsilon_r (T^4 - T_{wall}^4) \\ &= \sigma_B \varepsilon_r (T - T_{wall})(T + T_{wall})(T^2 + T_{wall}^2) \\ &= \underbrace{\sigma_B \varepsilon_r (T + T_{wall})(T^2 + T_{wall}^2)}_{h^*} (T - T_{wall}) \end{aligned} \quad (3.26)$$

The discrete form is then written:

$$\left\{ \begin{array}{l} \text{Find } T_h \in H_h^1(\Omega) \text{ such that:} \\ \int_{\Omega_h} \rho c_p \frac{T_h}{\Delta t} \omega_h d\Omega_h + \int_{\Omega_h} k \nabla T_h \cdot \nabla \omega_h d\Omega_h - \int_{\Gamma_{hconv}} h T_h \omega_h d\Gamma_{hconv} - \int_{\Gamma_{hrad}} h^* T_h \omega_h d\Gamma_{hrad} \\ = \int_{\Omega_h} q_e \omega_h d\Omega_h + \int_{\Omega_h} \rho c_p \frac{T_h^{i-1}}{\Delta t} \omega_h d\Omega_h - \int_{\Gamma_{hconv}} h T_{wall} \omega_h d\Gamma_{hconv} - \int_{\Gamma_{hrad}} h^* T_{wall} \omega_h d\Gamma_{hrad} \\ \forall \omega_h \in H_{0h}^1(\Omega) \end{array} \right.$$

Which leads to:

$$\begin{aligned} \forall i, \sum_{j=1}^{n_s} T_i \left(\int_{\tau_h} \frac{\rho c_p}{\Delta t} N_i N_j + \int_{\tau_h} k \nabla N_i \cdot \nabla N_j - \int_{\Gamma_{hconv} \cap \tau_h} h N_i N_j - \int_{\Gamma_{hrad} \cap \tau_h} h^* N_i N_j \right) \\ = - \sum_{j=1}^{n_s} \left(\int_{\Gamma_{hconv} \cap \tau_h} h T_{wall} N_j - \int_{\Gamma_{hrad} \cap \tau_h} h^* T_{wall} N_j + \int_{\tau_h} q_e N_j + \int_{\tau_h} \frac{\rho c_p}{\Delta t} T_i^{i-1} N_j \right) \end{aligned} \quad (3.27)$$

and finally, matrix components of our system $AT = b$ can be written :

$$a_{ij} = \int_{\tau_h} \frac{\rho c_p}{\Delta t} N_i N_j + \int_{\tau_h} k \nabla N_i \cdot \nabla N_j - \int_{\Gamma_{hconv} \cap \tau_h} h N_i N_j - \int_{\Gamma_{hrad} \cap \tau_h} h^* N_i N_j \quad (3.28)$$

$$b_j = \int_{\tau_h} q_e N_j + \int_{\tau_h} \frac{\rho c_p}{\Delta t} T_i^{t_i-1} N_j - \int_{\Gamma_{hconv} \cap \tau_h} h T_{wall} N_j - \int_{\Gamma_{hrad} \cap \tau_h} h^* T_{wall} N_j \quad (3.29)$$

3.5 Heating by Joule effect: Numerical tests

In this chapter, we discuss the coupling between the electrical and thermal problems. In fact, coupling appears, on the one hand, in the source term of the energy balance equation (3.20) and, on the other hand, in the physical properties since they are temperature dependent. First, the source term describes the power dissipated by Joule effect:

$$q_e = \sigma_e \|\nabla U\|^2 \quad (3.30)$$

The heating of the sample is then directly related to its electrical conductivity, but which also affects the potential gradient. Second, electrical conductivity, thermal conductivity, specific heat capacity and density are temperature dependent and their evolution must be taken into consideration to better follow the temperature distribution and evolution. In this chapter, we only deal with the thermal electrical coupling during the process. The powder is considered as a dense medium and the distribution of electrical current and temperature are modeled. Later on, in **Chapter 4**, we will see that coupling is much more complex, when the interaction with the mechanical problem is added. Heating will affect densification, besides, we are subjected to a variation in the volume of the compact and the porosity. Consequently, in this case, physical properties are considered as functions of the pore fraction as well as temperature.

At first, numerical tests are carried out to validate Joule heating by comparing with analytical results.

3.5.1 Numerical validation of Ohm's law

3.5.1.1 Modeling of Joule heating of a single material

Before simulating the coupling for the spark plasma sintering process, a simple test is chosen where heating by Joule effect of a 2D rectangular material is modeled. As seen in Figure 3.4, on the top an electrical flux is imposed, $J = 1.5 \times 10^8 \text{ A.m}^{-2}$, and on the bottom a zero potential. The material is copper and its electrical conductivity at room temperature is $\sigma_e = 6 \times 10^7 \Omega^{-1} \text{ m}^{-1}$. This simple test aims in validating the test, electrical thermal coupling. In this paragraph, validation is limited to the comparison with analytic results.

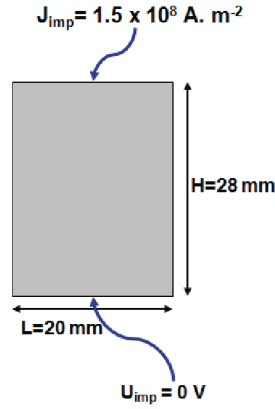


Figure 3.4: 2D geometry with boundary conditions of the electrical problem

Analytic solution The electrical resistance is given by: $\frac{L}{\sigma_e S}$, where L is the length of the plaque in m, σ_e the electrical conductivity $\Omega^{-1}\text{m}^{-1}$, S the surface of the plaque in m^2 (in fact we consider a third unitary dimension) and R the electric resistance in Ω . The electric current can be deduced from: $I = JS$, and finally, using Ohm's law, the electric potential generated by the electric resistance of the material is:

$$U = RI = \frac{L}{\sigma_e S} JS = \frac{L}{\sigma_e} J = 0.07 \text{ V} \quad (3.31)$$

Furthermore, considering an adiabatic flux, the thermal equation is reduced to:

$$\rho c_p \frac{\partial T}{\partial t} = \sigma_e \|\nabla U\|^2$$

so that in any point, considering a constant σ_e , the temperature increases during a time step $\Delta t = 1 \text{ s}$:

$$\Delta T = \frac{\sigma_e}{\rho c_p} \left(\frac{\Delta U}{\Delta L} \right)^2 \Delta t = 109.196^\circ \text{C}$$

Numerical solution Here, the electrical conductivity is constant in order to compare with the analytic solution. The electric problem with its boundary conditions is written as follows:

Find U at each node of Ω such that for each instant t :

$$\begin{cases} \nabla \cdot (-\sigma_e \nabla U) = 0 & \text{in } \Omega \\ U = 0 & \text{on } \Gamma_{\text{Bottom}} \\ \underbrace{-\sigma_e \nabla U \cdot \vec{n}}_J = \Phi_e & \text{on } \Gamma_{\text{Top}} \end{cases} \quad (3.32)$$

The problem is solved using CimLib library, the potential is linear in the axial direction decreasing from 0.07 V on Γ_{Top} to zero on Γ_{Bottom} . Once the potential computed, the source term of heat equation 3.30 is calculated and introduced in the thermal problem:

Find T at each node of Ω such that for each instant t :

$$\begin{cases} \nabla \cdot (-k\nabla T) + \rho c_p \frac{\partial T}{\partial t} = q_e & \text{in } \Omega \\ -k\nabla T \cdot \vec{n} = \Phi_T & \text{on } \Gamma \end{cases} \quad (3.33)$$

Numerical results show that the temperature is homogeneous. Besides, its increasing rate is 109.196 K/s. The numerical solution is found in perfect agreement with the analytical one.

3.5.1.2 Modeling of Joule heating of two materials in contact

In this paragraph, the heating of two materials is modeled in order to validate Ohm's law in a multidomain framework using a simple test. Two 2D rectangular materials are considered in perfect contact conditions. An electrical flux $J = 5 \times 10^7 \text{ A.m}^{-2}$ is imposed on the upper boundary and a zero potential on the bottom as seen in Figure 3.5. The two material are then connected in series. The properties of body 1 are $\sigma_{e1} = 10^6 \Omega^{-1}.m^{-1}$, $\rho_1 = 1850 \text{ kg}.m^{-3}$, $c_{p1} = 694 \text{ J}.kg^{-1}.K^{-1}$ and body 2 $\sigma_{e2} = 6.10^5 \Omega^{-1}.m^{-1}$, $\rho_2 = 8920 \text{ kg}.m^{-3}$, $c_{p2} = 385 \text{ J}.kg^{-1}.K^{-1}$.

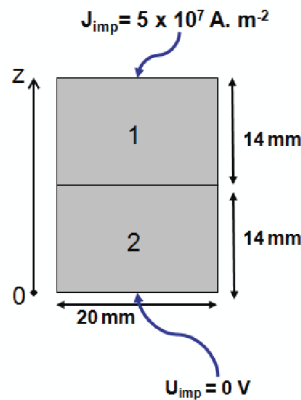


Figure 3.5: 2D geometry with two materials and the boundary conditions of the thermal-electrical problem

Analytic solution The total resistance of components in series is equal to the sum of their individual resistances: $R = R_i + R_j$. The electric potential is then equal to:

$$\begin{aligned} V &= (R_1 + R_2)I \\ &= (R_1 + R_2)JS \\ &= 1,8666V \end{aligned} \quad (3.34)$$

where S denotes the transverse section of domains 1 and 2. The variation of the electric potential along the height is drawn in Figure 3.6. The error between numerical results and analytic results is calculated after testing an arithmetic mixing law and an harmonic mixing law for the electrical conductivity. The graphic of Figure 3.8 shows that the harmonic mixing law reduces the error by 0.5%.

Moreover, considering as previously an adiabatic heat flux, temperature variation between two time steps can be simplified analytically as follows:

Given $\Delta t = 0,1s$ and $T_0 = 20^\circ C$:

$$\text{Material 1: } T_1 = \frac{\sigma_1}{\rho_1 c_{p1}} \frac{\|\Delta V_1\|^2}{(\Delta L)^2} \Delta t + T_0 \simeq 214,874^\circ C \quad (3.35)$$

$$\text{Material 2: } T_2 = \frac{\sigma_2}{\rho_2 c_{p2}} \frac{\|\Delta V_2\|^2}{(\Delta L)^2} \Delta t + T_0 \simeq 141,329^\circ C \quad (3.36)$$

The results of the simulation are in perfect agreement with the analytic solution as seen in Figure 3.7.

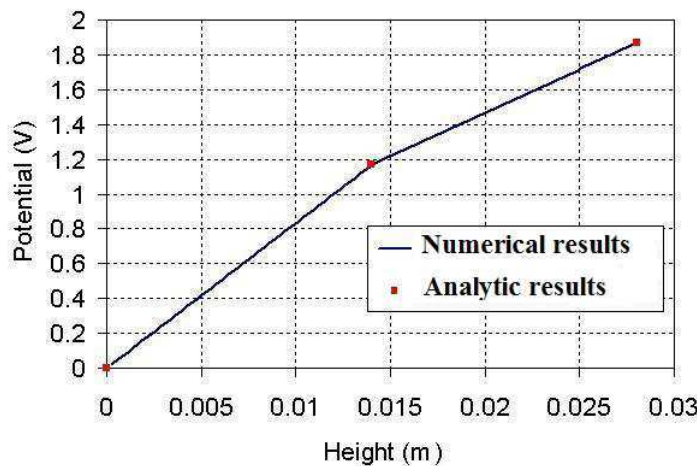


Figure 3.6: Variation of electrical potential along the vertical direction

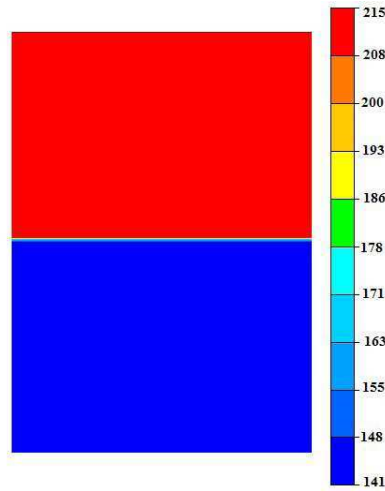


Figure 3.7: Distribution of the temperature ($^{\circ}\text{C}$) in the two domains

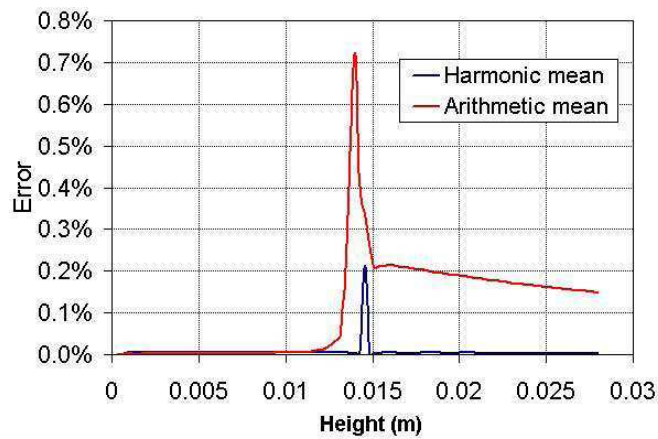


Figure 3.8: Comparison of the computational errors on the electrical potential using arithmetic mixing law and an harmonic mixing law for the electrical conductivity

3.6 Simulation of thermal electrical coupling for a simplified SPS geometry

Spark plasma sintering process can be applied to different kinds of materials, ceramics as well as metals. Physical properties vary from one powder to another. Consequently, differences are perceived during heating of the apparatus especially concerning temperature gradients inside the sample which affects densification. In addition, thermal dependence of these properties expands these differences.

The distribution of temperature during the SPS process is directly related to the dis-

tribution of current which is firstly affected by the geometry and secondly by the physical properties of the different components and materials involved in the whole set-up. Different samples, with different electrical conductivities are often used in the literature [14]-[1]- [10]-[11]-[15]-[8]-[7] to validate the accuracy of electrical thermal models, showing the effect of physical properties on the distribution of current and consequently on the distribution of temperature.

In this section, three compacted powder materials are chosen for comparison. These materials have different electrical conductivities. The difference of the compact properties highlights their influence on the distribution of current and temperature. The current density will be compared in the neighborhood of the sample as well as the temperature.

The different results are compared with the results of Couque *et al.* [3]. The experimental data of this publication are given by ICB³ which is a partner in the IRIS project.

Geometry and materials In this study, a 3D geometry is considered to simulate the electric thermal coupling (Figure 3.9). Because of axial symmetry, only a quarter of the apparatus is modeled (Figure 3.10). The generated mesh is composed of tetrahedral elements. Around the interface between the compact and tools, anisotropic elements are generated as explained previously. The total number of elements is 150 000, the background mesh size is 4.5 mm. In the refined zones (pistons with small section and neighborhood of the powder) the mesh size is equal to 1 mm. Concerning the anisotropic remeshing, the thickness of the remeshed zone is 1.5 mm, the number of anisotropic elements in the thickness is 25.

Temperature and current distributions are studied for conducting and non-conducting powder materials. Besides, the tools of the simplified geometry are all made of graphite. In order to compare our results with those of Couque *et al.* [3], three dense samples are considered: nickel, graphite and alumina. Their physical properties at room temperature are given in Table 3.1. In this first step, the influence of temperature on physical properties is neglected. As mentioned previously, powder is considered here as a continuum dense medium.

Furthermore, all contact surfaces between the parts of the SPS apparatus are considered ideal: as a consequence no contact resistance (thermal or electrical) is taken into account.

Boundary conditions Since at this step, we are only interested in showing the influence of thermal dependency in the coupled problems, boundary conditions are simplified. Radiation from the lateral surface is neglected and an adiabatic condition is considered. Besides, instead of considering a Neumann condition to model water cooling, a Dirichlet condition is imposed with a variable temperature, in such a way that temperature

³Institut Carnot De Bourgogne, Universite de Bourgogne, 9 avenue Savary, 21078 Dijon, France.

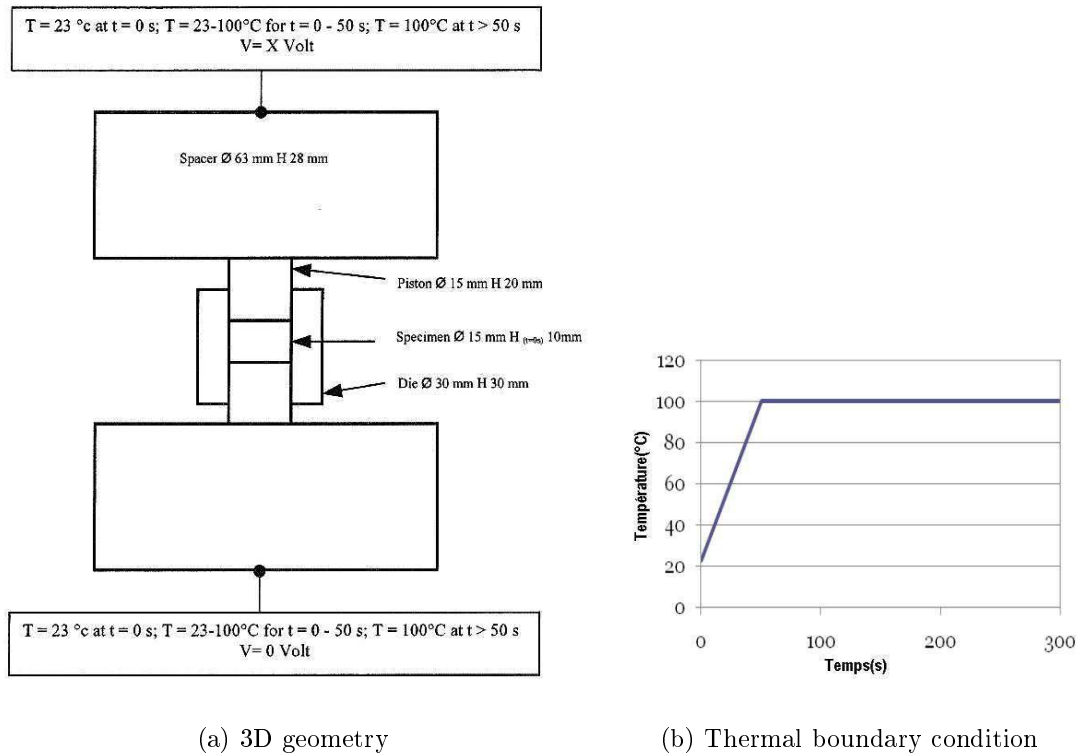


Figure 3.9: Geometry of the apparatus considered in order to compare with literature [3] and the variation of the temperature imposed at the lower and upper surface of graphite spacers

increases from 23°C up to 100°C in 50 s, then stabilize for $t > 50$ s at $T = 100^\circ\text{C}$ as expressed in Figure 3.9-(b). Concerning the electric problem, a constant voltage is applied, for each sample its value is shown in Table 3.2.

Consequently, without thermal dependency results can be compared with those obtained with Abaqus by Couque *et al.* [3].

3.6.1 Numerical results: *Electric problem*

In Figure 3.11, the norm of the current density is presented after applying a constant voltage. Since the temperature dependency of physical properties is not considered in these simulations, the distribution of the current is steady-state. In fact, for the three samples, the current density is always the highest in the pistons. The reason is the geometry of the apparatus and the small section of pistons where the current flux converge. More precisely, current is concentrated in pistons because they have the lowest section. Fluxes of electric current arrive from graphite spacer and converge together inside pistons increasing the local heating by Joule effect. Moreover, in the case of nickel, most of the

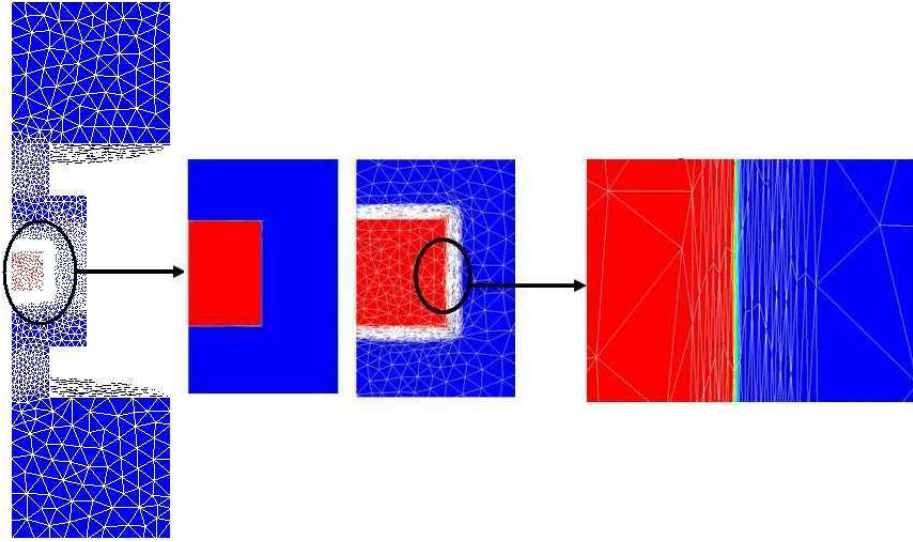


Figure 3.10: Representation of the 3D geometry with an overview on the mesh with anisotropic remeshing around the powder/die interface

Material	Density (g/cm^3)	Specific heat capacity ($J/kg/K$)	Thermal conductivity ($W/m/K$)	Electric conductivity ($\Omega^{-1}m^{-1}$)
Alumina	3.98	753	46	1.65×10^{-13}
Graphite	1.85	694	68	6.3×10^4
Nickel	8.90	446	91	1.40×10^7

Table 3.1: Physical properties of nickel, graphite and alumina at room temperature

current flows through the sample because of its high electrical conductivity. Whereas in the case of alumina, it is, as expected, relatively absent inside the sample. This means that alumina is heated only by conduction and not directly by Joule effect. Besides, for the graphite sample, the continuity of the field is remarkable this is due to the homogeneity of the physical properties in the whole assembly.

	Nickel	Graphite	Alumina
Potential (V)	2.43	2.41	3.34

Table 3.2: Constant voltage applied for the three different samples in the simulation of the simplified geometry

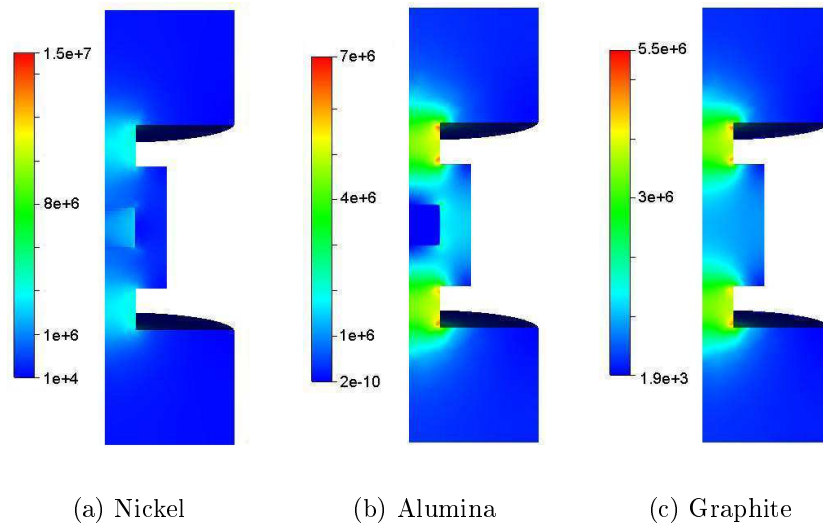


Figure 3.11: Influence of the electrical conductivities on the distribution of the norm of current density when thermal dependency is neglected

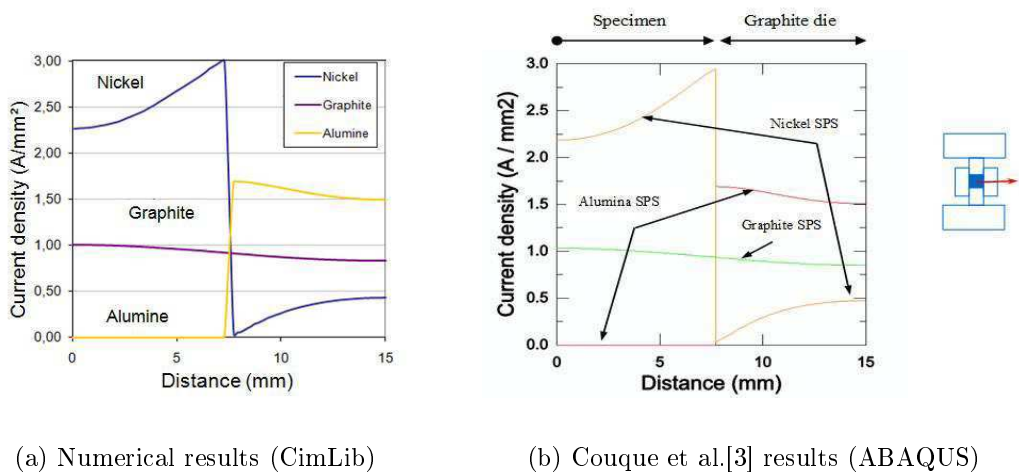
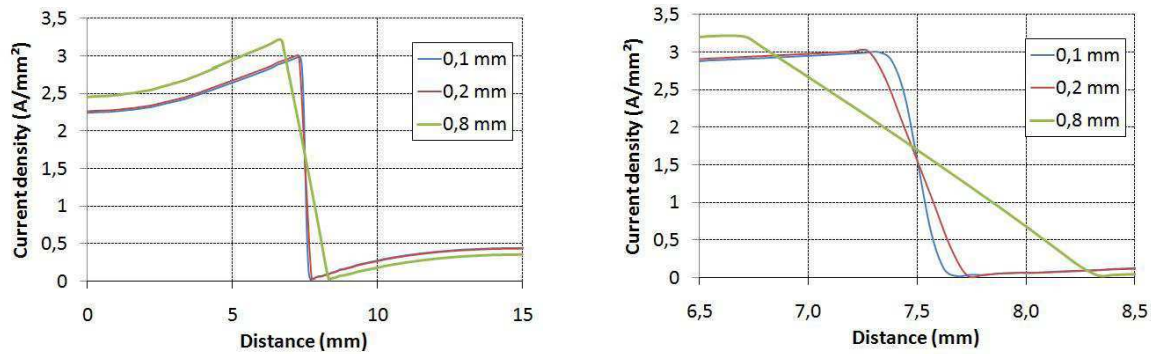


Figure 3.12: Radial variation of the density of the electrical current for the three samples: nickel, graphite and alumina from the centre of the sample towards the edge of the die, at mid-height of the sample

Thickness of the mixing law In Figure 3.12, the distributions of electrical current computed in CimLib and in Abaqus (Couque et al. work [3]) are compared. Curves describe the variation of the current density from the center of the specimen towards the die edge at mid height of the set-up. In the case of nickel, a maximum is reached inside the specimen at the level of the interface and is equal to 3 A/mm^2 . Besides, the current density drops to a minimum and tends to zero in the die. Then, it increases slightly when coming near the edge. In the case of graphite, the current is relatively homogeneous at

this level. Finally, in the case of alumina, the current is absent in the sample, it goes only through the die since the specimen is a non-conductor. At the interface, inside the die, the density is higher and its maximum is equal to 1.7 A/mm^2 , it decreases towards the edge to reach 1.5 A/mm^2 .

The main difference between CimLib and Abaqus appears in the neighbourhood of the sample/die interface. In fact, this is due to the two different numerical approaches applied in each work. In CimLib, as explained previously in section 3.2, a monolithic approach is used which explains the continuous transition between the specimen and die. Since the calculations are made on a single mesh, the domain occupied by each material is described with a level set function and mixing laws define respectively physical properties. Consequently, depending on the thickness chosen, the extension of the area of transition is more or less large.



(a) From the center of the specimen to the die edge

(b) Zoom at the neighbourhood of the interface

Figure 3.13: Radial variation of the electrical current density for nickel specimen from the center of the sample towards the edge of the die for different thickness considered in the mixing laws for the electric conductivity (Equation 3.7)

A study was carried out in the case of the nickel specimen, considering three thickness (ε_m in equation 3.2) values using the mixing law of Equation 3.7: 0.1 mm, 0.2 mm and 0.8 mm, while keeping the same mesh and nickel specimen knowing that the thickness of the remeshed zone is 1.5 mm. As seen in Figure 3.13, the higher the thickness, the larger the difference with Abaqus. More precisely, when the thickness is equal to 0.8 mm, the maximum of the current density reaches 3.21 A/mm^2 at the nickel surface whereas in the work of Couque *et al.* it reaches 2.95 A/mm^2 , besides, the transition covers a larger area around the interface.

3.6.2 Influence of the source term

Since the homogeneity of the microstructure in SPS-processed parts is dependent on the temperature homogeneity, it is interesting to understand the distribution of temperature during the process which is directly related to the source term in the heat equation. Actually, the differences in the electric field presented below won't lead necessarily to the same amplitude of differences concerning the source term. It should be noted that the electrical conductivity of the powder samples doesn't affect significantly the distribution of the source term. The source term is always higher in the graphite. In fact, the source term of the heat equation is balanced by the electrical conductivity, on the one hand, and by the potential gradient, on the other hand (the higher σ_e , the lower ∇U , and vice-versa).

$$q_e = \sigma_e \|\nabla U\|^2 \quad (3.37)$$

Whatever is the value of the electrical conductivity, the graphite surrounding the sample always has the highest source term. Hence, the powder is heated mostly by conduction from graphite in the axial direction.

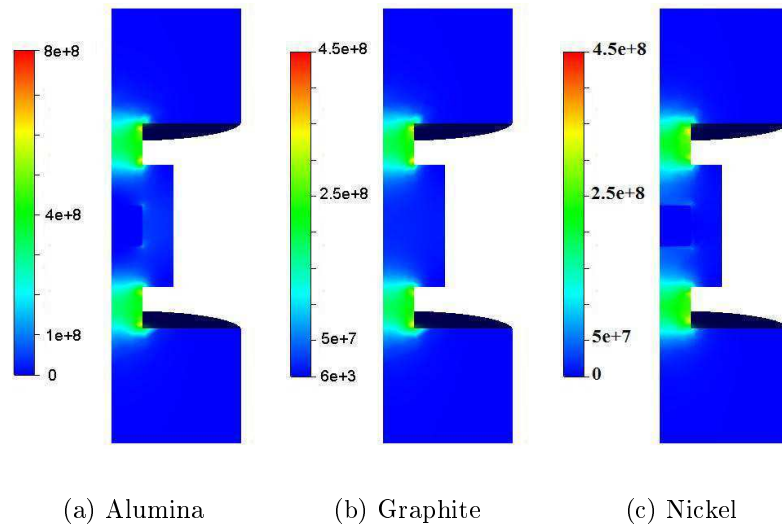
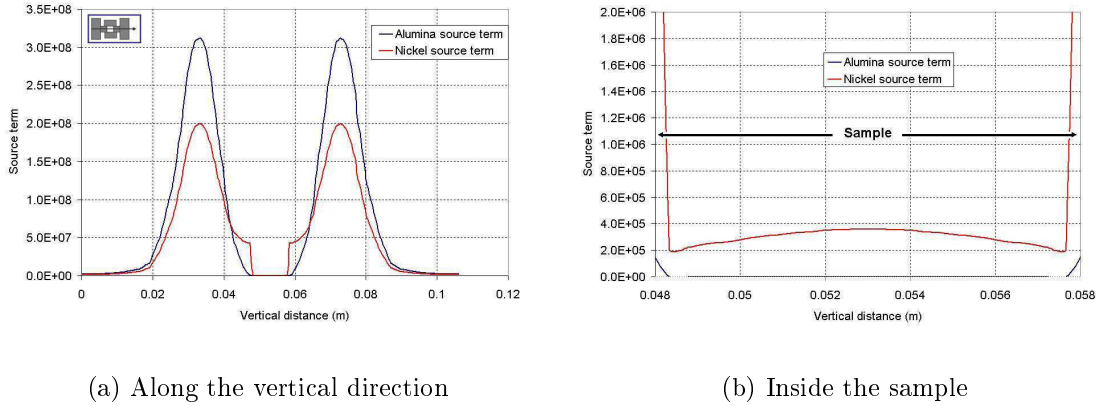


Figure 3.14: Distribution of the source term of the heat equation inside the simplified SPS apparatus

As shown in Figure 3.14, the results are comparable for alumina and nickel. The main difference occurs in the neighbourhood of the sample inside the graphite die and inside the graphite pistons. For alumina, heating by conduction is more influenced by the mould where the source term is higher, whereas for nickel, heating by conduction is more influenced by the pistons surrounding. Consequently, because of the low values of the source term inside the samples, conduction is the main phenomenon acting on temperature distribution. Concerning graphite sample, the source term in the mould and pistons is



(a) Along the vertical direction

(b) Inside the sample

Figure 3.15: Distribution of the source term of the heat equation along the vertical direction of the apparatus and a zoom inside the sample

about three times the one in the sample and we have a more continuous distribution. In the graphics of Figure 3.15, the variation of the source term of the heat equation is plotted along the vertical direction of the apparatus. Even though it is not equal to zero as for alumina, it is relatively low. This is why Joule effect contributes less in heating the nickel sample comparing to conduction coming from the hot graphite surroundings. As shown in Figure 3.15, there is a ratio of 10^3 between the sample and the piston.

3.6.3 Numerical results: *Temperature distribution*

As expected due to the similarities of the source term, temperature distribution is very similar for each material during the process. In fact, when neglecting heat losses by radiation and thermal dependence of physical properties, alumina and nickel are subjected to similar heating procedure. As seen in Figure 3.16, pistons are heated first during the first 30 s, then by conduction heat the sample. But later, the samples present the highest temperature.

Since an adiabatic flux is imposed at the lateral surface of the apparatus, the temperature keeps on increasing at the level of the mould and no heat losses can occur in this region. In addition, pistons with very high temperature conduct heat to this zone. Consequently, a time is reached (here at about 30s) where the temperature of the sample exceeds the temperature of the pistons since it receives heating from all the graphite in the surroundings in addition of Joule heating.

This is more clear in Figure 3.17 where temperature profiles are presented for a nickel specimen and especially when comparing 3.17(b) and 3.17(c). At 70 s, the temperature of the mould is higher than the temperature of pistons.

Figures 3.18-3.19-3.20, present temperature profiles which are compared with those of Couque *et al.* [3] in order to validate our CimLib[®] electrical thermal model. Temperature

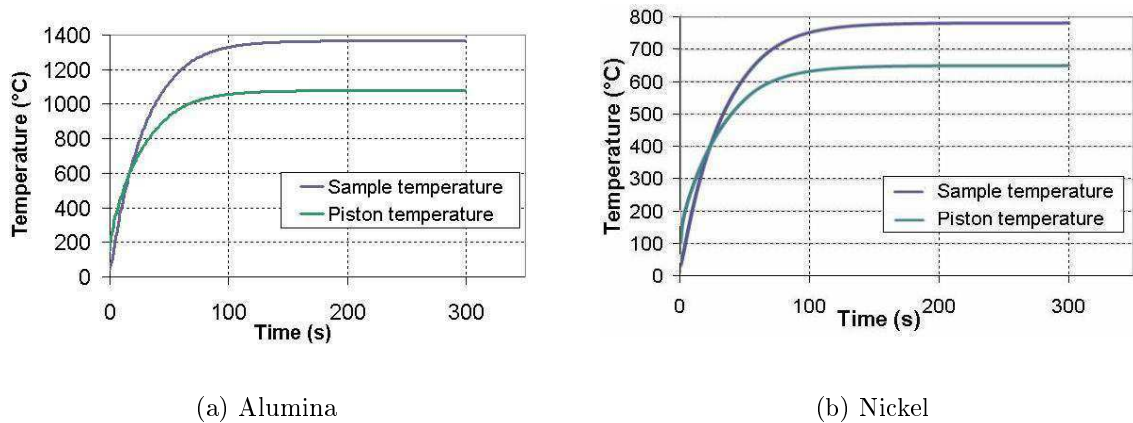


Figure 3.16: Temperature evolution with time, at the center of the specimen ($r = 0$ mm, $H = 5$ mm) and at the center of the piston ($r = 0$ mm, $H = 10$ mm)

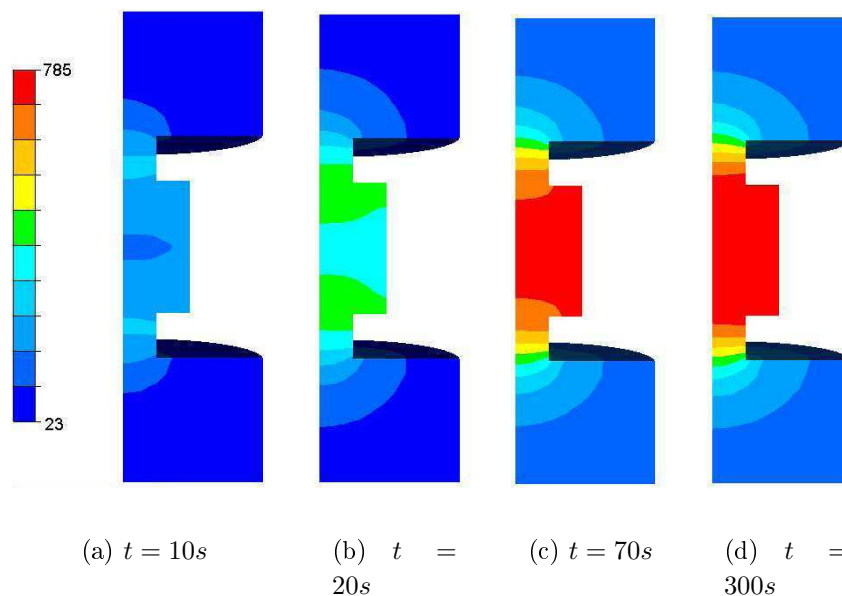


Figure 3.17: Time evolution of temperature distribution ($^{\circ}$ C) for nickel sample

is plotted along the vertical direction on the symmetry axis for different time steps. A difference of 20° C is observed after 10 s and it decreases progressively until results match.

Conclusion In this section, a simplified electric thermal model is simulated using three materials and where the dependence of the parameters on temperature is neglected. We observed that heating by conduction is dominant in the simulations. Results are compared with literature. A difference in the thermal results is observed in the first time steps, however, the maximum reached temperature is the same for CimLib and Abaqus

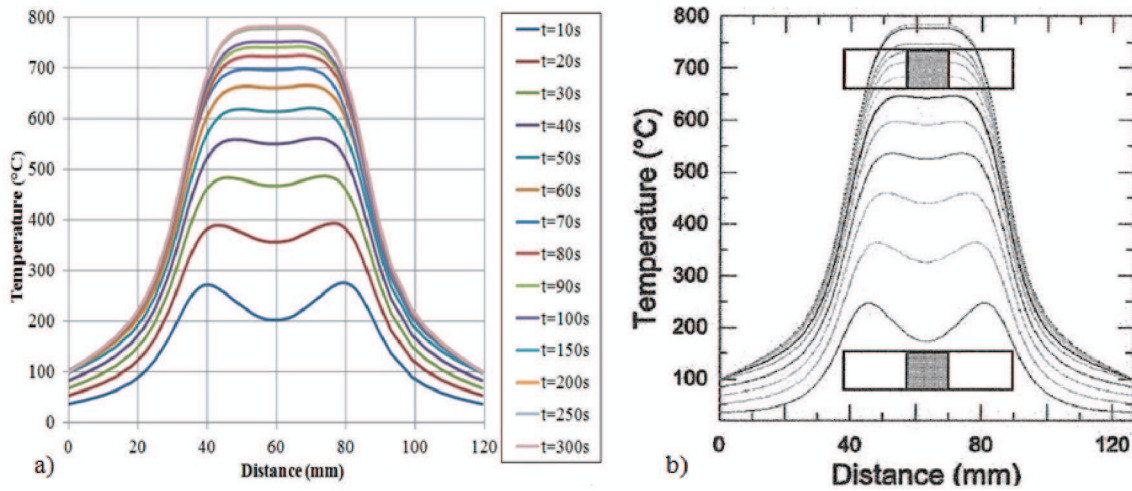


Figure 3.18: Comparison of CimLib® thermal results and Abaqus results [3]: Temperature plotted along the vertical direction of the apparatus for Nickel specimen

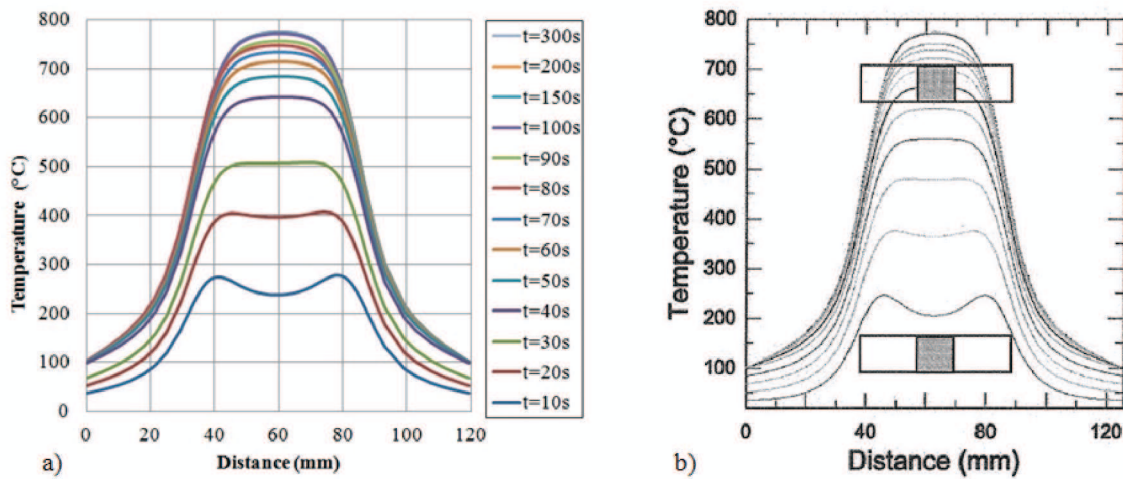


Figure 3.19: Comparison of CimLib® thermal results and Abaqus results [3]: Temperature plotted along the vertical direction of the apparatus for Graphite specimen

simulations.

3.6.4 Influence of thermal dependence of physical properties

When the apparatus is heated, materials are subjected to a variation in their physical properties. This is very specific to each material. For instance, electrical conductivity decreases with temperature for nickel but on the contrary it increases for alumina as seen in Figure 3.21 and Figure 3.27. In this section, the aim is to show the variation of the

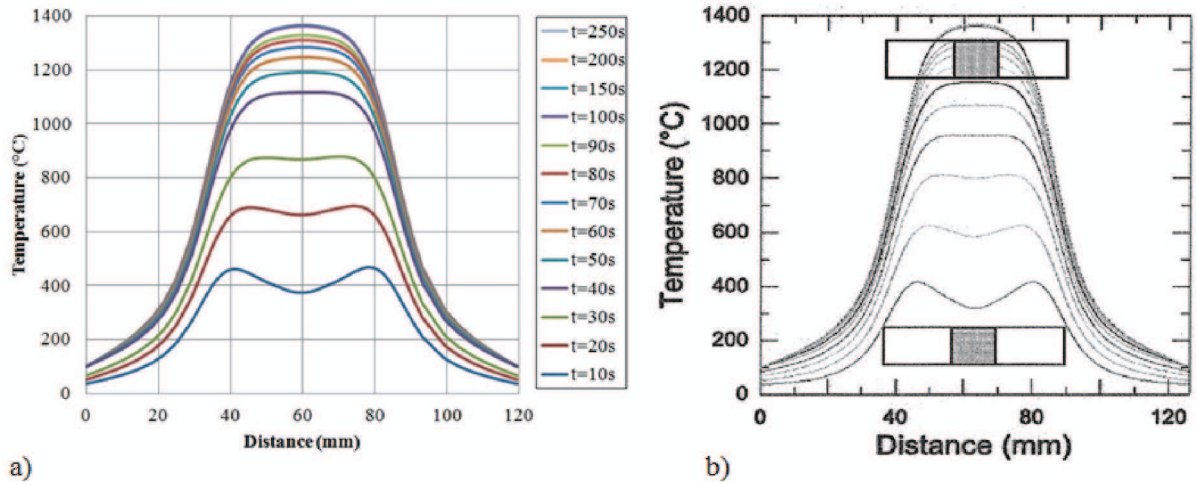


Figure 3.20: Comparison of CimLib[®] thermal results and Abaqus results [3]: Temperature plotted along the vertical direction of the apparatus for alumina specimen

temperature field when physical properties depend on temperature. For this reason, same geometry and same boundary conditions are chosen as in Figure 3.9 used in the previous section. Nickel sample is considered. Electric conductivity, thermal conductivity and specific heat capacity vary while heating, their values have been taken from [12] and are given in Figure 3.21.

In order to compare with previous results, a constant voltage is applied $U_{imp} = 2.43$ V. Temperature distribution with time evolution is presented in Figure 3.22. After 300 s of heating, temperature with thermal dependent properties exceeds significantly the one with constant properties. More precisely, temperature reaches $T = 1350^{\circ}\text{C}$ whereas the maximum observed in nickel for constant properties is 785°C as seen in Figure 3.23. The reason is that electric conductivity of nickel decreases with temperature thus potential gradient increases inside the sample and therefore the power dissipated by Joule effect is more significant.

Such results clearly show the requirement for accurate material characterization in view of predictive modelling of SPS processes. In the following section a study is achieved for an intermetallic and alumina where the comparison of temperature distribution is treated in more details.

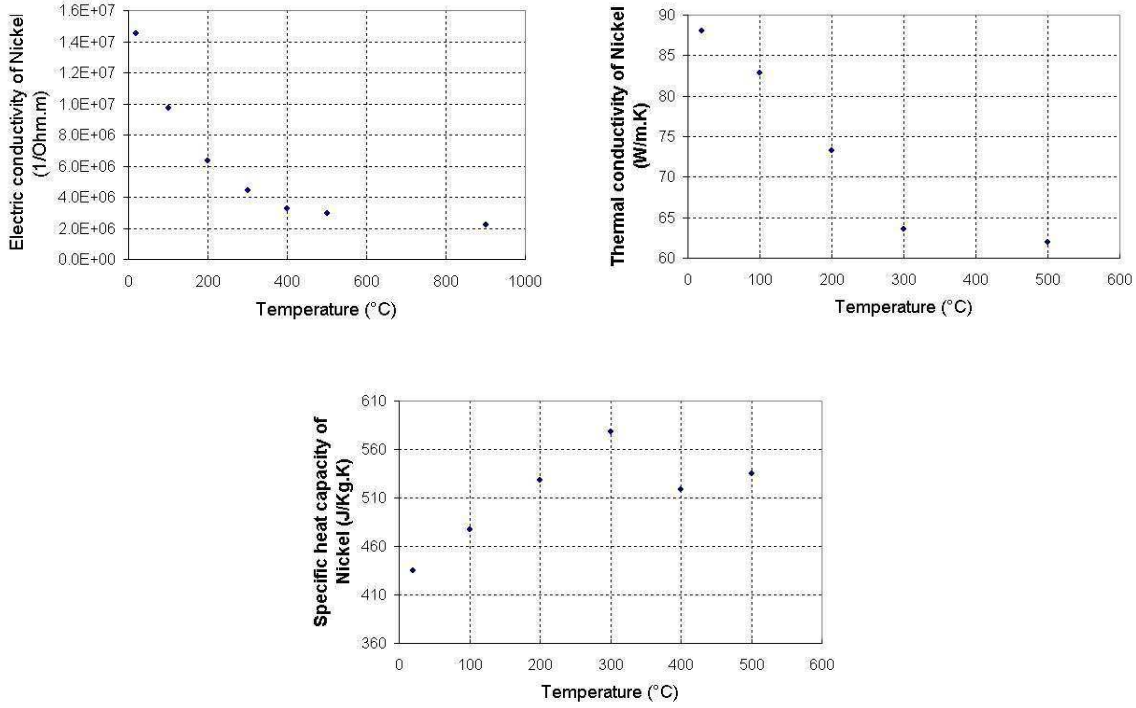


Figure 3.21: Variation of physical properties of nickel with temperature [12]

3.7 Simulation of electrical thermal coupling: Comparison between two codes and experiments

In this section, the work accomplished at CEMEF using CimLib is confronted to the work accomplished in CEMES using COMSOL as well as their experimental work.

COMSOL Multiphysics[®] is a commercial simulation software. It is used for modeling process, defining geometries, meshing, specifying physics problems, solving and finally visualizing results. Furthermore, the comparison involves the electrical thermal coupling during the SPS process. For the simulations, we considered the intermetallic alloy at the center of the IRIS project. It is a titanium-aluminium alloy: $Ti_{49}Al_{47}Nb_2Cr_2$. The simulations are also carried out for alumina. Here, thermal boundary conditions respect the experimental observations. As mentioned, only heat losses by radiation are considered at the lateral surfaces since the process takes place in a vacuum chamber so heat losses by convection and conduction at this region are neglected. The emissivity of graphite is assumed to be equal to 0.8 in this study [9]-[13] and the temperature of the chamber wall T_{wall} is assumed to be equal to 23°C.

▷ On the lateral surface of the apparatus, the radiative heat flux is imposed:

$$\Phi_{rad} = \sigma_B \varepsilon_r (T^4 - T_{wall}^4)$$

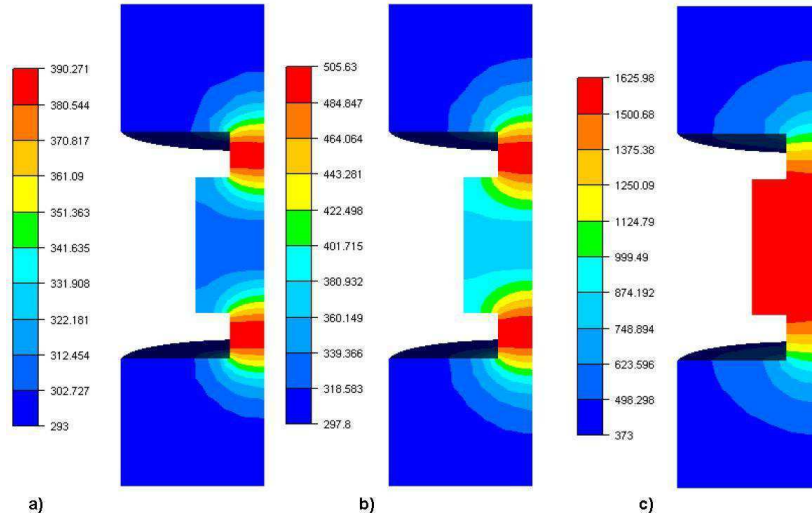


Figure 3.22: Temperature profile (in K) along the apparatus considering a nickel specimen with thermal dependent physical properties: a) $t = 1$ s, b) $t = 5$ s, c) $t = 300$ s,

- ▷ Two Inconel spacers are modelled at both ends of the graphite spacers pile-up. Their height is 55 mm , radius 30 mm . They are water cooled. Thus heat losses by convection are imposed along their surfaces:

$$\Phi_{cond} = h_{conv}(T - T_{water})$$

The heat transfer coefficient h_{cond} is equal to $880\text{ W}\cdot\text{m}^{-2}\cdot\text{K}^{-4}$. We assume that the water temperature is kept constant $T_{water} = 23^\circ\text{C}$. On the other hand, for the electrical problem even though our model allows controlling the temperature by a PID loop, here in order to compare with the work of our colleagues in the project, a constant voltage is applied. The 3D geometry presented in Figure 3.24 is considered in the simulation of the electric-thermal coupled problems. It corresponds to the SPS apparatus installed in the "Plate-forme Nationale de Frittage Flash/CNRS" in Toulouse (PNF2/CNRS-MHT, Paul Sabatier University, Toulouse, France). The SPS machine is a Dr. Sinter 2080 apparatus (Sumitomo Coal Mining Co., Japan). The total number of elements is equal to 614 000. The mesh size in the powder is equal to 1.2 mm and in the tools, it is equal to 6.4 mm . The porosity in the powder is neglected in this study, and the powder is considered as a dense medium. The height of the specimen is 6 mm and its radius is 18 mm . The die, pistons and spacers are made of graphite and their dimensions are specified in Figure 3.25.

Furthermore, all contact surfaces between the parts of the SPS apparatus are considered ideal: as a consequence no contact resistance is taken into account. Besides, all properties are temperature dependent their values are given in Table 3.7.

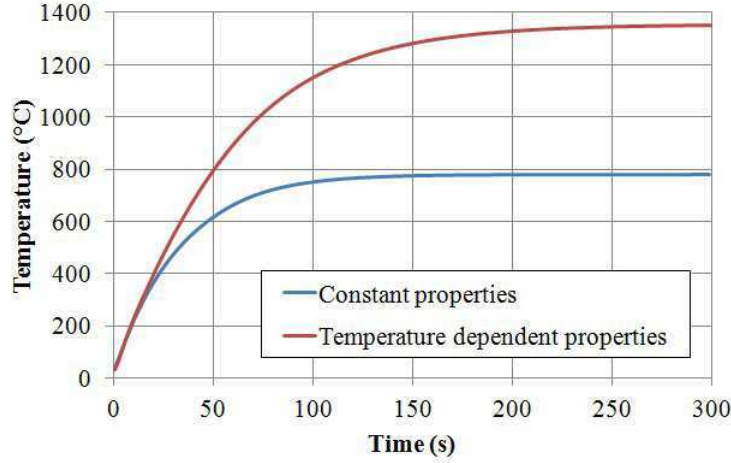


Figure 3.23: Comparison of temperature evolution with time when considering constant physical properties or temperature dependent physical properties

3.7.1 Numerical results: *Electrical problem*

A constant voltage $U_{imp} = 4.2$ V is applied in both cases. In Figure 3.26, the distribution of the norm of the current density is presented. Results are comparable to those of the previous section. Nickel and *TiAl* have the same current distribution due to the comparable ratio between their electric conductivity and graphite electric conductivity:

$$\frac{\sigma_{e_{Graphite}}}{\sigma_{e_{Nickel}}} = \frac{6.3 \times 10^4}{1.4 \times 10^7} = 4.5 \times 10^{-3}$$

$$\frac{\sigma_{e_{Graphite}}}{\sigma_{e_{TiAl}}} = \frac{6.3 \times 10^4}{1.7 \times 10^6} = 4.5 \times 10^{-2}$$

However, in this section, the influence of thermal dependence of the physical properties is remarkable in the case of alumina. The electrical conductivity of alumina increases with temperature. As seen in Figure 3.27, even though the electric conductivity of *TiAl* decreases, it remains much higher than graphite conductivity. For this reason, no change is observed in the distribution of electric current in case of the *TiAl* specimen. On the contrary, alumina behaves as a non conductor at low temperatures. The electric current avoids the sample and concentrates in graphite. Afterwards, when the temperature increases due to heat conduction, electrical conductivity of alumina attains a value of the same order of graphite. And so it acts like a conductor and we can see the current going through the sample and consequently the density is distributed differently in the whole apparatus. It becomes more homogeneous in the central region in the surrounding of the specimen (Figure 3.26 b) and c)).

Figure 3.28- a) presents the variation of current density in the radial direction from the center of the specimen towards the mould edge. Effectively, for *TiAl* the current variation keeps the same shape however the values differ since the physical properties vary and the

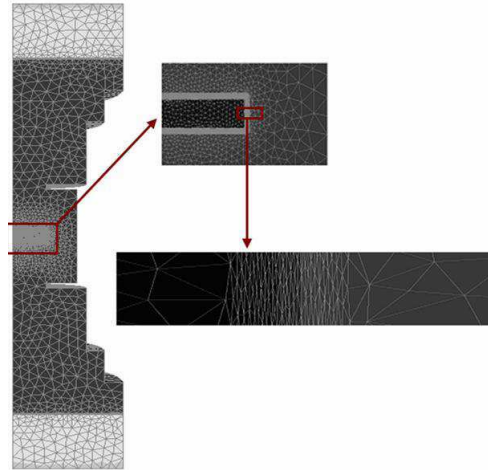


Figure 3.24: 3D Geometry used in the simulations with the mesh generated and a zoom in the region of the sample showing the refined elements around the sample/matrix interface)

electric problem is no longer stationary contrary to the previous simplified model where properties were kept constant (paragraph 3.6.1).

Besides, for alumina, in the radial direction a maximum is reached in graphite at $t = 1$ s while current is absent in the sample. At $t = 300$ s, the current is relatively homogeneous in the central region (Figure. 3.28-b).

3.7.2 Numerical results: *Thermal problem*

The model considered takes into account heat losses by radiation and heat losses by convection between water and Inconel.

Same time steps are chosen to compare temperature fields issued from both numerical codes. First, temperature variation along the vertical direction is compared for different time steps in Figure 3.29. It shows the good agreement between the thermal results issued from CimLib and COMSOL. In addition what is interesting in these curves is the temperature distribution. The pistons have always the highest temperature. In the previous model, where radiation was not taken into consideration, the central region of the apparatus was not cooled and stored heat so that its temperature became higher than the pistons temperature. This is no more the case here, as seen in Figure 3.29. Since, during the process temperature affects directly sintering and microstructure, heat losses must be modelled.

Thus, when considering radiation and water cooling, as seen in Figure 3.29, comparisons are very satisfying. More studies are carried out in particular in the region of the specimen-die interface. The evolution of temperature distribution in the radial direction is investigated for *TiAl* and alumina.

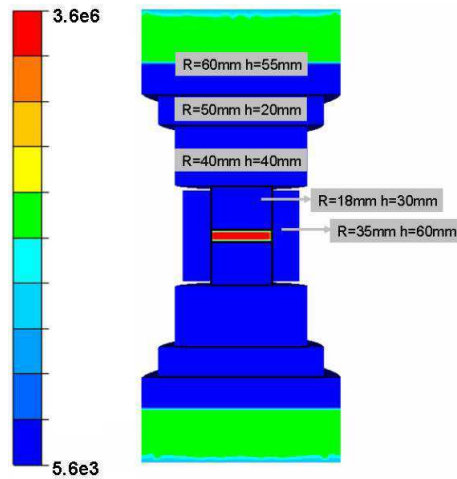


Figure 3.25: Electrical conductivity of the global simulated assembly. The different components (including the TiAl disc sample at the center) can be distinguished through the display of the distribution of their electrical conductivity ($\Omega^{-1} \cdot \text{m}^{-1}$)

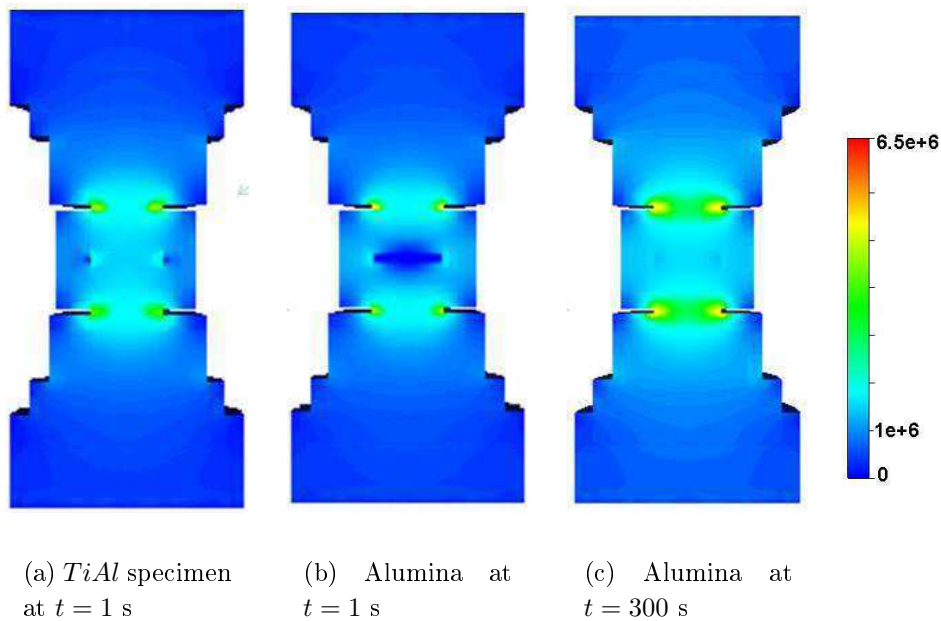


Figure 3.26: Distribution of the density of the electric current ($\text{A} \cdot \text{m}^{-2}$)

A closer look at the temperature along the radial axis inside the sample shows that the temperature is the highest in the center and decreases gradually towards the interface with the die. As mentioned previously, since the ratio of electrical conductivities doesn't vary significantly and due to radiation, temperature at the edge of the graphite mould stays lower than in the center of the sample.

Material	Specific heat ($J/kg/K$)	Thermal conductivity ($W/m/K$)
Inconel	$344 + 2.50 \times 10^{-1}T$	$10.09 + 1.57 \times 10^{-2}T$
Alumina	850	$39\,500 T^{-1.26}$
Graphite	$34.27 + 2.72T - 9.6 \times 10^{-4}T^2$	$82.85 + 0.06T + 2.58 \times 10^{-5}T^2$
<i>TiAl</i>	$583 + 0.094T$	$9.47 + 1.1910^{-2}T$

Material	Electrical resistivity ($\Omega \cdot m$)	Density (kg/m^3)
Inconel	$9.82 \times 10^{-7} + 1.6 \times 10^{-10}T$	8430
Alumina	$8.7 \times 10^{19}T^{-4.82}$	3899
Graphite	$2.14 \times 10^{-5} - 1.34 \times 10^{-8}T + 4.42 \times 10^{-12}T^2$	$1904 - 0.01414T$
<i>TiAl</i>	$4.06 \times 10^{-7} + 6.45 \times 10^{-10}T$	3900

Table 3.3: Thermal dependent physical properties of *TiAl*, Inconel, graphite and alumina [9]. Temperature should be expressed in Kelvin in these formulas

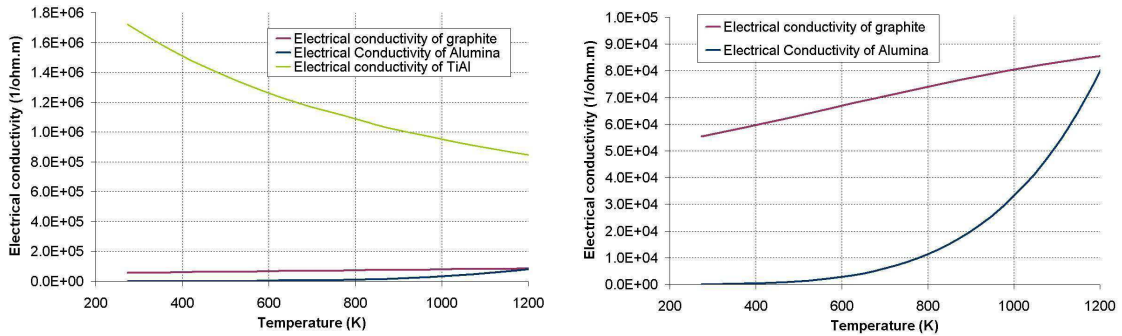
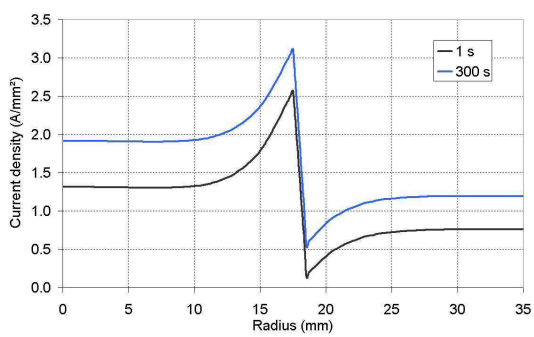
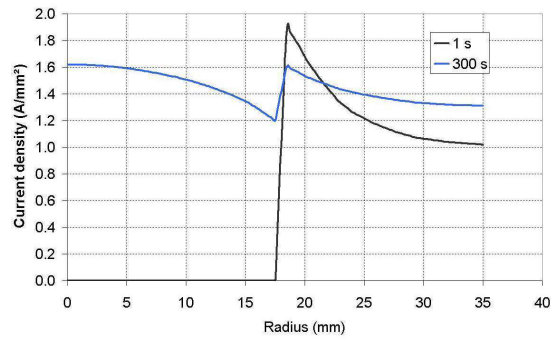


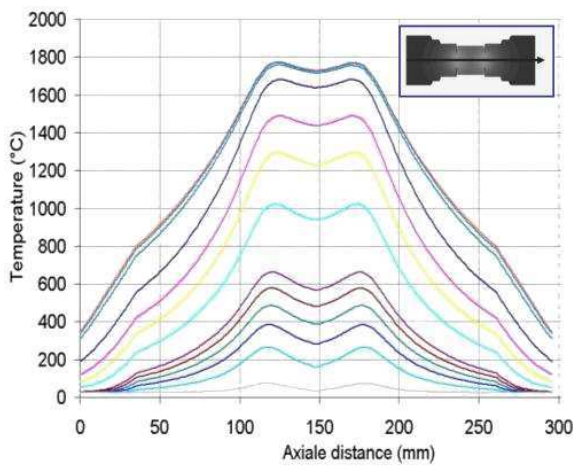
Figure 3.27: Evolution of the electrical conductivity ($\frac{1}{\Omega \cdot m}$) of graphite, *TiAl* and alumina with temperature

The temperature distribution of the alumina specimen is more complex. The conductivity of alumina increases dramatically with temperature (Figure 3.27). Then it becomes close to the graphite electric conductivity. As a consequence, the distribution of the current varies with time. The temperature is not homogeneous during the SPS process and its profile varies with time as presented in Figure 3.32. In the beginning, when the electrical conductivity is still relatively low, the temperature is the highest at the lateral surface of the specimen and it decreases towards the center. Afterwards, because the electrical conductivity of graphite doesn't increase significantly with temperature, the two conductivities become equal and finally the electrical conductivity of alumina exceeds the

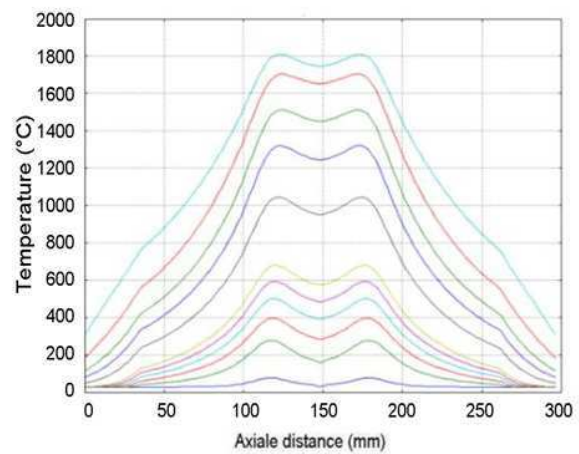
(a) *TiAl*

(b) Alumina

Figure 3.28: Variation of the current density along the radial direction from the center of specimen up to the edge of the die (A/mm^2)



(a) CimLib - CEMEF



(b) Comsol - CEMES

Figure 3.29: Comparison of the variation of temperature along the vertical axis for the *TiAl* sample every 10 s

3.7. Simulation of electrical thermal coupling: Comparison between two codes and experiments 71

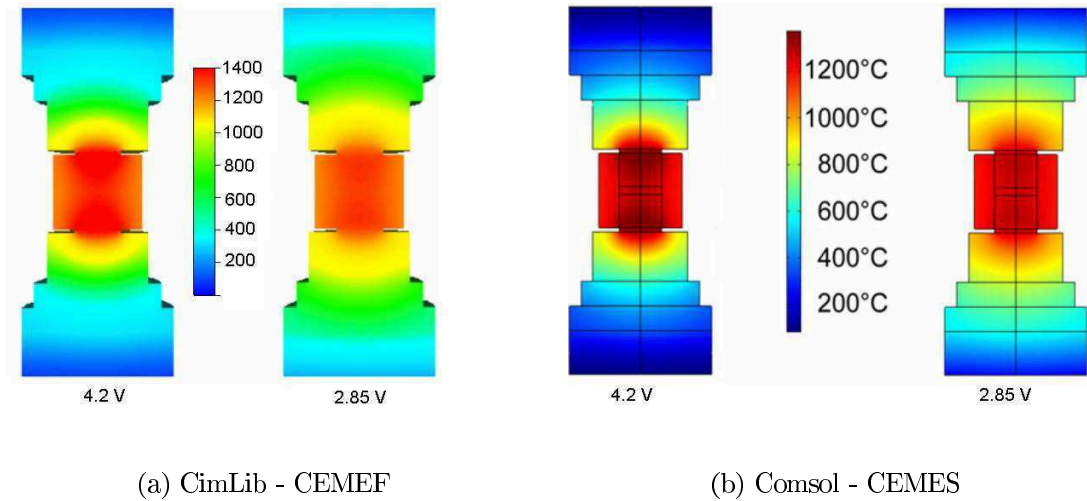


Figure 3.30: Comparison of the distribution of temperature along the vertical axis for the *TiAl* sample

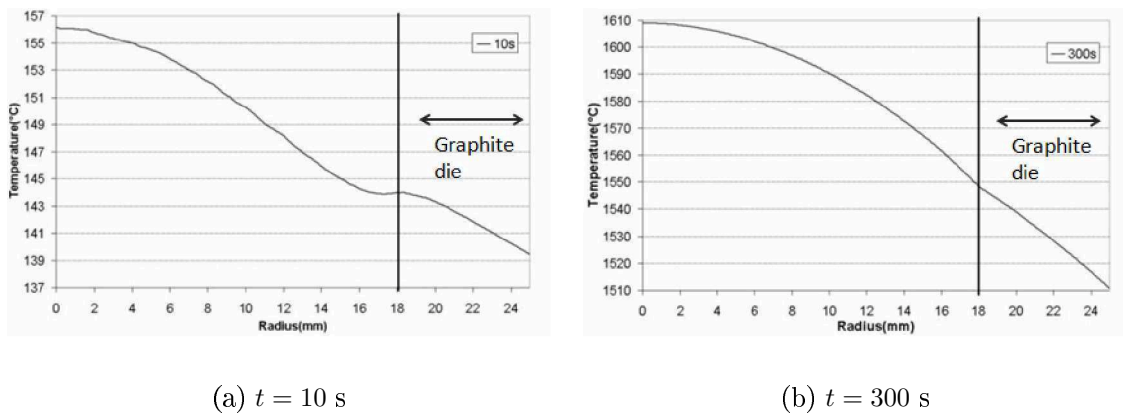


Figure 3.31: Variation of temperature in the radial direction in *TiAl* specimen and graphite die after 10 s and 300 s

one of graphite, which modifies completely the distribution of the current density and so the temperature distribution inside the specimen.

The temperature heterogeneities in the sample affect directly the mechanical problem. For that reason, modeling of thermal electrical coupled problems during the SPS process is very important in predicting microstructure and densification heterogeneities.

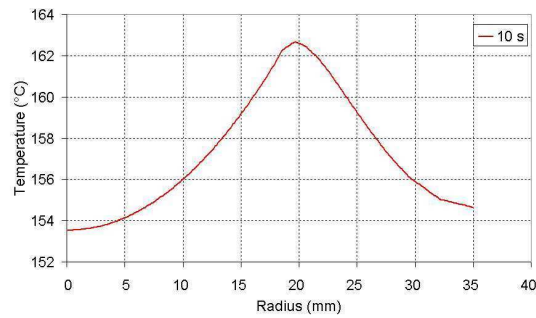
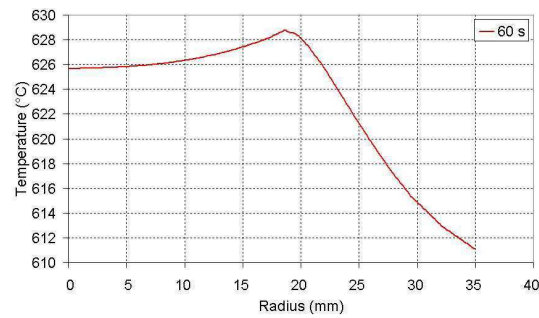
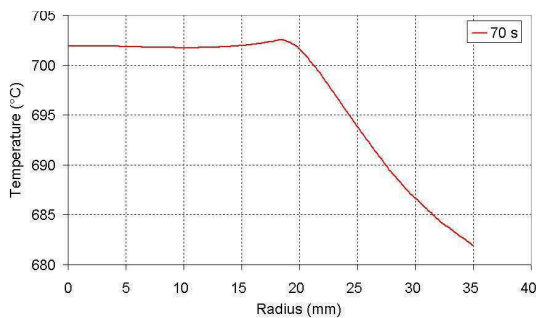
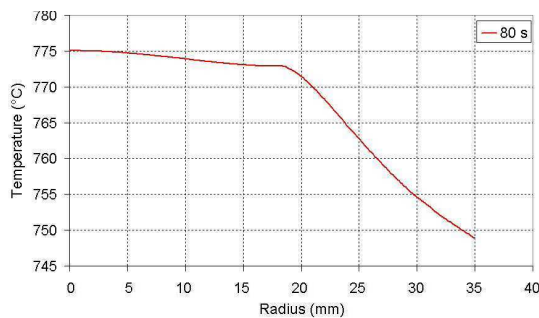
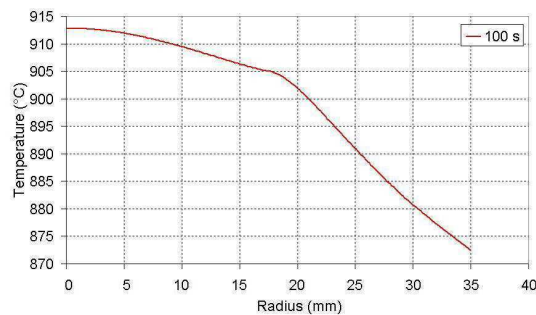
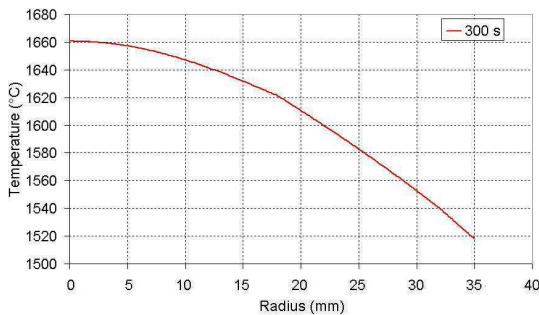
(a) $t = 10$ s(b) $t = 60$ s(c) $t = 70$ s(d) $t = 80$ s(e) $t = 100$ s(f) $t = 300$ s

Figure 3.32: Variation of temperature in the radial direction of the alumina specimen after 10 s and 300 s

3.8 Conclusion

A coupled thermo-electrical 3D finite element analysis was presented to simulate the evolution of current and temperature during the SPS process. A monolithic approach is chosen to model the electric and thermal problems. One single mesh represents the computational domain and level set functions are used to represent interfaces between the different materials. Coupling is first validated by comparing with analytic calculations for a simple 2D test.

A simplified 3D geometry is modeled and results are compared with Abaqus results from literature [3] for three samples: alumina, graphite and nickel. Comparisons are satisfying for both electrical and thermal problem.

Another geometry is modeled, which corresponds to a Sumitomo SPS apparatus. Two samples (alumina and TiAl) are considered with the same geometry. The results, which are calculated by the means of CimLib using a monolithic approach, are compared and validated thanks to numerical results issued from Comsol software. Besides, these latter results were validated as well by matching experimental measurements using the microstructure phase change. In this study, the distribution of temperature in the sample was shown to be mainly affected by heat transfer from graphite surrounding the sample. This heat transfer is influenced by the electrical conductivity of the compact. The results of this chapter show that the coupled electrical-thermal finite element simulation may be of great help in understanding the temperature distribution during the SPS process. They should allow engineers to better determine the nature of the involved tooling materials, as well as their shapes, to reduce temperature heterogeneities and, consequently, better control microstructure formation.

In the following chapter, the modeling of the mechanical problem is presented aiming to enrich the finite element model and the coupling hence to simulate powder densification.

Bibliography

- [1] U. Anselmi-Tamburini, S. Gennari, J.E. Garaya, and Z.A. Munir. Fundamental investigations on the spark plasma sintering/synthesis process ii. modeling of current and temperature distributions. *Materials Science and Engineering A*, 394:139–148, 2005.
- [2] T. Coupez. Stable-stabilized finite element for 3d forming calculation. Technical report, CEMEF, 1996.
- [3] H. Couque, C. Wolff, L. Minier, S. Legallet, F. Bernard, and G. Nicolas. Temperature distribution during the transitory and stationary phases for the electric field material processing sps of conducting and non-conducting materials. In *Proceedings of the advanced Processing for Novel functional Materials, Dresden, Germany, 2008*.
- [4] H. Digonnet, L. Silva, and T. Coupez. Cimlib: A fully parallel application for numerical simulations based on components assembly. In *Proceedings of the 9th International Conference on Numerical Methods in Industrial Forming Processes, Porto, Portugal, 2007*.
- [5] C. Gruau and T. Coupez. 3d tetrahedral, unstructured and anisotropic mesh generation with adaptation to natural and multidomain metric. *Computer Methods In Applied Mechanics And Engineering*, 194:4951–4976, 2005.
- [6] E. Hachem. *Stabilized Finite Element Method for Heat Transfer and Turbulent Flows inside Industrial Furnaces*. PhD thesis, Ecole Nationale Supérieure des Mines de Paris, 2009.
- [7] Matsugi K., Kuramoto H., Hatayama T., and Yanagisawa O. Temperature distribution at steady state under constant current discharge in spark sintering process of ti and al₂o₃ powders. *Journal of materials processing technology*, 134:225–232, 2003.
- [8] Yoneya M. and Ikeshoji T. A numerical calculation method advantageous for complex boundary problems - an application to the pulse discharge sintering process. *Materials transactions*, 42:2165–2171, 2001.

-
- [9] G. Molenat, L. Durand, J. Galy, and A. Couret. Temperature control in spark plasma sintering: An fem approach. *Journal of Metallurgy*, 2010:doi-10-1155/2010/145431, 2010.
- [10] S. Munoz and U. Anselmi-Tamburini. Temperature and stress fields evolution during spark plasma sintering processes. *Journal of materials science*, 45:6528–6539, 2010.
- [11] J. Rathel, M. Herrmann, and W. Beckert. Temperature distribution for electrically conductive and non-conductive materials during field assisted sintering (fast). *Journal of the european ceramic society*, 29:1419–1425, 2009.
- [12] Colin J. Smithells. *Metals reference book*. 5th Edition, 1976.
- [13] K. Vanmeensel, A. Laptev, J. Hennicke, J. Vleugels, and O. van der Biest. Modelling of the temperature distribution during field assisted sintering. *Acta Materialia*, 53:4379–4388, 2005.
- [14] X. Wang, S.R. Casolco, G. Xu, and J.E. Garay. Finite element modeling of electric current-activated sintering: The effect of coupled electrical potential, temperature and stress. *Acta Materialia*, 55:3611–3622, 2007.
- [15] J. Zhang, A. Zavaliangos, M. Kraemer, and J. Groza. Numerical simulation of thermal-electrical phenomena in field activation sintering. In *3rd Symposium on Modeling the Performance of Engineering Structural Materials, Columbus Ohio*, 2002.

Chapter 4

Numerical modeling of powder compaction

Contents

4.1	Introduction	79
4.2	State of the art: Modeling of powder sintering	79
4.3	Modeling of the mechanical problem	82
4.3.1	Modeling of the compressible thermal viscoplastic behaviour based on Abouaf law	82
4.3.2	Momentum equation	85
4.3.3	Mass conservation	89
4.4	Numerical simulation of powder compaction	90
4.4.1	Simulation of a powder free uniaxial compression	91
4.4.2	Simulation of a powder die compaction	95
4.4.3	Conclusion	99
4.5	Numerical simulation of coupled electric thermal mechanical problems during SPS	100
4.5.1	Introduction	100
4.5.2	Equations and algorithm of the simulation	100
4.5.3	Mesh adaptation with tools motion	104
4.5.4	Symmetry due to geometry	105
4.5.5	Dependence of conductivities with powder relative density	107
4.6	Conclusion	113

Résumé

Dans ce chapitre, on présente le modèle numérique choisi pour simuler le comportement de la poudre durant le procédé de frittage flash. Durant, la poudre atteint des températures très élevées en quelques minutes, pour cette raison, on considère un comportement viscoplastique compressible. Une loi de puissance de Norton-Hoff est choisie pour la modélisation du comportement viscoplastique, modifiée selon la loi d'Abouaf, pour tenir compte de la compressibilité et pour modéliser la densification. Le problème mécanique est présenté ainsi que sa discrétisation par éléments finis. Le modèle est validé avec deux tests numériques: une compression uniaxiale simple et une compression dans une matrice fermée. Tout d'abord, les deux tests sont résolus en utilisant une approche lagrangienne. Les résultats sont validés par comparaison avec des solutions analytiques et des résultats issus du logiciel R2Sol. Les résultats sont en très bon accord. Un test de compression de poudre en matrice fermée est ensuite modélisé en utilisant une approche eulérienne, et en considérant le moule et le piston supérieur ce qui nous oblige à introduire dans le modèle les fonctions level set et le maillage anisotrope. Les résultats issus de l'approche eulérienne sont comparés aux solutions analytiques et aux résultats issus de l'approche lagrangienne. Une fois l'implémentation de la loi de comportement validée, on présente la simulation du couplage électrique thermique mécanique du procédé. Dans ce chapitre, les conditions aux limites du modèle mécanique sont encore limités à l'application d'une vitesse constante imposée dans les outils cependant dans le procédé la pression est régulée avec un PID. Les propriétés physiques du problème couplé dépendent de la température et de la densité relative. La dépendance de la conductivité thermique à la densité relative est modélisée selon les travaux de Argento. Ensuite, la conductivité électrique est exprimée utilisant la loi de Wiedmann-Franz. Deux simulations sont effectuées dans ce chapitre pour tester l'influence de la dépendance à la densité relative. On constate la différence des températures n'est pas significative. Les simulations présentées dans ce chapitre sont effectuées considérant un contact glissant entre la poudre et le moule. Cependant, le frottement poudre/outil pourrait influencer la distribution de la température et de la densité.

4.1 Introduction

During spark plasma sintering process, while current flows through the apparatus, powder is subjected to pressure applied from the pistons. In order to predict the densification evolution and to help choosing process conditions (such as pressure, temperature, time), especially in case of complex shapes, a mechanical problem needs to be modeled to compute stresses generated in the powder and the variation of the density. Most papers dealing with SPS modeling are limited to electrical and thermal modeling. Some can be found where the mechanical problem is modeled but considering a dense medium where the densification is not computed [25]-[34]-[35]. In 2011, Song *et al.* [32] proposed a complete model where a compressible elasto-viscoplastic law is used to follow powder deformation. They studied the effect of external load on displacement field and on porosity distribution.

To model powder densification, two approaches can be followed, either a macroscopic or microscopic approach. In the macroscopic approach, the powder is considered as a continuous medium characterized by its porosity (or relative density) and the equations of continuum mechanics can be used. In the literature, many models can be found for hot compaction. A viscoplastic law is often used allowing modeling the global deformation of porous parts respecting the realistic conditions of the process (stress and temperature). On the other hand, in the microscopic approach, the particle deformation is studied which makes it more difficult. In fact, many assumptions need to be considered such as the shape of particles, their size and their distribution. Usually the particles are considered identical and spherical which is different from the reality. In addition, more parameters need to be identified in these models and they are limited to what happens between particles, for instance, mechanisms such as dislocation and deformation inside the structure.

In this chapter, first a brief review on modeling powder sintering is presented. In the following section, we detail the numerical model that is used in this thesis to simulate powder sintering during SPS. Free uniaxial compression tests and powder die compaction tests are then carried out to validate the numerical model. Finally, a coupled electric thermal mechanical simulation is achieved. The mechanical results are discussed as well as the problematic of the geometrical symmetry during the SPS process.

4.2 State of the art: Modeling of powder sintering

In the framework of SPS process, the most complete work about modeling the mechanical behaviour of the powder is the one of Olevsky and Froyen [28] where they modeled different phenomena involved in SPS. They considered that the strain rate tensor is the sum of the strain rate tensor modeling grain boundary mechanisms $\dot{\epsilon}^{gb}$ and the strain rate tensor corresponding to the deformation of powder particles due to the mechanism of power-law creep $\dot{\epsilon}^{cr}$.

Olevsky, in his paper about "Theory of sintering" [27], developed the expression of the sintering stress tensor based on Ashby deformation map:

$$\sigma_{ij} = \frac{\sigma(\dot{\varepsilon})}{\dot{\varepsilon}} \left(\varphi \dot{\varepsilon}_{ij}^{cr} + \left(\psi - \frac{1}{3} \varphi \right) Tr(\dot{\varepsilon}^{cr}) \delta_{ij} \right) + P_L \delta_{ij} \quad (4.1)$$

Where $\sigma(\dot{\varepsilon})$ denotes the effective stress and $\dot{\varepsilon}$ the equivalent effective strain rate, P_L is the effective sintering stress depending on porosity θ , ψ and φ functions of porosity representing respectively the bulk and shear modulus. The strain rate tensor corresponding to power law creep can be expressed using the above equation.

On the other hand, Olevsky and Froyen [28] decompose the grain boundary diffusion strain rate $\dot{\varepsilon}_{gb}$ into three contributions, $\dot{\varepsilon}_{gb} = \dot{\varepsilon}^{em} + \dot{\varepsilon}^{st} + \dot{\varepsilon}^{dl}$ corresponding to the three driving forces for a deformation by grain boundary diffusion:

- A deformation by electromigration due to the application of the current.

$$\dot{\varepsilon}^{em} = -\frac{\delta_{gb} D_{gb}}{kT} \frac{Z^* e_q}{(G + r_p)^2} \frac{1}{\|\nabla U\|} \nabla U \otimes \nabla U \quad (4.2)$$

- A deformation by surface tension observed at the contact surfaces of particles.

$$\dot{\varepsilon}^{st} = -\frac{3\delta_{gb} D_{gb}}{kT} \frac{\Omega}{(G + r_p)^2} \frac{\alpha}{G} \left[\frac{1}{r_p} - \frac{1}{2G} \right] I \quad (4.3)$$

- A deformation due to the load applied during the process.

$$\dot{\varepsilon}^{dl} = \frac{\delta_{gb} D_{gb}}{kT} \frac{\Omega}{(G + r_p) G^2} \sigma \quad (4.4)$$

where:

Z^* : the valence of a migrating ion

e_q : the electron charge

δ_{gb} : the grain boundary thickness

D_{gb} : the grain boundary diffusion coefficient

Ω : the atomic volume

G : the grain size

r_p : the pore radius

α : surface tension

U : electric potential.

These expressions require the identification of a large number of parameters, for example, the grain boundary thickness δ_{gb} , the grain boundary diffusion D_{gb} and atomic volume Ω . Moreover, in the work of Olevsky and Froyen [28], a study for aluminium is achieved concerning the amplitude of each contribution depending on grain size and porosity. As seen in Figure 4.1 the contribution of surface tension is only observed for low grain size

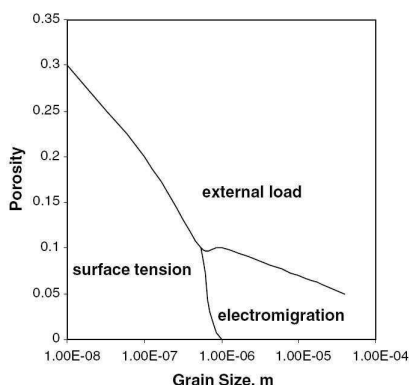


Figure 4.1: "Densification map for aluminum powder" [28]

and low porosity, whereas for higher grain size and low porosity electromigration is more significant. Besides, for high porosity, the external load contributes the most in the deformation.

Many authors used similar expressions in order to model the physical mechanisms during sintering. Particles are very often considered identical. Artz [4], Matthews [23], McMeeking [21] and Rao [30] considered packed spheres in order to model densification. Bouvard *et al.* [8] used as well the generalized equation of Hertz modified by Matthews [23] in order to model densification during hot isostatic pressing. This model is based on the contact of two elastic spheres and completed by an empirical equation. In fact, models used to simulate SPS process derive from classical sintering laws previously used for hot pressing.

Zavaliangos [24] and Song *et al.* [32] simulated spark plasma sintering process by coupling the three physical problems (electric-thermal-mechanical). Two different models were used for the mechanical numerical simulation. Zavaliangos [24] adopted the model of Bouvard [18] where a macroscopic Newtonian law is chosen for sintering stress, the strain rate tensor is written:

$$\dot{\epsilon} = \dot{\epsilon}^{gb} + \dot{\epsilon}^{cr} + \dot{\epsilon}^{el} \quad (4.5)$$

where $\dot{\epsilon}^{cr}$ is the viscous strain rate tensor, $\dot{\epsilon}^{el}$ the elastic strain rate tensor and $\dot{\epsilon}^s$ is the additional sintering strain rate expressed as follows:

$$\dot{\epsilon}^{gb} = \Omega(T)(\rho_{r\infty} - \rho_r)^n \quad (4.6)$$

$\rho_{r\infty}$ being the maximum relative density that can be reached during an isothermal test. Song *et al.* [32] also used an elasto-viscoplastic macroscopic model. The elastic modulus and Poisson's ratio were calculated as functions of relative density and introduced in Hooke's law for the elastic strain rate tensor. Moreover the viscoplastic behavior is modeled following a modified Abouaf macroscopic model [1] using the work of Kim *et al.* [19]. Abouaf model will be developed in the following section.

Abouaf macroscopic model was used a lot in the literature for hot pressing. Some authors used it and applied it as it is [7] and [11]. However, others like Geindreau *et al.* [13]-[14] and Stutz *et al.* [33] applied the Abouaf model after some modifications in order to correspond to their processes for example by adding the hardening. This model showed satisfying results in several works. Kim and Jeon [20] compared Abouaf and McMeeking models with experiments for sinter forging by plotting the axial and radial strain rate (Figure 4.2), they showed that Abouaf model matches with experiments whereas McMeeking model underestimates the deformation rate.

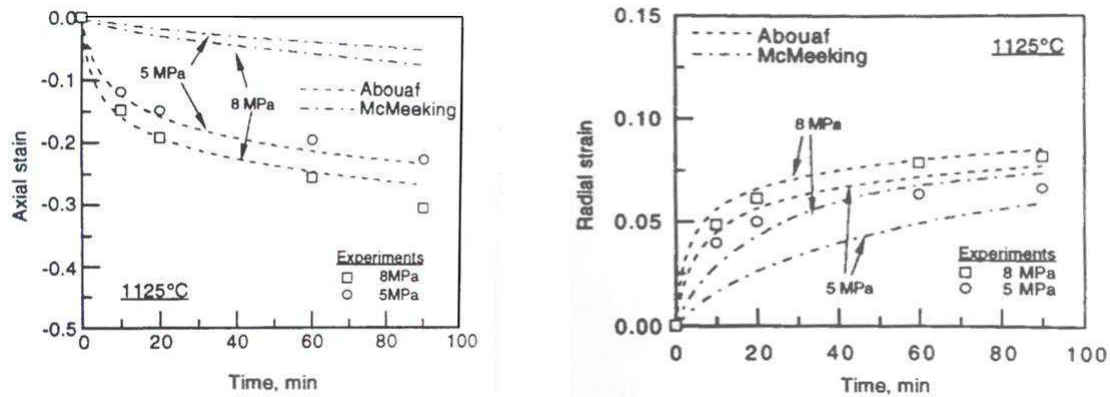


Figure 4.2: Comparison of the experimental and finite element results by the models of Abouaf and McMeeking issued from the work of Kim and Jeon [20]

Consequently, Abouaf model is very common in literature. This model is easy to set up and does not require the identification of a high number of parameters. This is why, in our work, we chose Abouaf model in order to simulate the mechanical problem during SPS process. Since many mechanisms occur during spark plasma sintering in the mesoscopic scale and since scientists still have lots of doubts concerning the contribution of each one of them, our work is limited to the macroscopic scale.

4.3 Modeling of the mechanical problem

In this section, we present the behaviour of the powder, the equations of the mechanical problem and their numerical resolution by finite element method as it is implemented in CimLib[®].

4.3.1 Modeling of the compressible thermal viscoplastic behaviour based on Abouaf law

The aim is to develop a model that can be applied to different geometries and different metallic materials, in a way to predict densification and avoid heterogeneities and defects when manufacturing industrial parts. The approach chosen in our work to model powder densification is issued from the work of Abouaf [1]. The porous material is represented by an equivalent continuum medium and can be described by the equations of continuum mechanics. It is considered as an average continuous medium characterized by its relative density ρ_r which is the ratio of the volume of the material by the apparent volume of the medium:

$$\rho_r = \frac{V_{material}}{V_{apparent}} \quad (4.7)$$

The relative density is consequently the fraction of the equivalent continuum medium occupied by the material particles. The framework is the same as the one proposed by Shima and Oyane [31], complemented by the thermodynamic justifications of Abouaf [1][2]. The equivalent stress is extended as follows:

$$\bar{\sigma}^2 = 3cJ_2 + fI_1^2 \quad (4.8)$$

and the equivalent effective strain rate is then written as follows:

$$\dot{\bar{\varepsilon}}^2 = \frac{2}{3c}\dot{\varepsilon} : \dot{\varepsilon} + \left(\frac{1}{9f} - \frac{2}{9c} \right) Tr(\dot{\varepsilon})^2 \quad (4.9)$$

J_2 is the second invariant of the deviatoric stress tensor and I_1 is the first invariant of the stress tensor:

$$\begin{aligned} J_2 &= \frac{1}{2} s : s \\ I_1 &= Tr(\sigma) \end{aligned} \quad (4.10)$$

Using Einstein summation $s : s = s_{ij}s_{ij}$ and $Tr(\sigma) = \sigma_{ii}$, where s denotes the deviatoric stress tensor:

$$s = \sigma - \frac{1}{3}Tr(\sigma)\mathbb{I} \quad (4.11)$$

c and f are two decreasing functions of the relative density ρ_r . In fact, c is directly related to the shear stress and to shape change and gets its minimum value 1 when $\rho_r = 0$, and f is related to the hydrostatic pressure and to volume change and its minimum value is 0 as seen in Figure 4.3. In fact, when densified ($\rho_r = 0$), the equivalent stress reduces to the usual von Mises stress. ρ_c in Figure 4.3 is defined as the minimum relative density that can be measured when powder particles are only linked by punctual contacts. c and f are the only two parameters related directly to the relative density which model the density change of the powder. Consequently, the stress is only influenced by these two coefficients concerning its dependency on the relative density. We assume that the

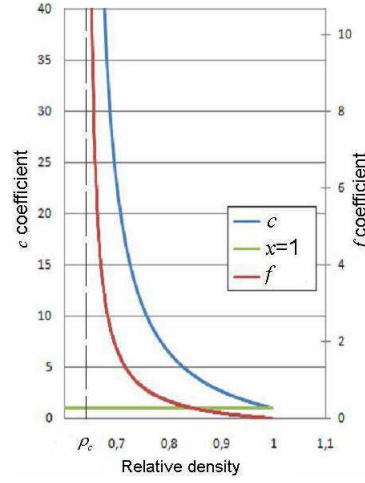


Figure 4.3: Schematic representation of the variation of coefficients c and f versus the relative density

viscoplastic deformation of the medium is dominant and we choose a Norton-Hoff potential $\tilde{\Omega}$ in order to deduce the expression of the strain rate:

$$\tilde{\Omega} = \frac{m}{m+1} K(T) \left(\frac{\bar{\sigma}}{K(T) \sqrt{3}} \right)^{\frac{m+1}{m}} \quad (4.12)$$

where m denotes the strain rate sensitivity coefficient and $K(T)$ the material consistency at the dense state. According to Abouaf [2], the equivalent strain rate $\dot{\tilde{\epsilon}}$ (here $\dot{\tilde{\epsilon}}$ is equivalent to $\dot{\tilde{\epsilon}}^{cr}$) in the porous state should be expressed the same as in the dense state:

$$\dot{\tilde{\epsilon}} = \frac{\partial \tilde{\Omega}}{\partial \bar{\sigma}} \quad (4.13)$$

$$= \left(\frac{\bar{\sigma}}{K(T) \sqrt{3}^{m+1}} \right)^{\frac{1}{m}} \quad (4.14)$$

The strain rate tensor is then written:

$$\dot{\epsilon} = \frac{\partial \tilde{\Omega}}{\partial \sigma} \quad (4.15)$$

$$= \frac{\partial \tilde{\Omega}}{\partial \bar{\sigma}} \frac{\partial \bar{\sigma}}{\partial \sigma} \quad (4.16)$$

Deriving 4.8, we have :

$$\frac{\partial \bar{\sigma}}{\partial \sigma} = \frac{1}{\bar{\sigma}} \left(\frac{3}{2} c s + f I_1 \mathbb{I} \right) \quad (4.17)$$

$$\text{and we get } \dot{\epsilon} = \frac{1}{\bar{\sigma}} \left(\frac{\bar{\sigma}}{K(T) \sqrt{3}^{m+1}} \right)^{\frac{1}{m}} \left(\frac{3}{2} c s + f Tr(\dot{\epsilon}) I_1 \mathbb{I} \right) \quad (4.18)$$

\mathbb{I} denotes the identity tensor. Here, $\dot{\varepsilon}$ is equivalent to $\dot{\varepsilon}^{cr}$ mentioned in paragraph 4.2. Taking the trace of this expression, it is possible to invert it, yielding the expression of the stress tensor as a function of the strain rate tensor:

$$\sigma = 3K(T) \left(\sqrt{3}\dot{\varepsilon} \right)^{m-1} \left(\frac{2}{3c}\dot{\varepsilon} + \left(\frac{1}{9f} - \frac{2}{9c} \right) Tr(\dot{\varepsilon})\mathbb{I} \right) \quad (4.19)$$

Separating the stress tensor into deviatoric and volumetric contributions, we get:

$$s = 3K(T) \left(\sqrt{3}\dot{\varepsilon} \right)^{m-1} \frac{2}{3c}\dot{\varepsilon} \quad (4.20)$$

$$\text{where } \dot{e} = \dot{\varepsilon} - \frac{1}{3}Tr(\dot{\varepsilon})\mathbb{I} \quad (4.21)$$

$$p = -\frac{1}{3}Tr(\sigma) = -K(T) \left(\sqrt{3}\dot{\varepsilon} \right)^{m-1} \frac{1}{3f}Tr(\dot{\varepsilon}) \quad (4.22)$$

In fact, Abouaf model and the power law creep proposed by Olevsky are very comparable:

$$\sigma_x = AW^{m-1} \left(\varphi\dot{\varepsilon}^{crx} + \left(\psi - \frac{1}{3}\varphi \right) (\dot{\varepsilon}^{crx} + \dot{\varepsilon}^{cry})\delta_{ij} \right) + P_L\delta_{ij} \quad (4.23)$$

In fact, c is comparable to φ , both are related to shear and f is comparable to ψ both are related to volume change and both models are related to a power law model. The difference is that Olevsky added the sintering stress P_L [27]. P_L is the Laplace effective stress applied by the gas trapped in the pores on the particles. This stress is dependent on the relative density.

Finally, we see that the relation between the two scalar invariants is the same as in the dense state:

$$\bar{\sigma} = K(T) \left(\sqrt{3} \right)^{m+1} \dot{\varepsilon}^m \quad (4.24)$$

To facilitate the notation we define $\bar{\mu} = K(T) \left(\sqrt{3}\dot{\varepsilon} \right)^{m-1}$.

4.3.2 Momentum equation

The numerical model is based on the fundamental equations of continuum mechanics: mass conservation and momentum equation. First, the problem will be presented in its general framework, then depending on the numerical test, boundary conditions will be discussed.

The mechanical problem is governed by the momentum equation:

$$\nabla \cdot \sigma + \rho \vec{g} = \rho \frac{d\vec{v}}{dt} \quad (4.25)$$

where \vec{v} denotes the velocity, σ the Cauchy stress tensor, ρ the density of the continuum and \vec{g} the gravity. Here, inertia and gravity effects can be neglected and the problem is reduced to:

$$\nabla \cdot \sigma = 0 \quad (4.26)$$

4.3.2.1 Weak formulation and discretization

Same as for the electric and thermal problem, we consider $\Omega \subset \mathbb{R}^3$ the computational domain and $\Gamma = \partial\Omega$ its boundary. The objective in this section is to express the weak form of the mechanical problem in such a way that it could be solved in the framework of a finite element velocity-pressure formulation. The problem to be solved is composed of two equations derived from Equation 5.13 and Equation 4.22, which are reduced to the following system:

$$\begin{cases} \nabla \cdot \sigma = 0 \\ p + K(T) \left(\sqrt{3\dot{\varepsilon}} \right)^{m-1} \frac{1}{3f} \nabla \cdot \vec{v} = 0 \end{cases} \quad (4.27)$$

Let us define the test functions $\vec{v}^* \in \mathcal{V}$ and $p^* \in \mathcal{P}$ where \mathcal{V} and \mathcal{P} are the functional appropriate spaces defined as:

$$\begin{aligned} \mathcal{V} &= \{ \vec{v} \in (H^1(\Omega))^3 / \vec{v} = \vec{v}_{imp} \text{ on } \Gamma \} \\ \mathcal{V}_0 &= \{ \vec{v} \in (H^1(\Omega))^3 / \vec{v} = 0 \text{ on } \Gamma \} \\ \mathcal{P} &= L^2(\Omega) \end{aligned}$$

After integrating by parts the equilibrium and the compressibility equations on the domain Ω , the equations of the system 4.27 can be written:

$$\begin{cases} \int_{\Omega} (\nabla \cdot \sigma(\vec{v})) \cdot \vec{v}^* d\Omega = - \int_{\Omega} \sigma(\vec{v}) : \dot{\varepsilon}(\vec{v}^*) d\Omega + \int_{\Gamma} \sigma \vec{n} \cdot \vec{v} d\Gamma = 0 \\ \int_{\Omega} \left(\frac{3f}{\bar{\mu}(\dot{\varepsilon})} p + \nabla \cdot \vec{v} \right) p^* = 0 \quad \forall (\vec{v}^*, p^*) \in (\mathcal{V}, \mathcal{P}) \end{cases} \quad (4.28)$$

Besides the stress σ is expressed as follows:

$$\int_{\Omega} \sigma(\vec{v}) : \dot{\varepsilon}(\vec{v}^*) d\Omega = \int_{\Omega} (s(\vec{v}) - p\mathbb{I}) : \dot{\varepsilon}(\vec{v}^*) d\Omega \quad (4.29)$$

$$= \int_{\Omega} s(\vec{v}) : \dot{\varepsilon}(\vec{v}^*) d\Omega - \int_{\Omega} p\mathbb{I} : \dot{\varepsilon}(\vec{v}^*) d\Omega \quad (4.30)$$

$$\text{But } s(\vec{v}) = \frac{2\bar{\mu}}{c} \left(\dot{\varepsilon} - \frac{1}{3} \underbrace{\text{Tr}(\dot{\varepsilon})}_{\nabla \cdot \vec{v}} \mathbb{I} \right) \quad (4.31)$$

$$\begin{aligned} \int_{\Omega} \sigma(\vec{v}) : \dot{\varepsilon}(\vec{v}^*) d\Omega &= \int_{\Omega} \frac{2\bar{\mu}}{c} \dot{\varepsilon}(\vec{v}) : \dot{\varepsilon}(\vec{v}^*) d\Omega - \int_{\Omega} \frac{2}{3c} \bar{\mu} \nabla \cdot \vec{v} \nabla \cdot \vec{v}^* d\Omega \\ &\quad - \int_{\Omega} p \nabla \cdot \vec{v}^* d\Omega \end{aligned} \quad (4.32)$$

Besides, since $\dot{\varepsilon}(\vec{v}^*)$ is a symmetric tensor, we can write:

$$\int_{\Omega} \frac{2\bar{\mu}}{c} \dot{\varepsilon}(\vec{v}) : \dot{\varepsilon}(\vec{v}^*) d\Omega = \int_{\Omega} \frac{2\bar{\mu}}{c} \dot{\varepsilon}(\vec{v}) : \nabla \vec{v}^* d\Omega \quad (4.33)$$

The weak formulation of the mechanical problem is then:

Find $(\vec{v}, p) \in (\mathcal{V}, \mathcal{P})$ such that for each instant t :

$$\begin{cases} \int_{\Omega} \frac{2\bar{\mu}}{c} \dot{\varepsilon}(\vec{v}) : \nabla \vec{v}^* d\Omega - \int_{\Omega} \frac{2}{3c} \bar{\mu} \nabla \cdot \vec{v} \nabla \cdot \vec{v}^* d\Omega - \int_{\Omega} p \nabla \cdot \vec{v}^* d\Omega - \int_{\Gamma} \sigma \vec{n} \cdot \vec{v} d\Gamma = 0 \\ \int_{\Omega} \left(\frac{3f}{\bar{\mu}} p + \nabla \cdot \vec{v} \right) p^* = 0 \quad \forall (\vec{v}^*, p^*) \in (\mathcal{V}, \mathcal{P}) \end{cases} \quad (4.34)$$

The first one is the weak form of the momentum equation. The second equation consists of the weak form of the volumetric part of the constitutive equation.

Space discretization Now that the weak formulation is presented, we are capable of computing the solution (\vec{v}, p) of the mechanical problem by introducing a spatial approximation using the finite element method. The discretization by finite element method consists in determining an approximate solution in subspaces of finite dimension. The computational domain Ω is approximated by the finite space Ω_h . Ω is substituted by a set of N_e elements, τ_h . The same triangulation is used to solve the velocity and the pressure. The finite subspaces should verify the Brezzi-Babuska condition [5]-[9]. This condition is necessary for the consistency of the equations. More details about this condition can be found in [15]. Here a $(P1^+, P1)$ element (also called "mini-element") is chosen (Figure 4.4). Velocity field and pressure are interpolated linearly between two

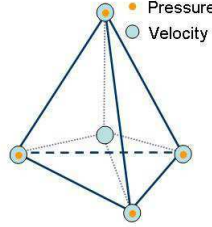


Figure 4.4: Tetrahedral $P1^+, P1$ mini-element

nodes of the mesh. Besides, the velocity field is enriched by adding a virtual node in the centre of the element, called bubble. This type of element allows a good compromise between computational times and results accuracy [12]. Another benefit is that it allows meshing very complex shapes. This element was used at CEMEF by Coupez in the framework of viscoplastic flow [10] and then by Basset [6] who implemented the Stokes solver in CimLib[®] for a multiphase flow. As defined in Chapter 3, $P1$ is the linear interpolation on the elements. We define the finite spaces:

$$\begin{aligned} \mathcal{P}_h &= \{p_h \in \mathcal{C}^0(\Omega_h) / \forall e \in \tau_h, p_h|_{\Omega_e} \in \mathbb{P}1(\Omega_e)\} = H_h^1(\Omega_h) \\ \mathcal{L}_h &= \{\vec{v}_h \in (\mathcal{C}^0(\Omega_h))^3 / \forall e \in \tau_h, \vec{v}_h|_{\Omega_e} \in (\mathbb{P}1(\Omega_e))^3 \text{ and } \vec{v}_h = v_{imp} \text{ sur } \partial\Omega_v\} \\ \mathcal{B}_h &= \{\vec{b}_h \in (\mathcal{C}^0(\Omega_h))^3 / \forall e \in \tau_h, \vec{b}_h|_{\Omega_e^e} \in (\mathbb{P}1(\Omega_e^e))^3 \text{ and } \vec{b}_h = 0 \text{ sur } \partial\Omega_i^e\} \\ \mathcal{V}_h &= \mathcal{L}_h \oplus \mathcal{B}_h \end{aligned} \quad (4.35)$$

We denote respectively $\{N_i^l\}_{i=1}^{N_s}$ and $\{N_i^b\}_{i=1}^{N_e}$ the basis of the finite spaces \mathcal{L}_h and \mathcal{B}_h (N_e is the number of elements). The velocity field and the pressure are consequently written:

$$\begin{aligned} \forall \vec{v}_h \in \mathcal{V}_h, \quad \vec{v}_h &= \sum_{i=1}^{N_s} \vec{v}_{li} N_i^l + \sum_{j=1}^{N_e} \vec{b}_j N_j^b \\ \forall p_h \in \mathcal{P}_h, \quad p_h &= \sum_{i=1}^{N_s} p_i N_i^l \end{aligned} \quad (4.36)$$

The bubble function b_h has two fundamental properties:

- b_h vanishes on each element boundary
- The gradient of b_h is orthogonal to each tensor which is constant per element:

$$\int_{\Omega_e} \nabla v_h : \nabla b_h d\Omega = 0$$

These properties allow us to express the mechanical problem (4.34) as follows:

Find $(\vec{v}_h, p_h) \in (\mathcal{V}_h, \mathcal{P}_h)$ such that for each instant t :

$$\left\{ \begin{array}{l} \int_{\Omega_h} \frac{2\bar{\mu}}{c} \dot{\varepsilon}(\vec{v}_l) : \nabla \vec{v}_l^* d\Omega_h - \int_{\Omega_h} \frac{2}{3c} \bar{\mu} \nabla \cdot \vec{v}_l \nabla \cdot \vec{v}_l^* d\Omega_h - \int_{\Omega_h} p_h \nabla \cdot \vec{v}_l^* d\Omega_h \\ - \int_{\Gamma_h} \sigma \vec{n} \cdot \vec{v}_l^* d\Gamma_h = 0 \\ \int_{\Omega_h} \frac{2\bar{\mu}}{c} \dot{\varepsilon}(\vec{b}_h) : \nabla \vec{b}_h^* d\Omega_h - \int_{\Omega_h} \frac{2}{3c} \bar{\mu} \nabla \cdot \vec{b}_h \nabla \cdot \vec{b}_h^* d\Omega_h - \int_{\Omega_h} p_h \nabla \cdot \vec{b}_h^* d\Omega_h = 0 \\ \int_{\Omega_h} \left(\frac{3f}{\bar{\mu}} p_h + \nabla \cdot \vec{v}_h \right) p_h^* = 0 \quad \forall (\vec{v}_h^*, p_h^*) \in (\mathcal{V}_h, \mathcal{P}_h) \end{array} \right. \quad (4.37)$$

Resolution of the system The matrix form of the problem is then written:

$$\begin{pmatrix} A^{vv} & 0 & A^{vp} \\ 0 & A^{bb} & A^{bp} \\ A^{pv} & A^{pb} & A^{pp} \end{pmatrix} \begin{pmatrix} v_h^l \\ b_h \\ p_h \end{pmatrix} = \begin{pmatrix} B^l \\ 0 \\ 0 \end{pmatrix} \quad (4.38)$$

The bubble test function can be expressed using the second line of the matrix 4.38 and then substituted in the third line:

$$\begin{aligned} b_h &= - (A^{bb})^{-1} (A^{bp} p_h) \\ A^{pv} v_h^l + \left(A^{pp} - A^{pb} (A^{bb})^{-1} A^{bp} \right) p_h &= 0 \end{aligned}$$

More details about the bubble condensation can be found in [6]-[16]-[17]. The matrix form of the mechanical problem is reduced to:

$$AX = \begin{pmatrix} A^{vv} & A^{vp} \\ A^{pv} & A^{pp} - A^{pb} (A^{bb})^{-1} A^{bp} \end{pmatrix} \begin{pmatrix} v_h^l \\ p_h \end{pmatrix} = \begin{pmatrix} B^l \\ 0 \end{pmatrix} = B \quad (4.39)$$

We should note that we are facing a non linear problem, in fact the term $2\bar{\mu}\dot{\varepsilon}(\vec{v}_h^l)$ is non linear due to $\bar{\mu} = K(T) (\sqrt{3}\dot{\varepsilon}(\vec{v}))^{m-1}$. This is why, $\bar{\mu}$ is fixed before each $k + 1$ iteration of the linear resolution. It is calculated as a function of the v_k , computed at the previous iteration.

4.3.3 Mass conservation

The aim of the numerical simulation being to predict densification especially in complex shapes, we need to model the evolution of the relative density in the powder. Since the problem is treated in a macroscopic scale, the density will be computed locally at each node of the computational domain Ω . As we said in the previous section, the model is based on the equations of continuum mechanics. The evolution of the relative density is governed by mass conservation:

$$\nabla \cdot (\rho \vec{v}) + \frac{\partial \rho}{\partial t} = 0 \quad (4.40)$$

The density of the powder ρ is written: $\rho = \rho_0 \rho_r$, where ρ_0 denotes the density of the material in its dense state, this is why the equation of mass conservation is reduced to:

$$\nabla \cdot (\rho_r \vec{v}) + \frac{\partial \rho_r}{\partial t} = 0 \quad (4.41)$$

\vec{v} is the velocity computed using the momentum equation presented previously. The equation is composed of three terms:

- A non stationary term: $\frac{\partial \rho_r}{\partial t}$
- A convection term: $\vec{v} \cdot \nabla \rho_r$
- A reaction term: $\rho_r \nabla \cdot \vec{v}$

and it is solved by finite element method in CimLib[®].

4.3.3.1 Weak formulation and discretization

The resolution of mass conservation equation is very similar to the resolution of the heat equation presented in Chapter 3. Identically, on the computational domain Ω , we use the following Sobolev spaces:

$$\begin{aligned} H^1(\Omega) &= \{\omega \in L^2(\Omega), \nabla \omega \in [L^2(\Omega)]^3\} \\ L^2(\Omega) &= \{\omega, \int_{\Omega} \omega^2 d\Omega < \infty\} \\ H_0^1(\Omega) &= \{\omega \in H^1(\Omega), \omega = 0 \text{ on } \Gamma\} \end{aligned}$$

After multiplying by the function test and time integration using an implicit Euler scheme, the weak form of the mass conservation equation is posed as follows:

$$\left\{ \begin{array}{l} \text{Find } \rho_r \in H^1(\Omega) \text{ such that:} \\ \int_{\Omega} \frac{\rho_r^t}{\Delta t} \rho^* d\Omega + \int_{\Omega} \vec{v} \cdot \nabla \rho_r \rho^* d\Omega + \int_{\Omega} (\nabla \cdot \vec{v}) \rho_r \rho^* d\Omega = \int_{\Omega} \frac{\rho_r^{t-1}}{\Delta t} \rho^* d\Omega \quad \forall \rho^* \in H_0^1(\Omega) \end{array} \right. \quad (4.42)$$

v is computed on each node of the domain Ω and is described by a linear interpolation on each element. This implies that its divergence is constant per element. For that reason, before introducing the reaction term in the mass conservation equation, we proceed to a nodal smoothing of $\nabla \cdot \vec{v}$:

If a_{P0} is constant per element we define a_{P1} the linear function as:

$$a_{P1} = \frac{1}{\sum_{\tau_h \in \tau_h(n_i)} |\tau_h|} \sum_{\tau_h \in \tau_h(n_i)} a_{P0} |\tau_h| \quad (4.43)$$

τ_h being the elements intercepting the node n_i , and $|\tau_h|$ their volume.

Discretization The mass conservation is discretized the same way as for the previous equations. This is why we won't go through all the details concerning the finite spaces. The work will lead to the following matrix form:

$$a_{ij} = \int_{\tau_h} \frac{1}{\Delta t} N_i N_j + \int_{\tau_h} \vec{v} \cdot \nabla N_i \nabla N_j + \int_{\tau_h} (\nabla \cdot \vec{v}) N_i N_j \quad (4.44)$$

$$b_j = \int_{\tau_h} \frac{1}{\Delta t} \rho_r^{t-1} N_j \quad (4.45)$$

4.4 Numerical simulation of powder compaction

Now that the equations have been presented, in this section the validation of the model will be discussed. First, we present a simple uniaxial test of powder compaction and we compare the results of CimLib[®] with analytic results when Abouaf coefficients are kept constant and with R2Sol results when they follow the density evolution. Second, a powder die compaction is simulated and similarly results of CimLib[®] are validated with analytic solutions. For these two tests, a Lagrangian approach is used. The mesh coordinates are updated at each time step according to the velocity field computed in the mechanical problem:

$$X_t(x, y, z) = X_{t-1}(x, y, z) + \vec{v} \Delta t \quad (4.46)$$

4.4.1 Simulation of a powder free uniaxial compression

Geometry and boundary conditions

The cylinder presented in Figure 4.5 is considered. The bottom of the cylinder is in contact with a fixed plane and the top is in contact with a tool having a constant vertical velocity of $\vec{v}_{imp} = (0, 0, -0.003) \text{ m.s}^{-1}$. Frictionless sliding conditions are considered between the porous cylinder and the tools. We consider that the initial relative density is equal to 65%.

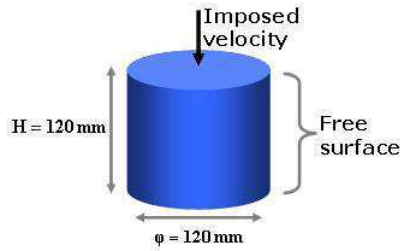


Figure 4.5: Powder uniaxial compaction

4.4.1.1 c and f constant

As a first step, c and f Abouaf coefficients are supposed constant, that way we can compare with an analytic solution. The aim is to compare the stress and velocity.

Analytic solution The velocity is expressed as:

$$\vec{v} = \begin{pmatrix} v_r(r, z) \\ 0 \\ v_z(z) \end{pmatrix} \quad (4.47)$$

Using the expression of the velocity we can write the strain rate tensor at each time t :

$$\dot{\epsilon} = \frac{1}{2} (\nabla \vec{v} + (\nabla \vec{v})^T) \quad (4.48)$$

$$\dot{\epsilon} = \begin{pmatrix} A(t) & 0 & 0 \\ 0 & A(t) & 0 \\ 0 & 0 & -\frac{v_{imp}}{h(t)} \end{pmatrix} \quad (4.49)$$

and the deviatoric stress strain rate tensor:

$$\dot{e} = \dot{\epsilon} - \frac{1}{3} Tr(\dot{\epsilon}) \mathbb{I} = \begin{pmatrix} \frac{1}{3}A(t) + \frac{1}{3}\frac{v_{imp}}{h} & 0 & 0 \\ 0 & \frac{1}{3}A(t) + \frac{1}{3}\frac{v_{imp}}{h} & 0 \\ 0 & 0 & -\frac{2}{3}A(t) - \frac{2}{3}\frac{v_{imp}}{h} \end{pmatrix} \quad (4.50)$$

Then using the constitutive law $\sigma = s - p\mathbb{I} = \frac{2\bar{\mu}}{c}\dot{\epsilon} - p\mathbb{I}$:

$$\sigma = \begin{pmatrix} \frac{2K}{3c}(A(t) + \frac{v_{imp}}{h}) - p & 0 & 0 \\ 0 & \frac{2K}{3c}(A(t) + \frac{v_{imp}}{h}) - p & 0 \\ 0 & 0 & -\frac{4K}{3c}(A(t) + \frac{v_{imp}}{h}) - p \end{pmatrix} \quad (4.51)$$

and the equation of momentum conservation $\nabla \cdot \sigma = 0$, we can deduce that the pressure is constant. Besides, we have $\sigma_{rr} = 0$. Thus, the pressure is expressed as:

$$p = \frac{2K}{3c}(A(t) + \frac{v_{imp}}{h}) \quad (4.52)$$

and the value of the vertical stress σ_{zz} at each time t is:

$$\sigma_{zz}(t) = -\frac{2\bar{\mu}}{c} \left(A(t) + \frac{v_{imp}}{h(t)} \right) \quad (4.53)$$

Using $p = -\frac{1}{3}Tr(\sigma) = -\frac{\bar{\mu}}{3f}Tr(\dot{\epsilon})$, this can lead to the expression of $A(t)$:

$$A(t) = \frac{v_{imp}}{h} \frac{c - 2f}{2(c + f)} \quad (4.54)$$

and finally:

$$\sigma_{zz}(t) = -K \left(\frac{3}{c + f} \right)^{\frac{m+1}{2}} \left(\frac{v_{imp}}{h(t)} \right)^m \quad (4.55)$$

The values that have been used for comparison are:

$$\begin{aligned} c &= 6.463 \\ f &= 0.45 \\ K &= 100 \text{ MPa.s}^m \\ m &= 0.3 \end{aligned}$$

Comparison between CimLib[®] and analytic solution Figure 4.6 shows the linear variation of the isovalues of the vertical component of the velocity with the velocity vectors. The mesh size is homogeneous and equal to 4 mm. The cylinder is subjected to a variation of its radius as well as its height. The time evolution of vertical stress computed with CimLib[®] is compared with the analytic solution in Figure 4.7. The agreement is excellent. The maximum error is 0.0076%. The variation of the radius can be calculated analytically. From Equation 4.49 we have:

$$\dot{\epsilon}_{rr} = A(t) = \frac{v_{imp}}{h} \frac{c - 2f}{2(c + f)} \quad (4.56)$$

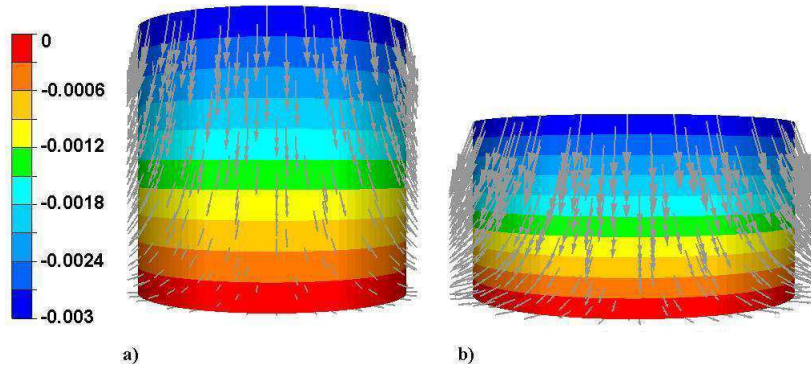


Figure 4.6: Isovalues of the vertical component of velocity and velocity vectors: a) at $t = 0$ s and b) $t = 15$ s

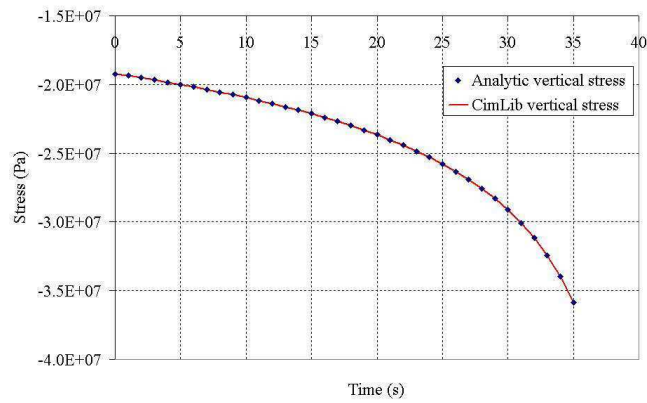


Figure 4.7: Vertical stress (in Pa) plotted over time computed with CimLib[®] and analytically with c and f constant

In addition, in simple uniaxial compaction:

$$\dot{\epsilon}_{rr} = \frac{\partial v_r}{\partial r} \quad (4.57)$$

By integrating these two equations, we get:

$$v_r |_{r=R} = \frac{\partial R}{\partial t} = \frac{v_{imp}}{h} \frac{c - 2f}{2(c + f)} R \quad (4.58)$$

Finally, the integration of this equation leads to:

$$R(t) = R_0 \left(\frac{h_0}{h} \right)^{\frac{c-2f}{2(c+f)}} \quad (4.59)$$

In Figure 4.8, the radius is plotted over time. Results are compared between CimLib and the analytic solution. As seen, the radius follows the same evolution and results are in good agreements. The maximum error is 0.855%.

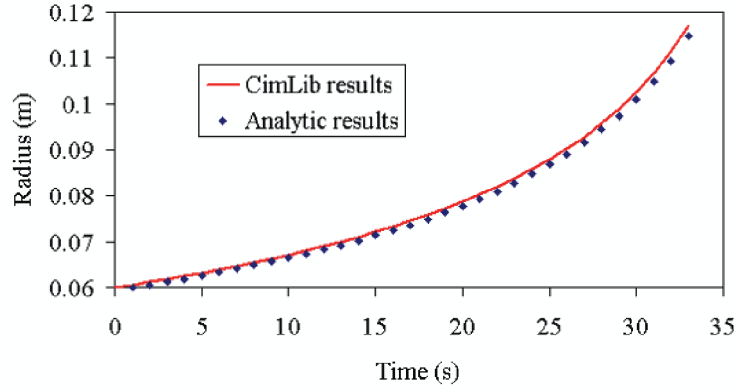


Figure 4.8: Comparison of the radius evolution with time when computed with CimLib and analytically

4.4.1.2 c and f updated with the relative density

The same test is considered with the same boundary conditions and geometry. However, c and f are here updated with the evolution of the relative density ρ_r at each time step. In the literature, several expressions can be found for these coefficients. In our simulation the expressions used for comparison are:

$$f(\rho_r) = k_f \frac{1 - \rho_r}{\rho_r - \rho_c}$$

$$c(\rho_r) = 1 + \alpha_c f$$

where $k_f = 0.4$ and $\alpha_c = 6$

By adding the update of c and f the analytic solution is no longer valid, for this reason we compare CimLib[®] results with R2Sol.

R2Sol is a numerical simulation software developed at CEMEF laboratory, in collaboration with *Ecole des Mines de Nancy*. It is a 2-dimensional finite element code essentially developed for the analysis of solidification processes [22]. The uniaxial free compression is solved in R2Sol in 2D considering the axi-symmetrical conditions of the cylinder.

The vertical component of the stress computed by the means of CimLib[®] and by the means of R2Sol is plotted over time in Figure 4.9.

Results of CimLib[®] numerical model are in excellent agreement with R2Sol results and the maximum error is 0.04 %.

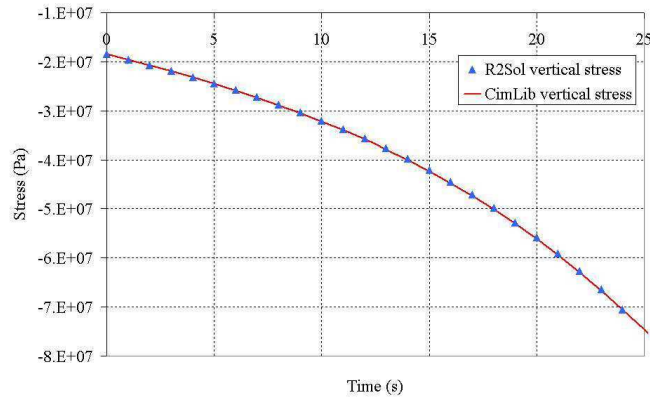


Figure 4.9: Vertical stress (in Pa) plotted over time computed with CimLib[®] and R2Sol when c and f are updated according to density evolution

4.4.2 Simulation of a powder die compaction

Geometry and boundary conditions

A porous cylinder is considered placed in a mould as presented in Figure 4.10. The bottom of the cylinder is in contact with a fixed plane and the top is in contact with a tool having a constant velocity of $v_{imp} = (0, 0, -0.0005) \text{ m.s}^{-1}$. All contacts between the cylinder, the tools and the mould are frictionless: $\sigma \vec{n} - (\sigma \vec{n} \cdot \vec{n}) \vec{n} = 0$. The relative density at $t = 0 \text{ s}$ is equal to 0.65. We only model the cylinder, which means that the mesh does not

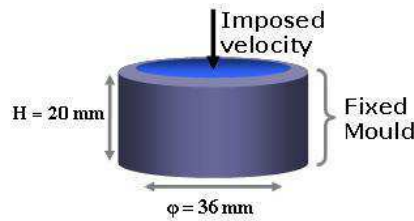


Figure 4.10: Powder die compaction

represent the tools. Besides, as previously, a Lagrangian approach is chosen where nodes coordinates are updated at each time step according to the velocity field.

4.4.2.1 c and f constant

As a first step, c and f Abouaf coefficients are supposed constant, that way we can compare with an analytic solution.

Analytic solution The velocity is expressed as:

$$\vec{v} = \begin{pmatrix} 0 \\ 0 \\ v_z(z) = \frac{-v_{imp}}{h}z \end{pmatrix} \quad (4.60)$$

Using the expression of the velocity we can write the strain rate tensor at each time t :

$$\dot{\epsilon} = \begin{pmatrix} 0 & 0 & 0 \\ 0 & 0 & 0 \\ 0 & 0 & -\frac{v_{imp}}{h(t)} \end{pmatrix} \quad (4.61)$$

Then using the constitutive law: $\sigma = s - p\mathbb{I} = \frac{2\bar{\mu}}{c}\dot{\epsilon} - p\mathbb{I}$ and the equation of momentum conservation $\nabla \cdot \sigma = 0$, in addition to $p = -\frac{\bar{\mu}}{3f}Tr(\dot{\epsilon})$ we can deduce the value of the vertical stress σ_{zz} at each time t :

$$\sigma_{zz}(t) = -\frac{\bar{\mu}}{3} \left(\frac{4}{c} + \frac{1}{f} \right) \frac{\vec{v}_{imp}}{h(t)} \quad (4.62)$$

The values that have been used for comparison are the same as for uniaxial free compression:

$$c = 6.463 \quad f = 0.45 \quad K = 100 \text{ MPa.s}^m \quad m = 0.3$$

Comparison between CimLib[®] and analytic solution Figure 4.11 shows the linear variation of the isovalues of the vertical component of the velocity with the velocity vectors, being along the vertical direction. The vertical stress computed with CimLib[®]

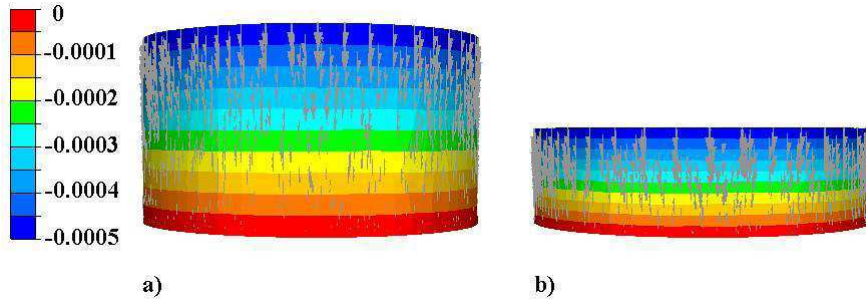


Figure 4.11: Vertical velocity field isovalues and velocity vectors for powder die compression when c and f are constant: a) at $t = 0$ s and b) at $t = 20$ s

is compared with the analytic solution in Figure 4.12. The variation of stress is plotted over time. Agreement is excellent and the error is 0.0076 %.

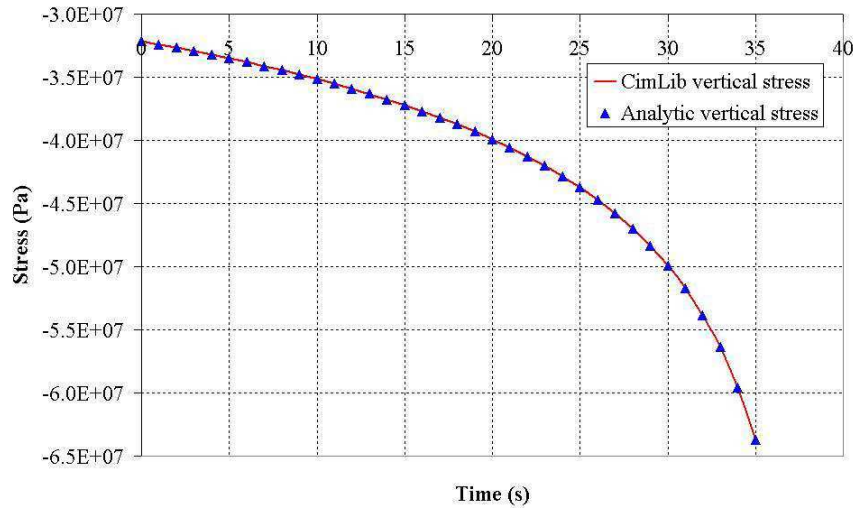


Figure 4.12: Vertical stress plotted over time: comparison between CimLib[®] results and analytic solution for powder die compression when c and f are constant

4.4.2.2 c and f updated with the relative density

The same test for powder die compression (4.10) is considered with the same geometry. However, c and f are here updated with the evolution of the relative density ρ_r at each time step and $v_{imp} = (0, 0, -0.0002)m.s^{-1}$. The expressions used for c and f are the same as for free uniaxial compression.

In fact, in this test, the radius does not vary and by imposing the velocity the variation of the height is easily calculated. Consequently the relative density can be computed by:

$$\begin{aligned} \rho_r(t = 0) &= \frac{V_{material}}{V_{apparent}(t = 0)} = 0.65 \\ \rho_r(t = i\Delta t) &= \frac{V_{material}}{V_{apparent}(t = i\Delta t)} \\ &= \rho_r(t = 0) \frac{h(t = 0)}{h(t = 0) - iv_{imp}\Delta t} \end{aligned} \quad (4.63)$$

For this test, we didn't have recourse to R2Sol for comparison, since the analytic equations are easily expressed because the radius is constant. In order to facilitate the calculations of the analytic solution, the equations are introduced in an algorithm in Matlab to extract automatically the results. Knowing the imposed velocity and since the radius is constant, the relative density is deduced directly from the volume variation. On the other hand, the strain rate tensor is calculated introducing equation 4.61. Then, the effective strain rate tensor is calculated according to equation 4.9. Finally, the vertical stress component is deduced. The graphic of Figure 4.13 shows the good agreement between results of CimLib[®] numerical model and analytic solution. The relative density increases and it reaches 0.98 at $t = 35 s$. The stress increases significantly as well, in fact when powder

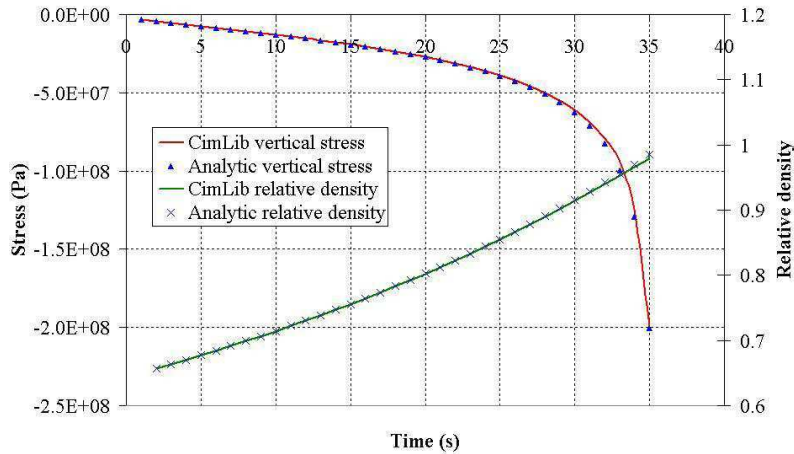


Figure 4.13: Vertical stress and relative density plotted over time: comparison between CimLib[®] results and analytic solution calculated with Matlab for powder die compression when c and f are updated with density

is densified the response to the applied velocity is amplified since the material is more resistant.

In the previous section, two numerical tests were used to validate the implementation of the powder compressible viscoplastic behavior law. Comparisons were in very good agreements. However, these tests are modeled using the Lagrangian approach. As mentioned in the introduction and previous chapters of the thesis, the aim is to model SPS using an Eulerian approach. Now, it is interesting to test the same models adding the mould and pistons. Thus, the level set functions are used to model each material as well as the anisotropic remeshing around the interfaces. Hence, the following tests respect the conditions that will be used later on in the thesis.

4.4.2.3 From Lagrangian to Eulerian approach

The same powder die compaction test is considered. The problem is solved using a Eulerian approach. More precisely, one mesh is generated. Tools are modeled in addition to the powder. The level set function is used to define the different materials. The geometry considered is presented in Figure 4.14. Only a quarter of the geometry is modeled to save computation time thanks to symmetry. A constant velocity is imposed in the piston $v_{imp} = (0, 0, -0.0005) \text{ m.s}^{-1}$, the mould is considered fixed and a zero velocity is imposed to the nodes covering the mould. A frictionless sliding contact is considered between the mould and the powder, using an intermediate body between the powder and the mould with a low viscosity (more details about the sliding conditions can be found in Chapter 5).

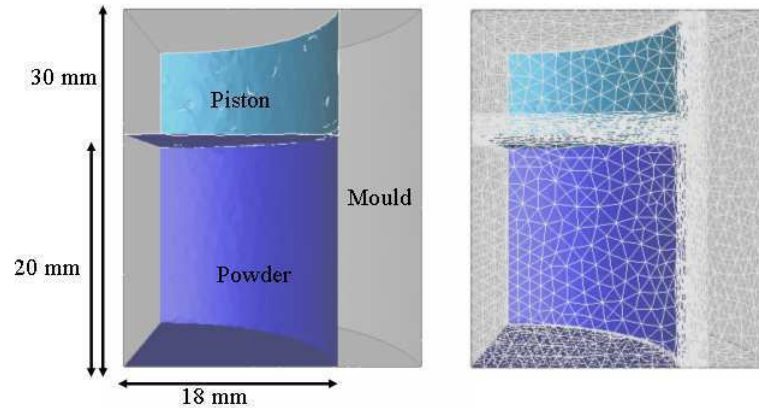


Figure 4.14: 3D geometry considered in the eulerian approach for solving the powder die compaction test with the mesh an anisotropic elements in the neighborhood of the interface

By imposing the velocity in the tools, the solution is only computed in the powder and pressure and stress are equal to zero in the mould and pistons (according to equation 4.37). The same parameters as in 4.4.2.1 are chosen. Vertical stress is compared in Figure 4.15 with the results issued from the Lagrangian approach and with the analytic solution. Comparison shows that results differ in the beginning with an error of 3.83%, the difference decreases with time and the error at the end is equal to 0.5%.

4.4.3 Conclusion

Two tests were carried out to validate the numerical model of CimLib[®] library. Both free uniaxial compression and powder die compression showed satisfying comparisons. First we compared results using the Lagrangian approach in CimLib[®], then before moving to the following section and the complete coupling model, the test was solved using the Eulerian approach. Results issued from the two approaches were compared, the comparison was satisfying. Moreover, the conditions used in these simulations are exaggerated. In fact, the displacement observed experimentally during SPS cycle is much lower, the time to densify the powder is about 10 minutes and the maximum velocity measured when applying the pressure during the cycle is about $2 \times 10^{-5} \text{ m.s}^{-1}$. However, it shows that the model is robust even for extreme conditions.

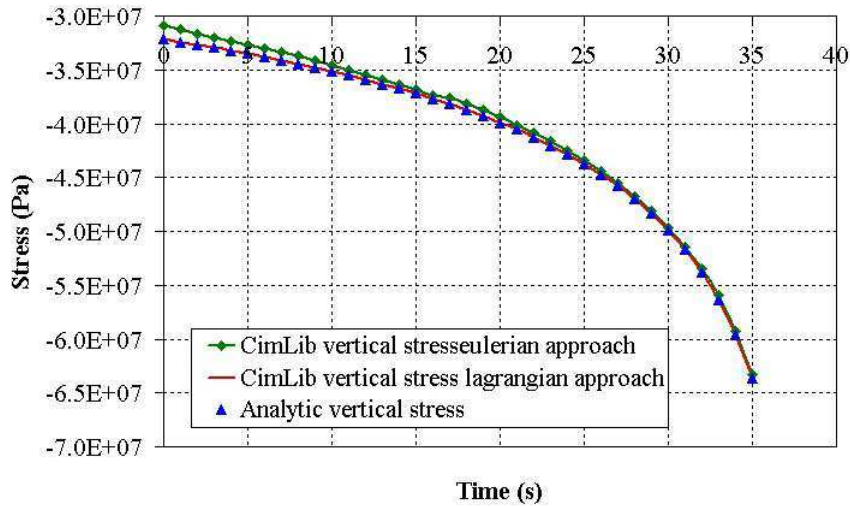


Figure 4.15: Vertical stress plotted over time: comparison between CimLib[®] results using lagrangian and eulerian approach and analytic solution for powder die compression when c and f are constant

4.5 Numerical simulation of coupled electric thermal mechanical problems during SPS

4.5.1 Introduction

In this section coupling between the electric problem, the thermal problem and the mechanical problem is considered. First, the equations are presented as well as the dependencies between the different parameters and variables. We discuss the approach used to compute conductivities when they depend of the density evolution. Then, the algorithm of the resolution is shown. Later, the mesh adaptation is discussed in addition to the motion of the tools. Finally, the results reveal the influence of the coupling between the three problems.

4.5.2 Equations and algorithm of the simulation

Here we consider that a current goes through the SPS apparatus. Consequently, heating is generated in the assembly. Simultaneously, a velocity field is applied in the upper tools of the apparatus generating stresses and density evolution in the powder. *TiAl* is chosen for the simulation, its electric and thermal properties have been given in **Chapter 3**.

Geometry and boundary conditions: The geometry considered is presented in Figure 4.16. The top and bottom Inconel spacers are not modeled in order to reduce com-

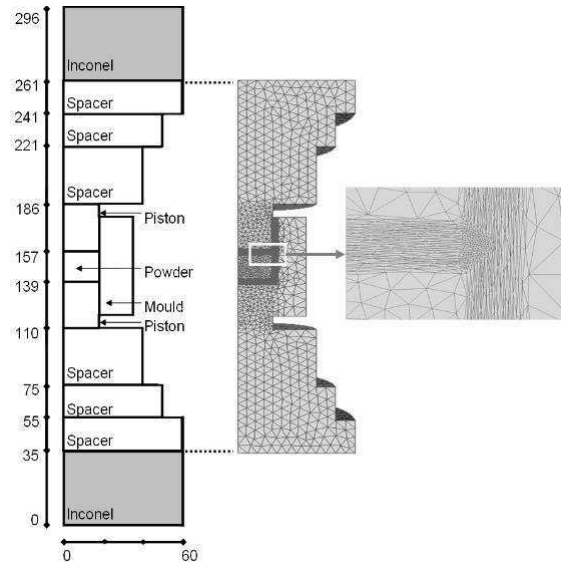


Figure 4.16: Geometry of the SPS set-up with the generated mesh used in the simulation and a zoom in the region of the sample showing refined elements around the sample/matrix interface (radius of the sample 18mm, of the matrix 35mm)

putation time. In fact, when taken into account, an anisotropic remeshing needs to be added between Inconel and graphite spacers. In addition, since upper tools are displaced at each increment, an incremental remeshing must follow at each time step. This will increase significantly the computational time.

However Inconel effect is taken into consideration by the thermal boundary conditions that are imposed directly on the boundaries of the top and bottom graphite spacers. This can be done as follows: Assuming a quasi-stationary state, the heat flux at the Inconel boundary is equal to the heat flux through the Inconel part, and to the heat flux through the interface between Inconel and graphite. Considering the upper Inconel spacer, we can write :

$$\Phi = h_{cond} (T_{inco\ sup} - T_{water}) \quad \text{at the Inconel boundary cooled by water} \quad (4.64)$$

$$\Phi = k_{inco} \frac{T_{inco\ inf} - T_{inco\ sup}}{e_{inco}} \quad \text{in the Inconel} \quad (4.65)$$

Assuming an ideal thermal contact with the graphite spacer, we have $T_{inco\ inf} = T_{gr\ sup}$, consequently:

$$\Phi = k_{inco} \frac{T_{gr\ sup} - T_{inco\ sup}}{e_{inco}} \quad (4.66)$$

$$= \frac{k_{inco}}{e_{inco}} \left(T_{gr\ sup} - \left(\frac{\Phi}{h_{cond}} + T_{water} \right) \right) \text{ by substituting } T_{inco\ sup} \quad (4.67)$$

$$= \frac{k_{inco}}{e_{inco} \left(1 + \frac{k_{inco}}{e_{inco} h_{cond}} \right)} (T_{gr\ sup} - T_{water}) \quad (4.68)$$

$$= \frac{h_{cond}}{h_{cond} \frac{e_{inco}}{k_{inco}} + 1} (T_{gr\ sup} - T_{water}) \quad (4.69)$$

$$= h_{eq} (T_{gr\ sup} - T_{water}) \quad (4.70)$$

It can be seen that under such hypothesis, a heat transfer boundary condition can be applied directly to the graphiate spacer under a convective form, using an equivalent heat exchange coefficient h_{eq} . Here $h_{cond} = 880 \text{ W.m}^{-2}.\text{K}^{-1}$ is a constant heat transfer coefficient, k_{inco} the Inconel thermal conductivity, e_{inco} its thickness, $T_{inco\ sup}$ the temperature of the Inconel upper edge, $T_{inco\ inf} = T_{gr\ sup}$ the Inconel/graphite interface temperature and T_{water} the water temperature (assumed constant 296 K). Moreover, the process taking place in a vacuum chamber, heat losses by convection and conduction are neglected. All lateral surfaces having heat losses by radiation towards chamber walls, which are held at room temperature (300 K), a radiative heat flux is considered:

$$\Phi_{rad} = \sigma_B \varepsilon_r (T^4 - T_{wall}^4) \quad (4.71)$$

where σ_B is the Stefan-Boltzmann's constant, $\sigma_B = 5.6704 \times 10^{-8} \text{ W.m}^{-2}.\text{K}^{-1}$, ε_r the emissivity of tools (assumed to be equal to 0.8 in this study), T the local temperature of the vertical boundary surfaces and T_{wall} the temperature of the chamber walls. On the other hand, a constant voltage is applied during the simulations $U_{imp} = 3.6 \text{ V}$. Furthermore, all contact surfaces between the parts of the SPS assembly are considered ideal: no contact resistance is taken into account. The powder follows the viscoplastic law for porous materials as mentioned previously. Besides, tools are assumed to be rigid (stresses are not calculated inside graphite) and a frictionless contact is considered between tools and powder. In fact in the framework of the monolithic approach that is used, mechanical contact conditions are detailed in Chapter 5. A numerical viscosity allows modeling friction or sliding between tools and powder. Moreover, a constant velocity of $6 \times 10^{-3} \text{ mm.s}^{-1}$ is applied to the upper tooling, whereas the mould and lower tooling are considered fixed. The initial porosity in the *TiAl* powder is considered to be equal to 30%. The consistency $K(T)$ and the strain rate sensitivity $m(T)$ are thermal dependent, their values are deduced from literature [26], where measurements were carried out on Ti-47Al-2Cr-2Nb. Samples were tested for temperatures equal to 800°C , 900°C and 1000°C .

Equations This multiphysics problem is governed by the following system of equations:

$$\begin{cases} \nabla \cdot (-\sigma_e(T, \rho_r) \nabla U) = 0 \\ \nabla \cdot (-k(T, \rho_r) \nabla T) + \rho_r \rho_0 c_p(T) \frac{\partial T}{\partial t} = \sigma_e(T, \rho_r) \|\nabla U\|^2 \\ \nabla \cdot \sigma = 0 \\ \nabla \cdot (\rho_r \vec{v}) + \frac{\partial \rho_r}{\partial t} = 0 \end{cases} \quad (4.72)$$

Figure 4.17 explains the order of the system resolution. At each time step, the electrical problem is solved first, then providing the source term of heat equation. Once the temperature computed, all thermal dependent parameters are updated. The mechanical problem is then solved, from which we deduce velocity and pressure. The velocity field is introduced in the mass conservation equation, and next we compute the relative density and update the parameters affected by its variation. Finally, the mesh is regenerated by updating the nodes coordinates and by remeshing the neighbourhood of the moving interface.

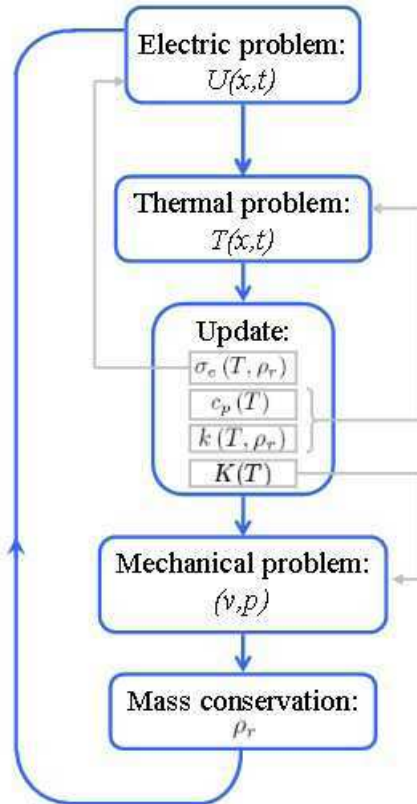


Figure 4.17: Resolution algorithm

Before showing and analysing the results, we explain how the mesh is adapted at each step according to the velocity field and we discuss the necessity of modeling the motion of the tools and their effect on the symmetry of temperature field and densification.

4.5.3 Mesh adaptation with tools motion

When using the Eulerian approach, signed distance functions are defined on the single mesh as mentioned before. A level set is associated to the powder and another one to the graphite tools. Since spacers and pistons have a vertical displacement, their motion is described at each time step by the translation of their level set functions. When necessary, the remeshing follows the translation so that anisotropic elements always surround the interface between the powder, the mould and piston.

In the SPS process, the pieces are placed in a vacuum chamber, which means that mixing laws between the vacuum and tooling are necessary as well as a fine anisotropic remeshing around these interfaces. As a consequence, the number of elements increases significantly which slows down the resolution. For that reason, a different approach is adapted. Figure 4.18 gives an example using a 2D geometry, when the void is added (red area) the number of nodes increases from 7000 to 11000, for a homogeneous background mesh size. The void won't be considered in the geometry simulated and the mesh only covers tools and powder. In addition, at each time step the nodes coordinates are updated as follows:

$$\vec{X}^{t+\Delta t} = \vec{X}^t + \vec{v}_{mesh}^t \Delta t \quad (4.73)$$

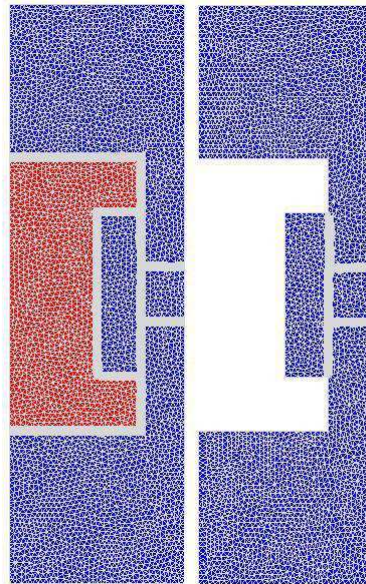


Figure 4.18: Example of a 2D geometry with and without the void around the mould showing the anisotropic elements added.

More precisely, v_{mesh} is fixed during the simulation and depends only on the imposed velocity on the tooling. Consequently, it is different from a Lagrangian approach, where

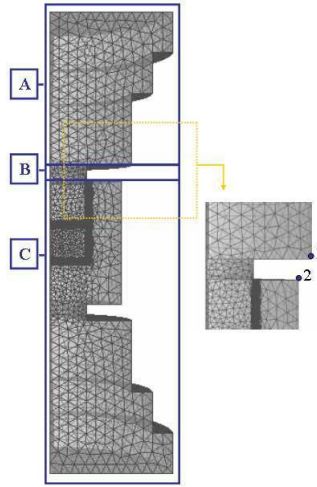


Figure 4.19: Regions of the geometry simulated where mesh velocity is controlled to update the coordinates

the nodes are updated according to the velocity field computed in the mechanical problem. Here, v_{mesh} is related to the characteristic function of three different regions, as seen in figure 4.19. So if we denote z_{top} the z coordinate of the node 1 and z_{fixed} the z coordinate of the node 2 of figure 4.19, v_{mesh} can be written:

$$\begin{aligned} \vec{v}_{mesh} &= \vec{v}_{imp} \quad \text{in A} \\ \vec{v}_{mesh} &= \vec{v}_{imp} \frac{z - z_{fixed}}{z_{top} - z_{fixed}} \quad \text{in B} \\ \vec{v}_{mesh} &= 0 \quad \text{in C} \end{aligned} \quad (4.74)$$

This expression will allow the translation of the nodes of the spacers, a linear transition between the moving spacer and the fixed mould and will keep the rest invariant. Consequently, the mesh follows the motion of the different parts without increasing calculation time which is advantageous comparing to a completely Eulerian approach where more elements need to be added.

4.5.4 Symmetry due to geometry

When the upper tools move down, the axial symmetry is lost. Consequently, temperature field is affected. In Figure 4.21, the axial temperature profiles after 25 s and 900 s show that once symmetry is lost, heating is no longer similar on both sides. When the piston enters into the mould, the height of the restricted section (between point 1 and 2 of Figure 4.19) is smaller. Consequently, the region where the current converges is reduced and Joule effect is less important.

Moreover, since conduction plays a very important role in heating the powder, the difference of temperatures between the two pistons as seen in Figure 4.22 causes a non

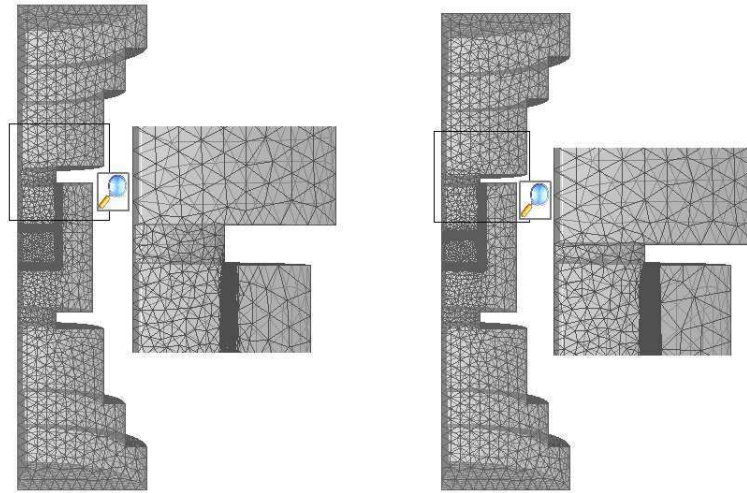


Figure 4.20: Regions of the geometry simulated where mesh velocity is controlled to update the coordinates: a zoom on the top corner where the piston penetrates in the mould

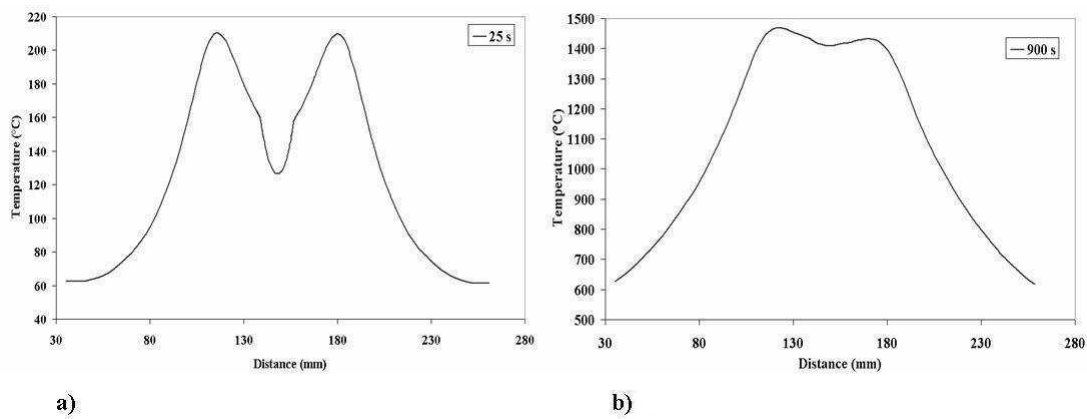


Figure 4.21: Temperature variation along the vertical axis for the TiAl sample for different time steps showing the effect of the symmetry

symmetrical temperature gradient inside the powder. Actually, non symmetrical temperature gradient inside the powder causes the dis-symmetry of the distribution of the consistency of the powder. As seen in Figure 4.23, the consistency is inversely proportional to temperature, besides the relative density is higher where the powder is less consistent. In conclusion, density is not symmetrical and is more important where the temperature is high.

In fact, the geometrical symmetry of the apparatus is one point that should be well understood. When dealing with larger parts the temperature gradients will be more important and so density gradients. This is why, dis-symmetry effects should be controlled

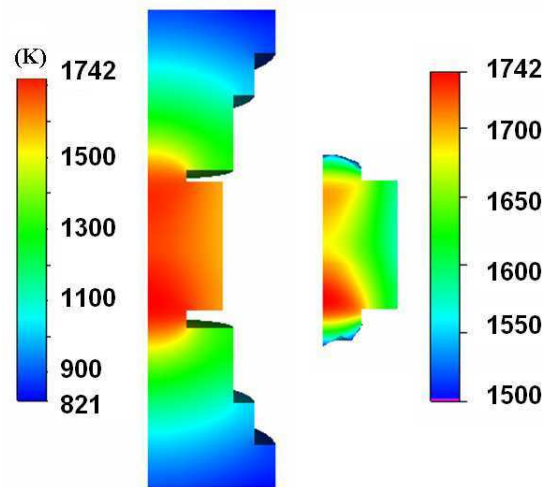


Figure 4.22: Temperature isovalues (in K) after 900 s when the symmetry is no longer respected

to optimize the quality of the industrial products.

However, in the SPS set up, actually the mould moves during SPS process and this helps conserving the symmetry. Friction between the mould, the papyex and pistons assures maintaining the mould while allowing its vertical motion.

Later on, in **Chapter 6**, the motion of the mould is modelled by adapting the mesh in the same approach as presented previously for upper tools.

4.5.5 Dependence of conductivities with powder relative density

When compacting a powder, the volume of pores decreases. Contact surfaces are more important, hence, electric and thermal fluxes diffuse differently through particles.

Since we model densification in a macroscopic scale, the conductivities should represent the material as a continuous homogeneous medium taking in consideration its porosity.

For the thermal conductivity, the model chosen is based on the work of Argento [3].

In his work, Argento developed two numerical models describing conduction and radiation. He concluded that in metallic powders, radiation is neglected compared to conduction. Hence, he considered that conduction between particles is the dominant heat transfer in the powder across the contact area, but under the condition that the density is high enough to create a contact network in the powder.

During SPS process the set up is placed in a vacuum chamber. In addition, when placed in the mould, the powder is manually pre-compacted at room temperature before introduction in the apparatus which allows particles rearrangement and reduces voids. Consequently and according to the results provided by Argento [3], the radiation between particles is neglected in front of conduction.

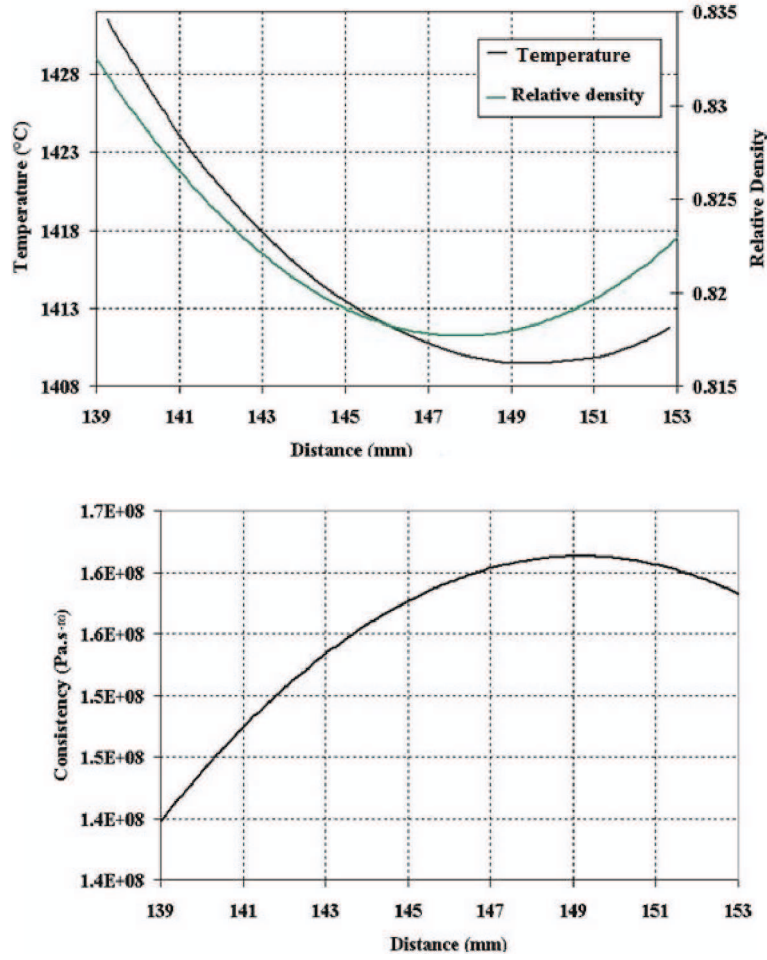


Figure 4.23: Temperature variation, consistency variation and relative density along the vertical axis inside the TiAl sample at $t = 900s$

Argento [3] went from a model at a microscopic scale, where he modeled heat transfer between particles in contact, to a macroscopic model where the thermal conductivity was expressed as follows:

$$k = k_s \left[\frac{\rho_r - \rho_c}{1 - \rho_c} \right]^{\frac{3}{2}(1-\rho_c)} \quad (4.75)$$

k_s denotes the conductivity of the dense state. The critical relative density ρ_c is the lowest density reached when the contact between particles is punctual. The main difficulty of this model, as it was described already by Argento, is the choice of ρ_c , which is the density corresponding to the value zero of the conductivity. In fact, this represents a limitation of the model since physically it is known that even for low temperatures, a residual conductivity remains for low densities.

Moreover, the electric conductivity is also dependent on the relative density. It is calculated according to the Wiedemann-Franz law. The Wiedemann-Franz law is a rela-

tion between the electrical and thermal conductivity [29]. It states that the ratio of the thermal conductivity k by the electrical conductivity σ_e of a metal is proportional to the temperature T :

$$L_e = \frac{k}{T\sigma_e} = 2.44 \times 10^{-8} \text{ W } \Omega \text{ K}^{-2} \quad (4.76)$$

In this equation, L_e denotes the Lorentz number.

Consequently, once the thermal conductivity calculated this relation allows deducing the electric conductivity as a function of the relative density.

$$\sigma_e = \frac{k_s}{L_e T} \left[\frac{\rho_r - \rho_c}{1 - \rho_c} \right]^{\frac{3}{2}(1-\rho_c)} \quad (4.77)$$

Two simulations are carried out in order to check if taking into account the variation of the porosity in the thermal and electrical problem has a big influence on the results. First we simulate the coupled electrical-thermal-mechanical problems and we consider that all parameters are thermal dependent without considering expression 4.75 (conductivities do not depend on relative density), the relative density value is not returned to the electrical and thermal problems. Second, same problems are simulated but computing conductivities as presented in expressions 4.75 and 4.77.

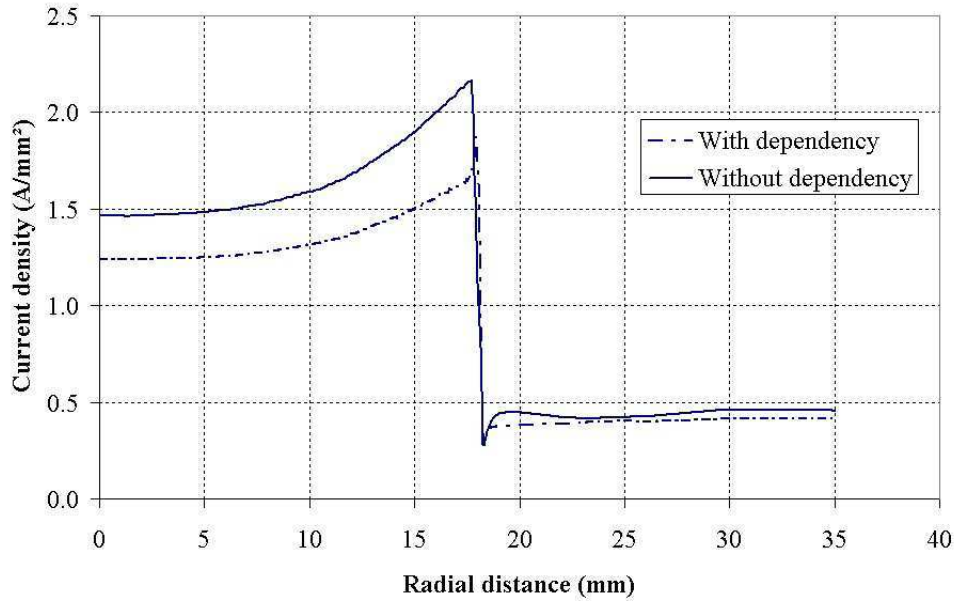


Figure 4.24: Radial variation of current density when considering or neglecting the dependence on the porosity of thermal and electrical conductivities

In Figure 4.24 the distribution of the norm of the current density is plotted along the radial direction from the center of the powder towards the die edge. The vertical level of the curve is 4 mm away from the lower edge of the powder. The current density is

higher when the evolution of the relative density is not considered in the electrical thermal problems. In fact, as conductivities decrease with porosity, the current is less concentrated in the powder with lower density.

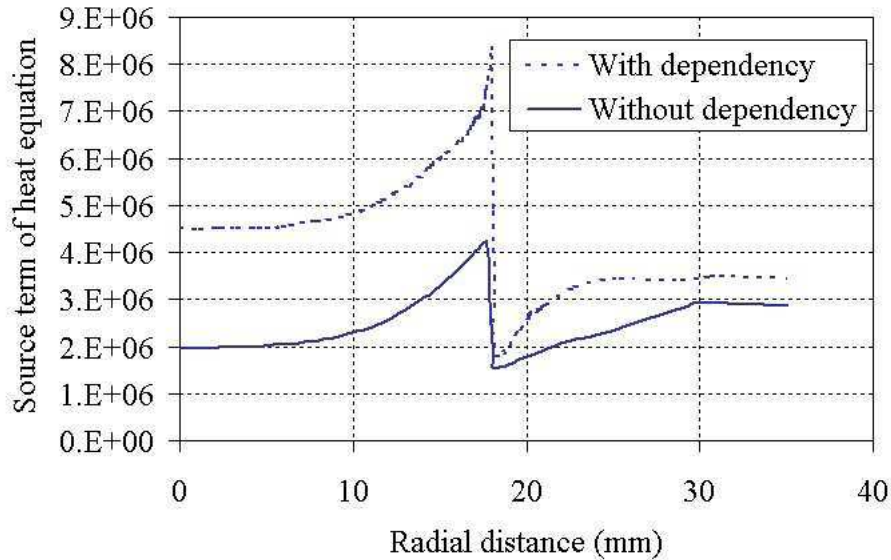


Figure 4.25: Radial variation of the source term of heat equation at 100 s when considering or neglecting the dependence on the porosity

The idea is the same as when we compared in Chapter 3 the temperature distribution of alumina and $TiAl$. Even though the current density is lower, the source term of the heat equation is higher when the electrical conductivity is lower as seen in Figure 4.25. This is due to the potential gradient that increases when conductivity decreases in the powder. Consequently, temperature is higher when the variation of relative density is considered in the thermal and electrical problem. In figure 4.27, the variation of temperature in the radial direction from the center of the powder towards the die edge is compared between the two simulations for different time steps. The temperature in the center is $15^{\circ}C$ higher at 100 s when the relative density evolution is considered and then the gap decreases to $4^{\circ}C$ at 1200 s.

The difference of temperature between the two types of simulation appears to be relatively low. It should be underlined that such a difference can be significant when predicting the occurrence of a phase change in the material. However, it can be thought that it might be not so critical to determine exactly the dependence of conductivities against relative density. When we want to predict microscopic phase change it is better to be as accurate as possible to reduce the error.

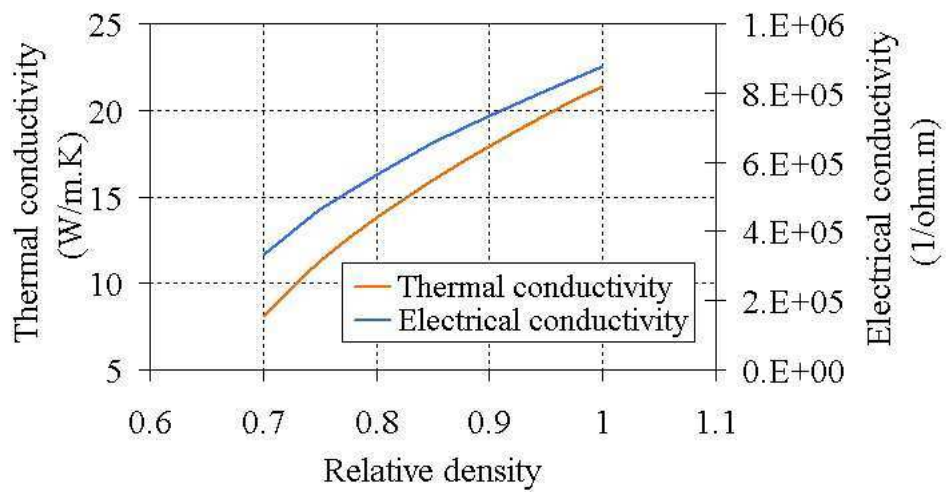


Figure 4.26: Variation of the thermal and electrical conductivities with relative density when temperature is fixed at $1000^{\circ}C$

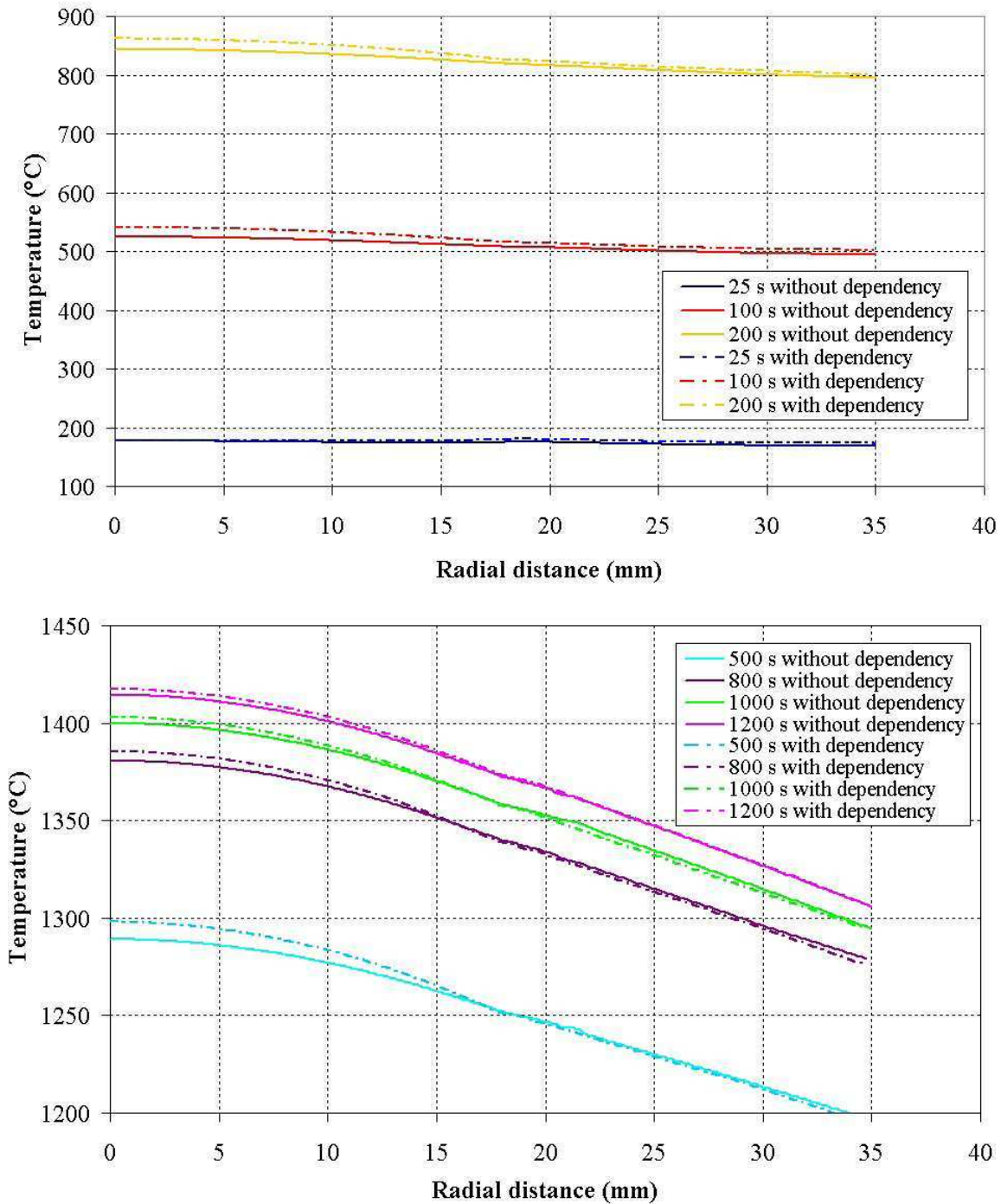


Figure 4.27: Radial variation of temperature at different time steps when considering or neglecting the dependence on the porosity

4.6 Conclusion

This Chapter presents the model describing the behavior of the powder during SPS process. The powder reaches high temperature in few minutes. For that reason, it follows a compressible viscoplastic behavior. A Norton-Hoff power law is chosen for the viscoplastic behavior modified according to Abouaf, to take into account the compressibility and to model densification. The mechanical problem is presented with its finite element discretization. The model is validated with two numerical tests: a simple uniaxial compression and a powder die compression. First, the two tests are solved using a Lagrangian approach. Results were validated by comparison with analytic solution and with the software R2Sol. Results were in very good agreements. The powder die compaction test was then modeled in the Eulerian approach considering the mould and the upper piston. Hence, the level set functions are introduced in the model as well as the anisotropic meshing. The results of the Eulerian approach were compared with analytic solutions and results issued from the Lagrangian approach. Comparisons were in very good agreements.

Once the implementation of the mechanical behavior law validated, the coupled electrical thermal mechanical problems are presented to simulate the SPS process. In this chapter, the boundary conditions of the mechanical model are still limited to the application of a constant imposed velocity however in the process the pressure is regulated according to a prescribed value. The physical properties in the coupled problem are dependent on temperature and relative density. The thermal conductivity is expressed as a function of relative density following the work of Argento. The electric conductivity is then expressed using the Wiedmann-Franz law. Two simulations were carried out in this chapter to test the influence when taking into account the dependence on relative density. It was found that the difference of temperature is not significant. The simulations in this chapter are all achieved considering sliding conditions between the powder and tooling. However, in SPS process friction might influence the distribution of temperature and density. The aim of the following chapter is to model friction in the framework of the monolithic Eulerian approach.

Bibliography

- [1] M. Abouaf. *Modélisation de la compaction de poudres métalliques frittées*. PhD thesis, Université scientifique et médicale et Institut national polytechnique de Grenoble, 1985.
- [2] M. Abouaf and J.L. Chenot. Modélisation numérique de la déformation à chaud de poudres métalliques. *Journal de Mécanique Théorique et Appliquée*, 5:121–140, 1986.
- [3] C. Argento. *Modélisation du comportement thermique et mécanique des poudres métalliques- Applications à la compaction isostatique à chaud*. PhD thesis, Université Joseph Fourier- Grenoble I, 1994.
- [4] E. Artz. The influence of an increasing particle coordination on the densification of spherical powders. *Acta Metallurgica*, 30:1883–1890, 1982.
- [5] I. Babuska. The finite element method with lagrangian multipliers. *Numerical Mathematics*, 20:179–192, 1973.
- [6] O. Basset. *Simulation numérique d'écoulements multi fluides sur grille de calcul*. PhD thesis, Ecole Des Mines De Paris, France, 2006.
- [7] O. Bouaziz, C. Dellis, and P. Stutz. Creation of a material data file for modelling HIPing of an austenitic stainless steel. In *International workshop on modelling of metal powder forming processes*, July 1997.
- [8] D. Bouvard and E. Ouedraogo. Modelling of hot isostatic pressing: A new formulation using random variables. *Acta Metallurgica*, 35:2323–2328, 1987.
- [9] F. Brezzi. On the existence, uniqueness and approximation of saddle-point problems arising from lagrange multipliers. *RAIRO Ser. Rouge*, 8:129–151, 1974.
- [10] T. Coupez. Stabilized finite element method for 3d forming calculation. *Intern communication, CEMEF, Sophia Antipolis*, 15, 1996.
- [11] E. Doege and A; Bagaviev. Fem-modelling of the non isothermal sintering of metal powder compacts. In *International workshop on modelling of metal powder forming processes*, July 1997.

-
- [12] C. Gay. *Contribution à la simulation numérique 3D du forgeage à froid*. PhD thesis, Ecole des Mines de Paris, 1995.
- [13] C. Geindreau, D. Bouvard, and P. Doremus. A unified viscoplastic constitutive equation for modelling hot isostatic pressing. In *International workshop on modelling of metal powder forming processes*, July 1997.
- [14] Christian Geindreau, Didier Bouvard, and Pierre Doremus. Constitutive behaviour of metal powder during hot forming.: Part ii: Unified viscoplastic modelling. *European Journal of Mechanics - A/Solids*, 18(4):597 – 615, 1999.
- [15] M. Gunzburger and R.A. Nicolaides. *Incompressible Computational Fluid Dynamics*. Cambridge University Press, 1993.
- [16] E. Hachem. *Stabilized Finite Element Method for Heat Transfer and Turbulent Flows inside Industrial Furnaces*. PhD thesis, Ecole des Mines de Paris, 2009.
- [17] O. Jaouen. *Modélisation tridimensionnelle par éléments finis pour l'analyse thermomécanique du refroidissement des pièces coulées*. PhD thesis, Ecole Nationale Supérieure des Mines de Paris, 1998.
- [18] HongGee Kim, Olivier Gillia, Pierre Dorémus, and Didier Bouvard. Near net shape processing of a sintered alumina component: adjustment of pressing parameters through finite element simulation. *International Journal of Mechanical Sciences*, 44(12):2523 – 2539, 2002.
- [19] H.S. Kim and D.N . Lee. Power-law creep model for densification of powder compacts. *Materials Science and Engineering A*, 271:424–429, 1999.
- [20] K.T Kim and Y.C. Jeon. Densification behavior of 316L stainless steel powder under high temperature. In *International workshop on modelling of metal powder forming processes, Grenoble*, July 1997.
- [21] L.T. Kuhn and R.M. McMeeking. Power-law creep of powder bonded by isolated contacts. *International Journal of Mechanical Science*, 34:563–573, 1992.
- [22] W. Liu. *Finite element modelling of macrosegregation and thermomechanical phenomena in solidification processes*. PhD thesis, Ecole des Mines de Paris, 2005.
- [23] JR. Matthews. Indentation hardness and hot pressing. *Acta Metallurgica*, 28:311, 1980.
- [24] Brandon McWilliams and Antonios Zavaliangos. Multi-phenomena simulation of electric field assisted sintering. *Journal of Materials Science*, 43(14):5031–5035, JUL 2008.

-
- [25] S. Munoz and U. Anselmi-Tamburini. Temperature and stress fields evolution during spark plasma sintering processes. *Journal of materials science*, 45:6528–6539, 2010.
- [26] T. Nieh, L. Hsiung, and J. Wadsworth. Superplastic behavior of a powder metallurgy alloy with a metastable microstructure. *Intermetallics*, 7:163–170, 1999.
- [27] E. Olevsky. Theory of sintering: From discrete to continuum, review. *Materials Science and Engineering*, R23:41–100, 1998.
- [28] E. Olevsky and L. Froyen. Constitutive modeling of spark-plasma sintering of conductive materials. *Scripta Materialia*, 55:1175–1178, 2006.
- [29] C. Pradille. *Vers une meilleure compréhension et caractérisation du comportement des aciers à très haute température*. PhD thesis, Ecole des Mines de Paris, 2011.
- [30] A. S. Rao and A. C. D. Chaklader. Plastic flow during hot-pressing. *Journal of the American Ceramic Society*, 55(12):596–601, 1972.
- [31] S. Shima and M. Oyane. Plasticity theory for porous metals. *International Journal of Mechanical Science*, 18:285–291, 1976.
- [32] JY. Song, Y. Li, Z. Zhou, Y. Lai, and Y. Ye. A multi-field coupled FEM model for one-step-forming process of spark plasma sintering considering local densification of powder material. *Journal of Material Science*, 46:5645–5656, 2011.
- [33] P. Stutz, G. Aryanpour, O. Bouaziz, and C. Dellis. A two strain rate model for the HIPing of austenitic stainless steel. In *International workshop on modelling of metal powder forming processes*, Grenoble, July 1997.
- [34] C. Wang, L. Cheng, and Z. Zhao. Fem analysis of the temperature and stress distribution in spark plasma sintering: Modelling and experimental validation. *Computational Materials Science*, 49:351–362, 2010.
- [35] X Wang, S.R. Casolco, G. Xu, and J.E. Garay. Finite element modeling of electric current-activated sintering: The effect of coupled electrical potential, temperature and stress. *Acta Materialia*, 55:3611–3622, 2007.

Chapter 5

Modeling of friction during SPS using the Eulerian approach

Contents

5.1	Introduction	121
5.2	Friction law	122
5.2.1	Powder/Wall friction models	124
5.2.2	Viscoplastic friction model for powder compaction	125
5.3	Modeling of friction in the Eulerian monolithic approach	126
5.3.1	Introduction	126
5.3.2	Description of the mechanical model	126
5.3.3	Description of the Eulerian model	127
5.3.4	Description of the Lagrangian model	129
5.3.5	Numerical study of the Eulerian approach	131
5.3.6	Possible developments in the Eulerian model	140
5.4	Conclusion	141

Résumé

Dans ce chapitre est présenté un modèle numérique de frottement utilisé dans l'approche eulérienne. Ce modèle est basé sur le principe de la couche limite, qui consiste à ajouter un troisième corps (une couche) entre le moule et la poudre. Une consistance est associée à cette dernière permettant de générer les mêmes effets de frottement que dans une approche lagrangienne, où une condition aux limites est imposée sur le bord Γ de la poudre. L'objectif de ce chapitre est de définir une relation entre le coefficient de frottement, l'épaisseur de la couche et la consistance de celle-ci. Pour cette raison, des essais sont effectués en faisant varier l'épaisseur e et le coefficient de frottement α_f . Pour chaque couple (e, α_f) , différentes consistances sont étudiées. Ensuite, les résultats correspondants à chacune des consistances du modèle eulérien sont comparés avec les résultats du modèle lagrangien calculés avec le même coefficient de frottement. Une erreur est déduite à partir de ces comparaisons. La consistance donnant la plus faible erreur pour le couple (e, α_f) est alors choisi. Ces valeurs sont utilisées dans un algorithme d'analyse inverse pour extraire l'expression de la consistance de la couche \tilde{K} et déduire une fonction de e et α_f . Cette étude a été réalisée en simplifiant certaines conditions telles que les hétérogénéités de température et l'évolution des fonctions d'Abouaf. Il serait intéressant de tester cette méthode avec le chauffage et les dépendances de température. En outre, l'expression trouvée pour \tilde{K} pourrait être étendue en considérant la dépendance au nombre d'élément à l'intérieur de la couche limite et la position de la couche par rapport à la poudre (centrée ou décalée dans le moule).

5.1 Introduction

During spark plasma sintering process, the mould is maintained in the set up by the forces generated between the pistons and the powder from one side and the mould itself on the other side. In addition, when sintering a sample of large dimensions, the gradient of porosity is remarkable which cannot be only resulting from temperature gradient. For instance, an interrupted SPS test is achieved on a powder cylinder (8 mm in diameter and 20.6 mm as the initial height). The powder is subjected to 50 MPa and heated at 100°C/min. At $T = 1050^{\circ}\text{C}$, the test is interrupted. The sample is extracted and is cut along the longitudinal direction. The porosity is measured using the Scanning Electron Microscopy (SEM). The measurements are then transformed using the software GIMP to get the result of Figure 5.1. The details of the procedure followed to reach this results (obtained at CEMES in the framework of the IRIS project) are presented in the following chapter. In Figure 5.1, the distribution of the porosity on the medium longitudinal section is presented. A difference of 10% is observed between the minimum porosity (measured on the part in contact with the die at the lateral edge) and the maximum porosity (measured on the edges under the two pistons). This gradient brings to light the effect of friction between powder and tools.

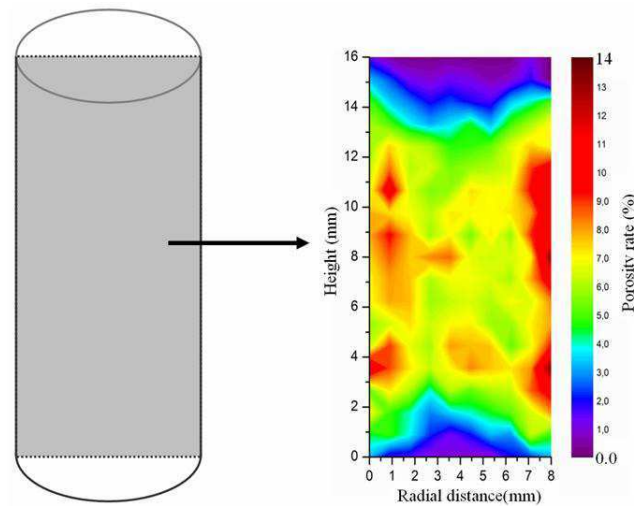


Figure 5.1: Distribution of the porosity on a longitudinal section of the powder cylinder at $T = 1050^{\circ}\text{C}$ for an interrupted SPS cycle

In fact, the distribution of porosity will depend on the ratio between the diameter and height of the sample. The gradient of porosity is higher when the ratio of height over diameter is higher.

A complete numerical model of spark plasma sintering process necessitates then the incorporation of a friction model. The model should allow predicting the friction forces and their influence on displacement field, stress and density.

The aim of the work in this chapter is to set up a simplified numerical model to take into account the friction between the powder and the mould.

Since a monolithic Eulerian approach is used in our work, the surface conditions cannot be imposed on each surface of the components by a classical boundary condition. The reason is that, as explained in the previous chapters, one mesh is used for the whole assembly. Besides, the level set function is used to model the interfaces. Hence, it intercepts the volumetric elements. In the literature [1]-[3], the transition between the surface integral to the volumetric integral is often found to model surface forces in the Eulerian approach with the use of the Dirac function. However, here the work is limited to a more simplified model inspired from the concept of the boundary layer in fluid mechanics.

In this chapter, first literature models of powder/tooling friction are presented. Second, the numerical test used to validate the model chosen for friction is described as well as the procedure followed to generalize the approach. Finally, in the perspectives, the sensibility of the method is discussed.

5.2 Friction law

When two bodies in motion are in contact, the physical phenomena that appear between the two surfaces are described by friction laws. More precisely, friction is the force generated on the interface between the two bodies that tends to resist to their relative tangential motion. In powder die compaction, if v is the velocity of the powder and v_m the velocity of the mould, we define the sliding tangential velocity at the interface as:

$$\vec{v}_g = (\vec{v} - \vec{v}_m) - ((\vec{v} - \vec{v}_m) \cdot \vec{n}) \vec{n}. \quad (5.1)$$

Besides the shear stress generated is written:

$$\vec{\tau} = \sigma \vec{n} - (\sigma \vec{n} \cdot \vec{n}) \vec{n}. \quad (5.2)$$

Behaviour laws often describe a relation between the shear stress $\vec{\tau}$ and the tangential velocity in addition to the different physical phenomena that influence friction. These phenomena are numerous, for instance:

- The nature of the materials in presence as well as their structure.
- The roughness of the surface.
- The addition or not of lubricants and their nature.

- The porosity in case of porous material.

Friction laws dealing with powders are based on the friction laws developed for dense materials and modified in order to integrate powder characteristics.

Coulomb law is often found in the literature. Coulomb and Tresca law are in fact based on a certain threshold, below which, no sliding can occur. Moreover, some papers use the Norton-Hoff friction law especially when it dealing with viscoplastic materials.

First, these models are presented in the framework of dense medium, then in the following paragraph their modification is discussed when applied to porous media.

Tresca law is written:

$$\text{if } \tau < g \text{ then } v_g = 0 \quad (5.3)$$

$$\text{if } \tau = g \text{ then } \exists \lambda \geq 0 \text{ such that } \vec{v}_g = -\lambda \vec{\tau} \quad (5.4)$$

g being a fixed adherence threshold. The graphic of this law is presented in Figure 5.2.

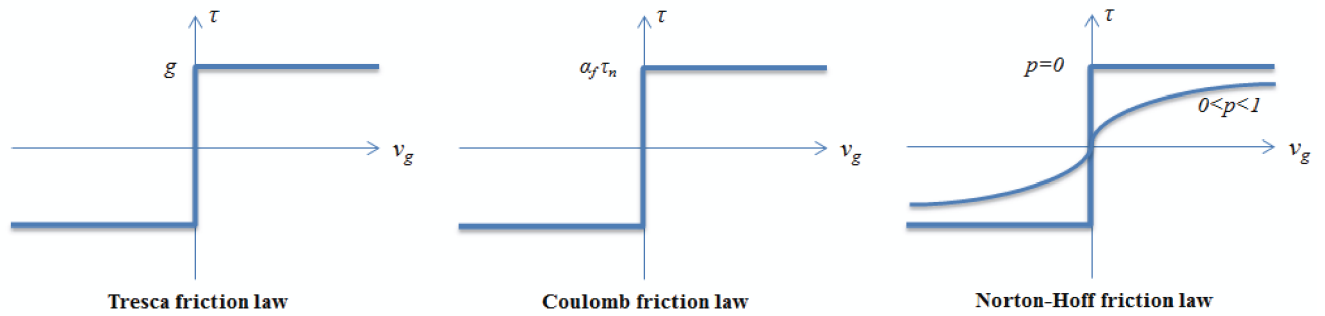


Figure 5.2: Graphic representation of the different friction laws

Coulomb friction law, which is the mostly used, is written similarly to Tresca law but describing the threshold as being proportional to the normal stress τ_n , modulus of the normal stress:

$$\text{if } \tau < \alpha_f \tau_n \text{ then } v_g = 0 \quad (5.5)$$

$$\text{if } \tau = \alpha_f \tau_n \text{ then } \exists \lambda \geq 0 \text{ such that } v_g = -\lambda \tau \quad (5.6)$$

α_f is the friction coefficient dependent on the materials and their surface.

The viscoplastic friction law derives from the viscoplastic behaviour of Norton-Hoff. It is mostly used for the viscoplastic materials without plasticity criterion:

$$\tau = -\alpha_f \cdot K \cdot |v_g|^{p-1} \cdot v_g \quad (5.7)$$

K denotes the consistency of the material. Since there is no third body or lubricant p is equal to m the strain rate sensitivity coefficient [15].

5.2.1 Powder/Wall friction models

Friction during powder compaction was studied by many authors. Understanding friction helps reducing defects when manufacturing products. The reason is that friction influences many physical aspects like density distribution [7], the velocity field when the load is applied and the final quality of the compact. Hence, in the literature, studies are carried out to understand the relation of friction with tooling chemical composition [12], lubricant [16] or applied load.

Keshavarz *et al.* [10] and Khoei *et al.* [11] studied friction in cold powder compaction process. The friction relation used in their work is derived from Coulomb friction law which is coherent with the use of the powder plasticity model. It is a stick-slip condition. The law is defined similarly as the definition of a plasticity surface. Considering that inside the surface, the criterion F corresponds to the stick condition and on the surface, it verifies the slip condition:

$$\begin{cases} F = \tau_T - \alpha_f \tau_n - c_f \\ \text{if } F > 0 \\ \text{if } F < 0 \end{cases} \begin{cases} = 0 \Rightarrow \text{slip} \\ < 0 \Rightarrow \text{adherence} \end{cases} \quad (5.8)$$

The friction coefficient is dependent on the angle of friction. It is expressed as $\alpha_f = \tan \phi$ (ϕ the friction angle). c_f denotes the cohesion between powder and tools.

Tran *et al.* [18] defined the friction law similarly for powder compaction processes, for a cylinder and "T" geometries, where the powder is considered elastoplastic. The parameters c_f and ϕ can be determined by simple laboratory tests.

Cunningham *et al.* [5] and Brinckmann *et al.* [2] use Coulomb friction law between powder and tools for the die compaction of tablets and NaCl powder respectively. The friction coefficient depends on the measured stress in the pistons. Their procedure is based on the method of differential slices using Figure 5.3. Cunningham *et al.* [5] showed that, in case of die uniaxial compression, friction coefficient can be expressed as:

$$\alpha_f = \frac{D}{4H} \frac{\sigma_B}{\sigma_{rr}(z)} \left(\frac{\sigma_T}{\sigma_B} \right)^{\frac{z}{H}} \ln \frac{\sigma_T}{\sigma_B} \quad (5.9)$$

where σ_T and σ_B denote respectively the top and bottom punch stresses. In fact, this expression is based on many assumptions, such as the uniformity of the stress at any horizontal level, the stress tensor is written in the principle directions and the friction obeys Coulomb law between the block and die. Tien *et al.* [17], Guyoncourt *et al.* [8] expressed identically the friction relation. This expression is found a lot in the literature for cold powder die compaction. In fact, it is often used when the work consists in determining the friction rate using a measurement system on a powder die compaction test since the ratio between the normal and tangential force is known.

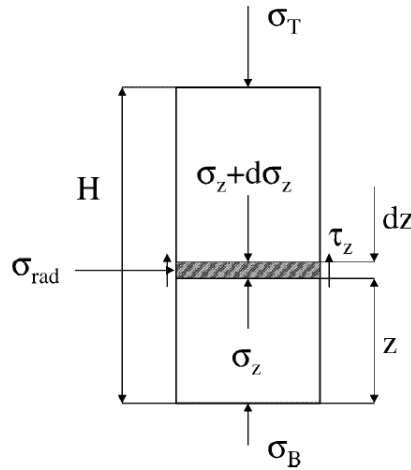


Figure 5.3: Scheme of the geometry considered in the work of Cunningham *et al.* [5] to determine the friction coefficient

Wilkman *et al.* [19] studied powder/wall friction for iron powder during cold pressing. Coulomb law was used with a friction coefficient dependent on the sliding velocity and relative density:

$$\tau = \alpha_f(1 + f_v f_\rho) \sigma_n \quad (5.10)$$

f_v , f_ρ being respectively two functions of the sliding velocity and the relative density. They found that the dependency on the sliding velocity is necessary in case of a large contact surface in particular for high velocity and pressure. Doremus and Pavier [6]-[14] also used the ratio of the normal and tangential forces to determine an expression for friction coefficient ($\alpha_f = \tau_t / \tau_n$). They studied friction for powder die compaction while the set up is fixed on a sliding slab and for a classical powder die compaction test. The friction coefficient is expressed similarly as in [19], it depends on the sliding velocity, the normal stress and the relative density. However the comparison between both models showed differences for low stresses [14].

In papers cited previously the powder was not subjected to high temperatures (highest equal to $60^\circ C$ in [6]), hence the conditions are not close to the framework of spark plasma sintering process, besides powder obeys either plastic or elastoplastic law.

5.2.2 Viscoplastic friction model for powder compaction

During spark plasma sintering process, the powder follows a viscoplastic behaviour which eliminates the restriction domain of plastic materials. Consequently, in order to keep the analogy with the friction law, Norton power law is chosen after being modified for porous media. The behaviour of the material at the interface is considered dependent on the relative velocity and on the material properties subjected to the viscoplastic deformation. In fact, this law was used in several papers.

Cho *et al.* [4] simulated a powder forging process. The aluminium powder with a cup-shape geometry is heated at 400°C and obeys to a viscoplastic isotropic compressible law. A Norton law is used to model the friction between the powder and the wall:

$$\vec{\tau} = -\alpha_f \cdot K \cdot A^{-\frac{2}{3}} \cdot \left| \frac{v_g}{A^{\frac{1}{3}}} \right|^{m-1} \cdot \vec{v}_g \quad (5.11)$$

where A is a function of the relative density.

Similarly, Jinka *et al.* [9] simulated a powder forging process. A similar expression is used in which the power of the function of the relative density is different. In our work, the expression that is used is the following (a justificatin can be found in the next pages, section 5.3.3

$$\vec{\tau} = -\alpha_f \cdot K \cdot c^{-\frac{m+1}{2}} \cdot |v_g|^{m-1} \cdot \vec{v}_g \quad (5.12)$$

α_f being the friction coefficient, K the consistency in $\text{MPa}\cdot\text{s}^{-m}$, m the coefficient of sensibility to strain rate, and finally, c Abouaf coefficient dependent on the relative density. However, in the coming tests, c is considered constant in order to simplify the validation test.

In the simulations carried out with the Lagrangian approach, expression 5.12 is considered.

5.3 Modeling of friction in the Eulerian monolithic approach

5.3.1 Introduction

In order to validate the method developed to model friction between powder and tooling, the powder die compaction test is chosen. The thermomechanical coupling is not considered in this section, temperature is considered constant during the process.

The method defined for the Eulerian approach is validated by the comparisons with the Lagrangian results where the friction condition is imposed directly on the lateral boundary of the powder sample.

The general problem is first presented describing separately the friction models for each approach. Second, results are discussed with the procedure followed to generalize the friction Eulerian model.

5.3.2 Description of the mechanical model

The powder is placed in a mould on a fixed plane while a constant velocity is imposed in the upper piston. Since the thermomechanical coupling is not considered in this section, all parameters are constant during the process. The powder follows the compressible viscoplastic law presented in the previous chapter. Identically, the problem model is based

on the momentum conservation equation where inertia and gravity effects are neglected:

$$\nabla \cdot \sigma = 0 \quad (5.13)$$

$$\sigma = s - p\mathbb{I} \quad (5.14)$$

The Norton-Hoff viscoplastic power law together with Abouaf law lead us to the expression of the stress tensor:

$$\sigma = 3K(T) \left(\sqrt{3}\dot{\varepsilon} \right)^{m-1} \left(\frac{2}{3c}\dot{\varepsilon} + \left(\frac{1}{9f} - \frac{2}{9c} \right) Tr\varepsilon\mathbb{I} \right) \quad (5.15)$$

The numerical resolution of this problem is treated in section 3.3.2 of chapter 3. The parameters of the powder used for comparison are:

$$c = 6.463 \quad f = 0.45 \quad K = 3000 \text{ MPa}\cdot\text{s}^m \quad m = 0.5 \quad (5.16)$$

5.3.3 Description of the Eulerian model

The set up of Figure 5.4 is considered. The powder is considered deformable whereas tools are considered rigid. The velocity is imposed in the mould and piston, more precisely the mould is fixed and the piston has a constant velocity $v = (0, 0, 0.5) \text{ mm}\cdot\text{s}^{-1}$. The computational domain Ω covers the whole set: tools and powder. The background mesh size is equal to 1.2 mm. Level set functions define the interfaces and an anisotropic remeshing surrounds the interfaces between the components as in Figure 5.4.

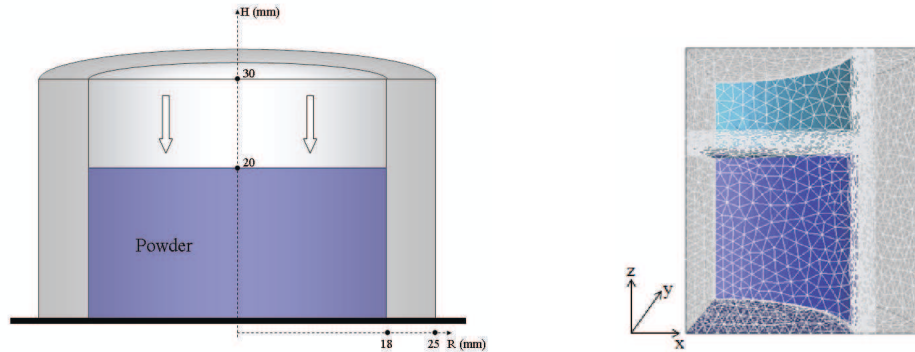


Figure 5.4: Geometry and dimensions of the set up and anisotropic meshing around the interface

Numerical approach to model friction

The approach chosen to model friction in the Eulerian approach is inspired from the boundary layer principle.

Let us suppose a thin layer of thickness e in the neighborhood of the contact surface

between the powder and the mould (Figure 5.5). This layer obeys to the same behaviour law as the powder and has a different consistency. The aim is to express the shear stress inside the layer and relate it to expression 5.7.

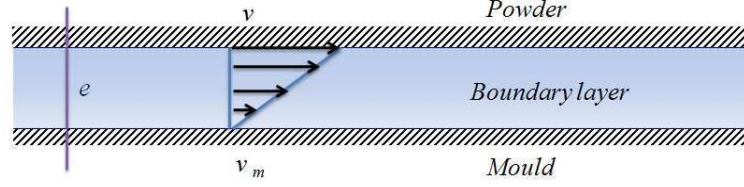


Figure 5.5: Schematic representation of the boundary layer

According to Figure 5.5, the shear rate in the boundary layer is expressed as:

$$\dot{\gamma} = \frac{|\vec{v}_g'}{e} \quad (5.17)$$

So the strain rate tensor can be written:

$$\dot{\epsilon} = \begin{pmatrix} 0 & \frac{v_g}{2e} & 0 \\ \frac{v_g}{2e} & 0 & 0 \\ 0 & 0 & 0 \end{pmatrix} \quad (5.18)$$

Using the expression of Abouaf equivalent strain rate, we write:

$$\dot{\epsilon} = \frac{1}{\rho_r} \left(\frac{2}{3c} \dot{\epsilon} : \dot{\epsilon} + \frac{1}{9f} Tr(\dot{\epsilon})^2 \right)^{\frac{1}{2}} = \frac{1}{\rho_r} \left(\frac{4}{3c} \left(\frac{v_g'}{2e} \right)^2 \right)^{\frac{1}{2}} = \frac{v_g'}{\rho_r e \sqrt{3c}} \quad (5.19)$$

And by substituting $\dot{\epsilon}$ in the behaviour law of equation 5.15, the stress tensor is expressed as :

$$\sigma = 2Kc^{-\frac{m+1}{2}} \left(\frac{v_g'}{e} \right)^{m-1} \dot{\epsilon} \quad (5.20)$$

and finally we extract the shear stress in the boundary layer:

$$\tau = 2Kc^{-\frac{m+1}{2}} \left(\frac{v_g'}{e} \right)^{m-1} \left(\frac{v_g'}{2e} \right) \quad (5.21)$$

$$= -\frac{K}{e^m} c^{-\frac{m+1}{2}} |v_g'|^{m-1} \cdot v_g' \quad (5.22)$$

whereas Norton friction law used in the Lagrangian approach is written:

$$\tau = -\alpha_f \cdot K \cdot c^{-\frac{m+1}{2}} \cdot |v_g'|^{m-1} \cdot v_g' \quad (5.23)$$

Let us denote \tilde{K} the consistency of the layer, the aim of the study is to define a relation between this consistency, the thickness of the layer and the friction coefficient using expression (5.23) and (5.22).

Hence, different thicknesses and friction coefficients are chosen. For each couple (α_f, e) , simulations are carried out to find the convenient \tilde{K} . This \tilde{K} should generate the same shear in the Eulerian model as in the Lagrangian model when applying the friction condition on the boundary of the powder, for a given α_f . For that reason, the layer is added at the level of the interface as seen in Figure 5.6. This study will allow to automatically deduce \tilde{K} from the value of the chosen thickness e and the given α_f when using the Eulerian approach.

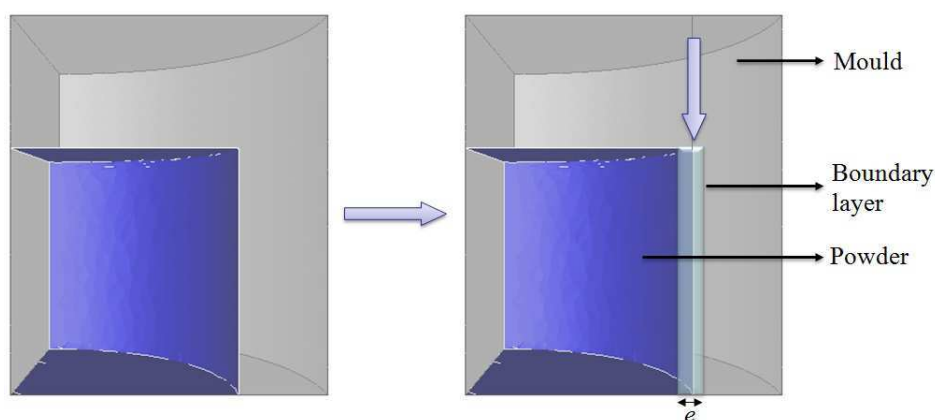


Figure 5.6: Geometry of the set up with the intermediate layer incorporated between the mould and powder

Moreover, in the Eulerian model, since a single mesh covers the whole assembly, a mixing law is used to compute the consistency on the domain Ω . The consistency of the powder K_{powder} and of the layer \tilde{K} are computed on the computational domain Ω using a mixing law defined per element:

$$K(\Omega_e) = \frac{K_{powder}|\Omega_e \cap \Omega_p| + \tilde{K}|\Omega_e \cap \Omega_{BL}|}{|\Omega_e|} \quad (5.24)$$

$|\Omega_e|$ being the volume of the element Ω_e , Ω_p the domain covered by the powder and Ω_{BL} the domain covered by the boundary layer. Consequently, the powder and the layer have their appropriate property and the element intercepted by the interface has an average consistency weighted by the volumes.

Before presenting the results of the study, the Lagrangian model is described.

5.3.4 Description of the Lagrangian model

Here, the main difference with the Eulerian approach is that the computational domain Ω covers only the powder. Tools are not modeled and the velocity field is imposed on the

boundary of the domain $\partial\Omega = \Gamma$.

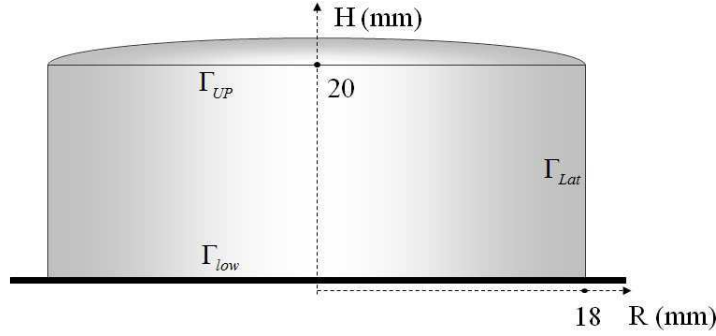


Figure 5.7: Geometry of the Lagrangian model with the dimensions of the powder cylinder

Moreover, the boundary conditions of the problem are summarized as follows:

$$v_z = -0.003 \text{ mm/s on } \Gamma_{UP} \quad (5.25)$$

$$v_z = 0 \text{ on } \Gamma_{UP} \quad (5.26)$$

$$\text{no penetration contact condition on } \Gamma_{Lat} \quad (5.27)$$

$$\text{Friction condition on } \Gamma_{Lat} \quad (5.28)$$

The friction condition is described previously in Equation 5.23. The no-penetration condition is detailed in [3], if $\alpha(x, t)$ denotes the signed distance function to the mould, the contact surface is defined as :

$$\Gamma_c(t) = \{x \in \Gamma(t), \alpha(x, t) \geq 0\} \quad (5.29)$$

And the condition respects:

$$\alpha(x, t) \leq 0 \quad \forall (x, t) \in \Gamma_c \times \mathbb{R}^+ \quad (5.30)$$

After linearization and differentiation of the function, the no-penetration condition is resumed to:

$$\frac{\alpha(x, t)}{\Delta t} + (\vec{v} - \vec{v}_m) \cdot \frac{\nabla \alpha}{\|\nabla \alpha\|}(x, t) \leq 0 \quad \forall (x, t) \in \Gamma_c \times \mathbb{R}^+ \quad (5.31)$$

Consequently, two surface integral are added to the weak form of the mechanical problem, and in the Lagrangian approach the problem to be solved is summarized as follows:

Find $(\vec{v}, p) \in (\mathcal{V}, \mathcal{P})$ such that for each instant t :

$$\left\{ \begin{array}{l} \int_{\Omega} \frac{2\bar{\mu}}{c} \dot{\varepsilon}(v) : \dot{\varepsilon}(v^*) d\Omega - \int_{\Omega} \frac{2}{3c} \bar{\mu} \nabla \cdot v \nabla \cdot v^* d\Omega - \int_{\Omega} p \nabla \cdot v^* d\Omega \\ + \int_{\Gamma_c} \alpha_f \cdot K \cdot c^{-\frac{m+1}{2}} \cdot |v_g|^{m-1} \cdot v_g \cdot v^* d\Gamma_c \\ + r \int_{\Gamma_c} \left[\frac{\alpha^t}{\Delta t} + (v - v_m) \cdot \frac{\nabla \alpha^t}{\|\nabla \alpha^t\|} \right]^+ v^* \cdot \frac{\nabla \alpha^t}{\|\nabla \alpha^t\|} d\Gamma_c = 0 \\ \int_{\Omega} \left(\frac{3f}{\bar{\mu}} p + \nabla \cdot v \right) p^* = 0 \quad \forall (v^*, p^*) \in (\mathcal{V}, \mathcal{P}) \end{array} \right. \quad (5.32)$$

where r denotes a penalty coefficient (large positive value).

5.3.5 Numerical study of the Eulerian approach

In order to define a generalized function $\tilde{K}(\alpha_f, e)$, the procedure below is followed.

First, the simulation of the powder die compaction test is carried out using the Lagrangian model for three different friction coefficients: $\alpha_{f1} = 0.7$, $\alpha_{f2} = 1.5$ and $\alpha_{f3} = 3.5$. The distribution of the vertical velocity is presented in Figure 5.8.

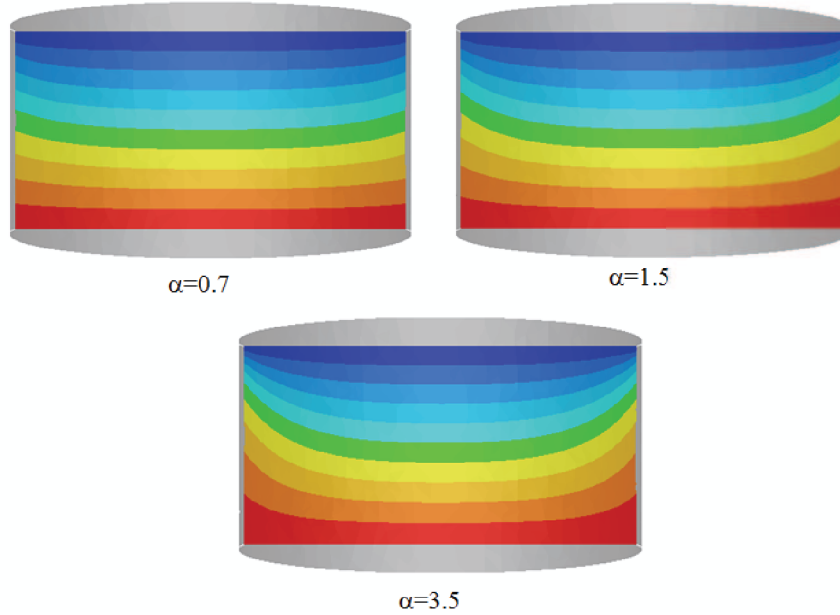


Figure 5.8: Profile of the vertical velocity in the sample computed with the Lagrangian approach imposing a friction condition for three different coefficient $\alpha_{f1} = 0.7$, $\alpha_{f2} = 1.5$ and $\alpha_{f3} = 3.5$

Second, the powder die test is simulated using the Eulerian approach. Figure 5.9 represents the mesh at the region of the interface. ε_{rem} denotes the thickness of the remeshing zone and e the thickness of the boundary layer. The added boundary layer is centered at the level of the interface and covers the same thickness $e/2$ at each side, powder and die.

Besides, the consistency takes different constant values in the boundary layer, in the powder and in the mould. Using the mixing law of equation 6.51, each element intercepted by the interface has an intermediate value of the consistencies. The background mesh size is fixed for all the test equal to 1.2 mm outside the refined region at the interface. Besides, concerning the anisotropic remeshing around the interface, the number of elements in the thickness in the orthogonal direction of the interface is also fixed to 20 anisotropic elements. For each couple (e_i, α_f) , different consistencies are tested, the aim is to find $\tilde{K}(\alpha_f)$ giving the lowest error when comparing with the Lagrangian model.

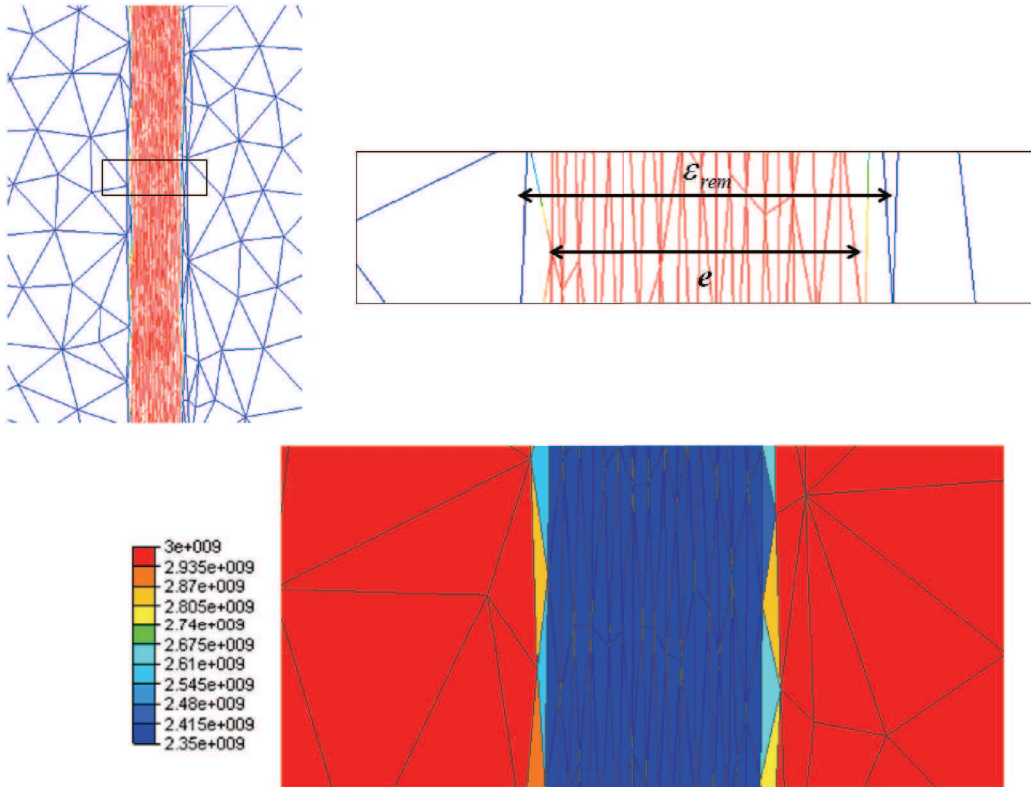


Figure 5.9: Representation of the remeshing around the interface and the boundary layer. In the bottom resulting consistency from mixing law 6.51 ($\text{Pa}\cdot\text{s}^{-\text{m}}$). The coloured anisotropic elements are intercepted by the interface

Three mesh thicknesses are tested $\epsilon_{rem} = 2.5 \text{ mm}$, $\epsilon_{rem} = 2 \text{ mm}$ and $\epsilon_{rem} = 1.5 \text{ mm}$. The thicknesses of the boundary layer corresponding to each mesh thickness are respectively $e_1 = 2.2 \text{ mm}$, $e_2 = 1.7 \text{ mm}$ and $e_3 = 1.07 \text{ mm}$. The thickness e_i is fixed according to the value of ϵ_{rem} in a way that the layer is completely situated in the remeshed zone as seen in Figure 5.9. The thickness of the layer is lower because we need to keep an anisotropic element on each side which will have the transitory mixed value of consistency.

Comparison and validation

In order to deduce the convenient consistencies, an error should be computed for each tested value. The calculation of the error is based on the vertical velocity using the Lagrangian results as reference. The vertical velocity v_z is plotted over the radial distance in the powder when fixing $y = 0$ and $z = 10$ mm (along the horizontal redline in Figure 5.10). In addition, v_z is also plotted over the vertical distance when fixing $y = 0$ and $x = 17.5$ mm (green vertical line) and then fixing $y = 0$ and $x = 9$ mm (orange vertical line). These plots can be obtained for both Lagrangian and Eulerian models as illustrated in Figure 5.10 (The reference is the same as in Figure 5.4). The contour lines represent the vertical velocity.

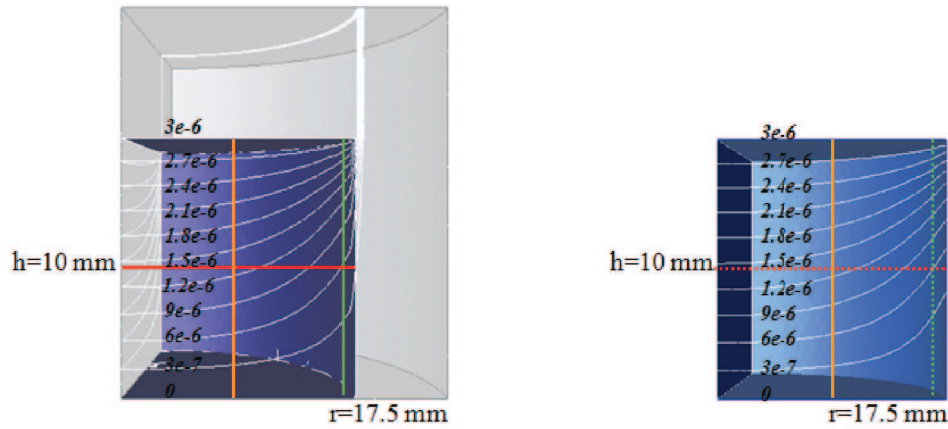


Figure 5.10: Contour lines of the vertical velocity (m/s) for the Eulerian and Lagrangian model and lines representing the plot points

Many tests were carried out using the different meshes described previously while varying the value of the consistency \tilde{K} in order to compare velocities. All the charts won't be detailed since the same concept of comparison is followed for all the tests. As an example, two charts are presented for two different plots for a fixed thickness $e = 1.07$ mm and $\alpha_f = 1.5$. In Figure 5.11, v_z is plotted over the vertical distance from the bottom to the top of the powder. The curves of the Eulerian model are compared to the Lagrangian model when using two values of the consistency. These consistencies are calculated with the following expression:

$$\tilde{K} = c_{correction} \alpha_f K e^m \quad (5.33)$$

The correction coefficient $c_{correction}$ was varied between 1.1 and 10 to test the influence on velocity distribution. The coefficients are respectively 1.94 and 2,12 for \tilde{K} equal to 857 and 935 MPa. Moreover, in Figure 5.12 v_z is plotted over the radial distance from the center of the powder towards its edge for the three simulations. As expected, closer to the interface the curves don't match. The zoom of Figure 5.13 shows the transition of

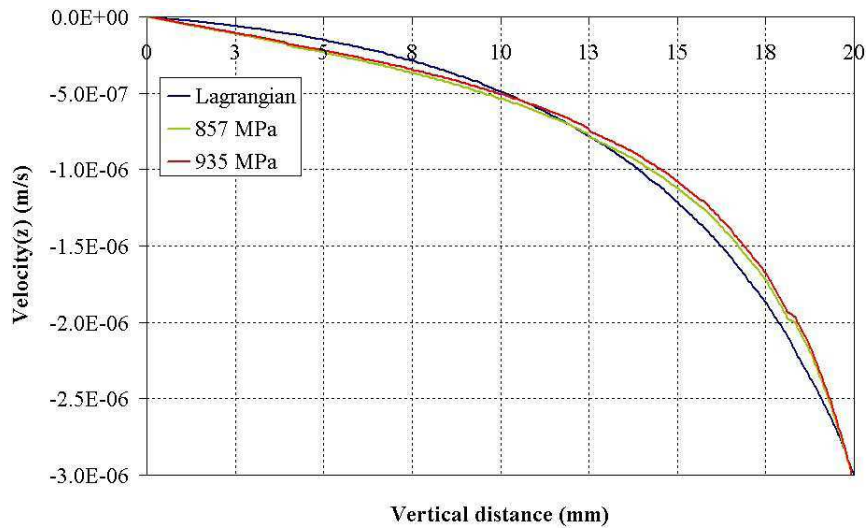


Figure 5.11: Vertical velocity plotted over the vertical distance (at $r = 17.5$ mm, green line): the results issued from two simulations using the Eulerian model for two consistencies and a fixed thickness $e = 1.07$ mm are compared with the results issued from the Lagrangian model for $\alpha_f = 1.5$

the velocity field inside the boundary layer. The thickness in this Eulerian simulation was set to 1.07 mm and the boundary layer is centered on the interface, which means that a thickness of 0.535 mm covers the powder edge. The dashed line represents the edge of the layer, when crossing the interface the slope of the velocity module decreases suddenly.

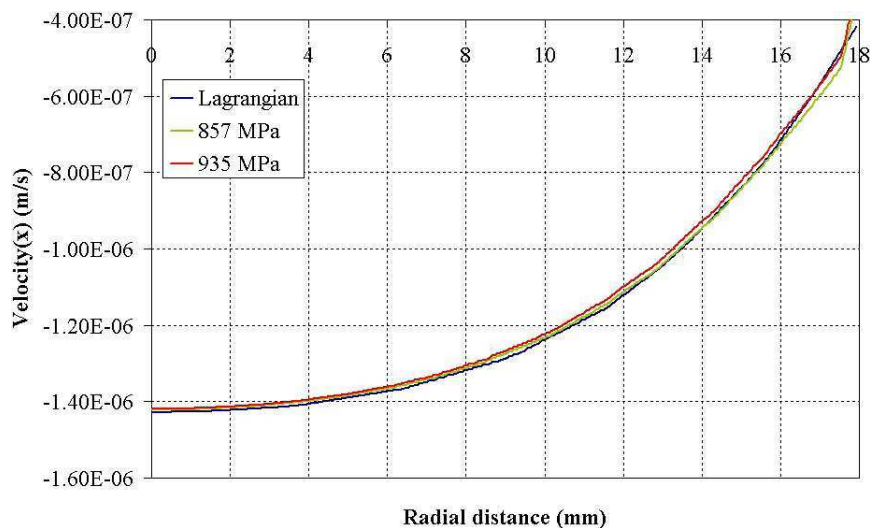


Figure 5.12: Comparison of the vertical velocity plotted over the radial distance (at $z = 10$ mm, red line) for $\alpha_f = 1.5$ in the Lagrangian model and $e = 1.07$ mm in the Eulerian model and for two consistencies

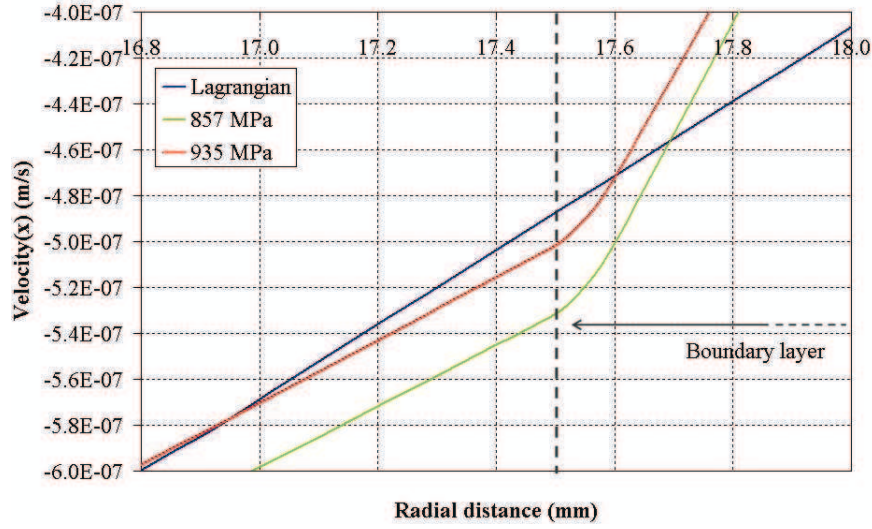


Figure 5.13: Zoom of the chart of Figure 5.12 at the region of the interface between the powder and boundary layer to the transition of the vertical velocity

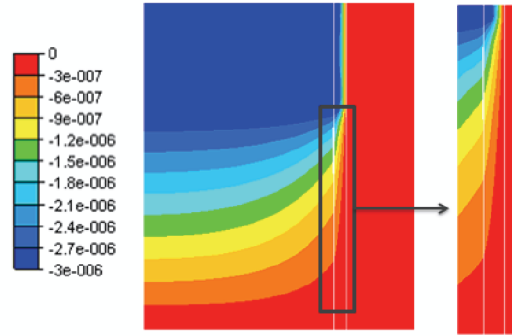


Figure 5.14: Distribution of the vertical velocity computed using the Eulerian approach and a zoom on the transition inside the layer for $\alpha_f = 1.5$

Figure 5.14 shows the vertical velocity distribution in powder, tools and boundary layer. The two vertical white lines limit the boundary layer. The global error between the Eulerian and Lagrangian velocity is calculated using the data points of the two vertical plots ($r = 10$ mm and $r = 17.5$ mm) and one radial plot ($z = 10$ mm):

$$Err = 100 \times \frac{\sum_i (v_{z\,Eul}(x_i) - v_{z\,Lag}(x_i))^2}{\sum_i v_{z\,Lag}^2(x_i)} + \frac{\sum_i (v_{z\,Eul}(z_i) - v_{z\,Lag}(z_i))^2}{\sum_i v_{z\,Lag}^2(z_i)} \quad (5.34)$$

300 points are distributed along the radial distance and along the vertical distance. x_i denotes the abscissa of the points of the radial plot and z_i the ordinate of the points of

vertical plot. The part in the boundary layer is not considered for the calculation of the error.

Using this expression, it is possible to draw for each couple (α_f, e) the variation of the error versus the values tested for \tilde{K} , for example for $(\alpha_f, e) = (0.7, 2.2)$ the variation is presented in Figure 5.15.

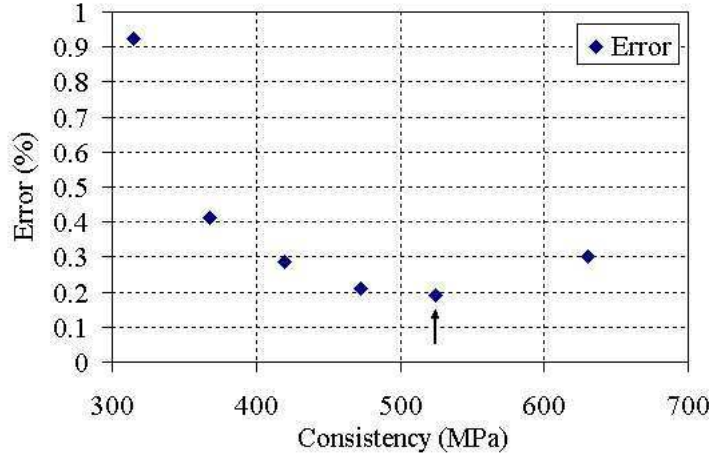


Figure 5.15: Calculated error using expression 5.34 for $\alpha_f = 0.7$ and $e = 2.2$ mm testing different consistencies \tilde{K} in the boundary layer

The arrow points out the lowest error that is reached for $\tilde{K} = 525$ MPa. And so on, the simulations are carried out for (α_{fi}, e_j) until \tilde{K} gives a minimum error. More precisely, for each α_f , different thickness e are chosen and then for each couple different \tilde{K} are tested. As a result, the chart of Figure 5.16 can be drawn. It summarizes the \tilde{K} chosen for each given couple (α_{fi}, e_j) .

In fact, as shown in the figure, for low friction coefficients, the thickness does not affect significantly the values of the boundary layer consistency. For $\alpha_f = 0.7$ the values of \tilde{K} converge for the different thicknesses whereas a gap of 2300 MPa is observed between $\tilde{K}(e = 2.2)$ and $\tilde{K}(e = 1.07)$ for $\alpha_f = 3.5$. However, the evolution of the boundary layer consistency varies linearly for each thickness but the slopes are different. The slope increases with the thickness.

In addition, the chart of Figure 5.16 shows a relation between the three parameters: \tilde{K} , e and α_f . For that reason, different expressions are tested in order to express \tilde{K} as a function f of e , α_f and the powder consistency K . That way, it would be possible to use the method of the boundary layer later on for other problems and processes. Among others, the following functions were tested:

$$f_1 = b \cdot K \cdot \alpha_f^a \cdot \text{Exp}(e) \quad (5.35)$$

$$f_2 = \alpha_f^a \cdot e^b \cdot K \quad (5.36)$$

$$f_3 = c \cdot \alpha_f^a \cdot e^b \cdot K \quad (5.37)$$

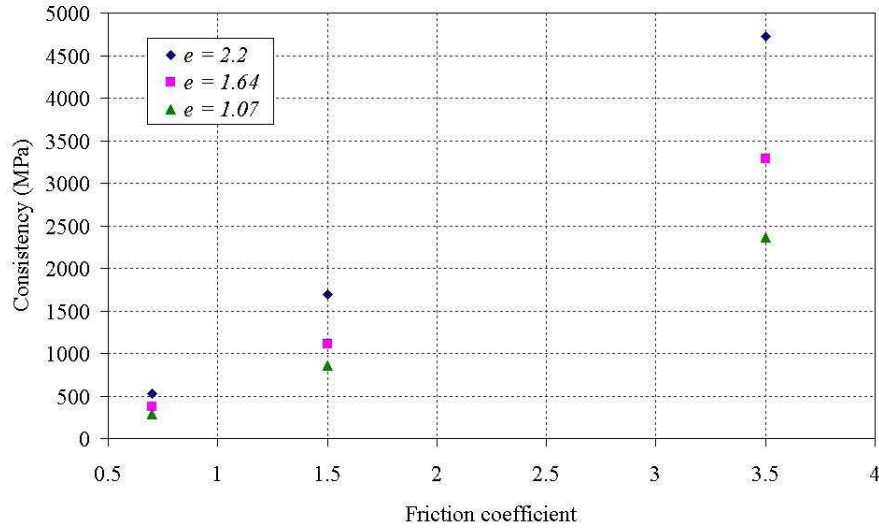


Figure 5.16: Variation of the selected \tilde{K} versus the different friction coefficient for the three fixed thicknesses (here given in mm)

In order to identify coefficients a , b and c , inverse analysis is applied. ” $f_{minsearch}$ ” function of Matlab is used. It determines the minimum using the Nelder-Mead simplex search algorithm, which is a derivative-free search technique [13]. The inverse algorithm is composed of:

- * The data of the chart of Figure 5.16 which are used as an input for inverse analysis and they are denoted \tilde{K}_{cal} .
- * The consistencies calculated using one of the functions f_1 or f_2 or f_3 (depending on which function we are optimizing) denoted \tilde{K}_{opt} .
- * The cost function which is defined as:

$$\Phi(x) = \frac{\sum_i \left(\tilde{K}_{opt}^i(x) - \tilde{K}_{cal}^i \right)^2}{\sum_i \tilde{K}_{cal}^{i2}}. \quad (5.38)$$

x being the vector of the variables that need to be identified (a , b and c). Using the algorithm of Figure 5.17, the aim is to minimize the cost function and find the parameters giving the minimum error for \tilde{K}_{opt} .

In fact, for each function f_i the inverse analysis algorithm is carried out multiple times for different starting data. The vector $x = (a, b)$ (or $x = (a, b, c)$ for f_3) is set initially at different values. Actually, after optimization we notice that the results obtained differ depending on the initial vector x , and this because a local algorithm is used.

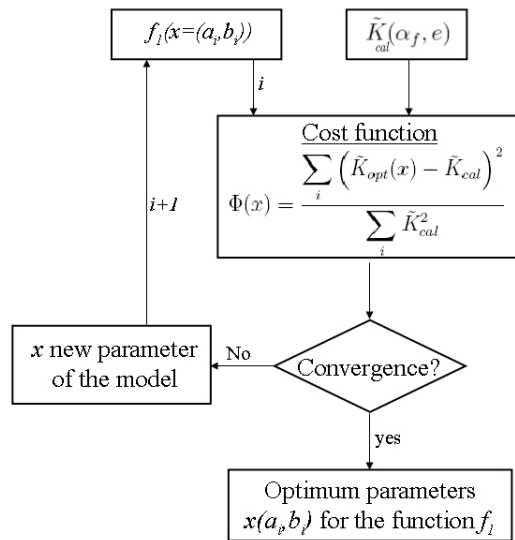


Figure 5.17: The inverse algorithm used for the identification of the parameters of the functions f_1 or f_2 or f_3 , once identified the function giving the lowest error is chosen later on for ulterior works

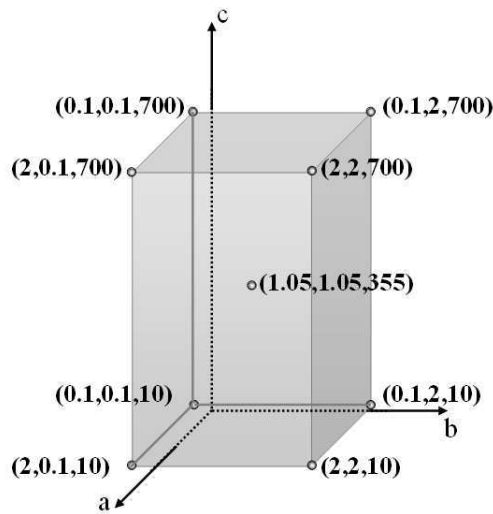


Figure 5.18: The interval of initial data of $x = (a, b, c)$ for minimizing the cost function of f_3

Hence, an interval is defined as seen in Figure 5.18 for the function f_3 . The coordinates of the cube are chosen for the initial data. The results of the optimization are gathered in the table of Figure 5.19.

The cost function varies from 0.002 to 0.473, this shows that testing different starting points is necessary in order to choose the efficient function. The green lines of the table refer to the lowest cost function that can be found for the function f_3 equal to 0.002. As

Initial data (a,b,c)	Error	a	b	c
(0.1,0.1,10)	0.0080	1.243	0.691	21.021
(2,2,700)	0.0050	1.231	1.243	700
(2,0.1,10)	0.0128	1.303	0.6	11.03
(2,2,10)	0.0020	1.257	1	146.98
(2,0.1,700)	0.4730	4.17	1.97	784.7
(0.1,0.1,700)	0.3393	6.797	2.365	700.0
(0.1,2,10)	0.0020	1.255	1.004	151.85
(0.1,2,700)	0.0051	1.231	1.243	700
(1.05,1.05,355)	0.0020	1.2548	1	152.41

Figure 5.19: Different starting points, cost functions and identified parameters of the function f_3

seen, it is reached each time for $x = (1.255, 1, 152)$.

Function \tilde{K}	Minimum error
$\tilde{K} = f_1 = 0.234K\alpha_f^{1.27}Exp(e)$	0.073
$\tilde{K} = f_2 = \alpha_f^{1.39}e^{0.245}K$	0.043
$\tilde{K} = f_3 = 152\alpha_f^{1.255}eK$	0.002

Table 5.1: Identified functions and their minimum errors optimized by inverse analysis

Table 5.1 summarizes the results of the inverse analysis for the different functions.

In conclusion, the different tests showed that f_3 gave the lowest error. Hence, the generalization of \tilde{K} is expressed as follows:

$$\tilde{K} = 152\alpha_f^{1.255}eK \quad (5.39)$$

Validation test

Three simulations are carried out using the Eulerian model in which expression 6.50 is applied considering three friction coefficients. In order to validate the method, results are compared with the Lagrangian results described previously. Table 5.2 presents the coefficients, the consistency of the boundary layer and the error when comparing with Lagrangian results.

The error found in the validation tests for $e = 2.2$, when \tilde{K} is computed with refKtilde-General, have the same order as the one chosen previously in Figure 5.15 (= 0.19 for 525 MPa). Figure 5.20 presents the vertical velocity plotted over the radial distance computed with the three simulations when varying the friction coefficient according to Table 5.2. The dashed blue line represents the limit powder/boundary layer. As expected, the value

α_f	\tilde{K} (MPa.s ^{-m})	Error (%)
0.7	641	0.11
1.5	1669	0.206
3.5	4831	0.24

Table 5.2: Friction coefficient, consistency of the boundary layer calculated using expression 6.50 and the error resulting from the Eulerian model when $e = 2.2$ mm

of the velocity at the interface between the powder and the boundary layer is higher when the friction coefficient is higher. As seen the slope of the curve inside the layer differs which is related to the value of the consistency \tilde{K} . In fact, the consistency of the powder is equal to 3000 MPa, the ratio \tilde{K}/K is relatively low when $\alpha_f = 0.7$, for that reason, an important change of the slope is observed when crossing the interface.

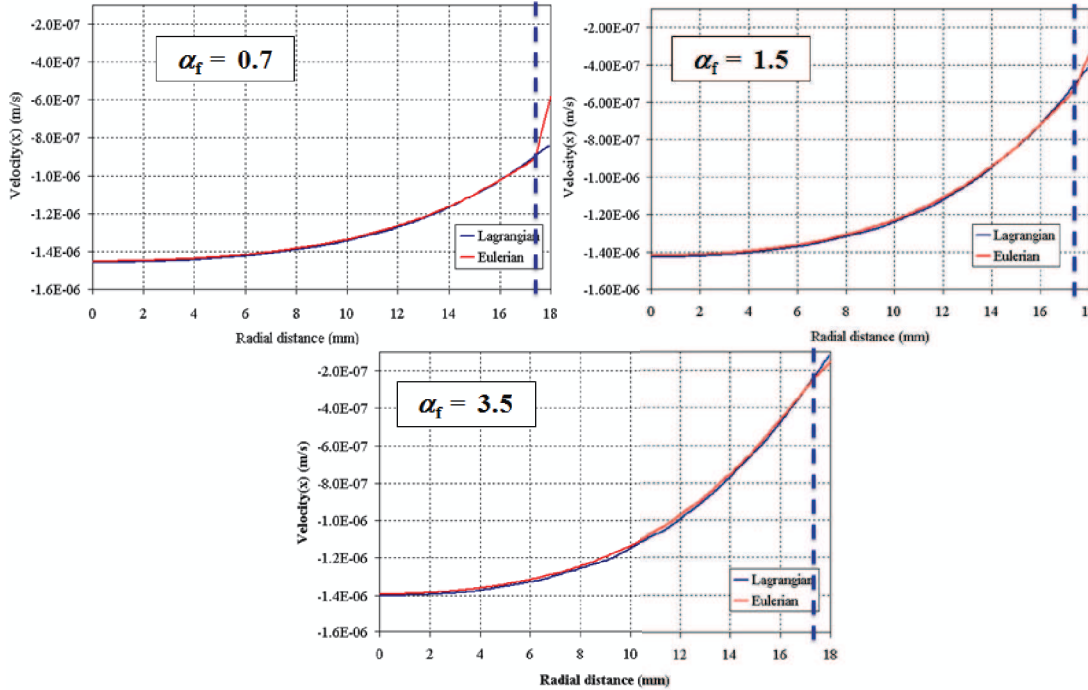


Figure 5.20: Different starting points, cost functions and identified parameters of the function f_3

5.3.6 Possible developments in the Eulerian model

The different tests presented in the previous section were studied for the same number of elements ($= 20$) in the thickness of the boundary layer. In order to check the validity of expression 6.50 for different number of elements, another test is carried out. The thickness

considered is $e = 1.07$ mm and the number of elements in the thickness is equal to 10 whereas previously was fixed to 20. The error of this Eulerian simulation is calculated by the use of the Lagrangian model (same procedure as previously).

α_f	\tilde{K} (MPa.s ^{-m})	Error using 10 elements (%)	Error using 20 elements (%)
0.7	312	0.21	0.09
1.5	812	0.23	0.20
3.5	2350	0.22	0.18

Table 5.3: Friction coefficient, consistency of the boundary layer calculated using expression 6.50 and the error resulting from the Eulerian model using 10 and 20 elements

As seen in Table 5.3, even though the error is smaller when using 20 elements, the difference is not high between both simulations. In addition, errors found when changing the number of elements to 10 are in the same range of order as in the previous tests.

Another factor that might influence the results is the position of the boundary layer relatively to the interface between the powder and the mould. The boundary layer might be moved into the mould in a way to cover less the powder. Moreover, many other factors could be studied, like the powder consistency, the mixing laws ($P0$ or $P1$ type) or the mesh size.

Furthermore, during spark plasma sintering, the temperature field is computed. Consequently, the temperature is heterogeneous on the domain and since consistency is temperature dependent, expression 6.50 leads to a heterogeneous \tilde{K} . Inverse analysis, in Chapter 5, allows optimizing the properties of the boundary layer.

5.4 Conclusion

This chapter presents the numerical model of friction used in the Eulerian approach. This model is based on the boundary layer principle. This technique consists in adding a third body (a layer) between the mould and powder. A consistency is associated to this boundary layer generating the same friction effects as in a Lagrangian approach where a boundary condition is imposed on the edge Γ of the powder. The aim in this chapter is to define a relation between the thickness of the layer, the friction coefficient and the layer consistency. For that reason, tests are carried out varying the thickness and the friction coefficient. For each couple (e, α_f) , different consistencies are studied. Then, results corresponding to each consistency in the Eulerian model are compared with the results of the Lagrangian model computed with the same friction coefficient. An error is deduced consequently to the comparisons. The consistency giving the lowest error for the

couple (e, α_f) is then picked. These values are used in an inverse analysis algorithm in order to extract an expression of the consistency of the layer \tilde{K} function of e and α_f . This study was achieved when simplifying some conditions such as the heterogeneities of temperature and Abouaf functions. It would be interesting to test this method with temperature dependencies. In addition, the expression found for \tilde{K} could be extended by including the dependency to the number of element inside the boundary layer and position to the layer relatively to the powder (centered or shifted to the mould).

Bibliography

- [1] J.U. Brackbill, D.B. Kothe, and C. Zemach. A continuum method for modeling surface tension. *Journal of computational physics*, 100:335–354, 1992.
- [2] S. Brinckmann, G. Gao, and T. Siegmund. A combined experimental-numerical study of the compaction behavior of nacl. *Powder Technology*, 194:197–206, 2009.
- [3] J. Bruchon, H. Digonnet, and T. Coupez. Using a signed distance function for the simulation of metal forming processes : Formulation of the contact condition and mesh adaptation. from a lagrangian approach to an eulerian approach. *International Journal for Numerical Method in Engineering*, 78(2):980–1008, 2009.
- [4] J. R. Cho and H. S. Jeong. Application of upper bound method to the powder-forging of cup-shaped axisymmetric preforms for estimating punch load. *International Journal for Numerical Methods in Engineering*, 51(4):429–448, 2001.
- [5] J.C. Cunningham, I.C. Sinka, and A. Zavaliangos. Analysis of tablet compaction. i. characterization of mechanical behavior of powder and powder/tooling friction. *Journal of Pharmaceutical Sciences*, 93(8):2022–2039, 2004.
- [6] P. Dorémus and E. Pavier. Friction behaviour of an iron powder investigated with two different apparatus. In *PM World congress*, pages 114–119, 1998.
- [7] A. Frachon. *Modélisation et Simulation Numérique de la Compression en Matrice de Poudres Métalliques*. PhD thesis, INPG, 2002.
- [8] D-M-M. Guyoncourt, J-H. Tweed, A. Gough, J. Dawson, and L. Patter. Constitutive data and friction measurements of powders using instrumented die. *Powder Metallurgy*, 44:25–32, 2001.
- [9] Ashoka G. K. Jinka, Michel Bellet, and Lionel Fourment. A new three-dimensional finite element model for the simulation of powder forging processes: application to hot forming of p/m connecting rod. *International Journal for Numerical Methods in Engineering*, 40(21):3955–3978, 1997.

-
- [10] Sh. Keshavarz, A.R. Khoei, and A.R. Khaloo. Contact friction simulation in powder compaction process based on the penalty approach. *Materials and Design*, 29(6):1199–1211, 2008.
- [11] A.R. Khoei, S.O.R. Biabanaki, A.R. Vafa, and Sh. Keshavarz I. Yadegaran. A new computational algorithm for contact friction modeling of large plastic deformation in powder compaction processes. *International Journal of Solids and Structures*, 46(2):287–310, 2009.
- [12] J. Kovacik, S. Emmer, J. Bielek, and L. Kelesi. Effect of composition on friction coefficient of cu-graphite composites. *WEAR*, 265:417–421, 2008.
- [13] J.C. Lagarias, J. A. Reeds, M. H. Wright, and P.E. Wright. Convergence properties of the Nelder-Mead Simplex method in low dimensions. *SIAM Journal of Optimization*, 9:112–147, 1998.
- [14] E. Pavier and P. Dorémus. Friction behaviour of an iron powder investigated with two different apparatus. In *International Workshop on Modelling of Metal Powder Forming Processes*, pages 335–344, July 1997.
- [15] M. Rappaz, M. Bellet, and M. Deville. *Modélisation numérique en science et génie des matériaux, Traité des Matériaux*, volume 10. Presses Polytechniques et Universitaires Romandes, 1998.
- [16] I.C. Sinka, J.C. Cunningham, and A. Zavaliangos. Analysis of tablet compaction. ii. finite element analysis of density distributions in convex tablets. *Journal of Pharmaceutical Sciences*, 93(8):2040–2053, 2004.
- [17] Y-M. Tien, P-L. Wu, W-H. Huang, M-F. Kuo, and C-A. Chu. Wall friction measurement and compaction characteristics of bentonite powders. *Powder Technology*, 173:140–151, 2007.
- [18] D-V. Tran, R-W. Lewis, D-T. Gethin, and A-K. Ariffin. Numerical modeling of powder compaction processes: displacement based finite element method. *Powder Metallurgy*, 36:257–266, 1993.
- [19] B. Wilkman, H. Haggblad, and M. Oldenburg. Modelling of powder-wall friction for simulation of iron powder pressing. In *International Workshop on Modelling of Metal Powder Forming Processes*, pages 149–157, July 1997.

Chapter 6

Inverse analysis and parameters identification

Contents

6.1	Introduction	147
6.2	Identification of the behavior law parameters: Required experiments	147
6.2.1	Identification of consistency and strain rate sensitivity on dense material	148
6.2.2	Identification of Abouaf functions	149
6.2.3	Limitation of the Paterson machine	156
6.3	Identification of Abouaf functions using SPS	165
6.3.1	SPS experiments and measurements	166
6.3.2	Calibration of c and f using Matlab	175
6.3.3	Calibration of the friction coefficient	181
6.3.4	Conclusion	188
6.4	Numerical simulation of the spark plasma sintering test	192
6.4.1	Description of the models	192
6.4.2	Results	196
6.5	Conclusion	202

Résumé

Dans la première partie de ce chapitre, on s'intéresse aux expériences nécessaires pour identifier les paramètres de la loi de comportement. Dans la deuxième partie on présente la simulation d'un cycle complet de frittage flash avec les paramètres identifiés et on compare les résultats avec les expériences. Des essais de fluage ont été utilisés pour identifier les paramètres de l'état dense: la consistance et le coefficient de sensibilité à la vitesse de déformation. Pour identifier f , il est nécessaire de réaliser des essais interrompus CIC à différentes températures et pressions. Ces essais permettent de déterminer l'expression de f en interpolant la courbe d'évolution de f en fonction de la densité relative. En ce qui concerne l'identification de la fonction c , des tests interrompus de compression uniaxiale avec pression latérale constante doivent être utilisés. Ces essais sont effectués pour différents cycles comme pour la fonction f . Dans le projet IRIS, la machine Paterson a été initialement choisie pour réaliser les caractérisations sur des poudres et déterminer f et c . Cependant, des problèmes sont rencontrés lors des essais préliminaires. Le four n'a pas résisté aux hautes températures souhaitées. Par conséquent, les expériences sont abandonnées. Dans la deuxième section de ce chapitre, on a présenté la procédure suivie pour identifier les fonctions d'Abouaf à l'aide du procédé SPS. Cette technique d'identification présente certains inconvénients. En fait, lors d'un cycle SPS la température n'est pas homogène dans l'échantillon et le frottement influence l'homogénéité de la densification ce qui rend l'identification complexe. Au CEMES, le déplacement et la température sont mesurés au cours des expériences. De plus, la distribution de la porosité est mesurée à l'aide du MEB. Dans un premier temps, Matlab est utilisé pour calibrer les fonctions d'Abouaf à l'aide de la solution analytique du problème mécanique, tout en négligeant les hétérogénéités de température et les effets de frottement. Une fois les fonctions calibrées, des simulations sont effectuées pour déterminer la valeur du coefficient de frottement. La dernière partie de ce chapitre traite la simulation d'un cycle complet SPS. Dans ces simulations, toutes les conditions expérimentales sont modélisées. La température et la pression sont régulées conformément à une consigne utilisant une boucle PID. Le couplage électrique thermique mécanique est résolu. Les résultats de la simulations sont comparés avec les expériences. Les comparaisons sont en très bon accord. On a constaté que la vitesse a la particularité de traverser une valeur maximale pendant la phase de densification. L'évolution de la densité relative a également été comparée et montre un bon accord. Certaines améliorations du modèle peuvent être envisagées. Pour améliorer les performances, il serait intéressant d'imposer directement la charge (ou contrainte) au bord de la poudre. Des développements et une étude poussée sont nécessaires, puisque on utilise l'approche monolithique eulérienne où l'interface de la poudre est définie par la fonction level set.

6.1 Introduction

The identification of Abouaf functions of the compressible law presented in Chapter 4 necessitates different mechanical tests. First, the experiments needed to determine the dense behavior and second, the expression of coefficients f and c are presented based on a bibliography review. In the the frame work of the Iris project, the Paterson machine had been initially selected to carry out the identification of f and c . This machine is described as well as the preliminary experiments that were tested. Problems that occur during the tests are discussed and the reason why they were abandoned. Due to the limitation of this machine, we had recourse to the SPS process directly. Identification has been achieved using an SPS machine, even though inconveniences occur when using the process such as heterogeneities of temperature and porosity or influence of friction, the effect of which is difficult to decouple from the bulk behaviour. We will describe our identification strategy which consists of two steps. First a calibration of the constitutive parameters is achieved using Matlab. These parameters are then used to calibrate a friction coefficient. A complete SPS cycle is finally simulated with the calibrated properties and results are compared with experiments.

6.2 Identification of the behavior law parameters: Required experiments

As presented in Chapter 4, a viscoplastic law is chosen to model the powder densification modified according to Abouaf law to take into account the evolution of the porosity. The viscoplastic behavior is based on a Norton-Hoff power law. Two functions are added depending on the relative density ρ_r : f and c . The deviatoric stress tensor is expressed as follows:

$$s = \frac{2K(T)}{c(\rho_r)} \left(\sqrt{3}\dot{\varepsilon} \right)^{m(T)-1} \dot{e} \quad (6.1)$$

where the equivalent strain rate is given by the Green's formula:

$$\dot{\varepsilon} = \left(\frac{2}{3c(\rho_r)} \dot{\varepsilon} : \dot{\varepsilon} + \left(\frac{1}{9f(\rho_r)} - \frac{2}{9c(\rho_r)} \right) (Tr(\dot{\varepsilon}))^2 \right)^{\frac{1}{2}} \quad (6.2)$$

In these two expressions, $\dot{\varepsilon}$ denotes the strain rate tensor and \dot{e} its deviatoric part $\dot{e} = \dot{\varepsilon} - \frac{1}{3}Tr(\dot{\varepsilon})\mathbb{I}$.

Four parameters need to be identified in this viscoplastic behavior law. The consistency K and the coefficient of sensibility to the strain rate m of Equation 6.1 are related to the dense state of the material and are supposed to depend on the temperature only. Functions c and f describe the porous state of the material, they are specific to each material and are supposed to be only dependent on the relative density of the material.

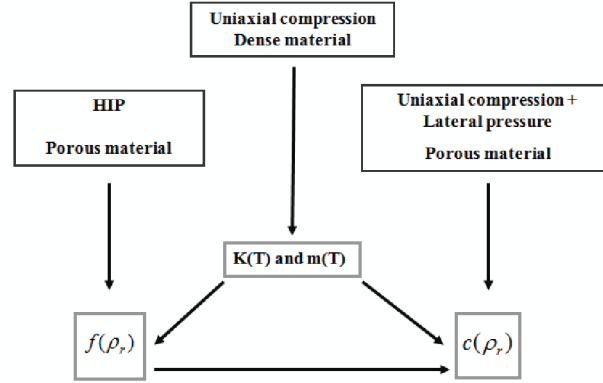


Figure 6.1: Required experiments in order to identify the four functions of the Abouaf model for compressible viscoplasticity

The scheme of Figure 6.1 summarizes the experimental procedure needed to identify the four functions K , m , c and f . During the SPS cycles applied on *TiAl*, the strain rate varies between 10^{-4} and 10^{-3} s^{-1} and the temperature during the sintering phase increases approximately from 750°C to 1250°C . The dense state functions K and m need to be identified first by classical creep tests. Knowing K and m , the Abouaf coefficients c and f can be determined. f can be identified by hot isostatic pressing of the powder material since it is related to the volumetric change of the powder. c can be identified in a next step, once the expression of f is determined. The test needed to determine c should include some shear. It can consist of a simple compression test or a "triaxial" test where an axial pressure and a lateral pressure are applied concurrently.

6.2.1 Identification of consistency and strain rate sensitivity on dense material

In order to use the viscoplastic power law of Norton-Hoff, the parameters K and m of the dense state need to be identified. These two parameters are dependent on temperature. Classical creep tests for plastic deformation at high temperature, such as compression tests for instance are needed to obtain the variation of K and m with temperature. Simple hot compression test could be applied on a dense sample. In practice, a creep test consists in applying a constant load on the sample. The deformation is measured as a function of the applied load and temperature. Having $\bar{\sigma}$ and $\dot{\epsilon}$, K and m define the equation of the lines plotted in the logarithmic scale as seen in Figure 6.2 :

$$\bar{\sigma} = \underbrace{K(T)\sqrt{3}^{m(T)+1}}_{k(T)} \dot{\epsilon}^{m(T)} \quad (6.3)$$

$$\log \bar{\sigma} = \log(k(T)) + m(T) \log(\dot{\epsilon}) \quad (6.4)$$

A number of tests should be repeated, varying each time the couple (T, σ) . For a given temperature, the stress is plotted versus the strain rate in a logarithmic scale as presented in the example graphic of Figure 6.2. The coefficient m is equal to the slope of the line plotted using the logarithmic scale and k the y-intercept. Hence, k and m are identified independently for each temperature. In the Iris project, the composition of the alloy

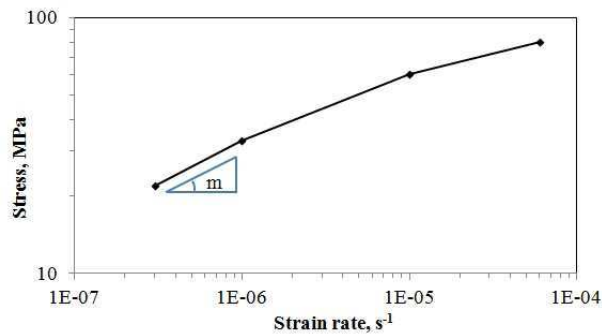


Figure 6.2: Example of the curve of stress plotted over the strain rate for a given temperature

that should be identified is $Ti - 48Al - 2Cr - 2Nb(\% \text{ at})$. The samples elaboration and the creep experiments were achieved by the french aerospace laboratory ONERA. The dense samples were elaborated by compacting the powder at $1200^{\circ}C$ and 140 MPa for 4h. The tests were carried out on a constant load creep testing machine under air. The deformation of the sample was recorded during the tests. The creep conditions were defined for three temperatures ($850^{\circ}C$, $950^{\circ}C$ and $1050^{\circ}C$) and three stress levels (50 MPa, 80 MPa and 150 MPa). Results are confidential and won't be presented in this thesis. The dense law found is comparable with the one found in the work of Lin *et al.* [5] and Nieh *et al.* [7] presented in Figure 6.3. As seen in this Figure, the Norton-Hoff type law is admissible in the domain of stress, temperature and strain rate that is adapted to SPS (typically: 100 MPa, $800^{\circ}C$, $1000^{\circ}C$, and $10^{-4} s^{-1}$). At $1000^{\circ}C$, the consistency value is in the order of $3000 \text{ MPa}\cdot\text{s}^{-m}$ and the strain rate sensitivity m is in the order of 0.45.

6.2.2 Identification of Abouaf functions

In order to identify functions c and f , mechanical tests should be carried out on the porous material. The aim is to choose experiments from which it is possible to express analytically the different fields such as strain or stress relating them to the functions. Hence, the experimental measurements with the analytic expressions allow the definition of the variation of c and f with the relative density. A similar procedure is followed in the work of Nicolle [6] for boron. In his work, hot isostatic compaction and simple uniaxial compaction were used to identify respectively f and c . In this work, hot isostatic pressing

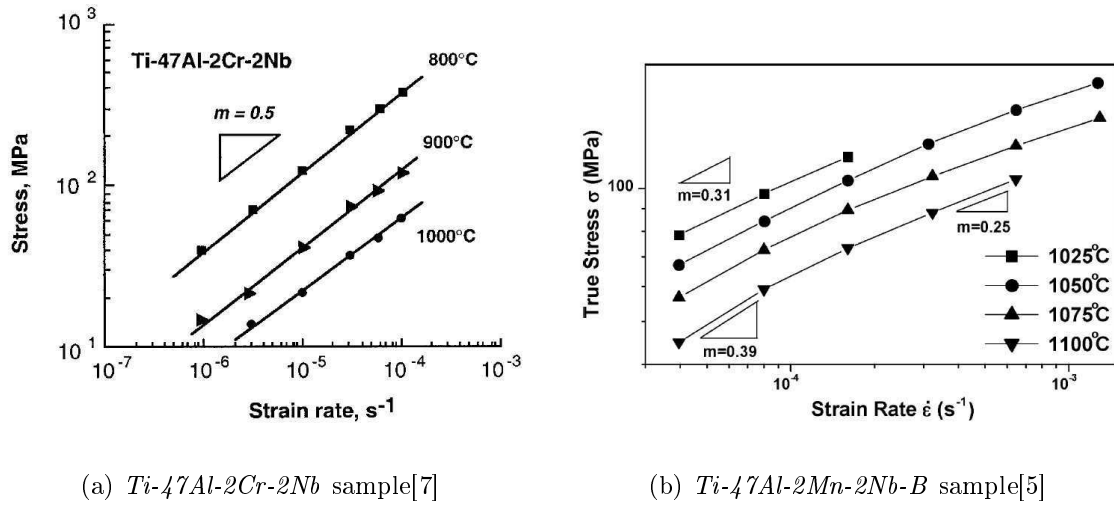


Figure 6.3: Stress plotted over the strain rate for different temperatures. Results taken from literature

is used to identify the function f . To identify c , the test consists in applying a uniaxial compression simultaneously with an applied lateral pressure. The two experiments should be carried out at high temperature to be in the same conditions as in SPS. The cycles of temperature and pressure follow the chart of Figure 6.4. The intermetallic sample is heated first. The load is applied when the temperature is equal to 750°C . When pressure and temperature stabilize, experiments are interrupted to measure the relative density in order to identify Abouaf functions.

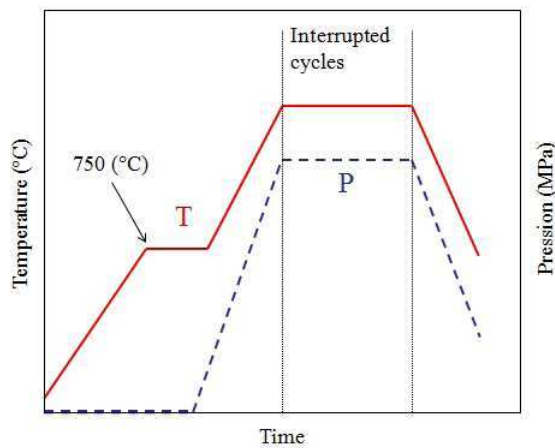


Figure 6.4: Pressure and temperature profiles applied in the identification experiments

6.2.2.1 Hot isostatic pressing: identification of f

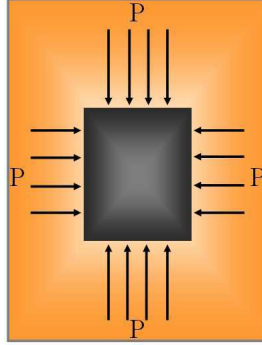


Figure 6.5: Hot isostatic pressing

During hot isostatic pressing (HIP), an isotropic pressure is applied on the hot sample as presented in Figure 6.5. The stress tensor is expressed as follows:

$$\sigma = \begin{pmatrix} -P & 0 & 0 \\ 0 & -P & 0 \\ 0 & 0 & -P \end{pmatrix} \quad (6.5)$$

Hence, the deviatoric part of the stress tensor is equal to zero:

$$s = \sigma + p\mathbb{I} = \sigma - \frac{1}{3}\text{Tr}(\sigma)\mathbb{I} \quad (6.6)$$

The Abouaf effective stress is reduced as follows:

$$\bar{\sigma} = \sqrt{\frac{3}{2}c s : s + f(\text{Tr}\sigma)^2} = \sqrt{f(\text{Tr}\sigma)^2} = \sqrt{f} |\text{Tr}\sigma| = 3P\sqrt{f} \quad (6.7)$$

The viscoplastic strain rate tensor can be obtained as a function of the stress tensor through the derivation of a potential φ :

$$\dot{\varepsilon} = \frac{\partial \varphi}{\partial \sigma} \quad (6.8)$$

Under the assumption of isotropy and incompressibility, the potential φ should be expressed as a function of the von Mises equivalent stress only $\bar{\sigma}$. Then the plastic strain rate tensor can be obtained as:

$$\dot{\varepsilon} = \frac{\partial \varphi}{\partial \bar{\sigma}} \frac{\partial \bar{\sigma}}{\partial \sigma} \quad (6.9)$$

Knowing that $\varphi = \frac{m}{m+1}K \left(\frac{\bar{\sigma}}{K\sqrt{3}}\right)^{\frac{m+1}{m}}$ and using Equations 6.7 and 6.9, the strain rate tensor is written as follows:

$$\dot{\varepsilon} = \frac{1}{\bar{\sigma}} \frac{\partial \varphi}{\partial \bar{\sigma}} f(\text{Tr}\sigma)\mathbb{I} = \frac{\dot{\varepsilon}}{\bar{\sigma}} f(\text{Tr}\sigma)\mathbb{I} \quad (6.10)$$

Hence, one can get:

$$\nabla \cdot v = \text{Tr} \dot{\varepsilon} = \frac{\dot{\bar{\sigma}}}{\bar{\sigma}} 3f \text{Tr} \sigma = -3\sqrt{f} \dot{\bar{\varepsilon}} \quad (6.11)$$

The relative density being defined as :

$$\rho_r = \frac{V_m}{V_a} \quad (6.12)$$

with V_m the volume of the material and V_a the apparent volume of the powder, we have:

$$\frac{\dot{\rho}_r}{\rho_r} = \frac{\dot{V}_m}{V_m} - \frac{\dot{V}_a}{V_a} = -\frac{\dot{V}_a}{V_a} = -\text{Tr} \dot{\varepsilon} \quad (6.13)$$

Using these equations, an expression can be deduced for f :

$$\frac{\dot{\rho}_r}{\rho_r} = -\nabla \cdot v = 3\sqrt{f} \dot{\bar{\varepsilon}} \quad (6.14)$$

$$= 3\sqrt{f} \left(\frac{\dot{\bar{\sigma}}}{k} \right)^{\left(\frac{1}{m}\right)} \quad (6.15)$$

$$= 3\sqrt{f} \left(\frac{3\sqrt{f} P}{k} \right)^{\left(\frac{1}{m}\right)} \quad (6.16)$$

$$= \left(3\sqrt{f} \right)^{\left(\frac{m+1}{m}\right)} \left(\frac{P}{k} \right)^{\left(\frac{1}{m}\right)} \quad (6.17)$$

Finally, we have

$$f = \frac{1}{9} \left(\frac{\dot{\rho}_r}{\rho_r} \right)^{\frac{2m}{m+1}} \left(\frac{k}{P} \right)^{\frac{2}{m+1}} \quad (6.18)$$

In this expression, coefficient k and m are known as temperature dependent functions, by means of the tests performed on the dense material. Therefore, a simple strategy to identify f can be the following:

- for each couple (T, P) perform interrupted compaction at different times t_i
- measure the corresponding relative density ρ_{ri}
- deduce a smooth interpolation curve $\rho_r(t)$ - derive this curve to express f as a function of ρ_r by means of 6.18. Nicolle [6] has used this strategy to identify f for boron, as presented in the Figure 6.6 and 6.7. A criticism may be that referring to real cycle, the compaction is not carried out at constant P and T but includes a transient phase during which P and T increase. During this phase, the specimen is compacted under variable P and T . This could affect, in a certain extent, the results obtained with this strategy.

6.2.2.2 Uniaxial compression with constant lateral pressure

The Abouaf function f is necessary to identify the function c . Since c is related to the deviatoric part of the stress tensor, we need an experimental test that evidences the

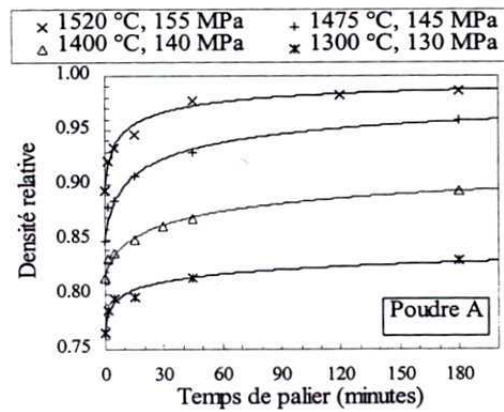


Figure 6.6: The relative density plotted over time for each couple (T, P) . Measurements issued from interrupted tests are interpolated, the functions allow computing the derivative $\dot{\rho}_r$ and the Abouaf function f [6]

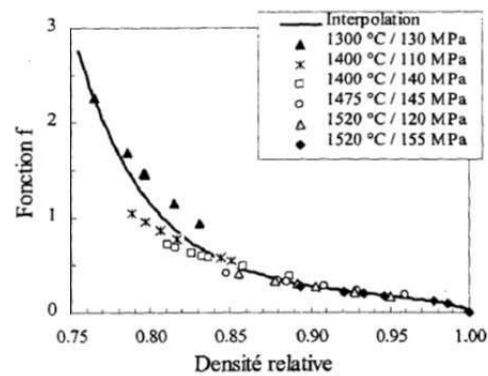


Figure 6.7: Abouaf function plotted over the relative density [6]

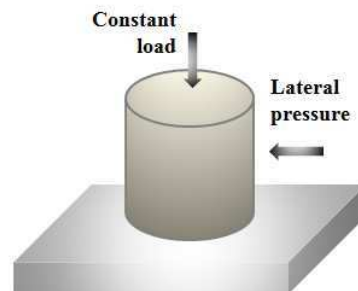


Figure 6.8: Triaxial compression test with constant lateral pressure

deviatoric behavior of the powder. In this work a triaxial compression test with a constant lateral pressure is chosen to identify c (Figure 6.8).

The stress tensor is expressed as follows, in cylindrical coordinates (r, θ, z) :

$$\sigma = \begin{pmatrix} -P & 0 & 0 \\ 0 & -P & 0 \\ 0 & 0 & -\frac{F}{S} \end{pmatrix} \quad (6.19)$$

This leads to:

$$p = -\frac{1}{3}(-2P + \sigma_{zz}) = \frac{2}{3}P - \frac{1}{3}\sigma_{zz} \quad (6.20)$$

and

$$s = \begin{pmatrix} -\frac{1}{3}P - \frac{1}{3}\sigma_{zz} & 0 & 0 \\ 0 & -\frac{1}{3}P - \frac{1}{3}\sigma_{zz} & 0 \\ 0 & 0 & \frac{2}{3}P + \frac{2}{3}\sigma_{zz} \end{pmatrix} \quad (6.21)$$

On the other hand, the strain rate tensor is written as follows:

$$\dot{\epsilon} = \frac{1}{\bar{\sigma}} \frac{\partial \varphi}{\partial \bar{\sigma}} \left(\frac{3}{2}cs + fTr(\sigma)\mathbb{I} \right) \quad (6.22)$$

$$\dot{\epsilon} = \begin{pmatrix} \dot{\epsilon}_{rr} & 0 & 0 \\ 0 & \dot{\epsilon}_{\theta\theta} & 0 \\ 0 & 0 & \dot{\epsilon}_{zz} \end{pmatrix} \quad (6.23)$$

Invoking the constitutive equation $s = \bar{\mu}\dot{\epsilon}$ and Equation 6.21, it can be noted that necessary, $\dot{\epsilon}_{rr} = \dot{\epsilon}_{\theta\theta}$ and denoting $\dot{\epsilon}_v = Tr \dot{\epsilon}$ we get:

$$\dot{\epsilon} = \begin{pmatrix} \frac{\dot{\epsilon}_v - \dot{\epsilon}_{zz}}{2} & 0 & 0 \\ 0 & \frac{\dot{\epsilon}_v - \dot{\epsilon}_{zz}}{2} & 0 \\ 0 & 0 & \dot{\epsilon}_{zz} \end{pmatrix} \quad (6.24)$$

The Green equivalent stress is then expressed as follows:

$$\bar{\sigma}^2 = \frac{3c}{2}s : s + f(Tr\sigma)^2 \quad (6.25)$$

$$= \frac{3c}{2} \left[2 \left(\frac{P + \sigma_{zz}}{3} \right)^2 + \frac{4}{9} (P + \sigma_{zz})^2 \right] + f(\sigma_{zz} - 2P)^2 \quad (6.26)$$

$$= c(P + \sigma_{zz})^2 + f(\sigma_{zz} - 2P)^2 \quad (6.27)$$

and the equivalent strain rate is written:

$$\bar{\epsilon}^2 = \frac{2}{3c}\dot{\epsilon} : \dot{\epsilon} + \left(\frac{1}{9f} - \frac{2}{9c} \right) (Tr\dot{\epsilon})^2 \quad (6.28)$$

$$= \frac{2}{3c} \left[2 \left(\frac{\dot{\epsilon}_v - \dot{\epsilon}_{zz}}{2} \right)^2 + \dot{\epsilon}_{zz}^2 \right] + \left(\frac{1}{9f} - \frac{2}{9c} \right) \dot{\epsilon}_v^2 \quad (6.29)$$

$$= \frac{1}{3c} \left[(\dot{\epsilon}_v - \dot{\epsilon}_{zz})^2 + \left(\frac{1}{9f} - \frac{2}{9c} \right) \dot{\epsilon}_v^2 + 2\dot{\epsilon}_{zz}^2 \right] \quad (6.30)$$

The power law gives the strain rate tensor which is written:

$$\dot{\epsilon} = \left(\frac{\bar{\sigma}^{1-m}}{k} \right)^{\frac{1}{m}} \left(f \text{Tr} \sigma \mathbb{I} + \frac{3}{2} c s \right) \quad (6.31)$$

and:

$$\nabla \cdot v = \text{Tr} \dot{\epsilon} = 3f (\sigma_{zz} - 2P) \left(\frac{\bar{\sigma}^{1-m}}{k} \right)^{\frac{1}{m}} = \dot{\epsilon}_v \quad (6.32)$$

On the other hand, a relation between the component of the strain rate tensor and the pressure and the vertical stress can be found using the deviator of the strain rate tensor. The deviatoric part of the strain rate tensor is written as follows:

$$\dot{\epsilon} = \begin{pmatrix} \frac{1}{6} \dot{\epsilon}_v - \frac{1}{2} \dot{\epsilon}_{zz} & 0 & 0 \\ 0 & \frac{1}{6} \dot{\epsilon}_v - \frac{1}{2} \dot{\epsilon}_{zz} & 0 \\ 0 & 0 & \dot{\epsilon}_{zz} - \frac{1}{3} \dot{\epsilon}_v \end{pmatrix} \quad (6.33)$$

and

$$\sqrt{\dot{\epsilon} : \dot{\epsilon}} = \sqrt{\frac{3}{2}} \left| \frac{\dot{\epsilon}_v}{3} - \dot{\epsilon}_{zz} \right| \quad (6.34)$$

But

$$\dot{\epsilon} = \frac{3c}{2} \left(\frac{\bar{\sigma}^{1-m}}{k} \right)^{1/m} s \quad (6.35)$$

thus

$$\sqrt{\dot{\epsilon} : \dot{\epsilon}} = \frac{3c}{2} \left(\frac{\bar{\sigma}^{1-m}}{k} \right)^{\frac{1}{m}} \sqrt{s : s} = \sqrt{\frac{3}{2}} c \left(\frac{\bar{\sigma}^{1-m}}{k} \right)^{\frac{1}{m}} |P + \sigma_{zz}| \quad (6.36)$$

Taking Equations 6.32,6.34 and 6.36 the following expression is found:

$$\frac{3f (\sigma_{zz} - 2P)}{c |P + \sigma_{zz}|} = \frac{\dot{\epsilon}_v}{\left| \frac{\dot{\epsilon}_v}{3} - \dot{\epsilon}_{zz} \right|} \quad (6.37)$$

Since the function f is identified first, c is deduced from the following expression:

$$c = \frac{3f \left| \frac{\dot{\epsilon}_v}{3} - \dot{\epsilon}_{zz} \right| (\sigma_{zz} - 2P)}{\dot{\epsilon}_v |P + \sigma_{zz}|} \quad (6.38)$$

The same procedure as in HIP is followed. The strategy to identify c can be summarized as follows:

- for each cycle (T, P) perform interrupted compaction at different time t_i
- measure the volume variation to get $\dot{\epsilon}_{zz}$ and $\dot{\epsilon}_v$, knowing P and σ_{zz}
- calculate f knowing the deduced ρ_r
- plot c versus ρ_r
- interpolate the curve into a function c dependent only on ρ_r .

6.2.3 Limitation of the Paterson machine

Once the dense model is identified, two tests are needed to identify Abouaf functions f and c . The first test consists in heating the powder and then applying an isostatic pressure in the three directions. The second test consists in heating the powder and then applying a uniaxial load simultaneously with a radial compression. For that reason, the use of the Paterson machine presented in Figure 6.9 is interesting as presented in the paragraph below. The Paterson machine is chosen in IRIS project to carry out the experiments on the powder. The machine is located at the institute PPRIME⁴ laboratory of Université de Poitiers and ENSMA (ENSMA being one of the partners in IRIS project).



Figure 6.9: The Paterson machine located at P' institute

6.2.3.1 Description of Paterson machine

The Paterson machine was conceived initially to study the deformation and rheology of rocks in the field of geology. The Paterson machine is interesting because it allows to carry out the two kinds of compression tests needed: hydrostatic compression for f , triaxial compression for c . The set up of the machine is presented in Figure 6.10. The region presented in purple is detailed in Figure 6.11. The precompacted powder is surrounded by an aluminium sheet, two alumina spacers separate the alumina pistons and the sample. The set is placed inside an iron container. The container is then placed inside the machine.

⁴UPR CNRS 3346, SP2MI, Téléport 2, Boulevard Marie et Pierre Curie, BP 30179, F86962 FUTUROSCOPE CHASSENEUIL Cedex

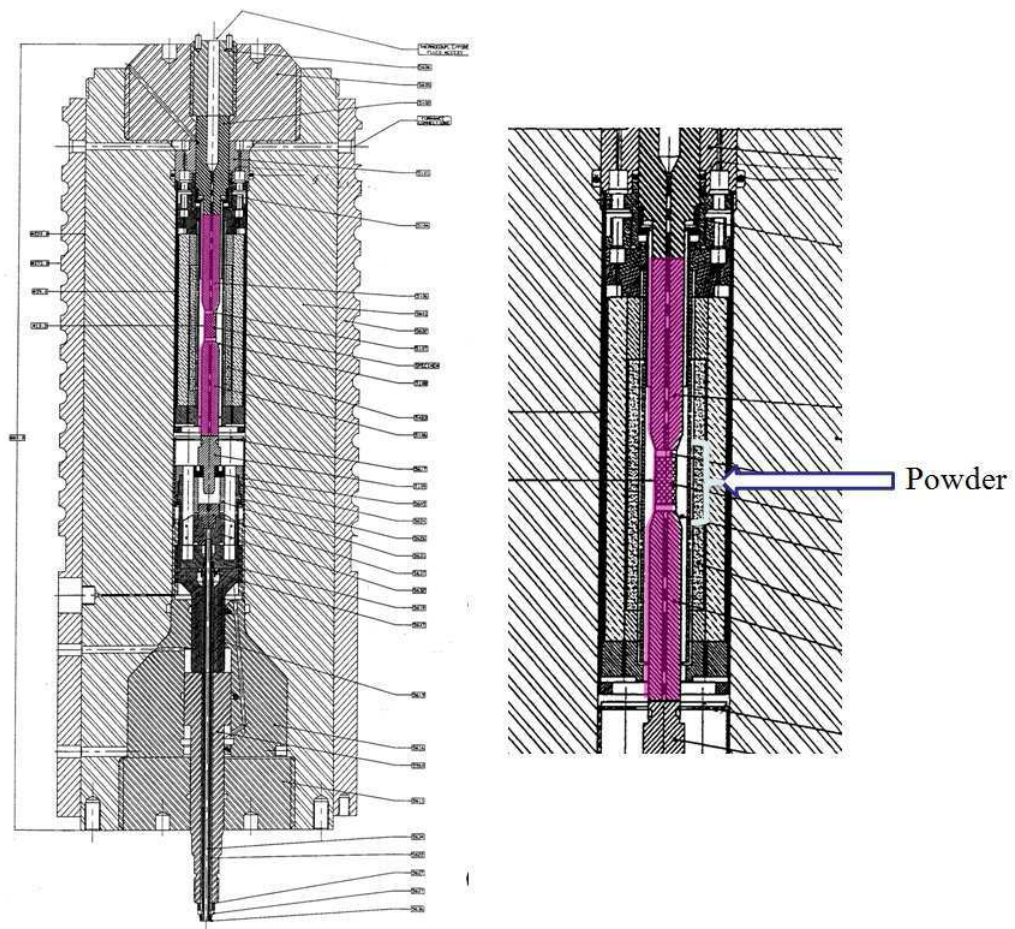


Figure 6.10: Representative scheme of the Paterson machine

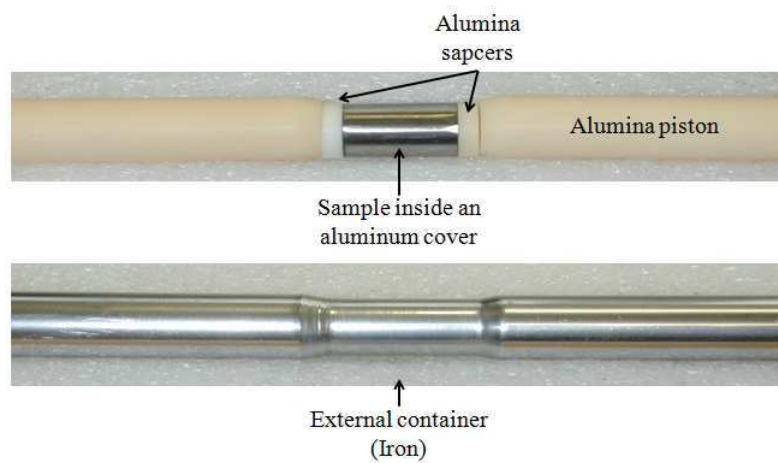


Figure 6.11: The set up inside of the machine

The Paterson machine allows a maximum pressure of 0.5 GPa . The range of temperature is between 20°C and 1000°C . The maximum axial load is 100 kN and the maximum axial displacement is 30 mm . The range of the strain rate is between 10^{-6} and 10^{-2} s^{-1} . The furnace doesn't work unless a minimum pressure of 50 MPa is reached. The diameters of the sample could be $7, 10$ or 15 mm . It is necessary to encapsulate the sample or else it is difficult to take it out of the mould. However, the powder can not be poured directly in the aluminium cover. This is why, it is precompacted into a cylinder respecting the corresponding measures of the machine with a relative density equal to 68% .

6.2.3.2 Suggested experiments

In order to define the needed experiments, we carried out numerical simulations using the finite element software R2Sol⁵. The precompacted sample has an initial radius of 7 mm and an initial height of 20 mm . The initial relative density is supposed to be 74% . The TiAl cylinder is subjected to a hydrostatic compression at different cycles of temperature and pressure. The pressure range is from 120 to 600 MPa and the highest temperature simulated is 1000°C . The boundary conditions applied take into account the capacities of Paterson machine. The heating rate and the pressure applied follow the chart of Figure 6.12. The pressure increases first, when it reaches 50 MPa the increasing of temperature begins.

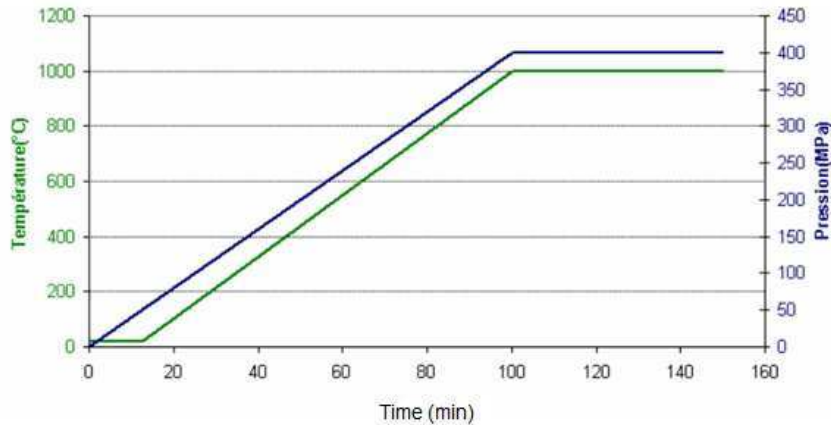


Figure 6.12: Temperature and pressure applied in the simulation of hot isostatic compression

The material follows the compressible viscoplastic behavior presented previously. The parameters related to the dense state k and m are issued from Nieh *et al.* [7] as described

⁵2D Finite element software (2D plane and axisymmetric), developed at CEMEF for the analysis of solidification process. R2Sol could be used to simulate powder compaction as well since the viscoplastic Abouaf law is integrated in its mechanical solver

in section 6.2.1. The expressions of c and f are as follows:

$$f = k_f \frac{1 - \rho_r}{\rho_r - \rho_{crit}} \quad (6.39)$$

$$c = 1 + \alpha f \quad (6.40)$$

ρ_{crit} being the lowest relative density that can be reached, fixed to 0.65.

Influence of the slopes of temperature and pressure First, the coefficients k_f and α are kept constant: $k_f = 0.4$ and $\alpha = 6$. The influence of the heating rate and the pressure increasing rate are studied. Results of the simulations are presented in the tables below.

P max	T max	Slope of P	Slope of T	Time needed for densification
400 MPa	1000°C	0.1 MPa/s	20°C/s	3137 s
		1 MPa/s		877 s

Table 6.1: Influence of pressure slope on densification

P max	T max	Slope of P	Slope of T	Time needed for densification
400 MPa	1000°C	5 MPa/s	0.1°C/s	8391 s (Figure 6.13)
			20°C/s	627 s (Figure 6.14)
			1°C/s	1397 s

Table 6.2: Influence of temperature slope on densification

As seen in table 6.1, when multiplying the slope of the pressure by 10, the densification is 3.5 times faster whereas when multiplying the slope of temperature by 10 as in table 6.2, the densification is 6 times faster. In conclusion, it is more interesting to keep heating rates low during the interrupted tests in a way to measure density evolution in a larger interval of time.

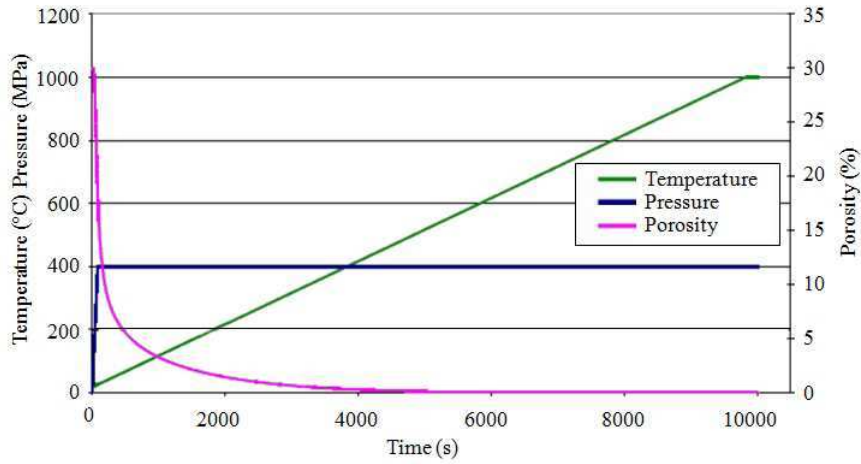


Figure 6.13: Variation of temperature, pressure and porosity when the slope of pressure is 5 MPa/s and the slope of temperature 0.1°C/s

Influence of maximum pressure The slope of the pressure is fixed at 10 MPa/s and the slope of temperature at 0.1°C/s , the maximum pressure is varied to study its influence on densification when the maximum temperature is 1000°C . Results are presented in table 6.3 and in Figure 6.15.

Maximum pressure	Time to reach 1% of porosity
120 MPa	6851 s
150 MPa	6031 s
200 MPa	4971 s
400 MPa	2487 s
600 MPa	1237 s

Table 6.3: Influence of the maximum pressure on densification

For low pressures, the closing of pores is not reached. The higher is the maximum pressure, the faster is densification and lower porosities are obtained.

Influence of Abouaf functions f and c During hot isostatic compression, the coefficient c doesn't affect powder densification. Simulations are carried out varying parameters k_f and α to validate the influence of Abouaf functions on densification.

Figure 6.16 shows the evolution of the relative density with time for the different parameters. When the parameter k_f is higher, the dense state is reached faster. In isostatic pressing the volume variation is directly proportional to the function f . The variation of Abouaf function c doesn't affect the densification during HIP. For that reason, this test is only used for the identification of f .

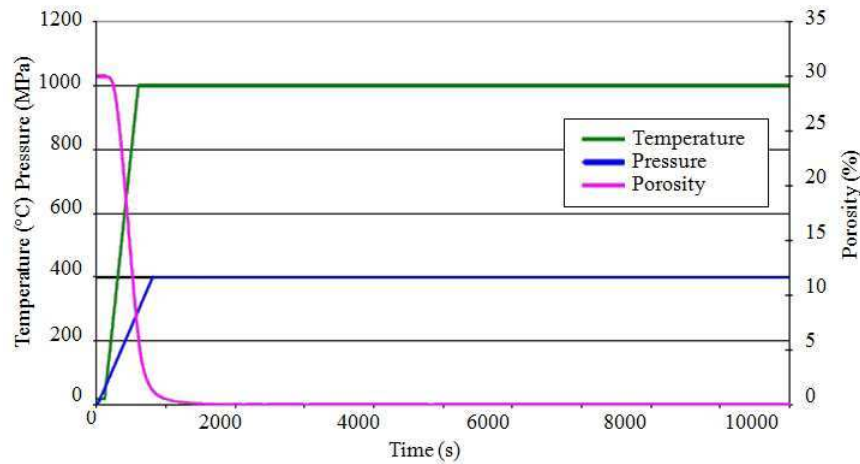


Figure 6.14: Variation of temperature, pressure and porosity when the slope of pressure is 5 MPa/s and the slope of temperature 20°C/s

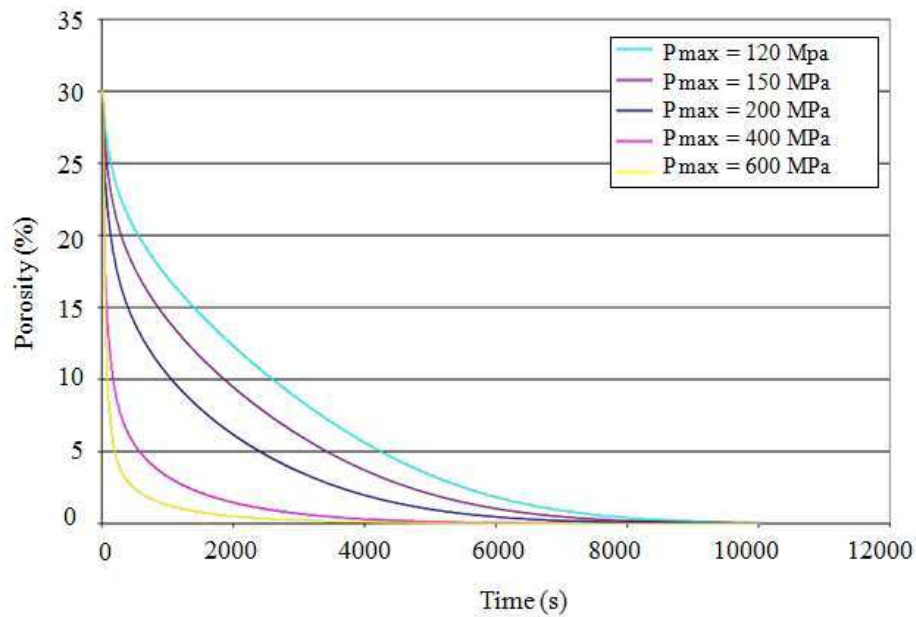


Figure 6.15: Comparison of the evolution of the average porosity with time when applying different maximum pressure

Conclusion The simulations allow the prediction of the tendency of the porosity evolution however it doesn't provide any precise values. Hot isostatic pressing simulations are carried out using, for the *TiAl* dense state, properties issued from the literature [7]. As seen in Figure 6.13 and 6.14, the reduction of porosity starts and sometimes is achieved

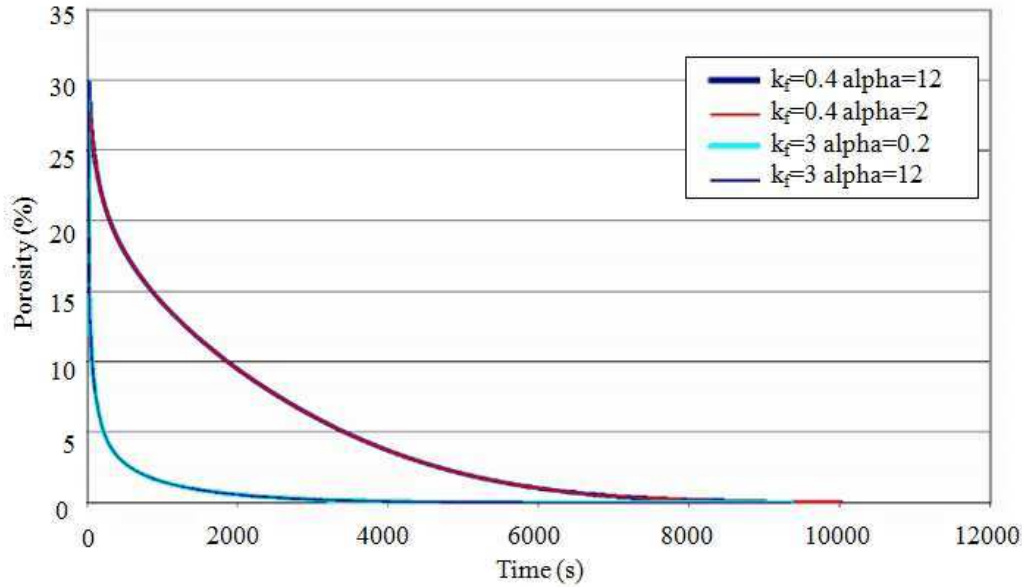


Figure 6.16: Comparison of the evolution of the average porosity with time for different coefficients k_f and α

during the transitory phase when temperature and pressure are still increasing. Hence, the condition of the Paterson machine are not ideal for HIP (pressure and temperature not constant during densification) and parameters cannot be identified analytically. For that reason it is necessary to use numerical simulation with the experiments to identify iteratively the parameters k_f and α through an inverse analysis. Besides, concerning the interrupted cycles, it is more interesting to use low kinetics for densification to increase the accuracy of the results and avoid the sudden closing of pores. Following these simulations, preliminary experiments were carried out at the institute PPRIME to test the capacities of the Paterson machine when used with an intermetallic powder. From the simulations we carried out at CEMEF, the design experiment presented in the chart of Figure 6.17 was suggested:

- The maximum pressure is fixed at 300 MPa otherwise the temperatures needed can not be reached.
- For each maximum temperature 600°C, 700°C and 800°C, four interrupted tests should be carried out.
- Since, during the test the pressure increases first, the tests should be interrupted before increasing the temperature (Point A Figure 6.17).
- An interruption when reaching the goal temperature(Point B Figure 6.17).
- An interruption 30 min after reaching the goal temperature(Point C Figure 6.17).

- An interruption an hour after reaching the goal temperature(Point D Figure 6.17).

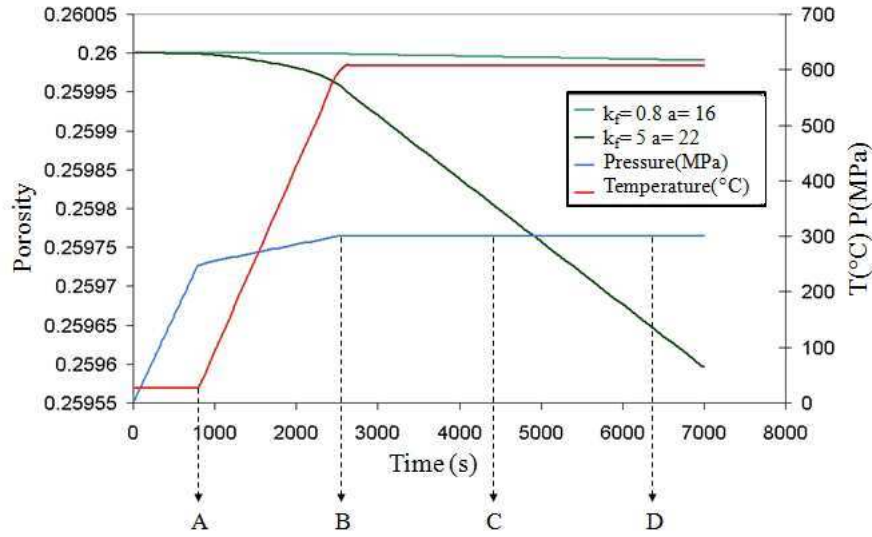


Figure 6.17: Experimental design proposed at CEMEF to identify Abouf functions using the Paterson machine

6.2.3.3 Preliminary experiments

Samples were prepared at ICB⁶. As mentioned previously, the powder can not be poured directly in the set up of the Paterson machine. Pre-compacted samples are needed to carry out the experiments. Hence, samples are compacted at ICB under SPS conditions. Different sets are prepared at ICB and are used at PPRIME to identify the compressible behaviour law of the powder. The details concerning the prepared samples and the conditions of the preliminary tests are presented in Appendix 1.

Goal temperature	Interruption A point	Interruption B point	Interruption C point	Interruption D point
600°C	★	★	★	★
700°C	★	★	★	★
800°C	★	★	★	★

Table 6.4: Summary of the experiments carried out on Paterson machine at the institute PPRIME (the red stars refer to the region that can not be explored)

Four experiments are carried out on Paterson machine at the institute PPRIME. Table 6.4 summarizes the interrupted tests. The red stars refer to the region that can

⁶Laboratoire interdisciplinaire Carnot de Bourgogne, UMR 6303 CNRS-Université de Bourgogne

not be explored. At room temperature when the pressure is increased upto 300 MPa (interruption at point A), no densification occurs. However, the section of the sample is reduced at the mid of the height, as seen in Figure 6.18.



Figure 6.18: Shape of the sample after applying the pressure (100 MPa , then 200 MPa , then 300 MPa during 30 min for each) at room temperature. Initial density 71.74%

The interruption at the level of point B is achieved for two maximum temperatures: $T_{max} = 600^{\circ}\text{C}$ and $T_{max} = 700^{\circ}\text{C}$. Both experiments are stopped because of a crack that appears on the aluminium cover which causes a leak and damages the machine. This can be observed in Figure 6.19 and Figure 6.20. The initial measured porosity for these two experiments was identical equal to 26% but this measure might be wrong because when using Archimède technique or when calculating by measuring the height and radius, densities obtained are not equal. Since the same conditions were applied, it is difficult to explain why the crack appears in one case at 600°C and in the other case at 680°C .

On the other hand, we observed that the machine is very sensitive to the size of the sample. A small reduction in the radius (0.1 mm) might generate a void between the sample and cover causing its crack as it was observed at 680°C . In fact, since then, the furnace is less stable. For that reason, the experiments for temperatures higher than 600°C are abandoned.

The experiment corresponding to $T_{max} = 600^{\circ}\text{C}$ is repeated and interrupted about half an hour after reaching the maximum temperature. A reduction of 4% in the porosity is measured with an initial porosity equal to 31%. However, the measurements during the temperature constant stage don't show any variation in the height.

Problems encountered during the identification of Abouaf functions result from two sources. The pre-compacted sample should have precise dimensions. Not any millimetre (less or more) is tolerated. The sections of the cylinder need to be parallel. The radius along the vertical axe need to be constant. When one of these conditions is not respected, the hot compaction with Paterson machine can not be carried out because the sample won't fit in the set up or it won't be successful because of cracks. In addition, the density of the



Figure 6.19: The set up when the experiment is interrupted at 680°C , the circle shows the crack that occurs and causes the leak

pre-compacted cylinder is not homogeneous. Hence, the application of isostatic pressure induces heterogeneous stresses in the sample which might explain the shape of Figure 6.18. On the other hand, the capacities of Paterson machine appeared to be less convenient. The experiments were started aiming to reach 1000°C for 100 MPa in a way to respect the SPS conditions. The preliminary tests showed that the furnace cannot assure high temperature unless the pressure is at least equal to 300 MPa . Even with 300 MPa , the maximum reached temperature was 680°C . In conclusion, despite the difficulty to set up the Paterson machine with the convenient sample, the range of temperature and pressure that can be applied do not conform with what is applied during SPS. The temperature should be lower than 600°C and pressure higher than 300 MPa . In that case, the material doesn't follow a viscoplastic plastic behaviour and any interpolation of Abouaf functions to the needed temperature and pressure will lead to inaccurate results.

Thus, the Paterson experiments are abandoned and the identification of Abouaf functions is achieved directly using the SPS machine assisted with numerical simulation and inverse analysis.

6.3 Identification of Abouaf functions using SPS

The use of Paterson machine to identify Abouaf functions appeared to be inconvenient. For that reason, experiments are carried out at CEMES⁷ directly on the SPS machine for identification. Three geometries are proposed for the experiments. Interrupted SPS cycles are accomplished. The evolution of the average relative density is deduced. In addition, a map of the porosity distribution is reproduced using the scanning electron microscopy

⁷CEMES, Center d'Elaboration de Matériaux et d'Etudes Structurales, 29 rue Jeanne Marvig, BP 94347, 31055 Toulouse Cedex 4, France



Figure 6.20: The experiment set up when interrupted at 600°C because of the aluminium cover break, the leak mark is visible on the photo of the bottom

(SEM).

6.3.1 SPS experiments and measurements

The TiAl powder is sintered under SPS conditions. All the SPS experiments and the experimental measurements are accomplished by Thomas Voisin at the laboratory CEMES. The machine used is a Sumitomo 2080 which is situated at the "Plateforme nationale de frittage flash/CNRS" in Toulouse France. The applied pressure is transmitted to the pistons through a number of piled spacers. The edge spacer is from inconel and the others from graphite. A graphite mould surrounds the powder. The set up is placed in a vacuum chamber. The inconel spacers are water cooled. A graphite felt is added around the mould when powder diameter is equal to 36 mm to reduce heat losses by radiation. In Figure 6.21, the two set ups are presented: without the graphite felt for $\phi = 8\text{ mm}$ and with the graphite felt for $\phi = 36\text{ mm}$. Heating is controlled via a PID loop. The controlled temperature is measured by an optical pyrometer 3 mm away from the sample from a hole made in the mould at its mid-height. In Figure 6.21, the square cut in the graphite felt can be observed. It allows measuring temperature with the pyrometer. During the experiments, it is possible to measure temperature, displacement, load, intensity and voltage. The use of graphite tooling allows reaching temperatures up to 2000°C and stresses up to 200 MPa .

Three different dimensions are chosen for the experiments varying the ratio height/radius as seen in Figure 6.22. In fact, before abandoning Paterson experiments, those geometries

were conceived to define a friction law for the powder and mould interface. And later on, the same geometries are used to identify on the one hand Abouaf functions and on the other hand friction.

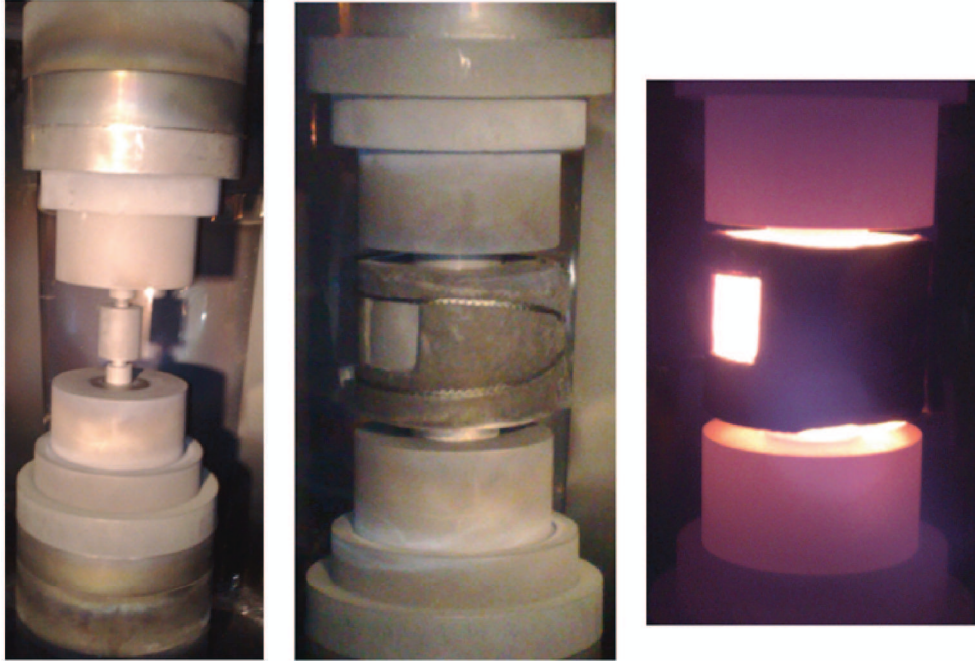


Figure 6.21: Photographs of the experimental set up: $\phi = 8\text{ mm}$, $\phi = 36\text{ mm}$ with the graphite felt before heating and $\phi = 36\text{ mm}$ with the graphite felt at $t = 15\text{ min}$

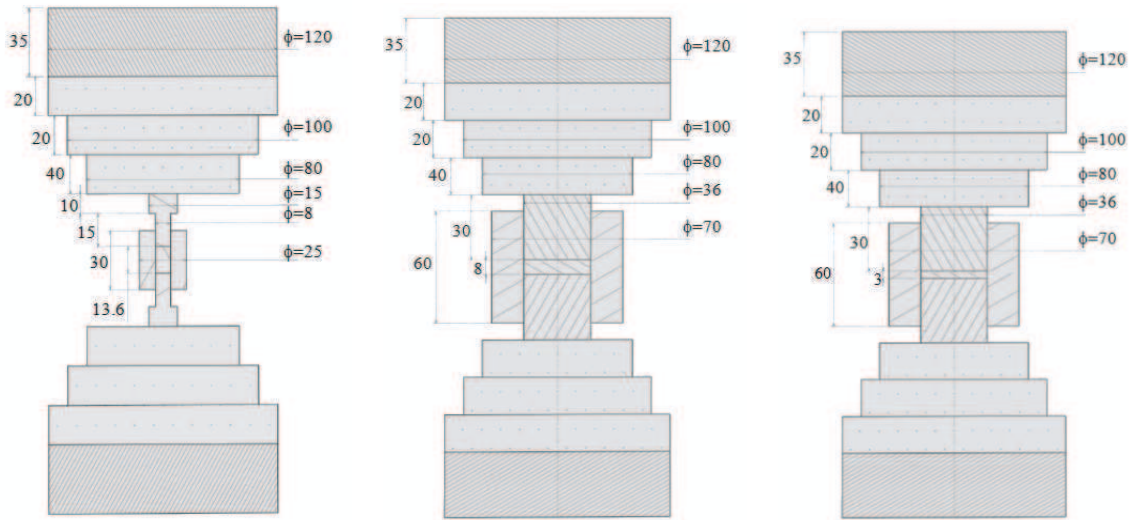
The ratio h/D (height over diameter) modifies the influence of friction. The higher is the ratio the more significant is friction. This is why a long sample, an intermediate and a thin sample are chosen. Table 6.5 summarizes the dimensions of the samples before and

	ϕ	$h_{initial}$	h_{final}
Sample A	8	20.6	13.6
Sample B	36	12	8
Sample C	36	4.5	3

Table 6.5: Initial and final dimensions of the three powder samples

after sintering. The set ups corresponding to each sample are presented in 6.22.

Experimental conditions The powder is encapsulated inside the graphite mould between the two pistons. A mechanical load is applied manually first on the two pistons in



(a) Sample A: $h = 13.6 \text{ mm}$,
 $\Phi = 8 \text{ mm}$

(b) Sample B: $h = 8 \text{ mm}$,
 $\Phi = 36 \text{ mm}$

(c) Sample C: $h = 3 \text{ mm}$,
 $\Phi = 36 \text{ mm}$

Figure 6.22: Dimensions of the samples and tooling. NB: the height of the sample is relative to its dense state at time=0

order to reduce the voids and air between the particles. A graphite sheet is introduced between the powder and the mould to facilitate the extraction of the sample. The samples are sintered with the SPS cycles presented in Figure 6.23, 6.24 and 6.25. The red

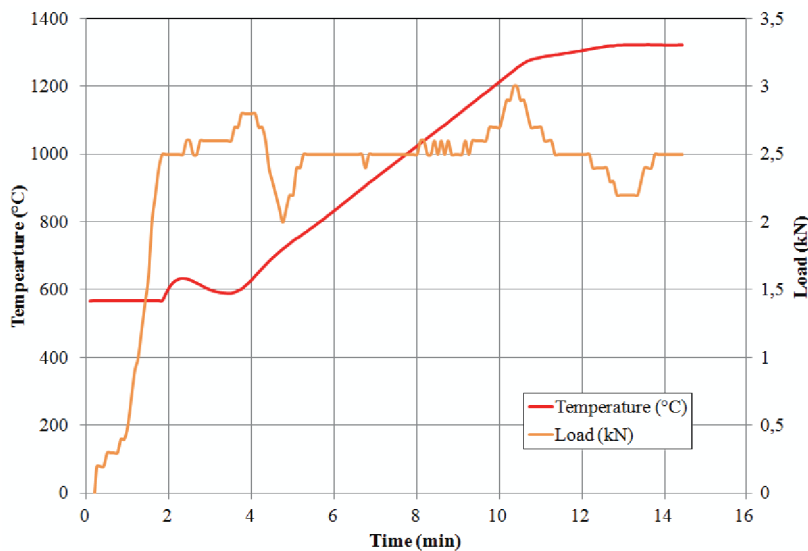


Figure 6.23: SPS cycles applied on Sample A: $h = 13.6 \text{ mm}$, $\Phi = 8 \text{ mm}$ and used in the identification experiments

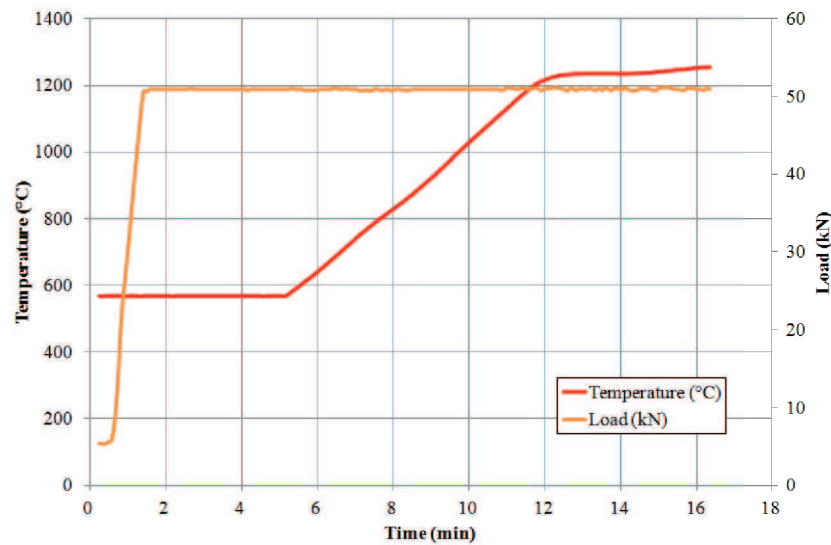


Figure 6.24: SPS cycles applied on Sample B: $h = 8 \text{ mm}$, $\Phi = 36 \text{ mm}$ and used in the identification experiments

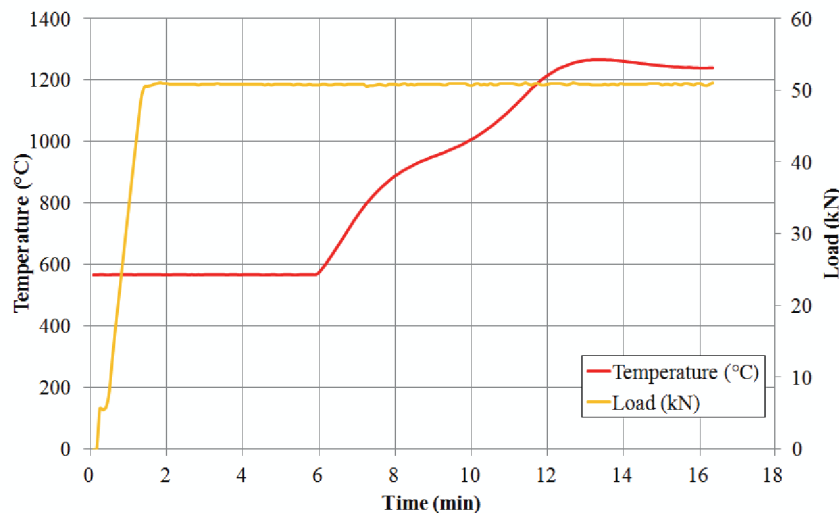


Figure 6.25: SPS cycles applied on Sample C: $h = 3 \text{ mm}$, $\Phi = 36 \text{ mm}$ and used in the identification experiments

curves show the variation of temperature measured by the pyrometer, which is operational above 600°C only. The heating rate is $100^\circ\text{C}/\text{min}$. The last three minutes heating rate is reduced to $25^\circ\text{C}/\text{min}$ to avoid any overshoot when temperature exceeds the desired set point. After the maximum temperature is reached, a two minutes constant phase is applied. For sample B, the temperature exceeds the desired set point as seen in Figure 6.24. Thus the constant phase lasts four minutes. The increasing phase for pressure takes

two minutes. A controlled load is applied to get the desired pressure equal to 50 MPa . The pressure reaches its constant phase before temperature. When the cycle is achieved, argon is injected in the chamber. And finally, the chamber is opened when temperature reaches 600°C .

Density measurement The measurement of displacement corresponds to the relative displacement between the two pistons. The displacement is observed when temperature reaches 800°C and the yield stress eventually is passed. The machine assures the measurement of displacement. This measurement is used to deduce an average relative density. In fact, since it is a die compaction, the volume variation is directly related to the height evolution as the radius is constant. Figure 6.26 represents the evolution of height during compaction. For each sample, the maximum displacement d_f is known, hence the final height h_f . At each time step, the displacement d is measured. Thus, the relative density is computed as follows:

$$\rho_r = \frac{h_f}{h} = 1 - \frac{d_f - d}{d_f - d + h_f} \quad (6.41)$$

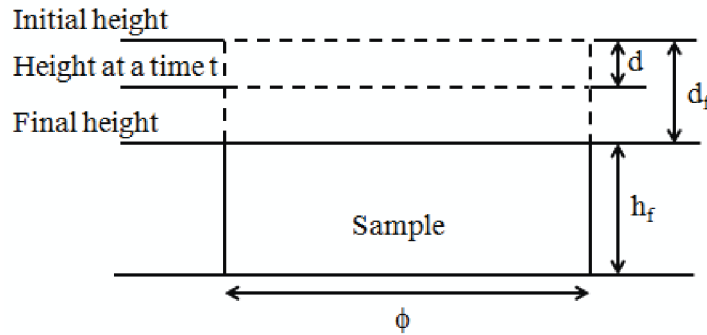


Figure 6.26: Representative scheme of the height evolution during compaction

First, a complete cycle is achieved. Then, according to the evolution of relative density estimated by equation 6.41, the time of the interrupted cycles is decided. For each sample, the evolution of relative density is plotted. In addition, at the end of each interrupted cycle, the sample is weighted and the volume is measured, thus, an additional information is deduced concerning the relative density. However, the sample extracted from the mould presents a layer of graphite that adhered from the papyex. The sample is polished and this might reduce the accuracy of the volume measurements. In Figure 6.30, the evolution is plotted over time in addition the values measured at the end of the experiments are represented with a margin of error.

According to the correction method used at CEMES, a trial test is achieved for each sample to check the elasticity of the machine and measure the thermal expansion of the tools. The SPS cycle is carried out without a powder which means that the pistons are directly in

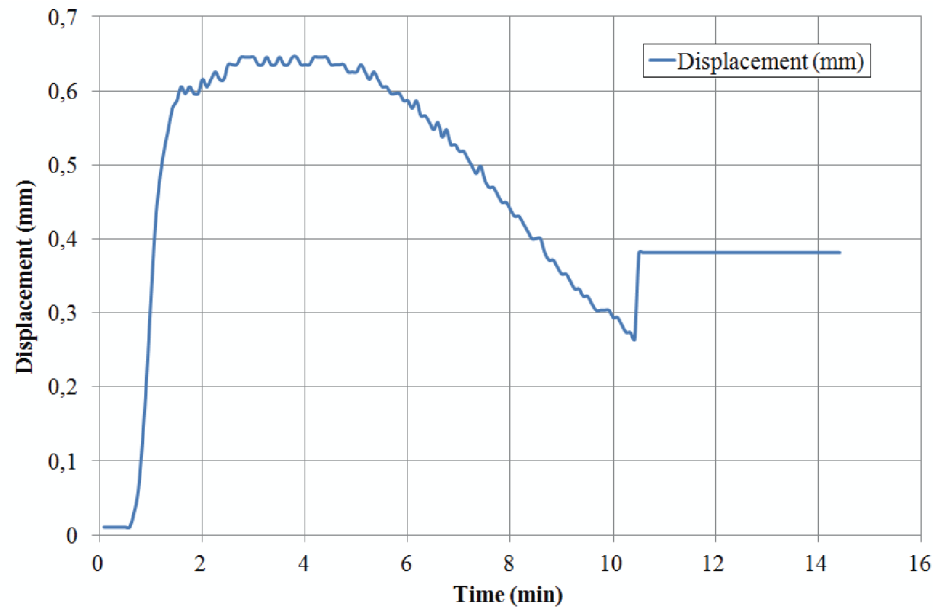


Figure 6.27: Evolution of the trial test displacement with time when the set up is composed of the tooling corresponding to the sample A $\phi = 8 \text{ mm}$ and $h_f = 13.6 \text{ mm}$

contact. This way it is possible to test the displacement of the tooling and their elasticity. The displacement that they measure during the trial test is presented in the graphics of Figure 6.27 and Figure 6.28. The displacement is hence adjusted by subtracting the trial displacement. The chart of Figure 6.29 shows the evolution of displacement with time when sintering the $\Phi 8$ sample before and after the correction according to the trial test. As seen in the chart, the error due to the elasticity of the machine is more important in the first stage. This is probably due to the piling up of the tools.

In Figure 6.27 and 6.28, two stages can be differentiated. The first stage is the loading till reaching 2.5 kN and 50 kN for the samples $\phi 8/h13.6$ and $\phi 36/h8$ respectively. This loading is accompanied by a displacement due to the elasticity of the machine. This first stage ($< 2 \text{ min}$) differs from one sample to another. In fact, even though the load applied is very different between the two samples (about twenty times higher for $\phi 36/h8$), the displacement is comparable which means that the rigidity of the machine is much higher for $\phi 36/h8$ than for $\phi 8/h13.6$. The second stage corresponds to the increasing in temperature. Due to the thermal expansion and in order to maintain the load stable, the displacement of the tools is in the inverse direction. Here as well, we can notice the different sensibilities between the two set ups.

Porosity distribution Another information provided by the experiments is the distribution of the porosity. Measurements were carried out at CEMES. The sample compacted to a certain porosity rate is subjected to a cut of 3 mm in the thickness, in the transverse

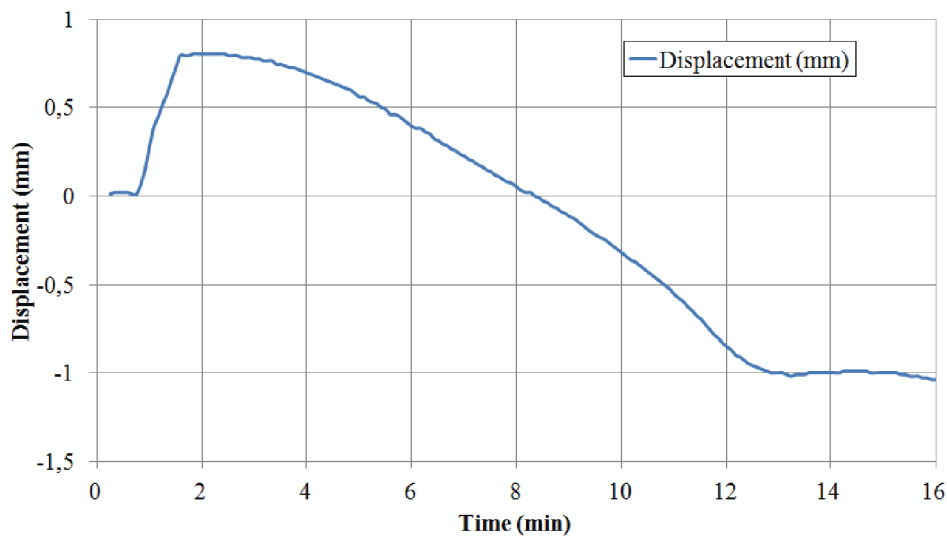


Figure 6.28: Evolution of the trial test displacement with time when the set up is composed of the tooling corresponding to the sample B $\phi = 36 \text{ mm}$ and $h_f = 8 \text{ mm}$

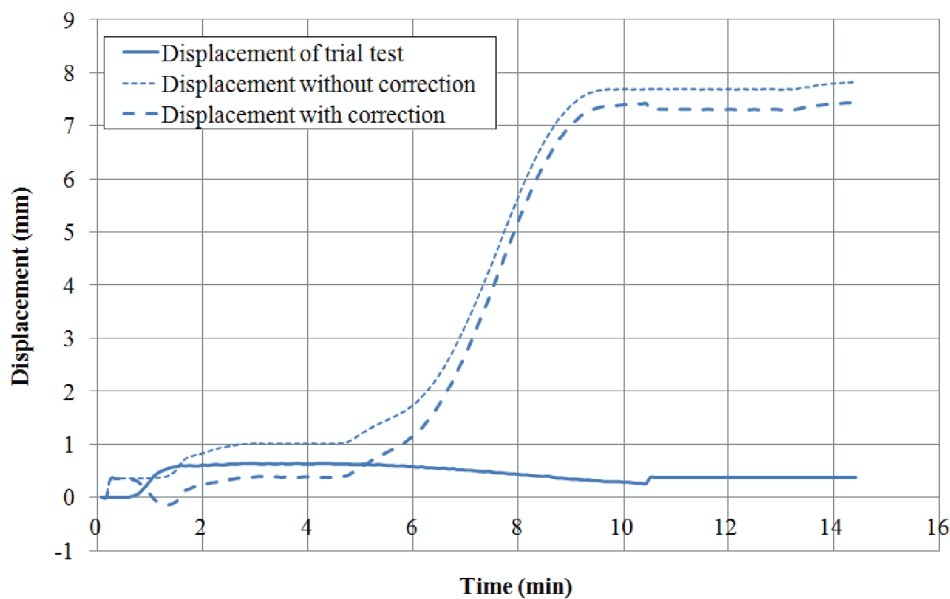


Figure 6.29: Evolution of the displacement during the trial test and during sintering the $\phi 8$ sample with and without correction

direction, as presented in Figure 6.31. Then, the section porosity distribution is measured by scanning electron microscopy. For sample A, three measurements are achieved. The first one is when the cycle is interrupted at 931°C when the sample height is equal to 17.6 mm denoted $AJ683$, the second the cycle is interrupted at 998°C when the sample

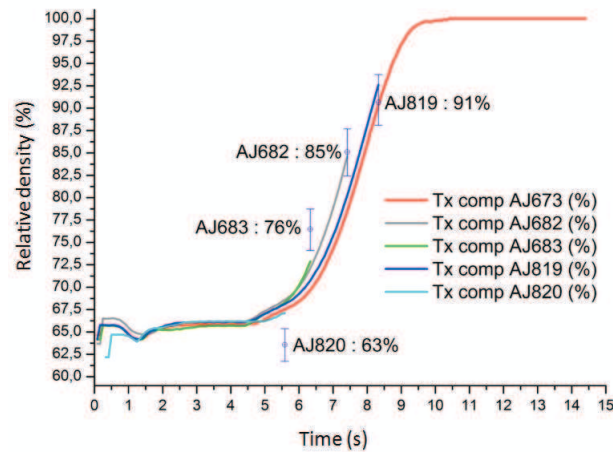
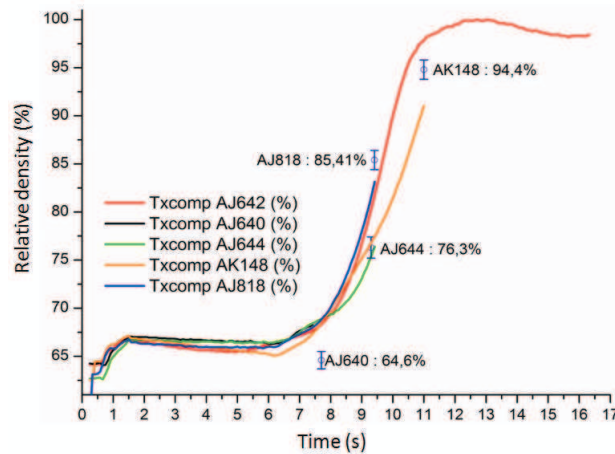
(a) $\Phi 8/h13.6$ (b) $\Phi 36/h8$

Figure 6.30: Experimental relative density plotted over time for the different interrupted cycles and the values measured at the end of the experiments represented with a margin of error

height is equal to 16 mm denoted *AJ682* and the third one the cycle is interrupted at 1175°C when the sample height is equal to 14.8 mm denoted *AJ819*. Concerning sample B, two measurements are achieved, when the cycle is interrupted at 1002°C when the sample height is equal to 9.6 mm denoted *AJ818* and when the cycle is interrupted at 1100°C when the sample height is equal to 8.4 mm denoted *AK148*.

Concerning the sample C $\Phi 36/h3$, two interrupted cycles are carried out. The first cycle is interrupted at $T = 1050^\circ\text{C}$ when the height is equal to 3.4 mm and the second at

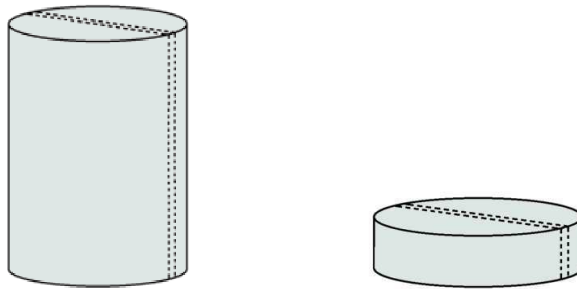


Figure 6.31: Cut in the transverse direction at the middle of the two samples in order to measure porosity distribution by the SEM

$T = 1110^{\circ}C$ when the height is equal to 3.1 mm . The porosity distribution for this sample is presented in Figure 6.32. We can see that there is no symmetry in the distribution of porosity. In fact, the sample is very thin and any inclination of the pistons induces an important modification in densification. Here, the upper piston has a slight inclination on the left. Hence, the stress is not distributed identically on the two sides. The left one is subjected to a higher stress and thus is more densified. In the simulations, this phenomenon is not reproducible. A vertical displacement is imposed and a symmetry is always observed regarding temperature, stress and porosity. For that reason, this sample won't be used in the comparison of the distribution of porosities. However, the experimental data issued from the displacement measurements are used in Matlab for the identification of Abouaf functions.

Our partners at CEMES used different commercial softwares to get a distribution of porosity from the experimental measurements. The images coming from SEM are converted to white and black using the software GIMP (General Image Manipulation Program) as seen in Figure 6.33. Then, the black and white image is divided into squares to get a grid as in Figure 6.34. The percentage of white in comparison to black is calculated in GIMP in each square. The black spots corresponds to the pores in the sample. Hence, the porosity in each square of the image is equal to the percentage of black space occupying the grid squares. The data are then transported to Excel then to Origin software to extract a map of porosity as in Figure 6.35. However, an adjustment of the porosity value is needed. When the image is exported to GIMP, the transformation to black and white is sensitive to the contrast of the image. This means that the distribution of the porosity is accurate but the values are not precise. The values vary when changing the contrast of the image but the proportions remain the same. For that reason, an adjustment is carried out according to the porosity measured after the interrupted cycles. For example, concerning the sample of the cycle interrupted at $998^{\circ}C$, the measured porosity (Eq.6.41) is equal to 15% and the average porosity computed with the GIMP data is equal to 5.6%. The difference is equal to 9.4%. The correction consists in calculating an adjustment

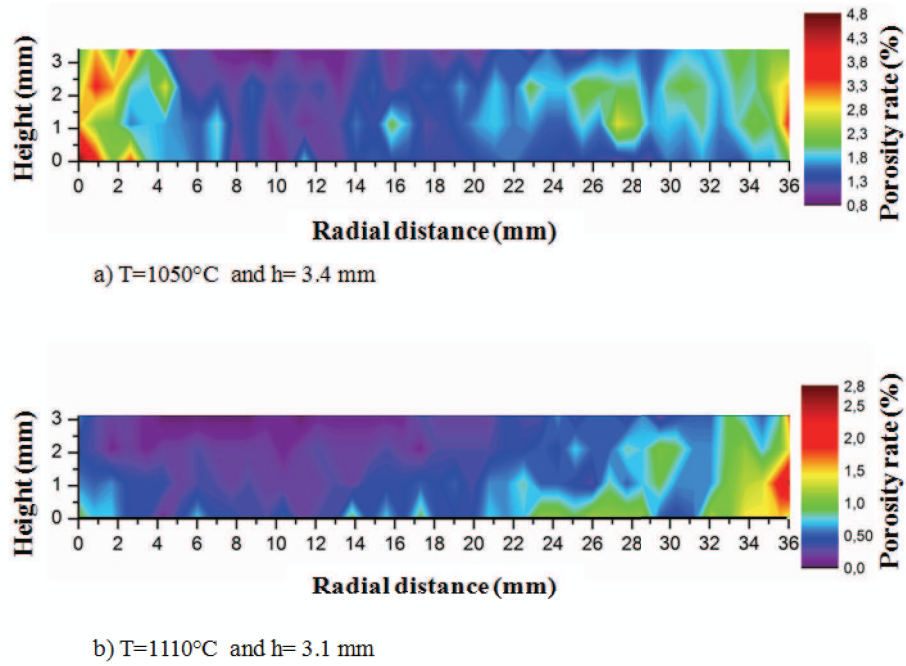


Figure 6.32: Porosity distribution when the cycles are interrupted at $T = 1050^{\circ}C$ and $T = 1110^{\circ}C$ for the $\Phi 36/h3$ sample

coefficient c_{adj} where:

$$c_{adj} = \frac{\rho_{r\ map}}{\rho_{r\ exact}} \quad (6.42)$$

$\rho_{r\ exact}$ being the one measured after the interrupted cycle and $\rho_{r\ map}$ the average calculated using GIMP data. The legend is corrected as follows:

$$\rho_r = \frac{\rho_{r\ map}}{c_{adj}} \quad (6.43)$$

Conclusion SPS experiments are carried out at CEMES. The evolution of relative density is measured during the experiments. Interrupted cycles are accomplished and after each an average relative density is deduced by measuring the sample volume. In addition, a cross section is observed by the SEM and a distribution of the porosity is calculated using commercial software Gimp and Origin.

6.3.2 Calibration of c and f using Matlab

The simulation of a complete SPS cycle requires solving four coupled equations and a frequent remeshing to follow the interface motion. Besides, a small time step is needed in order to control the stress to 50 MPa by imposing the appropriate displacement. Otherwise, with all the coupling, specially between the dense behavior law and temperature, it

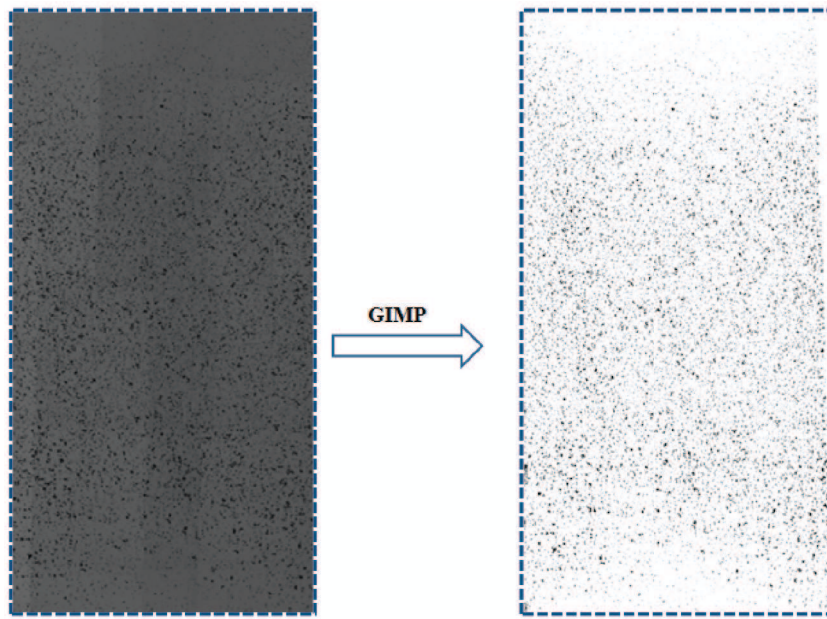


Figure 6.33: Transformation of the SEM image to black and white using the software Gimp

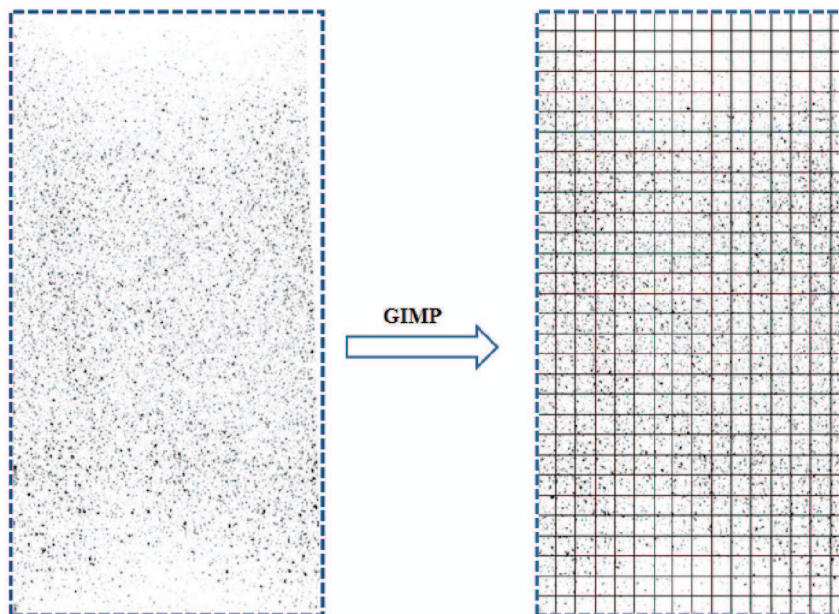


Figure 6.34: Grid covering the image used to compute the porosity rate represented by the percentage of black space in the squares of the grid

is impossible to follow the given stress. Inverse analysis necessitates several simulations for each cycle until converging to accurate parameters. This appeared to be time con-

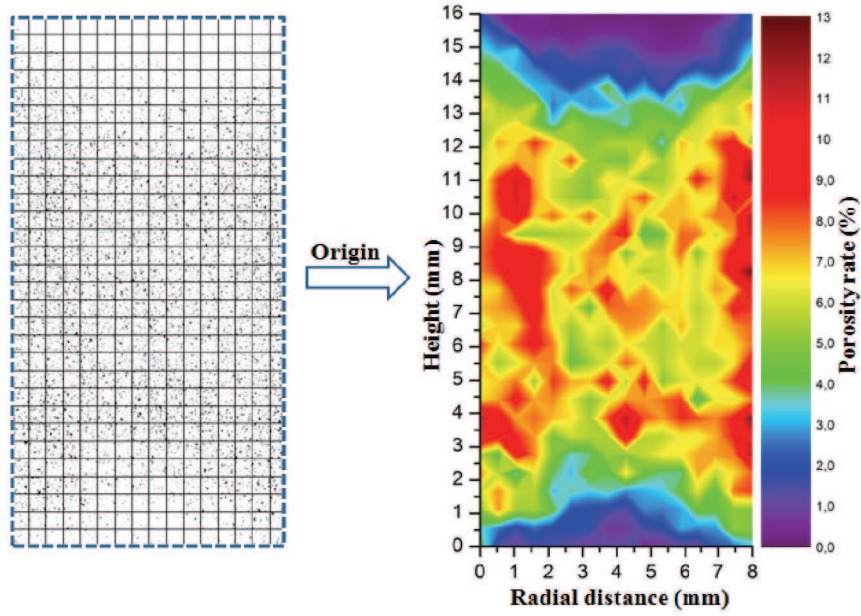


Figure 6.35: Grid covering the image used to compute the porosity and porosity distribution represented using Origin software before adjustment

suming. For that reason, we choose to use Matlab as a first approach to calibrate the parameters of Abouaf functions.

6.3.2.1 Algorithm used in Matlab

For Matlab calculations, two assumptions are considered:

1. The contact between the powder and the mould is frictionless
2. The temperature is homogeneous during compaction.

Thus, the vertical stress can be computed analytically as it was done in Chapter 4:

$$\sigma_{zz} = -\frac{K (\sqrt{3}\dot{\varepsilon})^{m-1}}{3} \left(\frac{4}{c} + \frac{1}{f} \right) \frac{v_{imp}}{h(t)} \quad (6.44)$$

The algorithm is presented in Figure 6.36. Three cycles corresponding to the three samples $\phi 8$, $\phi 36/h 8$ and $\phi 36/h 3$ are computed consecutively. For each cycle the following steps are followed. From the experimental measurements, temperature is used as an input. The initial temperature is set to $700^{\circ}C$ since in the experiments densification starts when this temperature is reached. The parameters of the dense state are functions of the given temperature. The velocity is continuously computed by a PID algorithm ("Proportional-Integral-Derivative") by controlling stress at each time step. The imposed velocity is the

function of the error between calculated and prescribed stresses. If K_p , K_i and K_d are the proportional, integral and derivative constants, v_{imp} is written:

$$v_{imp} = K_p \text{error} + K_i \int_t \text{error} + K_d \frac{\partial \text{error}}{\partial t} \quad (6.45)$$

$$\text{error} = \sigma_{computed} - \sigma_{prescribed} \quad (6.46)$$

Here, parameters are fixed to $K_p = 5$, $K_i = 6$ and $K_d = 0$.

The relative density is computed knowing the height variation (knowing the velocity and so displacement) according to equation 6.41 and these values $\rho_{r\ comp}(t)$ are stored. For the sample A, we have $D = 7\ mm$ and $e = 13.6\ mm$, for the sample B, $D = 4\ mm$ and $e = 8\ mm$ and for sample C $D = 1.4\ mm$ and $e = 3\ mm$. c and f are computed for a set of parameters k_f , α_c :

$$f(\rho_r) = k_f \frac{1 - \rho_r}{\rho_r - \rho_c} \quad c(\rho_r) = 1 + \alpha_c f \quad (6.47)$$

then the stress is computed, and using the PID, the new imposed velocity.

Inverse analysis is carried out to identify k_f and α_c . "**fminsearch**" function of Matlab is used. It determines the minimum using the Nelder-Mead simplex search algorithm [4]. The experimental data of the relative density $\rho_{r\ exp}$ are used as an input for the inverse analysis. The total function cost is the sum of the three functions calculated for each cycle:

$$f_c^{(A,B,C)} = \frac{\sum_t (\rho_{r\ exp}(t) - \rho_{r\ comp}(t))^2}{\sum_t \rho_{r\ exp}(t)} \quad (6.48)$$

and $F_c = f_c^A + f_c^B + f_c^C$. A new set of parameters is tested for each following cycle until convergence as presented in the algorithm of Figure 6.36.

The graphic of Figure 6.37 shows the variation of the functions c and f with the relative density for different set of parameters k_f and α_c . The variation of the functions is more important when the parameters are higher.

The inverse analysis on Matlab, showed that results are not affected by the variation of the function c . Concerning the parameter k_f , it converges to $k_f = 1.3$ independent of the value of α_c . In fact as explained previously in this chapter, c is related to shear which explains that for die compaction its value doesn't affect the results. α_c is fixed to 10.

Figure 6.38 and Figure 6.39 shows respectively the evolution of relative density and velocity for different set of parameters. The prescribed stress is equal to $50\ MPa$. The velocity is calculated by the PID loop and its value depends on the powder behavior which means on the evolution of Abouaf functions. As seen in the graphics, the densification is achieved faster when the function f is higher. Oscillations that occur in the beginning or at the

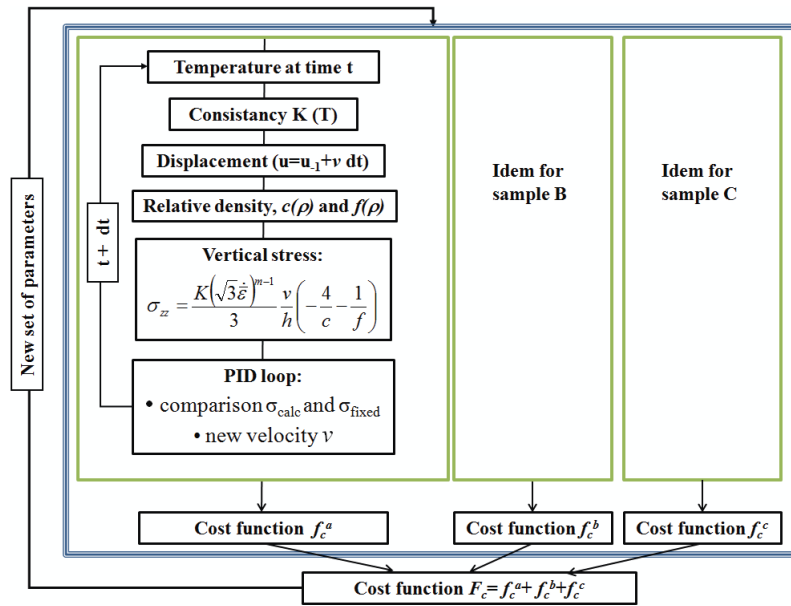


Figure 6.36: Algorithm used in Matlab to identify Abouaf functions using the analytic solution

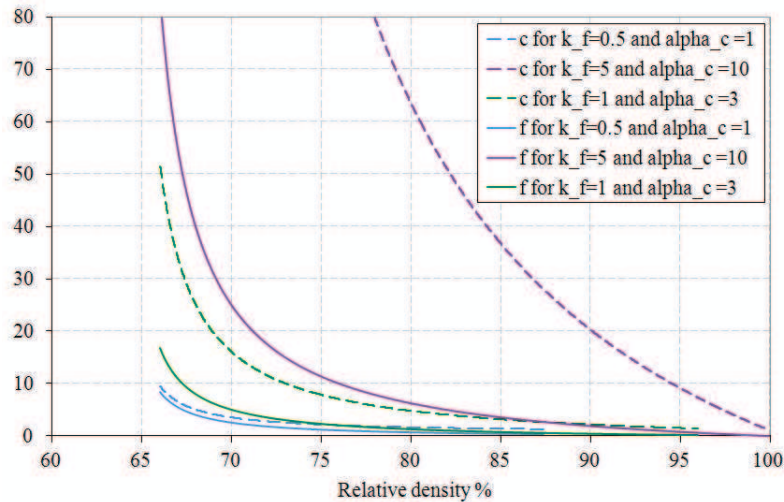


Figure 6.37: Variation of Abouaf functions with relative density for different set of parameters $k_f \alpha_c$

end of the velocity curve result from the PID control that tends to stabilise to reach the prescribed stress.

The relative density, computed with the optimum parameters, is plotted over time and compared to the one measured experimentally during the different interrupted cycles in Figure 6.40. As seen in the charts, for the same sample, the experimental measurements

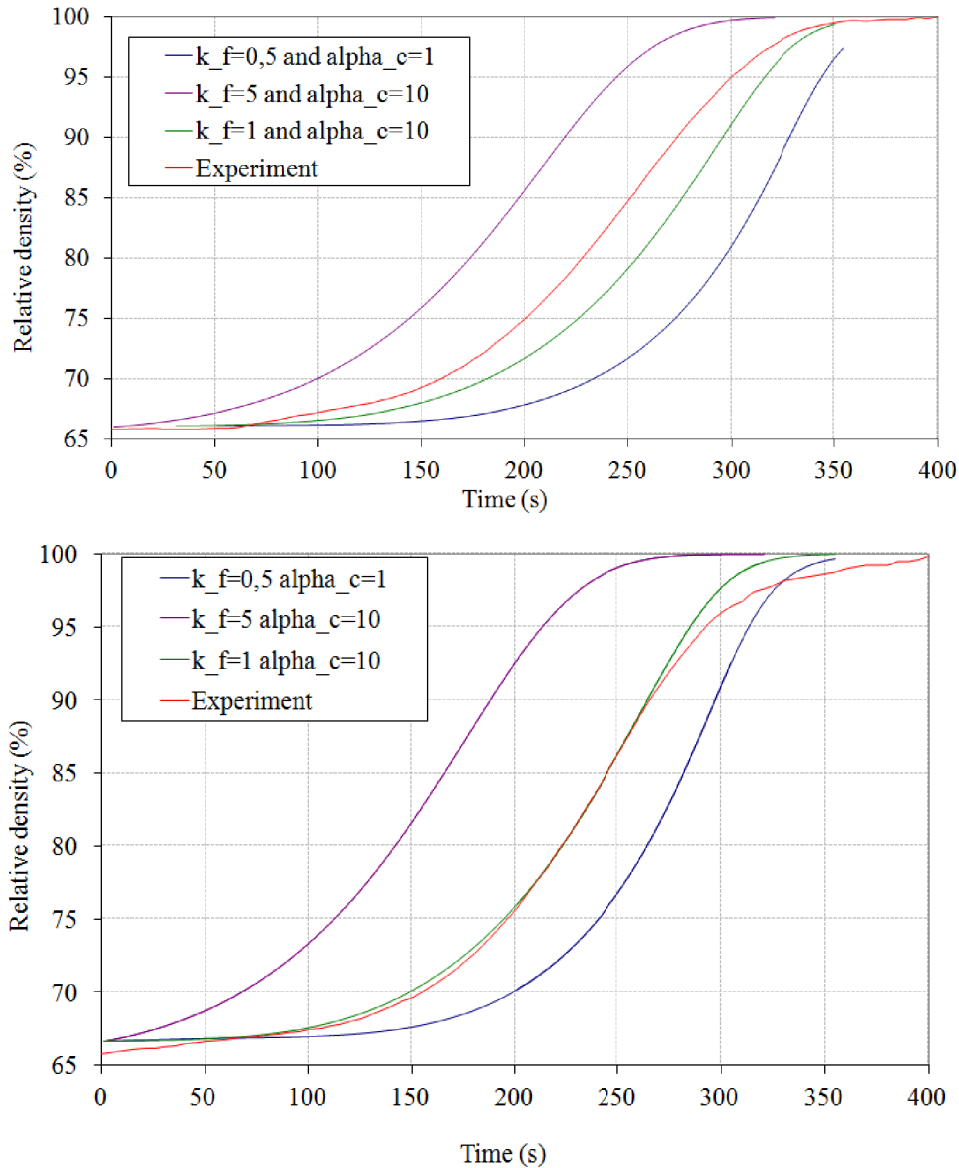


Figure 6.38: Evolution of the relative density for different set of parameters k_f and α_c : On top for the sample $\phi_8/h_{13.6}$ and bottom ϕ_{36}/h_8

differ for each interrupted cycle. Concerning the sample $\phi_8/h_{13.6}$, the difference can reach up to 8% between $AJ682$ and $AJ673$. The relative density computed with Matlab using the calibrated parameters k_f and α_c shows a very good agreement with the experimental results. However, in these calculations, the friction is not considered and temperature is considered homogeneous. For that reason, numerical simulations are carried out to calibrate a friction coefficient.

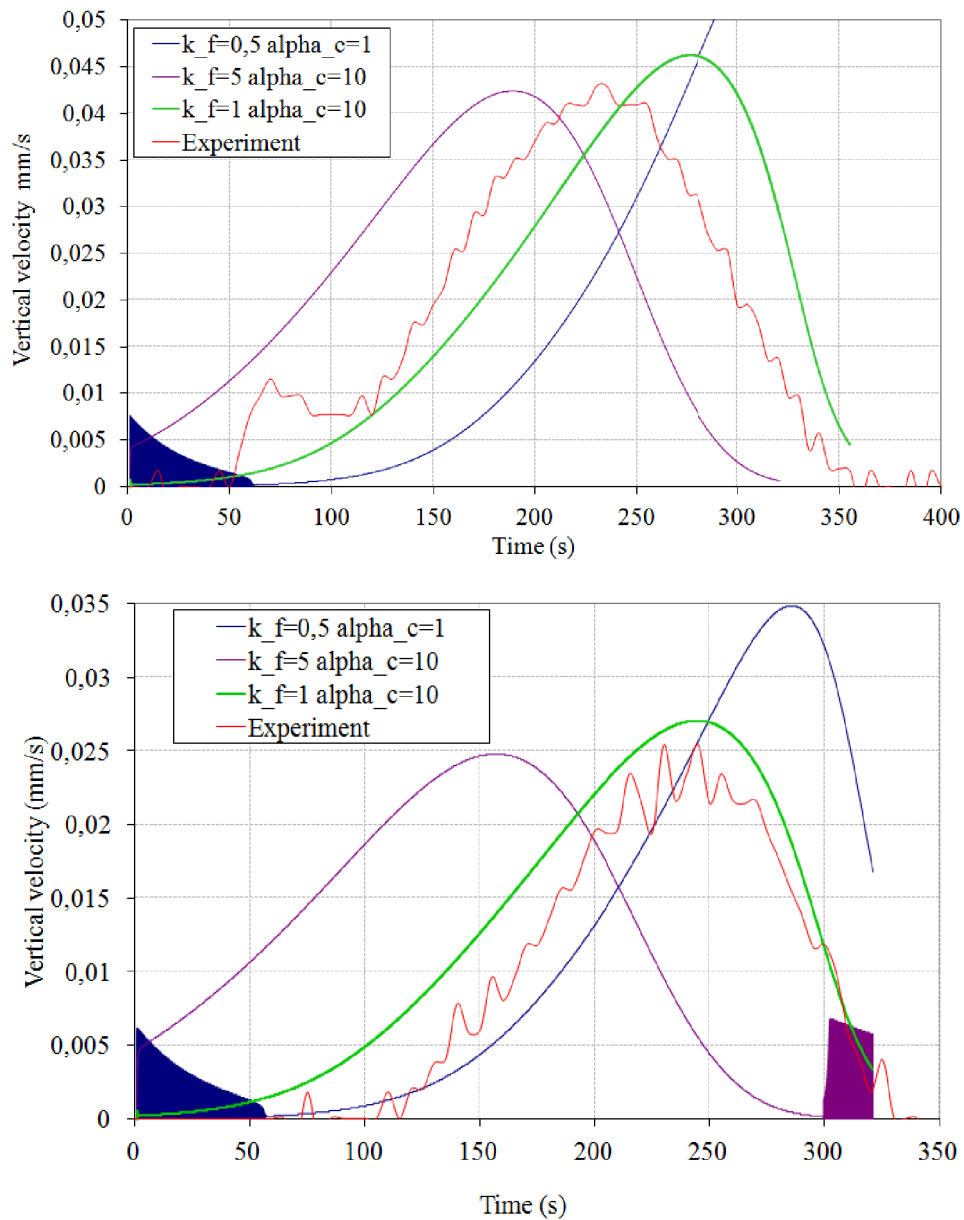


Figure 6.39: Evolution of the imposed velocity for different set of parameters k_f and α_c : On top for the sample $\phi_8/h13.6$ and bottom ϕ_{36}/h_8

6.3.3 Calibration of the friction coefficient

Geometries presented in Figure 6.22 are used in the simulations. Two samples are considered: $\phi_8/h13.6$ and ϕ_{36}/h_8 . The thin sample is not studied since the distribution of porosity is very sensitive to the inclination of the pistons as explained previously. In the simulations, now performed with the code we have developed in CimLib, the same temperature cycle as in the experiments is chosen. The temperature is controlled 3 mm

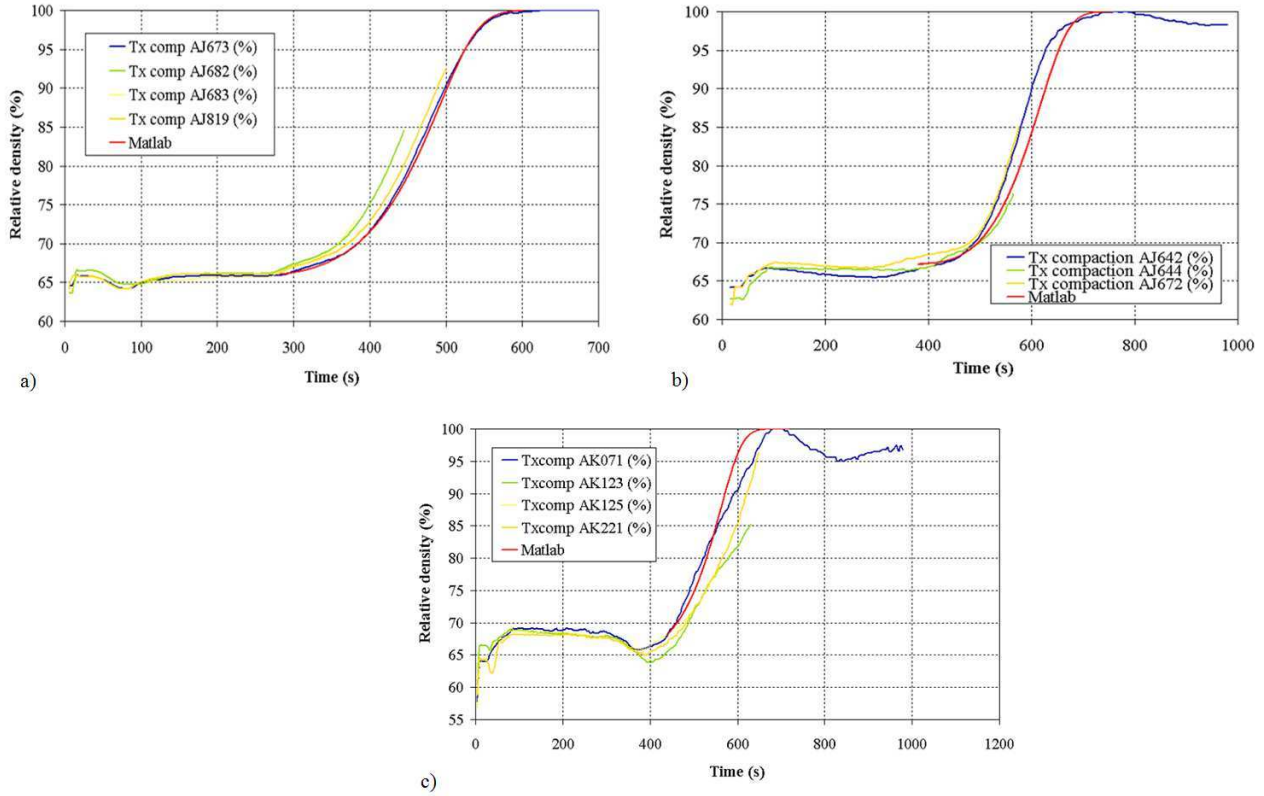


Figure 6.40: Comparison of the evolution of relative density measured during the different interrupted cycles and computed with Matlab when using the optimum Abouaf functions ($k_f = 1.3$, $\alpha_c = 10$): a) Sample A $\phi 8/h13.6$, b) sample B $\phi 36/h8$, c) sample C $\phi 36/h3$

away from the mould edge identically as during the experiments, using a PID loop. At each time step, the imposed electrical potential U is calculated as a function of the error between calculated and prescribed temperature. The regulated electrical potential is applied on the upper graphite edge and a constant zero potential is applied on the lower graphite edge. As regard the load, as a first approach in the simulation, the load is not controlled via a PID loop, since this technique is very sensitive and requires a reduced time step, or else the desired set-point of 50 MPa won't be respected.

The aim being here to define an average of friction, the measured displacement of the experiments is directly imposed in the simulations. More precisely, an experimental velocity is deduced from the measured displacement. This one is then linearized and used as an input for the boundary conditions of the mechanical problem as presented in Figure 6.41 for the sample $\phi 8/h13.6$ and in Figure 6.42 for the sample $\phi 36/h8$.

Densification starts when temperature exceeds 700°C . For that reason, the mechanical problem is solved once the convenient temperature is reached.

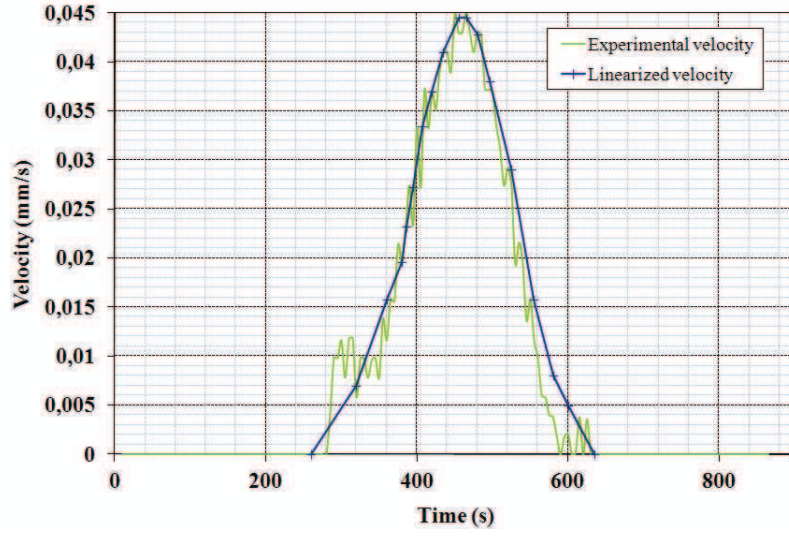


Figure 6.41: Experimental velocity and its linearization when temperature reaches the 660°C in the mould equivalent to 700°C in the centre of the powder for the sample $\phi 8/h13.6$

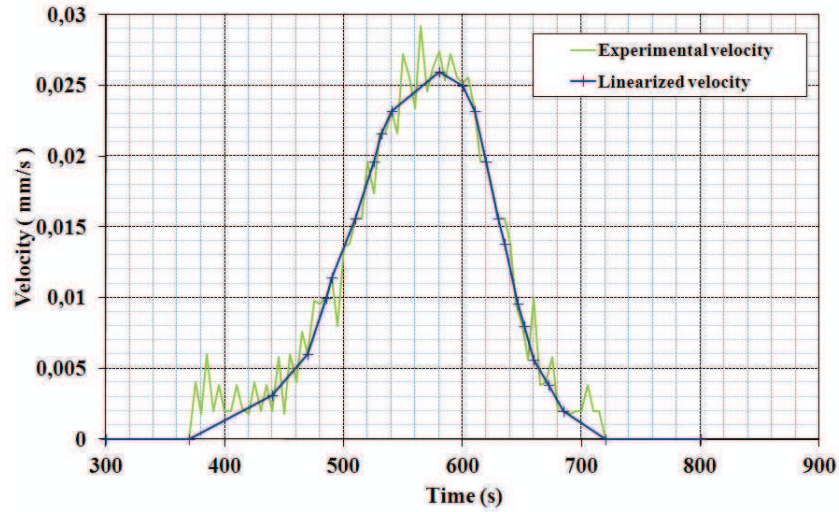


Figure 6.42: Experimental velocity and its linearization when temperature reaches the 660°C in the mould equivalent to 700°C in the centre of the powder for the sample $\phi 36/h8$

The numerical model is governed by the following system of equations:

$$\begin{cases} \nabla \cdot (-\sigma_e(T, \rho_r) \nabla U) = 0 \\ \nabla \cdot (-k(T, \rho_r) \nabla T) + \rho_r \rho_0 c_p(T) \frac{\partial T}{\partial t} = \sigma_e(T, \rho_r) \|\nabla U\|^2 \\ \nabla \cdot \sigma = 0 \\ \nabla \cdot (\rho_r v) + \frac{\partial \rho_r}{\partial t} = 0 \end{cases} \quad (6.49)$$

The finite element resolution of the system was presented in Chapter 3 and Chapter 4.

Modeling friction is based on the work of Chapter 5. A boundary layer covers the interface between the powder and the mould. The thickness of the layer is constant in this study: $e_{layer} = 1$ mm. The consistency of the boundary layer is computed as follows:

$$\tilde{K} = 152 \alpha_f^{1.255} e K \quad (6.50)$$

Since a single mesh covers the whole assembly, a mixing law is used to compute the consistency on the domain Ω . The consistency of the powder K_{powder} and of the layer \tilde{K} are computed on the computational domain Ω using a mixing law defined per element:

$$K(\Omega_e) = \frac{K_{powder} |\Omega_e \cap \Omega_p| + \tilde{K} |\Omega_e \cap \Omega_{BL}|}{|\Omega_e|} \quad (6.51)$$

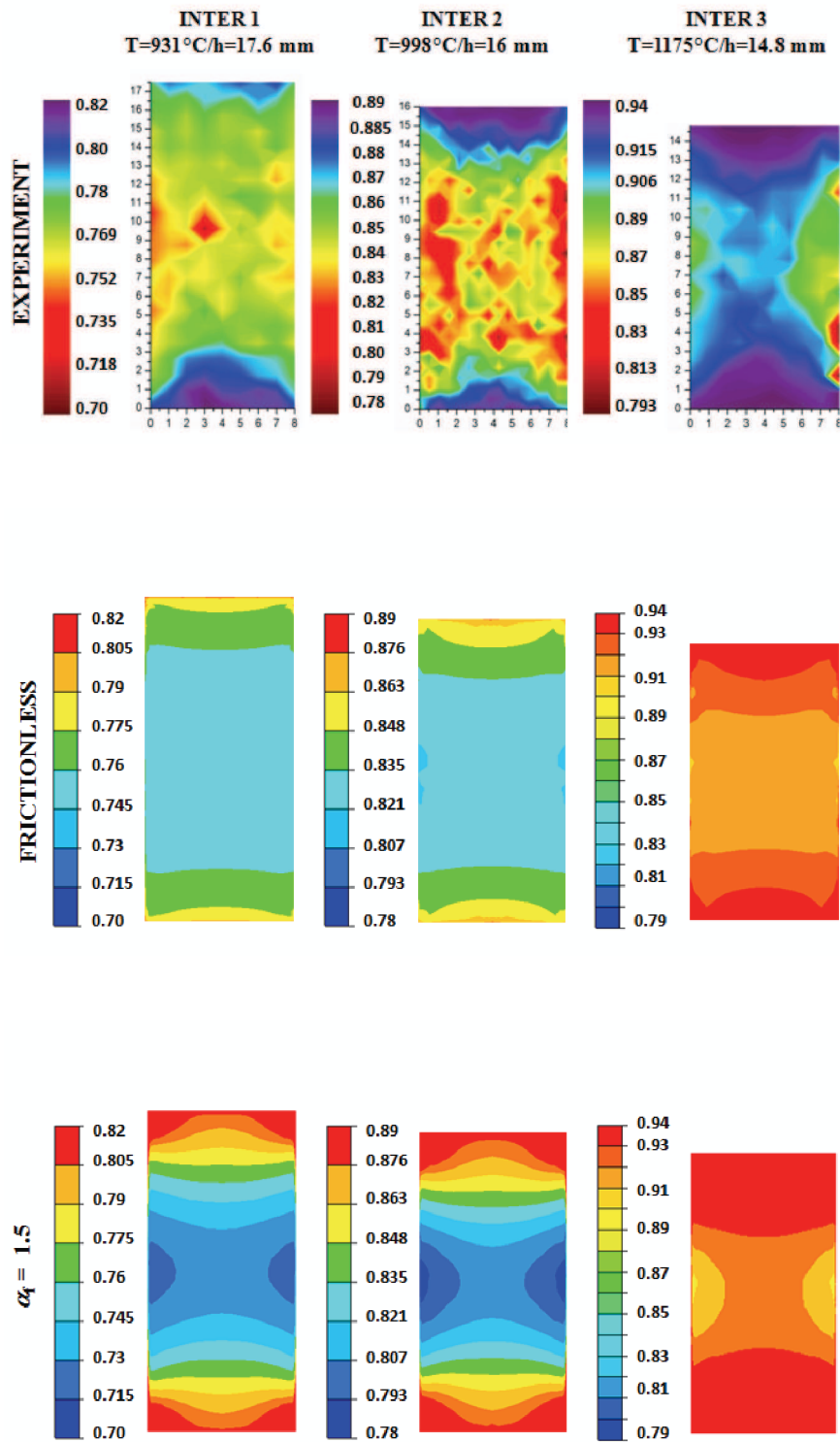
$|\Omega_e|$ being the volume of the element Ω_e , Ω_p the domain covered by the powder and Ω_{BL} the domain covered by the boundary layer.

Different friction coefficients are tested to deduce the one that gives the same order of density heterogeneities as in the experiments. Results are presented for two friction coefficients $\alpha_f = 1.5$ and $\alpha_f = 3.5$ and for a frictionless condition. The aim is to compare the distribution of the relative density between the experiments and the simulation at the time where the cycles are interrupted.

Sample $\Phi 8/h13.6$: Concerning the sample $\Phi 8/h13.6$, three interrupted cycles were carried out. The relative density map is given when the sample height is equal to 17.6 mm, when it is equal to 16 mm and when it is equal to 14.8 mm. Figure 6.43 shows the distribution of relative density measured experimentally and computed with frictionless condition or with friction for $\alpha_f = 1.5$ and for $\alpha_f = 3.5$.

In fact, the experimental distribution of the relative density is similar for the three interrupted cycles. The highest relative density is observed under the pistons and the lowest at mid height along the lateral faces of the sample.

In Figure 6.43, for $h = 17.6$ mm, the experimental distribution is not symmetric in the vertical direction. This could be explained by a non symmetric motion of the mould which causes a non symmetric distribution of temperature. This was discussed in Chapter 5 section 5.5.4.



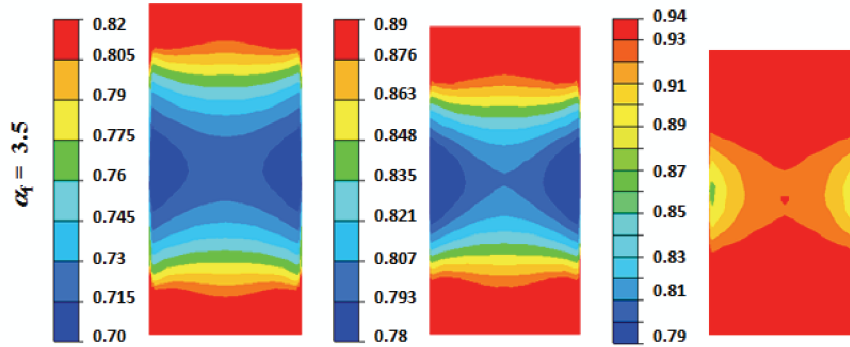


Figure 6.43: Sample $\Phi 8/h13.6$: Distribution of relative density measured experimentally and computed with frictionless condition or with friction for $\alpha_f = 1.5$ and for $\alpha_f = 3.5$: on the left when the sample height is equal to 17.6 mm, in the center when the sample height is equal to 16 mm and on the right when the sample height is equal to 14.8 mm

		$\nabla \rho_{r \max} (\%)$	$\rho_{r \min} (\%)$	$\rho_{r \max} (\%)$
h = 17,6 mm	Experiment	7	74	81
	Sliding condition	3	75	78
	Friction $\alpha_f = 1,5$	9,5	82	72,5
	Friction $\alpha_f = 3,5$	20	70	90
h = 16 mm	Experiment	10	79	89
	Sliding condition	5	81	86
	Friction $\alpha_f = 1,5$	11	78	89
	Friction $\alpha_f = 3,5$	20	77	97
h = 14,8 mm	Experiment	8	86	94
	Sliding condition	3	91	94
	Friction $\alpha_f = 1,5$	6	88	94
	Friction $\alpha_f = 3,5$	22,4	87	99,4

Figure 6.44: Sample $\phi 8/h13.6$: Comparison of density gradient, maximum and minimum relative density in the sample for the experimental results and simulations when a frictionless condition is applied, a friction with $\alpha_f = 1.5$ and a friction with $\alpha_f = 3.5$

Table 6.44 summarizes the results concerning the distribution of relative density. The maximum density gradient and the minimum and maximum of relative density are presented. The friction condition with $\alpha_f = 1.5$ gives the closest results to the experiments (on the base of $\rho_{max} - \rho_{min}$).

Sample $\Phi 36/h8$: Concerning the sample $\Phi 36/h8$, two interrupted cycles were carried out. The relative density map is given when the sample height is equal to 9.6 mm and when it is equal to 8.4 mm. In Figure 6.45, the experimental results are presented as well as the computed results. For this geometry, due to its large section, only the left top corner is treated using the SEM. Knowing that the distribution of the density is symmetric along the radial and axial direction, the map is completed by duplicating the quarter. The distribution of relative density for the height 9.6 mm is unexpected. All the maps, for $\Phi 8/h13.6$ and $\Phi 36/h8$ show a higher density next to the pistons apart from this one. A microscopic reaction might occur during the process and cause the densification in the center. It would have been interesting to repeat the experiment and check if the densification is achieved identically. For $h = 8.4$ mm, the relative density is quite homogeneous. It is slightly higher under the pistons with a maximum gradient equal to 0.4%. In fact, after exporting the images to GIMP, the grid that is used to calculate the concentration of porosity influences the local variation of density. This could explain the slight difference with the simulations.

Numerical results are presented in Figure 6.45 for a frictionless condition and with friction for $\alpha_f = 6.6$. The maximum gradient of relative density observed is about 2% for both conditions. In fact, the friction effect is proportional to the ratio h/D [1]. When decreasing the ratio h/D , the influence of friction is eliminated.

Comparing the experimental and simulated distributions for $h = 8.4$ mm, the maximum density gradient is higher in the simulations. In fact, after exporting the images to GIMP, the grid that is used to calculate the concentration of porosity influences the local variation of density. This could explain the slight difference with the simulations since the lowest and highest values are localised in a small area under the pistons and at the lateral edge. A comparison was made by our colleagues at CEMES to study the influence of the grid size for the sample $\Phi 8/h13.6$ at $h = 16$ mm. The maps are presented in Figure 6.46. As we can see, the global distribution is identical, however, locally the value of the relative density can differ. When using a coarse grid, the result is of course less precise.

6.3.4 Conclusion

Since the identification of Abouaf functions using Paterson machine was not completed due to the different problems encountered, the identification is achieved using the SPS process. Three samples are considered with three different dimensions. During the experiments the displacement evolution is measured. In addition interrupted cycles are carried out and density distribution is measured using the SEM. Inverse analysis applied on a complete SPS cycle is very time consuming. As a first step, a calibration of the parameters is achieved with Matlab considering a homogeneous temperature and a frictionless condition that way an analytic solution can be expressed. The calibrated parameters are then introduced in the numerical simulation in CimLib. The aim being to define the value

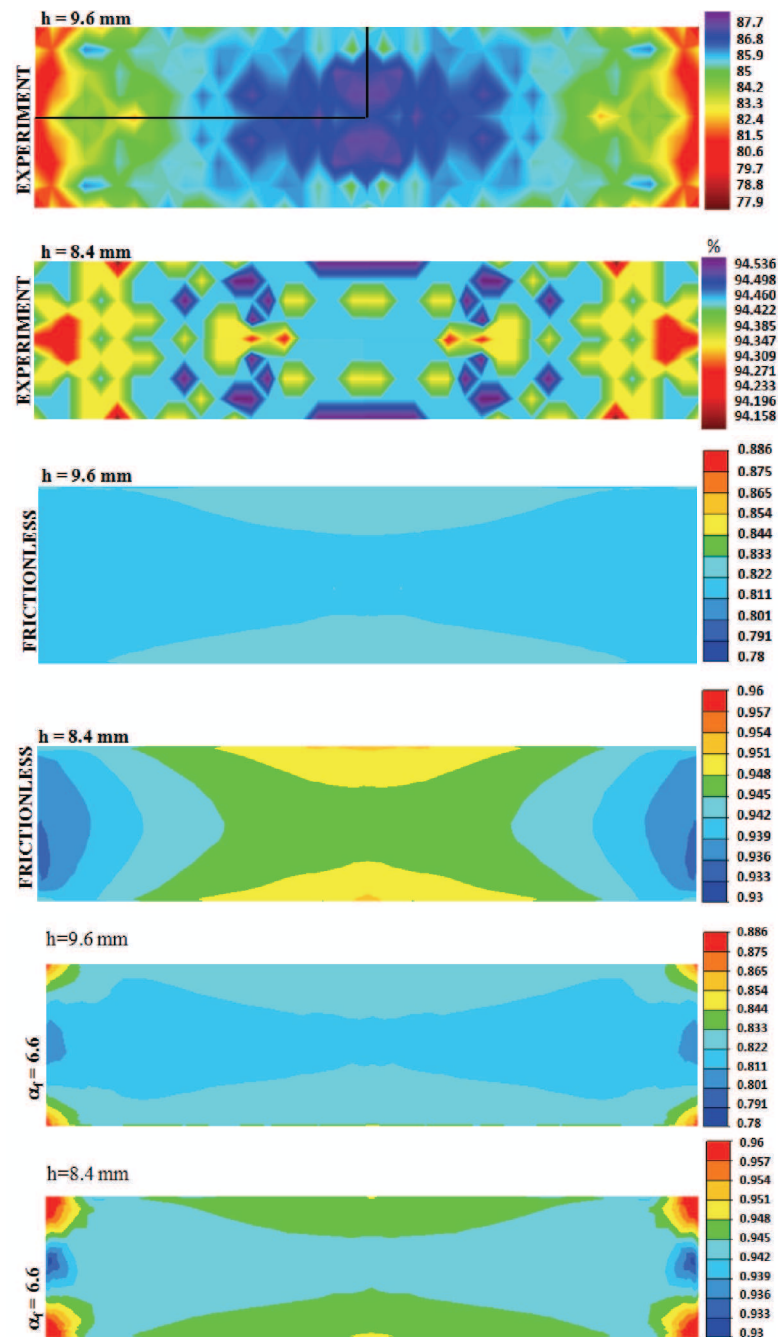


Figure 6.45: Sample $\Phi 36/h8$: Distribution of relative density measured experimentally and computed with frictionless condition or with friction for $\alpha_f = 6.6$: on top $h = 9.6$ mm, on the bottom $h = 8.4$ mm

of the friction coefficient giving the same order of homogeneities, in terms of density distribution, as in the experiments. In these simulations, the experimental velocity is applied as a boundary condition in the model to avoid the use of the PID loop in the

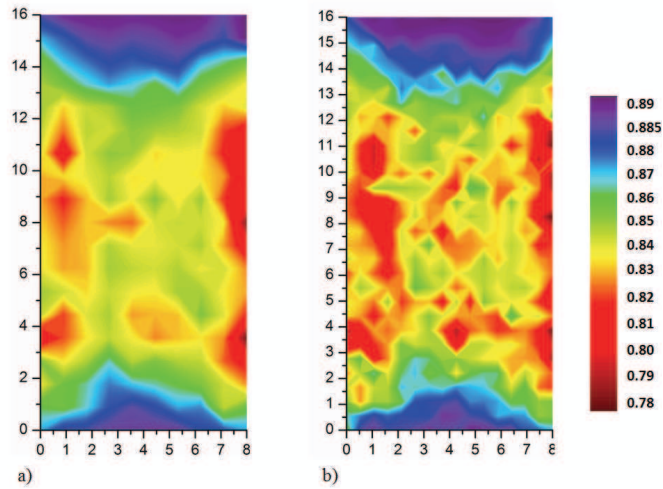


Figure 6.46: Comparison of the distribution of relative density issued from the experiment when using two different grids in GIMP, the sample is $\Phi 8/h13.6$ for $h = 16$ mm: a) coarse grid, b) fine grid

mechanical problem and increase computation time. Finally, the functions f and c are identified as follows:

$$f(\rho_r) = 1.3 \frac{1 - \rho_r}{\rho_r - \rho_c} \quad c(\rho_r) = 1 + 10f. \quad (6.52)$$

In addition, it is found that $\alpha_f = 1.5$ gives the same density gradients as in the experiments. For the thin sample $\Phi 36/h8$, the friction doesn't influence significantly stress and hence density distribution.

6.4 Numerical simulation of the spark plasma sintering test

6.4.1 Description of the models

The SPS experiments on the two samples $\Phi 8/h13.6$ and $\Phi 36/h8$ are simulated using CimLib. These geometries were already simulated in section 6.3.3. The difference between the simulations in this section and the previous one is the boundary conditions in the mechanical problem. Here, the load is regulated according to a prescribed value as in the experiments. The geometries presented in Figure 6.22 are considered. They are represented with the mesh in Figure 6.47, with a zoom at the region of the sample. Concerning the mesh of sample $\Phi 8/h13.6$:

- the number of nodes is equal to 64870
- the number of elements is equal to 339488
- there are 25 elements in the thickness of the remeshed zone.

Concerning the mesh of sample $\Phi 36/h8$:

- the number of nodes is equal to 59699
- the number of elements is equal to 321893
- there are 20 elements in the thickness of the remeshed zone.

The mesh size is indicated in Figure 6.47. Inconel spacers at both ends of the stock are not modeled in order to reduce computation time. Inconel effect is taken into account by the thermal boundary conditions that are imposed directly on the boundaries of the top and bottom graphite spacers. Assuming a quasi-stationary state, the heat flux at the Inconel boundary is equal to the heat flux through the Inconel part, and to the heat flux through the interface between Inconel and graphite. This was discussed in Chapter 4 section 4.5.2. On the upper and lower graphite surfaces, a conduction heat flux is imposed:

$$\Phi = \frac{h_{cond}}{h_{cond} \frac{e_{inco}}{k_{inco}} + 1} (T_{gr\ sup} - T_{water}) \quad (6.53)$$

where $h_{cond} = 880 \text{ W.m}^{-2}.\text{K}^{-1}$ is the constant heat transfer coefficient, k_{inco} the inconel thermal conductivity, e_{inco} its thickness, $T_{inco\ sup}$ the temperature of the inconel upper edge, $T_{inco\ inf} = T_{gr\ sup}$ the inconel/graphite interface temperature and T_{water} the water temperature (assumed constant 296 K). Moreover, the process taking place in a vacuum chamber, heat losses by convection and conduction are neglected. All lateral surfaces have heat losses by radiation towards chamber walls, which are held at room temperature ($T_{wall} = 300 \text{ K}$), a radiative heat flux is then considered:

$$\Phi_{rad} = \sigma_B \varepsilon_r (T^4 - T_{wall}^4). \quad (6.54)$$

ε_r the emissivity of tools is equal to 0.8.

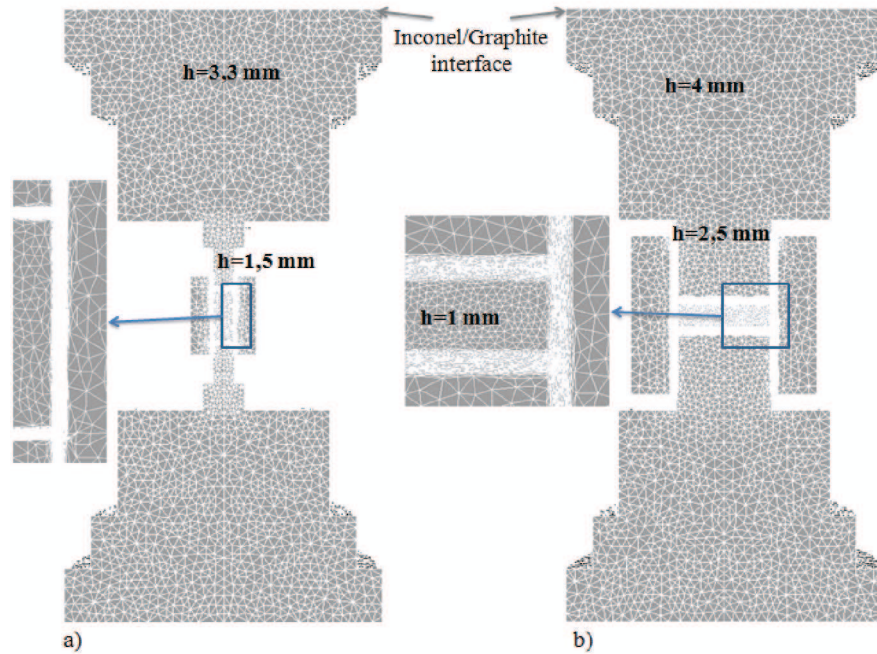


Figure 6.47: generated mesh used in the simulation and a zoom in the region of the sample showing refined elements around the sample/matrix interface: a) sample $\Phi 8/h13.6$, b) sample $\Phi 36/h8$

Actually, when dealing with large dimensions, a graphite felt is put around the mould to reduce radiation in a way to homogenize temperature in the sample and so homogenize densification.

Therefore, modeling graphite felt is complicated and it is a challenge by itself. The contact between the felt and the mould is not similar along the height as explained in Figure 6.48 and 6.49. In fact, the felt is flexible and is fixed with a thin rope to the mould. Consequently, it is difficult to define the contact area and so a contact resistance. Our colleagues at CEMES defined an equivalent emissivity lower than the graphite emissivity in order to reduce heat losses without facing the complications of contact resistance at the mould/felt interface. The objective is to model the heat losses that occur when the felt is used which are less important. Hence, they supposed that graphite has a lower emissivity. They found an emissivity $\varepsilon_{req} = 0.3$ representative of the graphite felt effect. This emissivity is used instead of modeling the graphite felt domain when the radius is equal to 18 mm .

Temperature is controlled in the mould, 3 mm away from the sample at his mid-height, via a PID loop. The PID was presented in section 6.3.2.1. Here, the PID parameters for temperature regulation are fixed to $K_p = 1$, $K_i = 1.5 \times 10^{-4}$ and $K_d = 10^{-7}$. The regulated electric potential is imposed on the top graphite edge with a zero potential on the bottom. Concerning the mechanical problem, the vertical stress is controlled also via

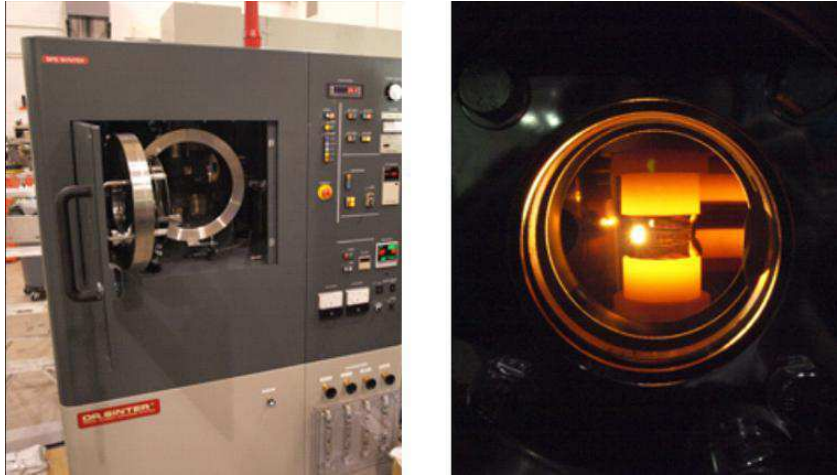


Figure 6.48: SPS apparatus and a zoom on the heated apparatus with the graphite felt surrounding the mould [3]

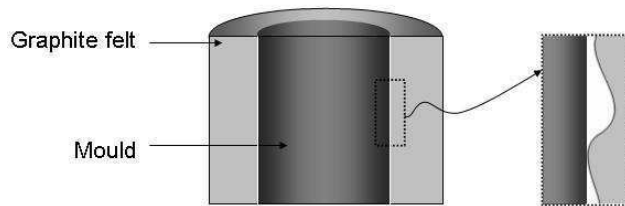


Figure 6.49: Representative scheme of the mould/graphite felt interface

a PID loop with a prescribed stress equal to 50 MPa. The stress is measured on the top of the sample. The stress is computed on each element. An average is then calculated on a transversal section on the top edge of the powder. Hence, we get a scalar value $\sigma_{computed}$ that we compare to $\sigma_{prescribed} = 50 \text{ MPa}$. A velocity is calculated with the PID loop. The regulated velocity is then imposed in the tooling. The velocity is imposed in a way to conserve the geometrical symmetry of the machine. The mould is supposed to move with a velocity equal to the half of the one imposed to the tools. Tools are considered rigid. The mechanical problem is solved only in the powder.

In Chapter 4, the mesh adaptation was detailed. The motion of the tools is described at each time step by the translation of their level set functions. When necessary, a remeshing follows the translation so that anisotropic elements always surround the interfaces between powder and mould components. In addition, At each time step the nodes coordinates are updated as follows:

$$\vec{X}^{t+\Delta t} = \vec{X}^t + \vec{v}_{mesh}^t \Delta t \quad (6.55)$$

\vec{v}_{mesh} is fixed during the simulation and depends only on the imposed velocity calculated by the PID. It is different from a Lagrangian approach, where the nodes are updated

according to the velocity field computed in the mechanical problem. This approach was presented in more details in Chapter 4. If we denote z_1, z_2, z_3 and z_4 respectively the z coordinate of the node 1, 2, 3 and 4 of figure 6.50, \vec{v}_{mesh} can be written:

$$\begin{aligned}
 \vec{v}_{mesh} &= \frac{\vec{v}_{imp}}{2} && \text{in A} \\
 \vec{v}_{mesh} &= -\frac{\vec{v}_{imp}}{2} && \text{in E} \\
 \vec{v}_{mesh} &= \vec{v}_{imp} \frac{z - z_2}{2(z_1 - z_2)} && \text{in B} \\
 \vec{v}_{mesh} &= -\vec{v}_{imp} \frac{z - z_3}{2(z_4 - z_3)} && \text{in D} \\
 \vec{v}_{mesh} &= \vec{0} && \text{in C}
 \end{aligned} \tag{6.56}$$

This expression will allow the translation of the nodes of the spacers, a linear transition between the moving spacer and the fixed mould and will keep the rest invariant. Consequently, the mesh follows the motion of the different parts without increasing calculation time which is advantageous comparing to a complete Eulerian approach where more elements need to be added.

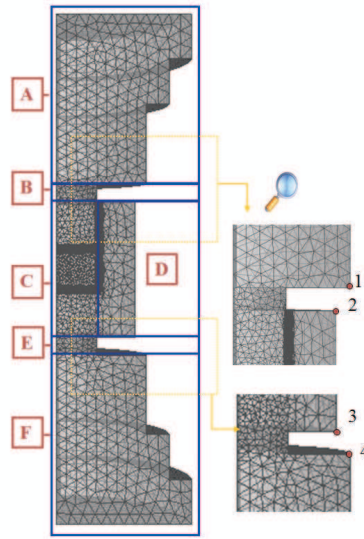


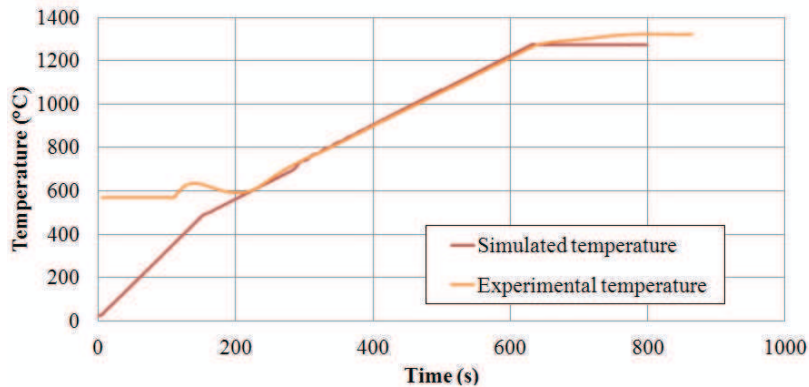
Figure 6.50: Regions of the geometry simulated where mesh velocity is controlled to update the coordinates

The numerical model is governed by the system of equations presented previously (Equation 6.49). The finite element resolution of the system was presented in Chapter 3 and Chapter 4. All physical properties are thermal dependant. The thermal conductivity is also dependant on relative density based on the work of Argento [2] as presented in

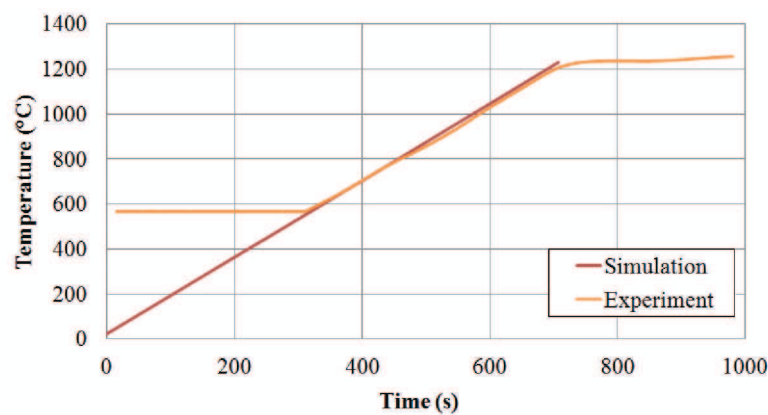
Chapter 4. The Wiedemann-Franz law is used to calculate the electrical conductivity knowing the thermal conductivity.

6.4.2 Results

The electric and thermal results won't be presented in this section since it was already discussed in the other chapters and the distribution of current and temperature do not differ in this model. Temperature evolution is presented in Figure 6.51. The experimental and simulated temperatures are compared at the PID regulation point. The PID behavior is excellent in the simulations, the temperature follows the prescribed values. In the experiments, the pyrometer is not functional below 600°C . This is why before 110 s the temperature is constant and equal to 600°C .



(a) $\Phi 8/h13.6$



(b) $\Phi 36/h8$

Figure 6.51: Comparison of the regulated temperature the experiment and the simulation

Figure 6.52 shows the evolution of the vertical stress. The regulated experimental and simulated stresses are compared. Since $TiAl$ powder densifies when temperature is above $700^{\circ}C$, in the simulation the mechanical problem is solved only after this temperature is reached at 270 s for $\Phi 8/h13.6$ and at 390 s for $\Phi 36/h8$. Before $700^{\circ}C$, the calculation is only electrical and thermal, in order to save computational time. Over $700^{\circ}C$, the simulation is fully coupled (electrical-thermal-mechanical). This makes the PID control for stress much more sensitive and forces us to deduce drastically the time step (by a factor 100, and $\Delta t = 0.01\text{ s}$). As seen in Figure 6.52, the regulation begins at 270 s for the sample $\Phi 8/h13.6$ and at 390 s for the sample $\Phi 36/h8$.

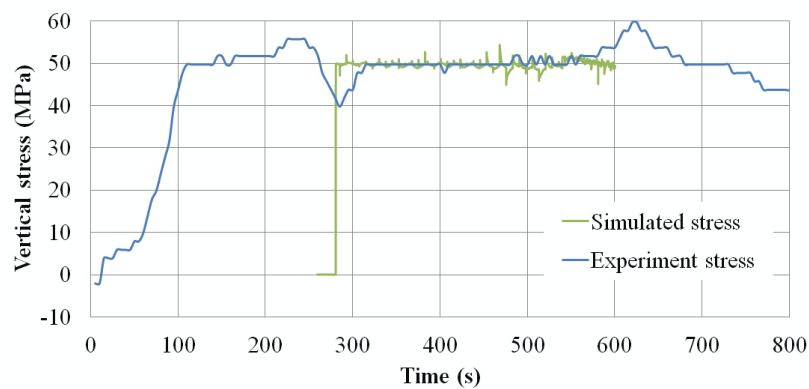
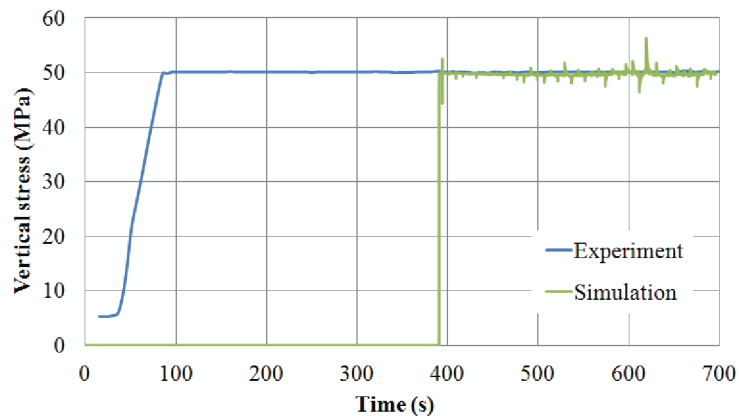
(a) $\Phi 8/h13.6$ (b) $\Phi 36/h8$

Figure 6.52: Comparison of the regulated vertical stress between the experiment and the simulation

The regulation of the load (or stress) numerically has a good behavior for both samples as seen in Figure 6.52. However, in the experiments, the regulation of sample $\Phi 8/h13.6$

presents some oscillations. This can have many explanations. In fact, for the sample $\Phi 8/h13.6$, the prescribed stress is equal to 50 MPa which leads to a very low load (2.5 kN) that is difficult to be maintained comparing to the sample $\Phi 36/h8$ where the load is equal to (50 kN). Besides, this could also be related to the regulation of temperature. As seen in Figure 6.51, around 150 s and close to the end around 600 s, the curve of temperature presents oscillations that corresponds in time to the stress oscillations.

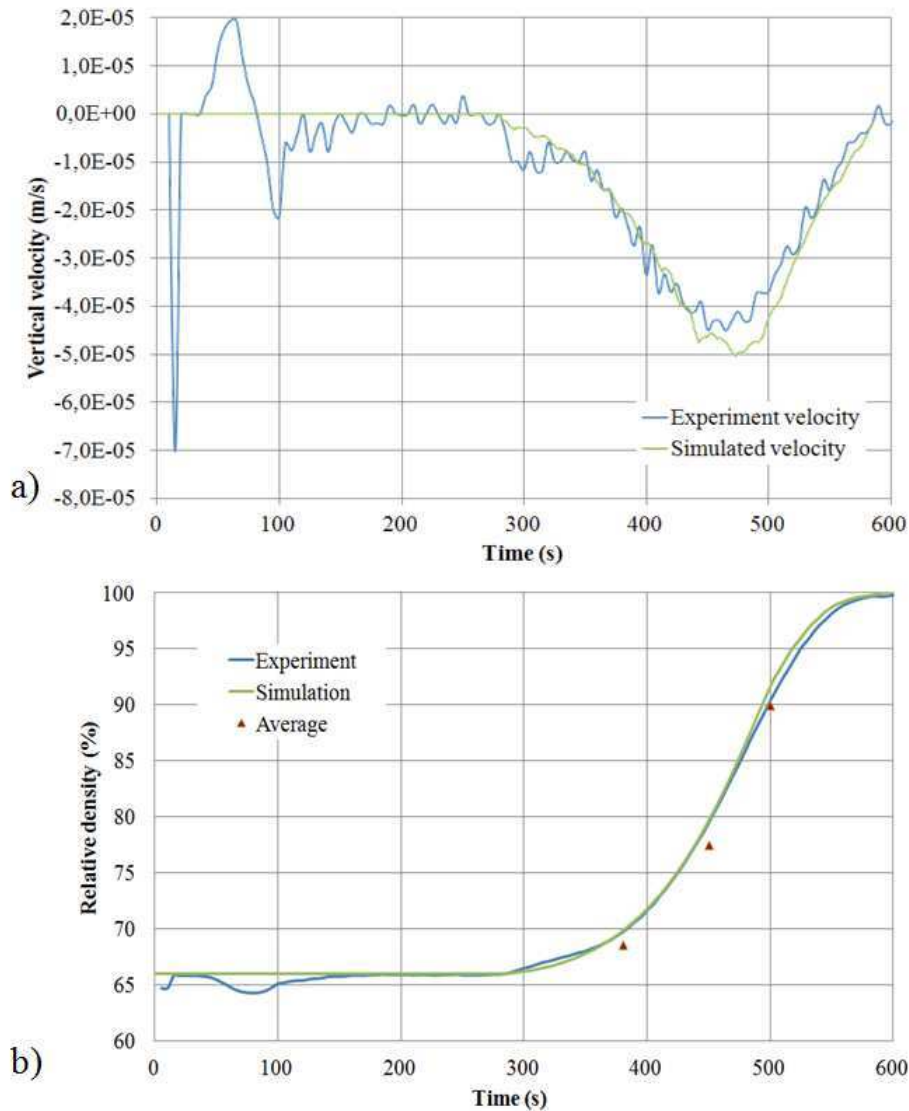


Figure 6.53: Comparison of the evolution of the vertical velocity (a) and average relative density (b) between simulation and and experiments for sample $\Phi 8/h13.6$

Figure 6.53 and Figure 6.54 show the evolution of the vertical velocity and average relative density computed with CimLib and measured during the experiments respectively for sample $\Phi 8/h13.6$ and $\Phi 36/h8$. Velocities computed with CimLib are in excellent

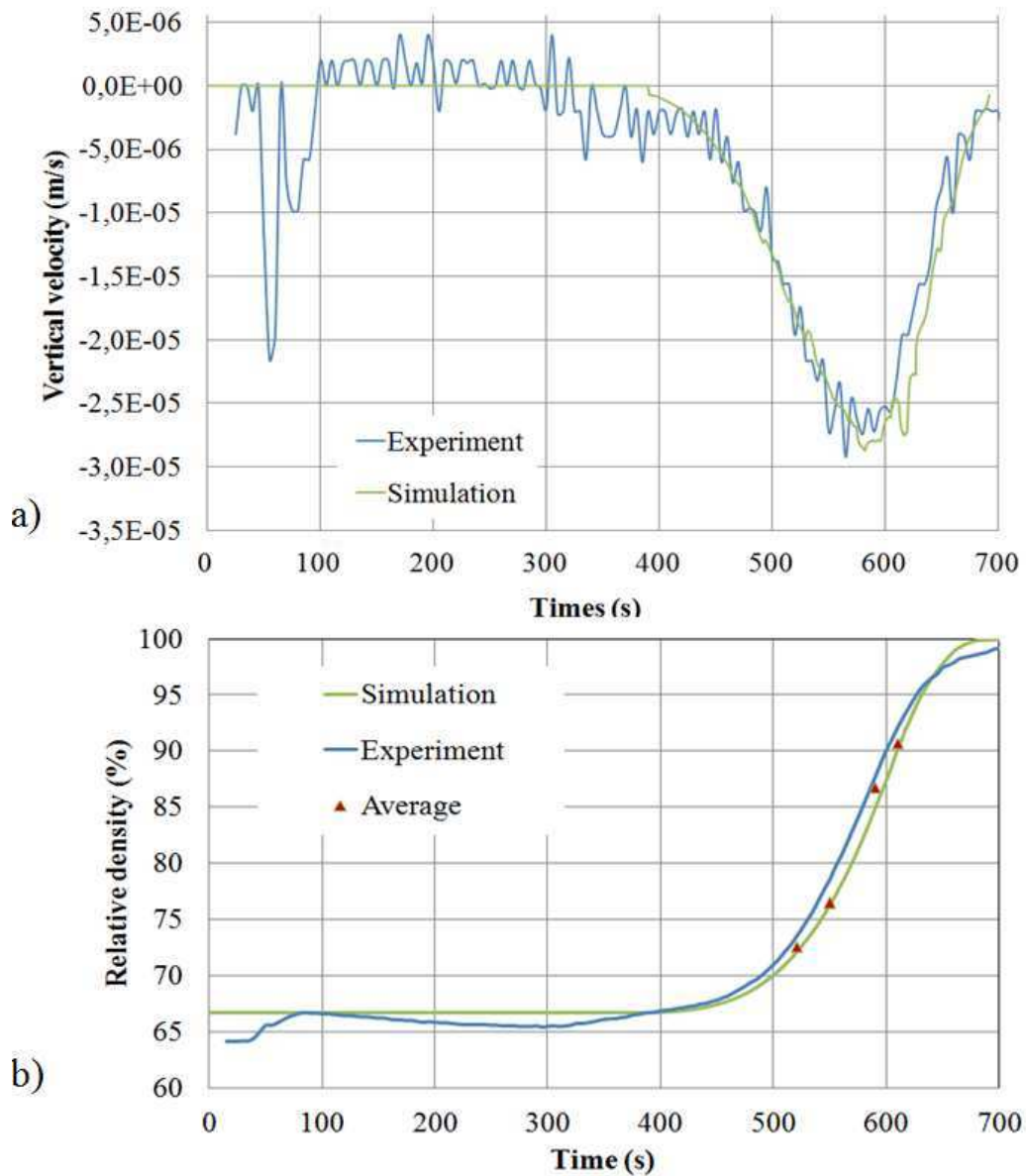


Figure 6.54: Comparison of the evolution of the vertical velocity (a) and average relative density (b) between simulation and experiments for sample $\Phi 36/h8$

agreement with the experiment. In addition, the particularity of the curves is that both cross a maximum value. This is due to the complex coupling between the three physical problems. Temperature increases which decreases the consistency that is temperature dependent. This leads to a less rigid material. Thus, to respect the constant prescribed stress, the velocity increases to its maximum. Simultaneously, the density increases and consequently the function f decreases. When densified, the material is more resistant, for that reason the velocity decreases after densification when the relative density reaches

about 95%. Not only the time evolution of the velocities are comparable, but also the value of the maximum and the time when the maximum is reached.

The comparison of the evolution of relative density is also in very good agreement. The relative density of the simulation is computed using the displacement as in the experiment in order to be coherent in the comparison (Equation 6.41). In addition, an average is computed in the simulation and is represented by the red triangles in the two charts. For both samples $\Phi 8/h13.6$ and $\Phi 36/h8$, the time steps chosen are the same as those of Figure 6.56 and Figure 6.57. As we can see, for the sample $\Phi 8/h13.6$, the comparison between the average of relative density computed on the powder (red triangles) and the average computed with displacement (green line) shows a small difference. This could be explained by the fact that the heterogeneity is more important in this sample.

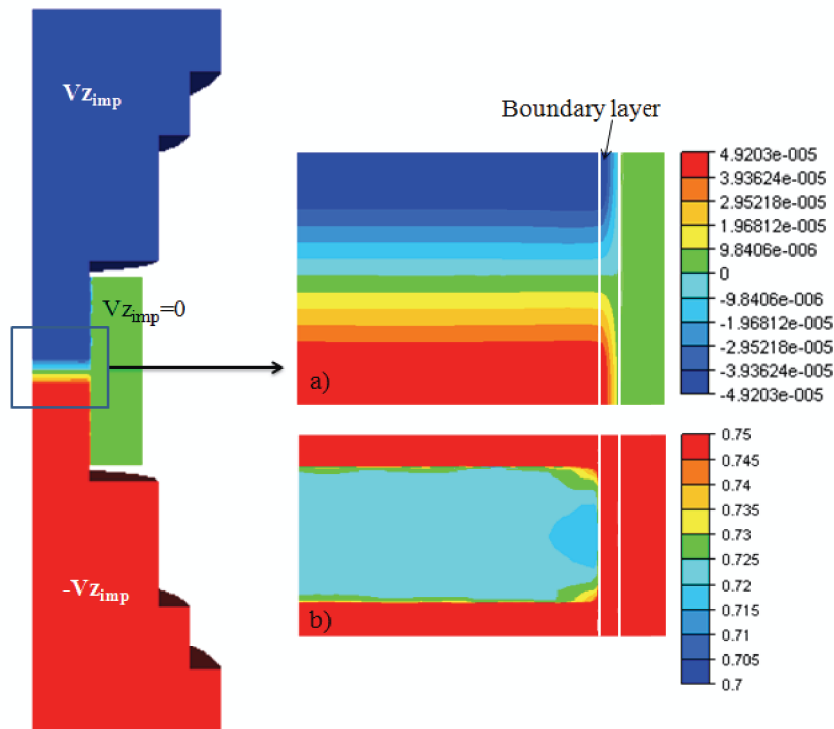


Figure 6.55: Distribution of vertical velocity for sample $\Phi 36/h8$ and a zoom on the transition in the boundary layer: a) vertical velocity and b) relative density

Figure 6.55 presents the distribution of the vertical velocity for the sample $\Phi 36/h8$. In this simulation, the friction model detailed in Chapter 5 was used for $\alpha_f = 1.5$. The transition of the velocity is observed in the zoom on the boundary layer. Besides, the distribution of relative density is presented.

Figure 6.56 shows the distribution of relative density at different times for the sample $\Phi 8/h13.6$. The regions next to the pistons densifies first. A heterogeneous distribution is observed due to friction and temperature heterogeneities. The maximum gradient,

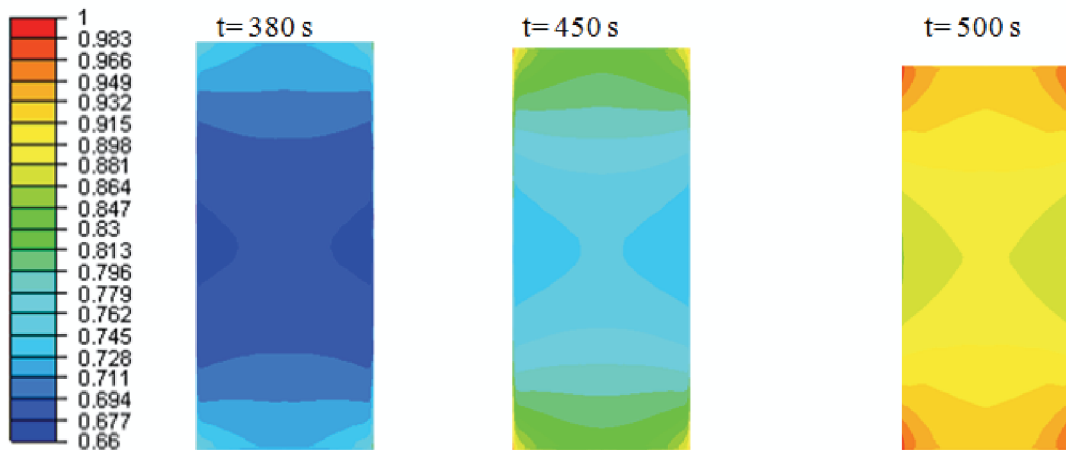


Figure 6.56: Distribution of relative density for sample $\Phi 8/h13.6$

in terms of difference between ρ_{rmax} and ρ_{rmin} , is about 8% which corresponds to the experimental gradient presented in section 6.3.3.

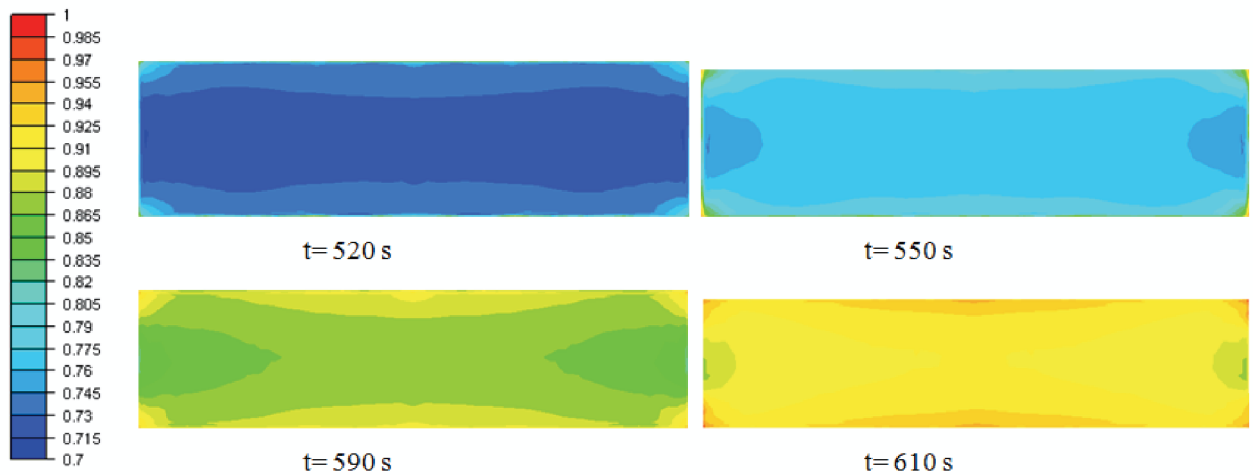


Figure 6.57: Distribution of relative density for sample $\Phi 36/h8$

Figure 6.57 shows the distribution of relative density at different times for the sample $\Phi 36/h8$. As for the sample $\Phi 8/h13.6$, the regions next to the pistons densifies first. The maximum gradient is lower than in the long sample because friction effects are less important due to the ratio height/radius that is lower. The maximum gradient is about 2%.

6.5 Conclusion

In the first part of this chapter, we presented the needed experiments to identify the parameters of the behavior law. The second part consisted in presenting the simulation of a complete SPS cycle with the identified parameters and compare it with experiments.

Creep tests could be used to identify the parameters of the dense state, consistency and sensitivity coefficient. The creep tests should be carried out on a dense sample. In order to identify f , hot isostatic pressing tests are needed. Interrupted cycles with different temperature and pressure allow to plot the evolution of the function f versus the relative density, thus it could be interpolated to deduce its expression. Concerning the function c , it was shown that uniaxial compression with constant lateral pressure tests could be used for the identification. Identically interrupted cycles with different temperature and pressure allow to get its final expression.

In IRIS project, the Paterson machine was chosen to carry out the experiments on powders and determine f and c . However, problems were encountered during the preliminary tests. The furnace didn't resist the desired high temperatures. Hence, the experiments were abandoned.

In the second section of the chapter, we presented the procedure followed to identify Abouaf functions using SPS. Interrupted cycles are accomplished using the SPS process. This technique has some disadvantages. In fact, during a SPS test the temperature is not homogeneous in the sample and friction effects influence the homogeneity of densification. This makes the identification complex. During the experiments accomplished by the CEMES, the evolution of displacement and temperature was measured. In addition, the distribution of porosity is measured in the powder using the SEM. As a first step, Matlab is used to calibrate the expressions of the functions neglecting heterogeneities of temperature and friction and using the analytic solution of the mechanical problem. Once the functions calibrated, simulations are carried out to define the value of the friction coefficient.

The last section consisted in simulating a complete SPS cycle and comparing it with experiments. In these simulations, all the experimental conditions were modeled. The temperature and stress were both regulated according to a prescribed value using a PID loop. The coupled electrical thermal mechanical problems were solved. Results were compared between experiments and simulations. The comparisons were in very good agreement. We saw that the evolution of velocity has the particularity to cross a maximum value during the densification phase. The evolution of relative density was also compared and showed also a good agreement. Further improvements in the model would be interesting. In fact, the PID regulation in the mechanical problem necessitates small time steps to avoid the sudden variation of the parameters that are coupled together. This has a disadvantage in increasing the computational time. To improve the performance, it would be interesting to impose directly the load (or stress) on the boundary of the powder. However, a development of the model is needed, since we are using the

monolithic Eulerian approach where the interface of the powder is defined by the level set function.

Bibliography

- [1] M. Abouaf. *Modélisation de la compaction de poudres métalliques frittées*. PhD thesis, Université scientifique et médicale et Institut national polytechnique de Grenoble, 1985.
- [2] C. Argento. *Modélisation du comportement thermique et mécanique des poudres métalliques- Applications à la compaction isostatique à chaud*. PhD thesis, Université Joseph Fourier- Grenoble I, 1994.
- [3] <http://www.mae.ufl.edu/subhash/facility.htm>. *Center for Dynamic Response of Advanced Materials*. University of Florida.
- [4] J.C. Lagarias, J. A. Reeds, M. H. Wright, and P.E. Wright. Convergence properties of the Nelder-Mead Simplex method in low dimensions. *SIAM Journal of Optimization*, 9:112–147, 1998.
- [5] D. Lin and F. Sun. Superplasticity in a large-grained tial alloy. *Intermetallics*, 12:875–883, 2004.
- [6] C. Nicolle. *Mise en forme de poudres de bore par compression isostatique à chaud: Détermination des propriétés rhéologiques et simulation numérique du procédé*. PhD thesis, Université de Bourgogne, 1999.
- [7] T.G. Nieh, L.M. Hsiung, and J. Wadsworth. Superplastic behavior of a powder metallurgy TiAl alloy with a metastable microstructure. *Intermetallics*, 7:163–170, 1999.

Chapter 7

Conclusion and perspectives

The main objective of the thesis was to develop a numerical model to simulate the Spark Plasma Sintering process, in view of predicting the sintering of industrial parts to be used in aeronautics. Modeling the process is complex due to the different physical phenomena that interact. Three coupled problems need to be simulated:

- The electric problem to study the distribution of current that causes heating by Joule effect, both in the tooling and in the part
- The thermal problem to understand the heating mechanisms during the process
- The mechanical problem to compute the stresses and densification.

In addition to the development of a numerical model to predict sintering, another objective was to identify a relevant behavior law for a *TiAl* alloy powder.

Before describing the implementation of the numerical model, a bibliography review was presented in Chapter 2. In the bibliography review we have shown that most of the models found in the literature were limited. First developments in numerical modeling in SPS were limited to electric thermal problems. Then, an elastic behavior was considered in the first developments of modeling the mechanical problem. Later on, around 2008, the models were more representative, the three coupled problems were solved and the evolution of densification was computed. We have shown that it exists a real need for 3D models including the major physical phenomena.

As a first step in the development of such a 3D model, we implemented the resolution of the electric thermal problem using the monolithic approach in CimLib. This approach consists in using a single mesh which encompasses the powder domain and the different tools. Level set functions define the interfaces of the different domains and mixing laws are used to associate the corresponding physical properties to each material. This electric thermal solver was validated. First, a simplified model was simulated with simplified boundary conditions. This model was validated by comparison with literature where three dense samples were considered: nickel, graphite and alumina. We found that the

electric current was concentrated at the level of the pistons. This was due to their small section comparing to mould and spacers. An interesting result was heating of the sample by conduction in addition to Joule effect. In fact, the distribution of the source term along the geometry was very comparable for the three materials. The source term was very low inside the sample. Hence, the sample was mainly heated by conduction from the surrounding graphite. When comparing thermal results, it was shown that, the thermal dependency of physical properties should be taken into account in the model since the temperature varied from 785°C to 1350°C . Another coupled electric-thermal model was simulated considering a complete SPS set-up. The Sumitomo machine installed at the "Plateforme Nationale de Frittage Flash, Toulouse" was simulated. Results were compared between CimLib and Comsol for *TiAl* and alumina samples. Comsol results were achieved by our colleagues at CEMES. The comparison of temperature and current distribution and evolution were found in very good agreement. This comparison allowed to validate indirectly with experiments, since Comsol results were compared to experimental results using the microstructure phase change in *TiAl* at 1350°C .

In a second step, the electric thermal model was completed by the resolution of the mechanical problem. The powder followed a compressible viscoplastic law. The Norton-Hoff power law was considered for the viscoplastic behavior. The densification was modeled using the Abouaf macroscopic model. The powder was considered as a continuum characterised by its relative density. The model was implemented in CimLib. First validations consisted in comparing the results of a simple uniaxial compaction and a die compaction with analytic results in a Lagrangian framework. The second step was to validate the model in the Eulerian approach where die and piston were modeled. Once the implementation validated, electric thermal and mechanical problems were coupled and a simulation was carried out where the evolution of relative density was computed. This simulation necessitated the updating of the mesh at each time increment. The mesh update was a combination between the Eulerian and Lagrangian approaches. Hence, by calculating the position of the nodes it was possible to model the piston travel without increasing the number of elements. Two simulations were compared considering or not the dependence of the conductivities on relative density. In the case of *TiAl* the temperature differences were found to be equal to 5°C . It is important to consider the dependency because temperature refers to the microstructure phase and it would be more accurate. It was shown that a dissymmetry was observed in densification in case of a null displacement of one end of the compact. In fact, the dissymmetry of the geometry caused a dissymmetry in the temperature field. Hence, the temperature dependent parameters were not symmetric in the axial direction and so the densification. For that reason, we deduced that during the SPS process the mould moved with the piston due to friction in a way to conserve symmetry. This phenomenon is quite complex and was not considered in this thesis, the mould being considered to be moving depending on the piston displacement in a way to

respect symmetry.

The experimental observations from IRIS partners showed a heterogeneous distribution of relative density when sintering a long sample. The difference might reach up to 14% inside the powder compact. Temperature heterogeneities were not sufficient to cause such rates. Friction was in part responsible of this distribution. This is why, a friction model was integrated in the framework of the Eulerian monolithic approach. The model was inspired from the boundary layer principle. A boundary layer was introduced between the mould and the powder taking advantage of the capacities of the adaptive meshing procedure in Cimlib. This layer obeys the same behavior law as the powder and has a consistency that results in the shear stress reproducing the effect of friction. A numerical study was carried out to relate the consistency layer to its thickness and to the friction coefficient of the Norton friction law. This study was achieved assuming a homogeneous constant temperature.

The last chapter of this thesis discussed the identification of the behavior law parameters. The experimental procedure needed to the identification was presented. First, the dense state should be determined by simple creep tests at different cycles of temperature and load. Once the consistency and the sensibility coefficient to the strain rate determined, it was possible to identify the Abouaf function f by a hot isostatic pressing test. Then, the Abouaf function c could be determined carrying out a uniaxial compression test with the application of a constant lateral pressure. The dense state was identified thanks to experiments carried out by our partners at ONERA. Unfortunately, the identification of Abouaf functions did not succeed as planned. At PPRIME (ENSMA), the Paterson machine chosen for the experiments appeared to be very sensitive to high temperatures. The preliminary tests showed many problems. Unpredicted deformations of the powder caused damage of the machine components. For that reason, we had recourse to the SPS process and we proposed an identification of Abouaf functions using directly SPS, based on experiments conducted in CEMES. Such a direct identification was challenging, because the densification is heterogeneous and the friction is unknown between the mould and powder. This is why, inverse analysis was applied. An algorithm was developed in Matlab to calibrate the parameters of Abouaf functions using the results of SPS interrupted cycles. A friction coefficient was also calibrated carrying out a simplified simulation using CimLib. Finally, the parameters of Abouaf functions and the optimized friction coefficient were then used to simulate the complete SPS cycle. The evolution of relative density as well as its distribution was compared with the experiments. Results are very satisfying. It was found that the $TiAl$ powder densifies when reaching $700^{\circ}C$. Friction effects can be neglected when the ratio of height over diameter is low. However, the limits of this approach are clear: the coefficient c cannot be identified reliably through this approach. In the future, it would be preferable to come back to triaxial tests for parameters identification. As mentioned, this function is related to shear and can

not be deduced from a die compaction test. The identification of Abouaf functions using SPS experiments is not sufficient. Despite of the fact that the function c could not be identified, the densification is not homogeneous in the powder due to friction. It would have been more accurate to use the tests proposed in Chapter 6, more precisely, the hot isostatic pressing and the uniaxial compression with the application of lateral pressure. Unfortunately, in the framework of IRIS project, we didn't have the opportunity to perform the needed experiments.

Regarding now the perspectives that can be envisaged following the present work, it should be noted first that the Spark Plasma Sintering process differs from other mechanical processes by the number of phenomena interfering simultaneously which makes its numerical modeling a challenge. The mechanical model developed in this thesis can be enlarged to simulate more mechanisms and conditions.

The mechanical model that we developed could be enriched by the consideration of the deformation by thermal expansion. As seen in the experimental displacement curves, at the beginning, the pistons moved in the opposite direction due to the powder expansion. In addition, the mechanical model could be completed by other microscopic mechanisms similarly to the models proposed by Olevsky where electromigration, surface diffusion and diffusion under load were considered. However, as seen in the literature review, the complexity of the SPS conditions, application of an electric current and load and high heating rates, caused a misunderstanding in the mechanisms interfering during densification. Opinions diverged concerning neck formation between powder particles and the effect and existing of plasma and electric sparks. For that reason, it is quite a challenge to model these phenomena.

The deformations that occur at the particle/particle level, could influence local heating and local stress in the powder. Even if the first macroscopic expressions suggested by Olevsky and Froyen are to be considered in a first approach, simulation at the microscopic scale would help to develop models to be used in the mesoscopic scale using RVEs. A homogenisation could be then carried out to define more complete macroscopic models. This might be a great help to complete the mechanical model of the powder behavior in SPS. The macroscopic model will assure the boundary conditions for the RVE, and, on the other side, the mesoscopic calculations will help understanding the particle to particle mechanisms. At CEMEF, developments have recently been carried out in that direction, in view of modeling high temperature powder compaction in the framework of the hot isostatic pressing [1].

Eventhough the mechanical model chosen was shown to be very satisfying, when simulating the complete SPS cycle, the mechanical problem appeared to be time consuming. The PID loop in the mechanical boundary conditions necessitated a small time step in order to follow the prescribed load. It was very sensitive to the coupling between the three

problems that causes parameters variation with temperature and density. It would be less cost effective to apply the load directly at the interface boundary of the powder. More research in this field is interesting to model the application of the load on the interface defined only by the level set function in the Eulerian approach.

In addition, another improvement could be the simulation of the tools behavior. Now, the mechanical problem is limited to the densification of the powder. It would be important to consider the tools behavior in our numerical problem using the monolithic approach. This will consist in considering two different types of material laws and incorporate them in one equation that will be solved on one mesh using the monolithic approach in CimLib.

Concerning the perspectives of the electric and thermal problems, the electric and thermal contact resistances could be added. They might influence heating by conduction mostly at the vertical interfaces. In the orthogonal direction to the applied load, spacers are squeezed and the contact is close to a perfect condition. A study could be carried out to see the impact of adding such a contact resistance. Considering the high SPS heating rates, it is not sure that the global temperature distribution would be affected. However, it would be interesting to add more thermocouples in the machine and measure temperature at different locations to check the accuracy of the model.

As discussed, numerous perspectives could be envisaged. However, this could be integrated in the model developed in this work to build a precise numerical model and a predictive tool for SPS process since today the spark plasma sintering process attracts more and more engineers in industrial applications.

Bibliography

- [1] A. Zouaghi, M. Bellet, Y. Bienvenu, G. Perrin, and M. Bernacki D. Cédât. Modélisation de la phase de compaction du procédé cic à l'échelle mésoscopique. In *Proc. Congrès Français de Mécanique, Besancon, France, published (DVD) by Association Francaise de Mécanique*, page 6 pages, 28 August - 2 September, 2011.

Appendix 1: Paterson preliminary tests

The sets that were prepared by ICB and the preliminary tests accomplished at PPRIME are presented here below. Problems encountered are specified after the presentation of each experimental conditions

1. First set is sintered by SPS at $800^{\circ}C$ and $100\ MPa$ for $0'$ maintain time, the compact has a relative density equal to 67.8%. These samples are difficult to manipulate because they are very crumbly. For that reason, the dimension of the cylinder should have precise dimension. During SPS, a layer of carbon might stick to the compact increasing its diameter. This layer is removed by polishing the sample. When dealing with high porosities, it is not possible to manipulate the compact.
2. Second set is sintered at $850^{\circ}C$ and $100\ MPa$ for $0'$ maintain time, the compact has a relative density equal to 71.74%. A preliminary isostatic pressing test is achieved with Paterson machine on this sample. At room temperature, the compact is subjected to $100\ MPa$, then $200\ MPa$, then $300\ MPa$ during 30 min for each pressure. No variation of the height is registered. However, the sample is deformed and takes the shape of Figure 6.18. This deformation might be caused from the heterogeneities in density when pre-compacting by SPS. In fact, for a temperature lower than $700^{\circ}C$, it is difficult to compact a *TiAl* powder or else high pressures are needed.
3. The third set is sintered at $900^{\circ}C$ and $100\ MPa$ for $0'$ maintain time, the compact has a relative density equal to 74.3%. Another set with the same conditions but for 3 min of maintain is prepared where the compact has a relative density equal to 82.4%. At institute PPRIME, the sample with 74.3% relative density is chosen to carry out the experiment at high temperature. The goal temperature is $700^{\circ}C$, the pressure needed so the furnace assures such temperature is $300\ MPa$. The slope of temperature is $10^{\circ}C/min$ until reaching $125^{\circ}C$ and then $20^{\circ}C/min$. A problem occurs when temperature reaches $680^{\circ}C$. The aluminium cover breaks and a leak is observed at this level. As a consequence, the experiment is interrupted to avoid any damage of the machine. Figure 6.19 shows the set up extracted after the interruption. The crack is on the right side between the sample and the piston.

The aluminium cover is very sensitive, any empty space between the sample and the cover causes the crack and hence the leak.

4. Another experiment was carried out with the second set (initial density approximately 70%). This time the goal temperature is reduced to 600°C and identically for 300 MPa . The initial height and radius of the sample are respectively 15.3 mm and 12.7 mm with a rate of porosity equal to 31%. The temperature is maintained at 600°C for 37 minutes. The experiment is interrupted. The final height and radius of the sample are respectively 15.08 mm and $12 - 12.2\text{ mm}$ which means a final porosity of 26%. The measurements during the phase of constant temperature show the absence of any variation of the height. But since no measurements are possible during the increasing phase, we can not be sure when the reduction occurs.
5. From the same set, a sample is chosen with an initial porosity equal to 29.6%. The initial height of the sample is 15.5 mm and the radius 12.9 mm . The sample height is larger than what the machine can tolerate. For that reason, the compact is polished at the upper and lower sides to get a height equal to 15 mm . As previously, the same slope of temperature is applied with a pressure equal to 300 MPa . Just when 600°C is reached, the aluminium cover breaks and a leak occurs. The experiment is interrupted. The photos of figure 6.20 show the crack on the lower edge of the compact. The trace of the leak is visible on the aluminium cover.

Modélisation numérique du procédé de frittage flash

RESUME : Le SPS (Spark plasma sintering) ou frittage flash est une technique innovante de compaction de poudre. Ce procédé fait intervenir le courant électrique pour chauffer l'échantillon en appliquant simultanément une pression. Grâce à la vitesse de chauffage, le procédé SPS apparaît comme étant une technologie prometteuse dans le secteur aéronautique servant à produire des matériaux denses à microstructure fine, composés par des intermétalliques difficiles à fondre, à former et à usiner avec les procédés conventionnels. Cependant, la fabrication de formes complexes est problématique à cause des hétérogénéités en densité qui peuvent apparaître lors de la compaction et qui proviennent de la distribution de la température et des contraintes dans la poudre compactée. La distribution du courant, de la température et des contraintes, ainsi que leurs différents effets, font l'objet d'une large étude, étant responsables de l'homogénéité de la microstructure. Une modélisation numérique 3D du procédé est réalisée, dans le cadre de la librairie CimLib. Elle englobe trois problèmes physiques fortement couplés : électrique, thermique et mécanique. Nous utilisons une approche monolithique qui consiste à résoudre une équation pour chaque problème sur un maillage unique représentant outils et poudre. Tout d'abord le couplage électrique-thermique est modélisé et les simulations numériques sont validées. Une loi de comportement viscoplastique compressible s'appuyant sur un modèle d'Abouaf est utilisée pour modéliser la densification de la poudre de TiAl. Ce modèle est validé par plusieurs cas tests de compaction de poudre dans un contexte lagrangien puis eulérien avant de passer à une simulation complète de couplage électrique-thermique-mécanique. Dans ce contexte monolithique, nous développons un modèle pour prendre en compte les effets du frottement entre la poudre et le moule. Enfin, la loi de comportement utilisée est identifiée pour la poudre intermétallique de TiAl. Le frittage par SPS d'échantillons de différentes tailles est simulé. Les résultats en termes de distribution de densité et déplacement sont validés grâce à une comparaison avec l'expérience.

Mots clés : frittage de poudre, couplage électrique-thermique-mécanique, méthode des éléments finis, loi viscoplastique compressible d'Abouaf, identification de paramètres

Numerical modeling of the spark plasma sintering process

ABSTRACT : Spark plasma sintering process (SPS) is a breakthrough technology for producing high quality sintered materials. An electric current is applied simultaneously with a vertical load to sinter the powder placed in a graphite mould. Joule effect leads to high heating rates which are favorable for enhancing the microstructure and physical properties. However, manufacturing complex shapes is problematic due to heterogeneities in density distribution that may appear during compaction. For that reason, the development of a numerical model to predict sintering is necessary. The model should help controlling temperature and stress distributions, which are responsible for the microstructure homogeneity. A 3D numerical model is developed to ensure a predictive tool for SPS using CimLib, a code developed at CEMEF. The numerical model presents three physical problems strongly coupled: an electric problem, a thermal problem and a mechanical problem. A monolithic approach is used which consists in solving one equation for each problem using one unique mesh for tools and powder. First the electric thermal coupling is modeled and the numerical simulations are validated by comparison with commercial codes. A viscoplastic compressible law based on Abouaf model is implemented to model the densification of TiAl powder. This model is validated by comparing the numerical results of different compaction tests with analytic solutions using a Lagrangian and Eulerian framework. Then a fully coupled electric-thermal-mechanical simulation is carried out. In the monolithic framework, a model is developed to take into account friction effects between powder and mould. Finally, the parameters of the selected material law are identified for TiAl powder using our numerical model and SPS experiments. Sintering of different samples is then simulated. Results are compared with the experiments in terms of density distribution and displacement.

Keywords : powder sintering, electric-thermal-mechanical coupling, finite element method, viscoplastic compressible law, Abouaf model, parameter identification